

CARBON DIOXIDE REFORMING OF METHANE
ON NI-BASED BIMETALLIC CATALYSTS

A THESIS SUBMITTED TO
THE GRADUATE SCHOOL OF NATURAL AND APPLIED SCIENCES
OF
MIDDLE EAST TECHNICAL UNIVERSITY

BY

HALE AY

IN PARTIAL FULFILLMENT OF THE REQUIREMENTS
FOR
THE DEGREE OF DOCTOR OF PHILOSOPHY
IN
CHEMICAL ENGINEERING

JUNE 2014

Approval of the thesis:

**CARBON DIOXIDE REFORMING OF METHANE
ON NI-BASED BIMETALLIC CATALYSTS**

submitted by **HALE AY** in partial fulfillment of the requirements for the degree of
**Doctor of Philosophy in Chemical Engineering Department, Middle East
Technical University** by,

Prof. Dr. Canan Özgen
Dean, Graduate School of **Natural and Applied Sciences**

Prof. Dr. Halil Kalıpçılar
Head of Department, **Chemical Engineering**

Prof. Dr. Deniz Üner
Supervisor, **Chemical Engineering Dept., METU**

Examining Committee Members:

Prof. Dr. Saim Özkar
Chemistry Dept., METU

Prof. Dr. Deniz Üner
Chemical Engineering Dept., METU

Prof. Dr. Timur Doğu
Chemical Engineering Dept., METU

Prof. Dr. Zeynep İlksen Önsan
Chemical Engineering Dept., Boğaziçi University

Assist. Prof. Dr. Harun Koku
Chemical Engineering Dept., METU

Date: 04.06.2014

I hereby declare that all information in this document has been obtained and presented in accordance with academic rules and ethical conduct. I also declare that, as required by these rules and conduct, I have fully cited and referenced all material and results that are not original to this work.

Name, Last name: Hale AY

Signature:

ABSTRACT

CARBON DIOXIDE REFORMING OF METHANE ON NI-BASED BIMETALLIC CATALYTS

Ay, Hale

Ph.D., Department of Chemical Engineering

Supervisor: Prof. Dr. Deniz Üner

June 2014, 201 Pages

Carbon dioxide reforming of methane is a promising process for the utilization of two important greenhouse gases and the production of synthesis gas with a lower H₂/CO ratio which is preferred in Fischer–Tropsch synthesis. Ni catalysts have taken great interest in dry reforming of methane due to their high catalytic activity, easy availability and low cost. However, the main restriction of Ni-based catalysts is the formation of carbon which causes catalyst deactivation. The objective of this thesis was to reduce carbon formation and improve the life time of Ni based catalysts.

Al₂O₃ supported and CeO₂ supported Ni, Co and Ni-Co catalysts were prepared via incipient wetness impregnation method. Al₂O₃ was used as support material due to its high thermal stability. CeO₂ was used as another support material due to its redox Ce⁴⁺/Ce³⁺ sites and ability to exchange oxygen. Co was introduced to the Ni-based catalyst in order to understand the effect of bimetallic catalysts in dry reforming of methane. The catalysts prepared by incipient wetness impregnation method were calcined at two different temperatures (700°C and 900°C) to elucidate the effect of calcination temperature. As an alternative to conventional preparation methods, Ni/Al₂O₃ catalysts were also prepared by polyol method.

Ni/Al₂O₃ and Ni-Co/Al₂O₃ catalysts exhibited comparable activities in terms of CH₄ and CO₂ conversion; H₂ and CO yield. While doing the calcination at 700°C or 900°C did not really affect the catalytic performances of Ni/Al₂O₃ and Ni-Co/Al₂O₃, it had significant influence on the performance of Co/Al₂O₃. Carrying out the calcination at higher temperatures was found to be more preferable in terms of carbon deposition. Higher amount of coke was deposited on Ni-Co/Al₂O₃ compared to Ni/Al₂O₃ when the calcination was done at 700°C. DRIFTS and microcalorimetry studies showed that CO₂ activation took place on Al₂O₃ for both Ni/Al₂O₃ and Ni-Co/Al₂O₃ catalysts. ¹³C NMR characterization of deposited coke demonstrated that it not only originated from CH₄, but CO₂ had also significant role in coke formation.

Polyol process was employed to obtain Ni/Al₂O₃ catalysts in the presence of PVP as stabilizer and ethylene glycol as both solvent and reducing agent. The effect of PVP/Ni ratio was studied. Ni/Al₂O₃-without-PVP and Ni/Al₂O₃-PVP/Ni=2.5 catalysts exhibited quite high performance at 600°C and 700°C without making a reduction step before the reaction.

The activities of CeO₂ supported catalysts decreased with increasing calcination temperature. While Ni/CeO₂ and Ni-Co/CeO₂ provided comparable high activities, Co/CeO₂ was shown to be an inactive catalyst for dry reforming of methane reaction at the specified operating conditions.

O₂ and CO pulse experiments were done to get information about the redox properties of different kinds of ceria samples, including commercial ceria, coprecipitated ceria and ceria fibers. The ceria fibers having the lowest surface area was shown to have the highest oxygen uptake value. This phenomenon demonstrated that the oxygen storage capacity of the ceria samples depended strongly on the morphology.

Keywords: dry reforming of methane, carbon dioxide, coke, ¹³C NMR, Ni, Co, Al₂O₃, CeO₂

ÖZ

Nİ-BAZLI BİMETALİK KATALİZÖRLERDE METANIN KARBONDİOKSİT REFORMASYONU

Ay, Hale

Doktora, Kimya Mühendisliği Bölümü

Tez Yöneticisi: Prof. Dr. Deniz Üner

Haziran 2014, 201 sayfa

Metanın karbon dioksit reformasyonu, iki önemli sera gazının kullanımı ve Fischer–Tropsch sentezinde tercih edilen düşük H₂/CO oranlı sentez gazı üretimi için ümit verici bir prosestir. Yüksek katalitik aktivitesi, elde edilmesindeki kolaylığı ve düşük maliyeti nedeniyle Ni katalizörleri metanın kuru reformasyonunda büyük ilgi çekmiştir. Ancak, Ni bazlı katalizörlerin başlıca kısıtlaması katalizör deaktivasyonuna sebep olan karbon oluşumudur. Bu tezin amacı, Ni bazlı katalizörlerin karbon oluşumunu azaltmak ve yaşam süresini artırmaktır.

Al₂O₃ destekli ve CeO₂ destekli Ni, Co ve Ni-Co katalizörleri ıslaklık başlangıcı emdirme metoduyla hazırlanmıştır. Yüksek ısıl kararlılığı nedeniyle Al₂O₃, destek maddesi olarak kullanılmıştır. Ce⁴⁺/Ce³⁺ redoks siteleri ve oksijen alıp verebilme yeteneğinden dolayı CeO₂, diğer bir destek maddesi olarak kullanılmıştır. Çift metalli katalizörlerin metanın kuru reformasyonundaki etkisini anlayabilmek için Ni-bazlı katalizöre Co eklenmiştir. Kalsinasyon sıcaklığının etkisini açıklamak için ıslaklık başlangıcı emdirme metoduyla hazırlanan katalizörler iki farklı sıcaklıkta (700°C ve 900°C) kalsine edilmiştir. Geleneksel hazırlama metotlarına alternatif olarak Ni/Al₂O₃ katalizörleri, poliol metodu ile de hazırlanmıştır.

Ni/Al₂O₃ ve Ni-Co/Al₂O₃ katalizörleri CH₄ ve CO₂ dönüşümü; H₂ ve CO verimi bakımından karşılaştırılabilir aktivite sergilemiştir. Kalsinasyonun 700°C ya da 900°C'de yapılması Ni/Al₂O₃ ve Ni-Co/Al₂O₃'ün katalitik performansını ciddi şekilde etkilemezken, Co/Al₂O₃'ün performansı üzerinde önemli etkisi olmuştur. Karbon birikimi açısından kalsinasyonunun yüksek sıcaklıkta yapılması daha tercih edilir bulunmuştur. Kalsinasyon 700°C'de gerçekleştirildiğinde, Ni/Al₂O₃'e kıyasla Ni-Co/Al₂O₃ üzerinde daha fazla miktarda kok birikmiştir. DRIFTS ve mikroklorimetri çalışmaları, hem Ni/Al₂O₃ hem de Ni-Co/Al₂O₃ katalizörü için CO₂ aktivasyonunun Al₂O₃ üzerinde gerçekleştiğini göstermiştir. Biriken kokun ¹³C NMR karakterizasyonu, kokun sadece CH₄'ten kaynaklanmadığını, CO₂'nin de kok oluşumunda önemli rolü olduğunu göstermiştir.

Ni/Al₂O₃ katalizörleri, bağlayıcı olarak PVP, çözücü ve indirgen madde olarak etilen glikol varlığında poliol prosesi kullanılarak elde edilmiştir. PVP/Ni oranı etkisi çalışılmıştır. Ni/Al₂O₃-PVP-içermeyen and Ni/Al₂O₃-PVP/Ni=2.5 katalizörleri 600°C ve 700°C'de tepkime öncesinde indirgeme yapmaksızın oldukça yüksek performans sergilemiştir.

CeO₂ destekli katalizörlerin aktiviteleri artan kalsinasyon sıcaklığıyla beraber düşmüştür. Ni/CeO₂ ve Ni-Co/CeO₂ karşılaştırılabilir yüksek aktivite gösterirken, Co/CeO₂'nin belirlenen çalışma koşullarında metanın kuru reform reaksiyonu için aktif bir katalizör olmadığı gösterilmiştir.

Ticari seryum, beraber çökeltile seryum ve seryum liflerini kapsayan farklı seryum örneklerinin redoks özellikleri hakkında bilgi sahibi olmak için O₂ ve CO vurum deneyleri yapılmıştır. En düşük yüzey alanına sahip seryum liflerinin en yüksek oksijen alma değerine sahip olduğu gösterilmiştir. Bu olay seryum örneklerinin oksijen depolama özelliklerinin ciddi şekilde morfolojiye bağlı olduğunu ortaya koymuştur.

Anahtar kelimeler: metanın kuru reformasyonu, karbon dioksit, kok, ¹³C NMR, Ni, Co, Al₂O₃, CeO₂

To my beloved mother and father...

ACKNOWLEDGEMENTS

I would like to thank my thesis supervisor Prof. Dr. Deniz Üner for her support, advice and guidance throughout the study. Not only I developed strong academic skills, but also deep insight in research equipment as a result of her uncompromising do-it-yourself philosophy in the laboratory.

My brief visits to Prof. Dr. Joerg Schneider's laboratory at Technical University of Darmstadt and Prof. Dr. Martin Mühler's laboratory at Ruhr University Bochum broadened my perspective both academically and personally. I am thankful to Prof. Dr. Joerg Schneider and Prof. Dr. Martin Mühler for giving me the opportunity to work in their laboratories.

Thanks are due to Prof. Dr. Jeffrey A. Reimer and his team from University of California, Berkeley for NMR measurements.

I would like to thank former and present CACTUS research group members for their companionship and help.

I would like to present my thanks to the technical staff of Chemical Engineering Department.

Special thanks are due to METU Central Laboratory for TEM characterizations.

Project grant of TUBITAK 112M561 and TUBITAK Inten-C-107M447 are gratefully acknowledged.

Most importantly I would like to express my endless thanks to my beloved mother and father for their continuous love, encouragement and support through my life.

TABLE OF CONTENTS

ABSTRACT	v
ÖZ	vii
ACKNOWLEDGEMENTS	x
TABLE OF CONTENTS	xi
LIST OF TABLES	xv
LIST OF FIGURES	xvi
CHAPTERS	
1. INTRODUCTION.....	1
1.1 Energy and Synthesis Gas	1
1.2 Greenhouse Gases and Global Warming.....	3
1.3 Objectives	4
2. REFORMING OF METHANE TO SYTHESIS GAS.....	7
2.1 Steam Reforming of Methane	7
2.2 Partial Oxidation of Methane	8
2.3 Carbon dioxide Reforming of Methane	9
2.3.1 Thermodynamic Analysis of Carbon dioxide Reforming of Methane	10
2.3.2 Mechanism of Carbon dioxide Reforming of Methane	14
2.3.3 Deactivation due to Carbon Deposition	19
3. EXPERIMENTAL	25
3.1 Catalyst preparation	25
3.1.1 Preparation of Ni/Al ₂ O ₃ , Co/Al ₂ O ₃ and Ni-Co/Al ₂ O ₃ by incipient wetness impregnation method	25
3.1.2 Preparation of Ni/Al ₂ O ₃ by polyol method	26
3.1.3 Preparation of Ni/CeO ₂ , Co/CeO ₂ and Ni-Co/CeO ₂ by incipient wetness impregnation method	27
3.1.4 Preparation of CeO ₂ by exotemplating method	27
3.2 Catalyst characterization	29

3.2.1 X-Ray Diffraction (XRD) Analysis	29
3.2.2 Surface Area, Pore Size Distribution and Adsorption-Desorption Isotherms.....	29
3.2.3 Temperature Programmed Reduction (TPR) Analysis	29
3.2.4 DRIFTS	30
3.2.5 Microcalorimetry	31
3.2.6 Thermal Gravimetric Analysis (TGA).....	33
3.2.7 Transmission Electron Microscopy (TEM)	33
3.2.7.1 High Resolution Transmission Electron Microscopy(HRTEM)	33
3.2.7.2 High Contrast Transmission Electron Microscopy (HCTEM)	33
3.2.8 Scanning Electron Microscopy (SEM)	34
3.2.9 Nuclear Magnetic Resonance (NMR)	34
3.3 Dry Reforming Reaction Tests	34
3.4 Redox Experiments on Ceria Samples	37
4. DRY REFORMING OF METHANE ON Al ₂ O ₃ SUPPORTED Ni, Co and Ni-Co CATALYSTS PREPARED BY INCIPIENT WETNESS IMPREGNATION METHOD	39
4.1 Introduction	39
4.2 Results and Discussion	45
4.2.1 Characterization of commercial Al ₂ O ₃	45
4.2.1.1 X-Ray Diffraction (XRD) Analysis	45
4.2.1.2 Surface Area, Pore Size Distribution and Adsorption-Desorption Isotherms.....	46
4.2.2 Characterization of fresh catalysts	48
4.2.2.1 X-Ray Diffraction (XRD) Analysis	48
4.2.2.2 Surface Area, Pore Size Distribution and Adsorption-Desorption Isotherms	50
4.2.2.3 High Resolution Transmission Electron Microscopy (HRTEM)	54
4.2.2.4 Temperature Programmed Reduction (TPR) Analysis	57
4.2.2.5 DRIFTS.....	61
4.2.2.6 Microcalorimetry	67
4.2.3 Dry reforming reaction results	69
4.2.4 Characterization of spent catalysts	84

4.2.4.1 Thermal Gravimetric Analysis (TGA)	84
4.2.4.2 High Contrast Transmission Electron Microscopy (HCTEM)	86
4.2.5 Source of Coke Determination Reactions and Characterization Results .	89
4.3 Conclusions	97
5. DRY REFORMING OF METHANE ON Al₂O₃ SUPPORTED Ni CATALYSTS PREPARED BY POLYOL METHOD	99
5.1 Introduction	99
5.2 Results and Discussion	103
5.2.1 Characterization of fresh catalysts.....	103
5.2.1.1 X-Ray Diffraction (XRD) Analysis	103
5.2.1.2 Surface Area, Pore Size Distribution and Adsorption-Desorption Isotherms	105
5.2.1.3 Thermal Gravimetric Analysis (TGA)	106
5.2.1.4 High Contrast Transmission Electron Microscopy (HCTEM)	108
5.2.2 Dry reforming reaction results	113
5.2.3 Characterization of spent catalysts	117
5.2.3.1 Thermal Gravimetric Analysis (TGA)	117
5.2.3.2 High Contrast Transmission Electron Microscopy (HCTEM)	119
5.3 Conclusions	122
6. DRY REFORMING OF METHANE ON CeO₂ SUPPORTED Ni, Co and Ni-Co CATALYSTS PREPARED BY INCIPIENT WETNESS IMPREGNATION METHOD	123
6.1 Introduction	123
6.2 Results and Discussion	128
6.2.1 Characterization of fresh catalysts.....	128
6.2.1.1 X-Ray Diffraction (XRD) Analysis	128
6.2.1.2 Surface Area, Pore Size Distribution and Adsorption-Desorption Isotherms	131
6.2.1.3 Temperature Programmed Reduction (TPR) Analysis	135
6.2.2 Dry reforming reaction results	138
6.2.3 Characterization of spent catalysts	145
6.2.3.1 Thermal Gravimetric Analysis (TGA)	145

6.2.3.2 High Contrast Transmission Electron Microscopy (HCTEM)	146
6.3 Conclusions	149
7. MORPHOLOGY DEPENDENT REDOX PROPERTIES OF CeO ₂	151
7.1 Introduction	151
7.2 Results and Discussion	154
7.2.1 Characterization of fresh catalysts	154
7.2.2 Redox Properties of CeO ₂ samples	155
7.3 Conclusions	161
8. CONCLUSIONS	163
REFERENCES	165
APPENDICES	
A. EFFLUENT MOLE FRACTIONS DURING REDOX EXPERIMENTS ON COC, ESC AND CPC.....	187
B. TESTING FOR TRANSPORT LIMITATIONS	197
CURRICULUM VITAE	199

LIST OF TABLES

TABLES

Table 1. Structure sensitivity of CO ₂ adsorption [28]	16
Table 2. Reaction steps for CO ₂ reforming of CH ₄ over Ru/SiO ₂ [48]	17
Table 3. Reaction steps for CO ₂ reforming of CH ₄ over Ru/Al ₂ O ₃ [48]	18
Table 4. Types and reactivities of carbon species formed by CO decomposition on nickel [53]	21
Table 5. Operating conditions of gas chromatograph	36
Table 6. Textural properties of commercial Al ₂ O ₃ powder	46
Table 7. Textural properties of pure Al ₂ O ₃ , Ni/Al ₂ O ₃ , Co/Al ₂ O ₃ and Ni-Co/Al ₂ O ₃ calcined at 700°C	51
Table 8. Textural properties of pure Al ₂ O ₃ , Ni/Al ₂ O ₃ , Co/Al ₂ O ₃ and Ni-Co/Al ₂ O ₃ calcined at 900°C	51
Table 9. The weight gain of Al ₂ O ₃ supported powder catalysts after being used in the reaction at 600°C for 10 minutes under 30 sccm CO ₂ and 30 sccm CH ₄	90
Table 10. Comparison of textural properties of pure Al ₂ O ₃ with the catalysts prepared by polyol method	105
Table 11. Textural properties of pure CeO ₂ , Ni/CeO ₂ , Co/CeO ₂ and Ni-Co/CeO ₂ calcined at 700°C	131
Table 12. Textural properties of pure CeO ₂ , Ni/CeO ₂ , Co/CeO ₂ and Ni-Co/CeO ₂ calcined at 900°C	131
Table 13. Oxygen storage of ceria samples at 600°C during Step 3	156
Table 14. Oxygen release of ceria samples at 600°C during Step 4	158
Table 15. Oxygen storage of ceria samples at 600°C during Step 5	159
Table 16. Oxygen release of ceria samples at 600°C during Step 6	161
Table 17. The influence of flow rate on conversion at constant contact time	198

LIST OF FIGURES

FIGURES

Figure 1. Estimated contribution of various energy resources in total primary energy, expressed as % [1].....	1
Figure 2. Main usage areas of synthesis gas [adapted from 6]	2
Figure 3. Globally averaged a) CO ₂ and b) CH ₄ mole fractions from 1984 to 2012 [12]	4
Figure 4. Equilibrium constants of reactions involved in dry reforming of methane as a function of temperature	11
Figure 5. Variation of standard Gibbs free energies of reactions involved in dry reforming of methane as a function of temperature	12
Figure 6. Equilibrium conversions of CH ₄ and CO ₂ for dry reforming of methane as a function of temperature at P=1 atm and CH ₄ /CO ₂ /Ar=1/1/3.....	13
Figure 7. Equilibrium conversions of CH ₄ and CO ₂ for simultaneous dry reforming of methane and RWGS reaction as a function of temperature at P=1 atm and CH ₄ /CO ₂ /Ar=1/1/3	14
Figure 8. Possible coordination geometries of adsorbed CO ₂ ⁻ [adapted from 42] ...	16
Figure 9. Formation, transformation and gasification of carbon on nickel (a:adsorbed, g:gaseous, s:solid) [53]	20
Figure 10. Formation and transformation of coke on metal surfaces (a:adsorbed, g:gaseous, s:solid) [53]	21
Figure 11. a) HRTEM of carbon nanofiber growth, b) Illustration of growth mechanism [57]	22
Figure 12. Carbon limit diagram (principle of equilibrated gas) Curve 1: graphite data, Curve 2: whisker carbon [adapted from 52]	24
Figure 13. Electrospinning set-up.....	28
Figure 14. Experimental set up of DRIFTS measurements	31

Figure 15. Experimental set up of microcalorimetry measurements	32
Figure 16. Experimental set up for the catalytic reaction tests	35
Figure 17. XRD pattern of commercial Al ₂ O ₃ powder	46
Figure 18. Nitrogen adsorption-desorption isotherms of commercial Al ₂ O ₃ powder	47
Figure 19. BJH pore size distribution of commercial Al ₂ O ₃ powder	47
Figure 20. XRD pattern of pure Al ₂ O ₃ , Ni/Al ₂ O ₃ , Co/Al ₂ O ₃ and Ni-Co/Al ₂ O ₃ calcined at 700°C	48
Figure 21. XRD pattern of pure Al ₂ O ₃ , Ni/Al ₂ O ₃ , Co/Al ₂ O ₃ and Ni-Co/Al ₂ O ₃ calcined at 900°C	49
Figure 22. Nitrogen adsorption-desorption isotherms of pure Al ₂ O ₃ , Ni/Al ₂ O ₃ , Co/Al ₂ O ₃ and Ni-Co/Al ₂ O ₃ calcined at 700°C	52
Figure 23. Nitrogen adsorption-desorption isotherms of pure Al ₂ O ₃ , Ni/Al ₂ O ₃ , Co/Al ₂ O ₃ and Ni-Co/Al ₂ O ₃ calcined at 900°C	53
Figure 24. BJH pore size distribution of pure Al ₂ O ₃ , Ni/Al ₂ O ₃ , Co/Al ₂ O ₃ and Ni-Co/Al ₂ O ₃ calcined at 700°C	53
Figure 25. BJH pore size distribution of pure Al ₂ O ₃ , Ni/Al ₂ O ₃ , Co/Al ₂ O ₃ and Ni-Co/Al ₂ O ₃ calcined at 900°C	54
Figure 26. HRTEM images of fresh Ni/Al ₂ O ₃ -I-900	55
Figure 27. HRTEM images of fresh Ni-Co/Al ₂ O ₃ -I-900	56
Figure 28. TPR profiles of Ni/Al ₂ O ₃ , Co/Al ₂ O ₃ and Ni-Co/Al ₂ O ₃ calcined at 700°C	57
Figure 29. TPR profiles of Ni/Al ₂ O ₃ , Co/Al ₂ O ₃ and Ni-Co/Al ₂ O ₃ calcined at 900°C	58
Figure 30. TGA profiles of Co/Al ₂ O ₃ -I-700 and Co/Al ₂ O ₃ -I-900 under N ₂ environment	60
Figure 31. DRIFT spectra of CO ₂ adsorption on Ni/Al ₂ O ₃ -900 with increasing CO ₂ dosage	61

Figure 32. DRIFT spectra of CO ₂ adsorption on Ni/Al ₂ O ₃ -900 with increasing temperature at 500 torr	63
Figure 33. DRIFT spectra of CO ₂ adsorption on Ni-Co/Al ₂ O ₃ -900 with increasing temperature at 500 torr	64
Figure 34. Comparison between the DRIFT spectra of CO ₂ adsorption on Ni/Al ₂ O ₃ -900 and Ni-Co/Al ₂ O ₃ -900 at 500 torr	65
Figure 35. DRIFT spectra of CH ₄ adsorption on Ni/Al ₂ O ₃ -900 with increasing temperature at 500 torr	66
Figure 36. Differential heat of CO ₂ adsorption on commercial Al ₂ O ₃ , Al ₂ O ₃ -900, Ni/Al ₂ O ₃ -900 and Ni-Co/Al ₂ O ₃ -900	68
Figure 37. Coverage as a function of pressure for CO ₂ adsorption on commercial Al ₂ O ₃ , Al ₂ O ₃ -900, Ni/Al ₂ O ₃ -900 and Ni-Co/Al ₂ O ₃ -900	68
Figure 38. Comparison of CH ₄ and CO ₂ conversion versus time on stream over the catalysts calcined at 700°C, Ni/Al ₂ O ₃ -I-700-pellet ◆, Co/Al ₂ O ₃ -I-700-pellet ◆, Ni-Co/Al ₂ O ₃ -I-700-pellet ◆, (Reaction conditions: 700°C, 1 atm).....	70
Figure 39. Comparison of H ₂ and CO yield versus time on stream over the catalysts calcined at 700°C, Ni/Al ₂ O ₃ -I-700-pellet ◆, Co/Al ₂ O ₃ -I-700-pellet ◆, Ni-Co/Al ₂ O ₃ -I-700-pellet ◆, (Reaction conditions: 700°C, 1 atm).....	71
Figure 40. Comparison of H ₂ /CO ratio versus time on stream over the catalysts calcined at 700°C, Ni/Al ₂ O ₃ -I-700-pellet ◆, Co/Al ₂ O ₃ -I-700-pellet ◆, Ni-Co/Al ₂ O ₃ -I-700-pellet ◆, (Reaction conditions: 700°C, 1 atm).....	72
Figure 41. Comparison of CH ₄ and CO ₂ conversion versus time on stream over the catalysts calcined at 900°C, Ni/Al ₂ O ₃ -I-900-pellet ▲, Co/Al ₂ O ₃ -I-900-pellet ▲, Ni-Co/Al ₂ O ₃ -I-900-pellet ▲, (Reaction conditions: 700°C, 1 atm)	74
Figure 42. Comparison of H ₂ and CO yield versus time on stream over Ni/Al ₂ O ₃ -I-900-pellet ▲ and Ni-Co/Al ₂ O ₃ -I-900-pellet ▲, (Reaction conditions: 700°C, 1 atm)	75
Figure 43. Comparison of H ₂ /CO ratio versus time on stream over Ni/Al ₂ O ₃ -I-700-pellet ▲ and Ni-Co/Al ₂ O ₃ -I-900-pellet ▲, (Reaction conditions: 700°C, 1 atm)	76
Figure 44. Comparison of CH ₄ and CO ₂ conversion versus time on stream over the catalysts calcined at 900°C, Ni/Al ₂ O ₃ -I-900-powder ●, Ni-Co/Al ₂ O ₃ -I-900-powder ●, (Reaction conditions: 700°C, 1 atm).....	77

Figure 45. Comparison of H ₂ and CO yield versus time on stream over Ni/Al ₂ O ₃ -I-900-powder ● , Ni-Co/Al ₂ O ₃ -I-900-powder ● , (Reaction conditions: 700°C, 1 atm)	78
Figure 46. Comparison of H ₂ /CO ratio versus time on stream over Ni/Al ₂ O ₃ -I-900-powder ● , Ni-Co/Al ₂ O ₃ -I-900-powder ● , (Reaction conditions: 700°C, 1 atm).....	79
Figure 47. Comparison of CH ₄ and CO ₂ conversion versus time on stream over the catalysts calcined at 700°C, Ni/Al ₂ O ₃ -I-700-powder ◆ , Ni-Co/Al ₂ O ₃ -I-700-powder ◆ , (Reaction conditions: 700°C, 1 atm).....	80
Figure 48. Comparison of H ₂ and CO yield versus time on stream over the catalysts calcined at 700°C, Ni/Al ₂ O ₃ -I-700-powder ◆ , Ni-Co/Al ₂ O ₃ -I-700-powder ◆ , (Reaction conditions: 700°C, 1 atm)	81
Figure 49. Comparison of CH ₄ and CO ₂ conversion versus time on stream over the catalysts calcined at 900°C, Ni/Al ₂ O ₃ -I-900-powder ✕ , Ni-Co/Al ₂ O ₃ -I-900-powder ✕ , (Reaction conditions: 600°C, 1 atm).....	82
Figure 50. Comparison of H ₂ and CO yield versus time on stream over the catalysts calcined at 900°C, Ni/Al ₂ O ₃ -I-900-powder ✕ , Ni-Co/Al ₂ O ₃ -I-900-powder ✕ , (Reaction conditions: 600°C, 1 atm).....	83
Figure 51. Comparison of H ₂ /CO ratio versus time on stream over Ni/Al ₂ O ₃ -I-900-powder ✕ , Ni-Co/Al ₂ O ₃ -I-900-powder ✕ , (Reaction conditions: 600°C, 1 atm).....	84
Figure 52. TGA curves in air atmosphere for Ni/Al ₂ O ₃ -I-700-pellet, Co/Al ₂ O ₃ -I-700-pellet and Ni-Co/Al ₂ O ₃ -I-700-pellet after being used in reaction at 700°C for 5 hours	85
Figure 53. TGA curves in air atmosphere for Ni/Al ₂ O ₃ -I-900-pellet, Co/Al ₂ O ₃ -I-900-pellet and Ni-Co/Al ₂ O ₃ -I-900-pellet after being used in reaction at 700°C for 5 hours	85
Figure 54. HCTEM of Ni/Al ₂ O ₃ -I-900-powder after being used in reaction at 600°C for 5 hours	87
Figure 55. HCTEM of Ni-Co/Al ₂ O ₃ -I-900-powder after being used in reaction at 600°C for 5 hours	88
Figure 56. The effect of CH ₄ /CO ₂ ratio in the input stream on a) amount of carbon deposition b) type of carbon deposition over Ni/Al ₂ O ₃ -700-powder after being used in the reaction at 600°C for 10 minutes	90

Figure 57. Effect of CH ₄ /CO ₂ ratio in the input stream on a) CH ₄ conversion and b) H ₂ /CO ratio	92
Figure 58. ¹³ C NMR spectra of the coke deposited on Ni/Al ₂ O ₃ -I-700-powder after being used in the reaction at 600°C for 10 minutes under 30 sccm ¹³ CO ₂ and 30 sccm CH ₄	93
Figure 59. HCTEM of Ni/Al ₂ O ₃ -I-700-powder catalyst after being used in the reaction at 600°C for 10 minutes with ¹³ CO ₂ / ¹² CH ₄ ratio of 10/50	95
Figure 60. HCTEM of Ni/Al ₂ O ₃ -I-700-powder catalyst after being used in the reaction at 600°C for 10 minutes with ¹³ CO ₂ / ¹² CH ₄ ratio of 30/30	96
Figure 61. HCTEM of Ni/Al ₂ O ₃ -I-700-powder catalyst after being used in the reaction at 600°C for 10 minutes with ¹³ CO ₂ / ¹² CH ₄ ratio of 50/10	97
Figure 62. Comparison of the XRD pattern of pure alumina with those of catalysts prepared by polyol method	104
Figure 63. Comparison of nitrogen adsorption-desorption isotherms of pure Al ₂ O ₃ with the catalysts prepared by polyol method	106
Figure 64. Comparison of BJH pore size distribution of pure Al ₂ O ₃ with the catalysts prepared by polyol method	107
Figure 65. TG analysis of pure ethylene glycol, pure PVP and the catalysts prepared by polyol method	107
Figure 66. Derivative weight loss analysis of pure ethylene glycol, pure PVP and the catalysts prepared by polyol method	108
Figure 67. TEM of fresh Ni/Alumina-without-PVP catalyst	109
Figure 68. TEM of fresh Ni/Alumina-PVP/Ni=2.5 catalyst	111
Figure 69. TEM of fresh Ni/Alumina-PVP/Ni=5.0 catalyst	112
Figure 70. Comparison of CH ₄ and CO ₂ conversion versus time on stream over the catalysts prepared by polyol method, Ni/Al ₂ O ₃ -without PVP ◆, Ni/Al ₂ O ₃ -PVP/Ni=2.5 ◆, Ni/Al ₂ O ₃ -PVP/Ni=5.0 ◆, (Reaction conditions: 700°C, 1 atm, no reduction	113
Figure 71. Comparison of H ₂ and CO yield versus time on stream over the catalysts prepared by polyol method, Ni/Al ₂ O ₃ -without PVP ◆, Ni/Al ₂ O ₃ -PVP/Ni=2.5 ◆, Ni/Al ₂ O ₃ -PVP/Ni=5.0 ◆, (Reaction conditions: 700°C, 1 atm, no reduction)	114

Figure 72. Comparison of H ₂ /CO ratio versus time on stream over the catalysts prepared by polyol method, Ni/Al ₂ O ₃ -without PVP ◆, Ni/Al ₂ O ₃ -PVP/Ni=2.5 ◆, Ni/Al ₂ O ₃ -PVP/Ni=5.0 ◆, (Reaction conditions: 700°C, 1 atm, no reduction	115
Figure 73. Comparison of CH ₄ and CO ₂ conversion versus time on stream over the catalysts prepared by polyol method, Ni/Al ₂ O ₃ -without PVP ▲, Ni/Al ₂ O ₃ -PVP/Ni=2.5 ▲, Ni/Al ₂ O ₃ -PVP/Ni=5.0 ▲, (Reaction conditions: 600°C, 1 atm, no reduction	116
Figure 74. Comparison of H ₂ and CO yield versus time on stream over the catalysts prepared by polyol method, Ni/Al ₂ O ₃ -without PVP ▲, Ni/Al ₂ O ₃ -PVP/Ni=2.5 ▲, Ni/Al ₂ O ₃ -PVP/Ni=5.0 ▲, (Reaction conditions: 600°C, 1 atm, no reduction)	116
Figure 75. Comparison of time dependent H ₂ /CO ratio over the catalysts prepared by polyol method, Ni/Al ₂ O ₃ -without PVP ▲, Ni/Al ₂ O ₃ -PVP/Ni=2.5 ▲, Ni/Al ₂ O ₃ -PVP/Ni=5.0 ▲, (Reaction conditions: 600°C, 1 atm, no reduction)	117
Figure 76. Comparison of weight losses between the fresh and the used polyol catalysts in the reaction at a) 600°C and b) 700°C	118
Figure 77. Comparison of derivative weight losses between the fresh and the used polyol catalysts in the reaction at 600°C and 700°C	119
Figure 78. HCTEM of Ni/Al ₂ O ₃ -without PVP catalyst after being used in reaction at 600°C for 5 hours	120
Figure 79. HCTEM of Ni/Al ₂ O ₃ -PVP/Ni=2.5 catalyst after being used in reaction at 600°C for 5 hours	121
Figure 80. Standard Gibbs free energy as a function of temperature for CeO ₂ based nickel catalyst.....	124
Figure 81. XRD pattern of pure CeO ₂ , Ni/CeO ₂ , Co/CeO ₂ and Ni-Co/CeO ₂ calcined at 700°C	129
Figure 82. XRD pattern of pure CeO ₂ , Ni/CeO ₂ , Co/CeO ₂ and Ni-Co/CeO ₂ calcined at 900°C	130
Figure 83. Nitrogen adsorption-desorption isotherms of pure CeO ₂ , Ni/CeO ₂ , Co/CeO ₂ and Ni-Co/CeO ₂ calcined at 700°C	132
Figure 84. Nitrogen adsorption-desorption isotherms of pure CeO ₂ , Ni/CeO ₂ , Co/CeO ₂ and Ni-Co/CeO ₂ calcined at 900°C	133

Figure 85. BJH pore size distribution of pure CeO ₂ , Ni/CeO ₂ , Co/CeO ₂ and Ni-Co/CeO ₂ calcined at 700°C	134
Figure 86. BJH pore size distribution of pure CeO ₂ , Ni/CeO ₂ , Co/CeO ₂ and Ni-Co/CeO ₂ calcined at 900°C	134
Figure 87. TPR profiles of pure CeO ₂ , Ni/CeO ₂ , Co/CeO ₂ and Ni-Co/CeO ₂ calcined at 700°C	135
Figure 88. TPR profiles of pure CeO ₂ , Ni/CeO ₂ , Co/CeO ₂ and Ni-Co/CeO ₂ calcined at 900°C	137
Figure 89. Comparison of CH ₄ and CO ₂ conversion versus time on stream over the catalysts calcined at 700°C, Ni/CeO ₂ -I-700-pellet ◆ , Co/CeO ₂ -I-700-pellet ◆ , Ni-Co/CeO ₂ -I-700-pellet ◆ , (Reaction conditions: 700°C, 1 atm).....	139
Figure 90. Comparison of H ₂ and CO yield versus time on stream over the catalysts calcined at 700°C, Ni/CeO ₂ -I-700-pellet ◆ , Co/CeO ₂ -I-700-pellet ◆ , Ni-Co/CeO ₂ -I-700-pellet ◆ , (Reaction conditions: 700°C, 1 atm)	140
Figure 91. Comparison of H ₂ /CO ratio versus time on stream over the catalysts calcined at 700°C, Ni/CeO ₂ -I-700-pellet ◆ , Co/CeO ₂ -I-700-pellet ◆ , Ni-Co/CeO ₂ -I-700-pellet ◆ , (Reaction conditions: 700°C, 1 atm)	141
Figure 92. Comparison of CH ₄ and CO ₂ conversion versus time on stream over the catalysts calcined at 900°C, Ni/CeO ₂ -I-900-pellet ▲ , Co/CeO ₂ -I-900-pellet ▲ , Ni-Co/CeO ₂ -I-900-pellet ▲ , (Reaction conditions: 700°C, 1 atm).....	142
Figure 93. Comparison of H ₂ and CO yield versus time on stream over the catalysts calcined at 900°C, Ni/CeO ₂ -I-900-pellet ▲ , Co/CeO ₂ -I-900-pellet ▲ , Ni-Co/CeO ₂ -I-900-pellet ▲ , (Reaction conditions: 700°C, 1 atm)	143
Figure 94. Comparison of H ₂ /CO ratio versus time on stream over the catalysts calcined at 900°C, Ni/CeO ₂ -I-900-pellet ▲ , Co/CeO ₂ -I-900-pellet ▲ , Ni-Co/CeO ₂ -I-900-pellet ▲ , (Reaction conditions: 700°C, 1 atm)	144
Figure 95. TGA curves in air atmosphere after being used in reaction at 700°C for 5 hours for the catalysts calcined at a) 700°C, b) 900°C	145
Figure 96. Derivative weight losses after being used in reaction at 700°C for 5 hours for the catalysts calcined at a) 700°C, b) 900°C	146
Figure 97. HCTEM of Ni/CeO ₂ -I-700 catalyst after being used in reaction at 700°C for 5 hours	147

Figure 98. HCTEM of Ni-Co/CeO ₂ -I-700 catalyst after being used in reaction at 700°C for 5 hours	148
Figure 99. Scanning electron micrographs of ceria fiber mats	155
Figure 100. O ₂ consumption during Step 3	156
Figure 101. CO consumption during Step 4.....	157
Figure 102. CO ₂ production during Step 4	157
Figure 103. O ₂ consumption during Step 5	159
Figure 104. CO consumption during Step 6	160
Figure 105. CO ₂ production during Step 6	160
Figure 106. Effluent mole fraction of O ₂ during O ₂ pulse experiment on COC at 600°C (Step 3)	187
Figure 107. Effluent mole fraction of O ₂ during O ₂ pulse experiment on ESC at 600°C (Step 3)	188
Figure 108. Effluent mole fraction of O ₂ during O ₂ pulse experiment on CPC at 600°C (Step 3)	188
Figure 109. Effluent mole fraction of CO during CO pulse experiment on COC at 600°C (Step 4)	189
Figure 110. Effluent mole fraction of CO during CO pulse experiment on ESC at 600°C (Step 4)	189
Figure 111. Effluent mole fraction of CO during CO pulse experiment on CPC at 600°C (Step 4)	190
Figure 112. Effluent mole fraction of CO ₂ during CO pulse experiment on COC at 600°C (Step 4)	190
Figure 113. Effluent mole fraction of CO ₂ during CO pulse experiment on ESC at 600°C (Step 4)	191
Figure 114. Effluent mole fraction of CO ₂ during CO pulse experiment on CPC at 600°C (Step 4)	191

Figure 115. Effluent mole fraction of O ₂ during O ₂ pulse experiment on COC at 600°C (Step 5)	192
Figure 116. Effluent mole fraction of O ₂ during O ₂ pulse experiment on ESC at 600°C (Step 5)	192
Figure 117. Effluent mole fraction of O ₂ during O ₂ pulse experiment on CPC at 600°C (Step 5)	193
Figure 118. Effluent mole fraction of CO during CO pulse experiment on COC at 600°C (Step 6)	193
Figure 119. Effluent mole fraction of CO during CO pulse experiment on ESC at 600°C (Step 6)	194
Figure 120. Effluent mole fraction of CO during CO pulse experiment on CPC at 600°C (Step 6)	194
Figure 121. Effluent mole fraction of CO ₂ during CO pulse experiment on COC at 600°C (Step 6)	195
Figure 122. Effluent mole fraction of CO ₂ during CO pulse experiment on ESC at 600°C (Step 6)	195
Figure 123. Effluent mole fraction of CO ₂ during CO pulse experiment on CPC at 600°C (Step 6)	196
Figure 124. The effect of catalyst particle size on CH ₄ and CO ₂ conversion, ◆: Ni/Al ₂ O ₃ -700-pellet, ◆: Ni/Al ₂ O ₃ -700-powder	197
Figure 125. Experimental evaluation of the effect of interphase mass transport ▲: W=0.1 g and F=50 sccm, ◆: W=0.15 g and F=75 sccm, ●: W=0.2 g and F=100 sccm	198

CHAPTER 1

INTRODUCTION

1.1 ENERGY AND SYNTHESIS GAS

Energy demand is quickly increasing worldwide, especially due to growing economies, mainly in Asia. Production of energy is still based primarily on combustion processes using fossil fuels, a fact which is improbable to change in the near future (Figure 1) [1 and references therein]. In the twentieth century oil played the most essential role [2]. However, the finite and readily accessible oil reserves are being rapidly depleted. One alternative is natural gas, which is composed mainly of methane [2 and references therein].

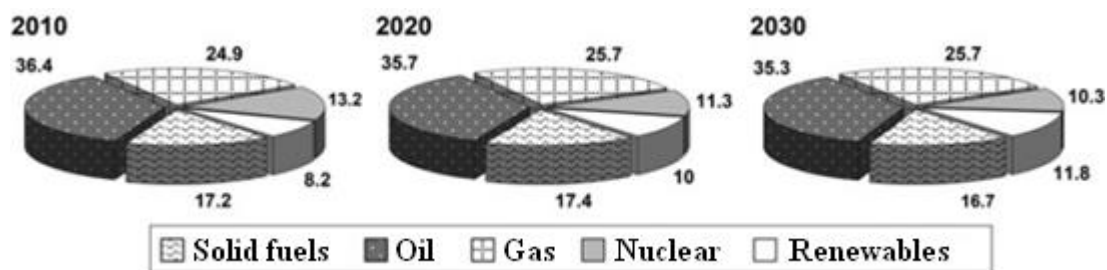


Figure 1. Estimated contribution of various energy resources in total primary energy, expressed as % [1]

The chemical usage of natural gas for the production of basic chemicals is one of the desirable purposes in the present chemical industry. Nevertheless, it is very difficult to transform natural gas directly into useful chemicals due to the chemical inertness of methane. The conversion of methane into useful chemicals has taken great

attention recently and several technologies and methods have been reported. Even though the direct conversion of CH₄ to very useful chemicals is the most fascinating way, no feasible catalyst or process has been developed. Nowadays, indirect transformation of CH₄ via synthesis gas is still the most competitive method [3 and references therein]. Synthesis gas is a mixture of carbon monoxide and hydrogen [4]. It serves as the feedstock for several important industrial processes such as ammonia synthesis, methanol synthesis, Fischer Tropsch synthesis and H₂ production, etc [2,4-6] (Figure 2).

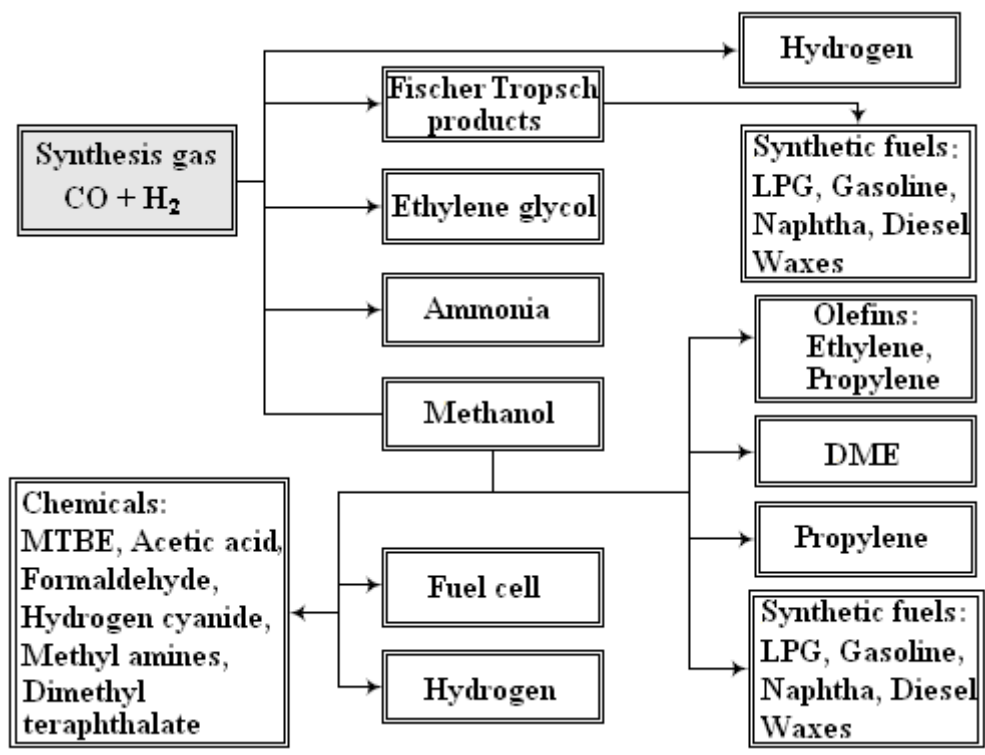


Figure 2. Main usage areas of synthesis gas [adapted from 6]

The effective commercial production of synthesis gas is taking important attention due to the growing worldwide interest in synthetic fuels and chemicals [7]. There are basically three different types of processes that can be employed to convert natural

gas into synthesis gas: steam reforming of methane, partial oxidation of methane and carbon dioxide reforming of methane (or dry reforming of methane) [8]. Carbon dioxide reforming of methane becomes industrially advantageous compared to partial oxidation and steam reforming in synthesis gas production due to the fact that the H₂/CO product ratio in dry reforming is close to one, which is appropriate for further use in the production of oxygenated compounds as well as Fischer Tropsch synthesis for liquid hydrocarbons production [9 and references therein]. In addition, dry reforming of methane provides the opportunity of using natural gas resources with high carbon dioxide content, avoiding the costly and complicated gas separation process [10]. Dry reforming of methane is also an attractive way of utilizing biogas, a clean and environment friendly fuel that is produced typically from anaerobic degradation of biomass and mainly composed of CO₂ and CH₄ [11 and references therein].

1.2 GREENHOUSE GASES AND GLOBAL WARMING

The World Meteorological Organization Global Atmosphere Watch Programme reveals that the globally averaged mole fractions of CO₂ and CH₄ reached new highs in 2012, with CO₂ at 393.1±0.1 ppm (Figure 3-a) and CH₄ at 1819±1 ppb (Figure 3-b) constituting 141% and 260% of pre-industrial (before 1750) levels, respectively. The National Oceanic and Atmospheric Administration Annual Greenhouse Gas Index reveals that radiative forcing by long-lived greenhouse gases increased by 32% from 1990 to 2012. CO₂, being the most important anthropogenic greenhouse gas in the atmosphere, contributes ~64% to radiative forcing by long-lived greenhouse gases. It is responsible for ~82% of the rise in radiative forcing over the previous five years and ~84% over the previous decade. Atmospheric CO₂ mainly comes from emissions due to the combustion of fossil fuels, deforestation and other land-use change. Methane contributes ~18% to radiative forcing by long-lived greenhouse gases. While about 40% of CH₄ emits to the atmosphere by natural sources such as termites and wetlands, approximately 60% of it originates from

anthropogenic sources such as fossil fuel exploitation, biomass burning and landfills [12].

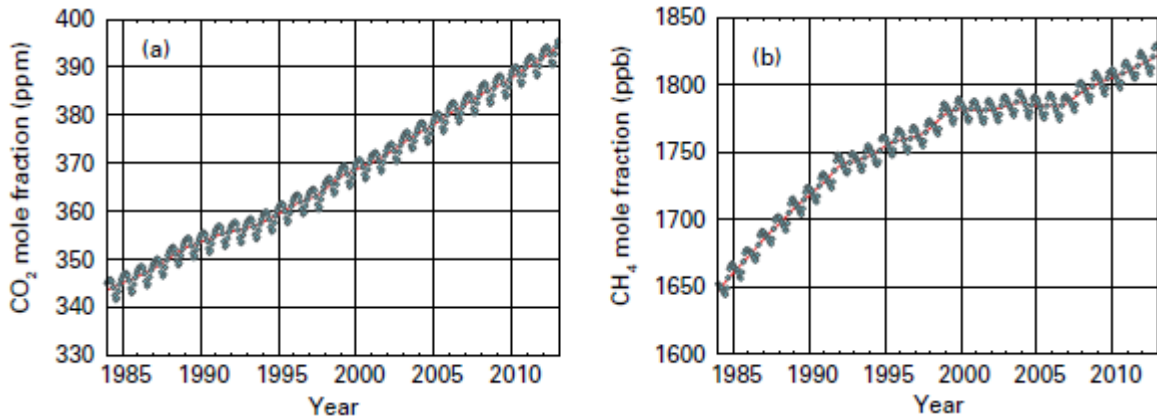


Figure 3. Globally averaged a) CO₂ and b) CH₄ mole fractions from 1984 to 2012 [12]

Global climate changes associated with the emission of greenhouse gases are of great concern around the world. Consuming two major greenhouse gases (CO₂ and CH₄) simultaneously to convert them into valuable feedstock, dry reforming of methane has taken great interest for environmental protection.

1.3 OBJECTIVES

Carbon dioxide reforming of methane has been studied extensively in the last years due to the following reasons:

- i) converts two main greenhouse gases, CO₂ and CH₄, with high global warming potential to precious synthesis gas [9]
- ii) generates synthesis gas with a low H₂/CO ratio which is favorable in the production of liquid hydrocarbons in Fischer Tropsch synthesis network [13]

- iii) enables the usage of natural gas resources with a high carbon dioxide content, without the requirement of costly and complicated gas separation process [10]
- iv) utilizes biogas as a promising raw material [1]

The major problem hindering the development of dry reforming of methane is the lack of an effective catalyst that can able to operate without deactivation by coke deposition. Although it is known that supported noble metals can provide good catalytic performance in terms of activity, selectivity and resistance to carbon deposition [14], Ni based catalysts have been preferred as good replacement due to their comparable catalytic performance, low cost and wide availability [15]. Nevertheless, Ni-based catalysts are well known for their high tendency for carbon deposition [15].

The most essential parameters influencing the activity, selectivity, and stability are the nature and particle size of the supported metal; the nature, texture, and structure of the support; and reaction conditions. Therefore, great efforts have been focused on throwing light on the significance and the control of these parameters by proper selection of metallic component and support, catalyst preparation method, and addition of promoters–modifiers, in order to retain high activity while preventing carbon formation [1].

For the aim of reducing carbon formation and improving the life time of Ni based catalysts, this PhD dissertation covers the following studies:

In the first part of the study, the activity of Al₂O₃ supported Ni, Co and Ni-Co catalyst by incipient wetness impregnation was investigated to elucidate the effect of introducing a second metal to the Ni-based catalysts. To understand the influence of calcination temperature, two different calcination temperatures were tested for each catalyst. In order to find out the source of carbon deposition, reaction tests were carried out with ¹³CO₂ and the spent catalysts were characterized by ¹³C NMR.

In the second part of the study, a new synthesis method, the polyol method, was tested for carbon dioxide reforming of methane reaction. In this study, it was aimed to obtain metallic Ni during synthesis which would stop the necessity of reduction prior to reaction. The effect of PVP/Ni ratio on the structure of the catalyst and the performance of catalysts during reaction was investigated.

In the third part of the study, to find out the effect of support, CeO₂ having excellent redox properties, was tested for dry reforming of methane. The TPR characteristics of CeO₂ supported Ni, Co and Ni-Co catalyst synthesized by incipient wetness impregnation and calcined at two different temperatures were investigated.

In the last part of the study, O₂ and CO pulse experiments were done in order to obtain information about the oxygen release/storage ability of different kinds of ceria samples, including commercial ceria, coprecipitated ceria and ceria fibers prepared by exotemplating method.

CHAPTER 2

REFORMING OF METHANE TO SYNTHESIS GAS

There are basically three different types of processes that can be used to convert methane to synthesis gas [1,2,16] :

- steam reforming of methane
- partial oxidation of methane
- carbon dioxide reforming of methane

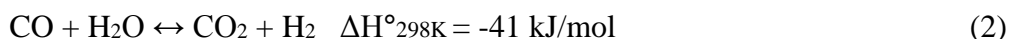
2.1 Steam Reforming of Methane

Steam reforming of methane is a well known commercial method employed to produce synthesis gas.



The reaction is highly endothermic [3,16]. It must be carried out at high temperatures and large amounts of energy is used to drive the reaction [3] making the process very expensive.

Another disadvantage of this reaction is the high H₂/CO ratio which is higher than the ratio required for synthesizing byproducts, such as methanol or derivatives from the Fischer-Tropsch reaction. In industry, water gas shift reaction (Reaction 2) is used to adjust the H₂/CO ratio [17 and references therein].



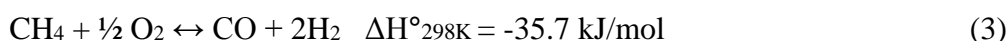
The combination of water gas shift reaction for adjusting the H₂/CO ratio requires additional cost and makes the overall process more expensive. Furthermore, excess steam must be introduced to prevent the deactivation of the catalysts because of

carbonaceous deposits. As a result operation expenses and consumption of energy rises [17 and references therein]. The concern related with the economic viability issue led to the investigation of alternative processes to steam reforming which are partial oxidation and dry reforming.

2.2 Partial Oxidation of Methane

The partial oxidation of methane to produce synthesis gas is well established to take place in a non-catalytic homogeneous reaction at very high temperatures (>1127°C). The utilization of a catalyst could reduce the operating temperature. The first investigation of the catalytic partial oxidation of methane was done with nickel catalysts, and since then numerous transition metals such as cobalt and iron have been reported in literature [2].

The main advantage of partial oxidation of methane is its slightly exothermic nature making it much more energy efficient than steam reforming. It also produces H₂/CO ratio of two which is proper for methanol synthesis or Fischer Tropsch synthesis without further adjustment [18]



One of the main drawbacks of partial oxidation of CH₄ is the requirement of pure oxygen which means additional cost for separating oxygen from air [19]. It is also difficult to control the process due to the fact that it involves feeding CH₄-O₂ mixture together and reaction under flammable or even explosive conditions. Local hot spots commonly form which can harm the active component in an irreversible way [20].

In addition to the direct route shown in Equation 3, partial oxidation of methane can also proceed via an indirect route which is a two-step mechanism. The first step is the total oxidation of some CH₄ to CO₂ and H₂O. The second step is the steam and

carbon dioxide reforming of the remaining unconverted methane to acquire synthesis gas during which water gas shift reaction also occurs. The temperature of the catalyst bed is considerably higher in the front section than in the latter section due to the initial highly exothermic total oxidation reaction followed by endothermic reforming reactions. Formations of hot spots usually take place at the front of the catalyst bed. The huge amount of evolved heat can melt the supported metal and split it from the support, which results in catalyst deactivation [21,22].

2.3 Carbon dioxide Reforming of Methane

Dry reforming of CH_4 is an essential process that converts two of the most plentiful greenhouse gases in the atmosphere, CO_2 and CH_4 , into synthesis gas [23]. Since fossil fuels are expected to remain as the dominant energy source through 2035, efforts are directed to make strides in carbon management by developing the infrastructure needed to capture and permanently store CO_2 emissions [24]. Dry reforming of methane is one of the most promising applications for the mitigation of CO_2 .

Dry reforming of CH_4 is a suitable way for the exploitation of biogas, consisting mainly of CO_2 and CH_4 [1]. Biogas is obtained from wastewater and sewage treatment plants, landfills, livestock and poultry manure, organic industrial waste, biomass residues, etc [25-27]. The composition and features of biogas strongly depend on the type of feedstock, the technical design of digester-fermenter and operating conditions [1 and references therein]. Methane and carbon dioxide are always the major components of the biogas. It can also contain hydrogen sulfide, ammonia, water vapor, some higher hydrocarbons and aromatics as impurities [1 and references therein].

Due to its high heat of endothermic reaction (exceeding that of steam reforming of methane) and reversibility, dry reforming of methane has “potential thermochemical

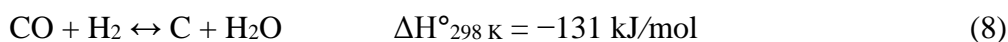
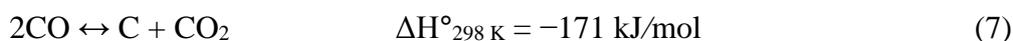
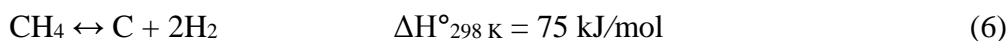
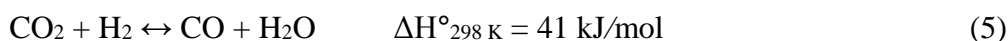
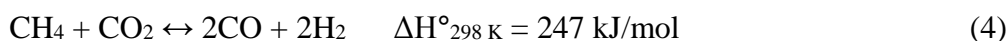
heat-pipe applications for the recovery, storage, and transmission of energy from solar and other renewable sources in chemical energy storage and transmission systems.” [1 and references therein]. Compared to partial oxidation of methane, it is simpler to obtain higher selectivity to synthesis gas with lower safety risks [1].

Since no steam is used, dry reforming of methane can be applied in areas where water is not available [28]. Easier installation is needed, decreasing both operational and equipment expenses when compared to steam reforming [1]. Another advantage of dry reforming compared to steam reforming is that it yields synthesis gas with a lower H₂/CO ratio, which is a preferable feedstock for the production of long-chain hydrocarbons via Fischer–Tropsch synthesis and adequate for producing oxygenated derivatives [17].

The major problem in dry reforming of methane is catalyst deactivation which can be due to carbon formation [1,28,29], sintering at high temperature [30,31] and oxidation of metallic sites [32,33]. Coke formation has been accepted as the primary reason of deactivation [34].

2.3.1 Thermodynamic Analysis of Carbon dioxide Reforming of Methane

CO₂ reforming of CH₄ (Equation 4) is a strongly endothermic reaction [35]. In general, it is affected by the simultaneous reverse water–gas shift reaction (RWGS) (Equation 5) resulting in H₂/CO ratio lower than unity [28]. In addition to RWGS, some other side reactions may take place, having important effect on the target reaction [36]:



Equilibrium constants of the reactions taking place during CO₂ reforming of CH₄ were calculated and shown in Figure 4 as a function of temperature.

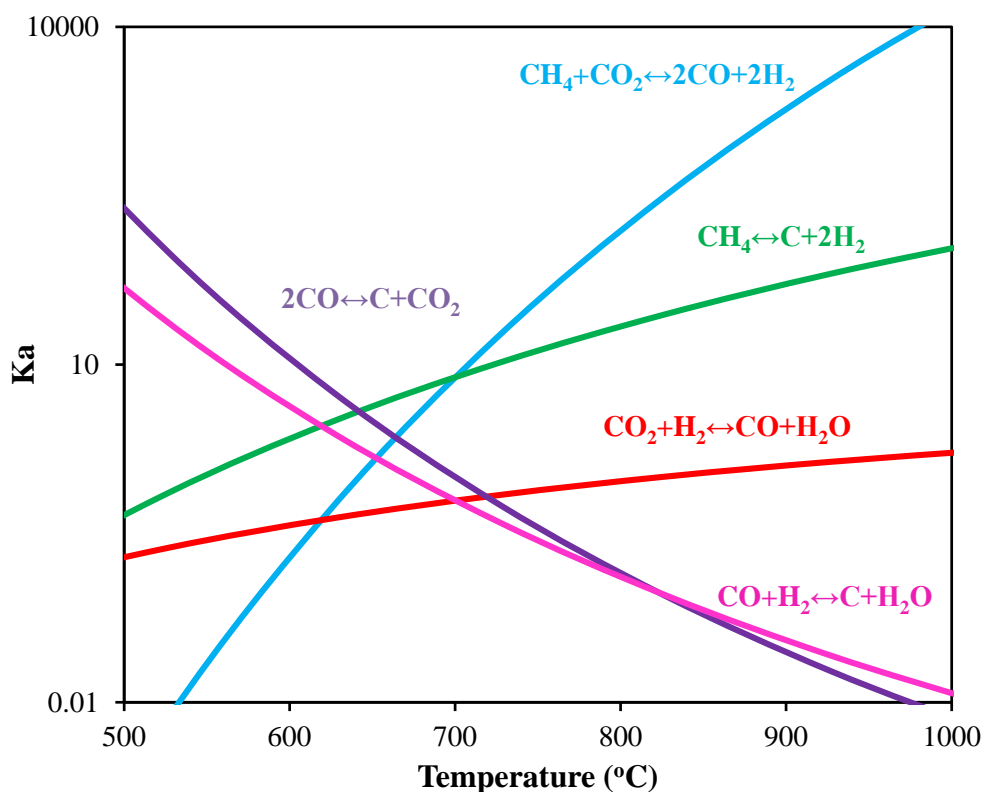


Figure 4. Equilibrium constants of reactions involved in dry reforming of methane as a function of temperature

Being highly endothermic, the equilibrium constant of dry reforming of methane exhibits an excessive increase with an increase in temperature. Therefore, high temperatures are preferred to obtain high conversions. Being moderately endothermic, the equilibrium constants of RWGS reaction and methane decomposition (Equation 6) reaction increase with increasing temperature. On the other hand, Boudouard reaction (Equation 7) and reverse carbon gasification reaction (Equation 8) are exothermic, the equilibrium constants of which decrease with rising temperatures.

Standard Gibbs-free energy changes (ΔG°) of the reactions taking place during dry reforming of methane were calculated at different temperatures and shown in Figure 5.

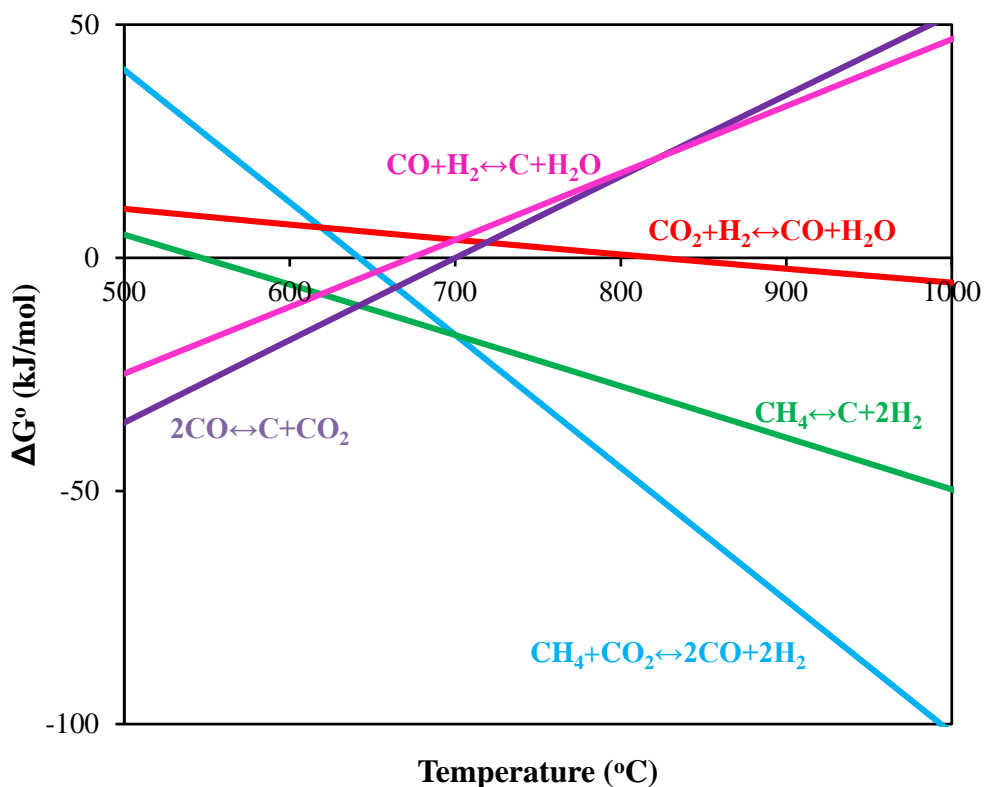


Figure 5. Variation of standard Gibbs free energies of reactions involved in dry reforming of methane as a function of temperature

Standard free energy change was used to determine the lower limiting temperatures for endothermic reactions and upper limiting temperatures for exothermic reactions. Minimum operating temperatures were calculated as 643°C, 557°C and 830°C for dry reforming of methane, methane decomposition and RWGS reaction, respectively. While Boudouard reaction can not occur above 702°C, reverse carbon gasification reaction is impeded above 675°C.

The equilibrium conversions of CO₂ and CH₄ in dry reforming of methane reaction for an inlet stream composition of CH₄/CO₂/Ar=1/1/3 and 1 atm total pressure were calculated and shown in Figure 6. The equilibrium conversions of CO₂ and of CH₄ by taking into consideration the simultaneous occurrence of reverse water gas shift reaction for an inlet stream composition of CH₄/CO₂/Ar=1/1/3 and 1 atm total pressure were calculated and shown in Figure 7. When RWGS reaction takes place, CO₂ conversion becomes greater than that of CH₄.

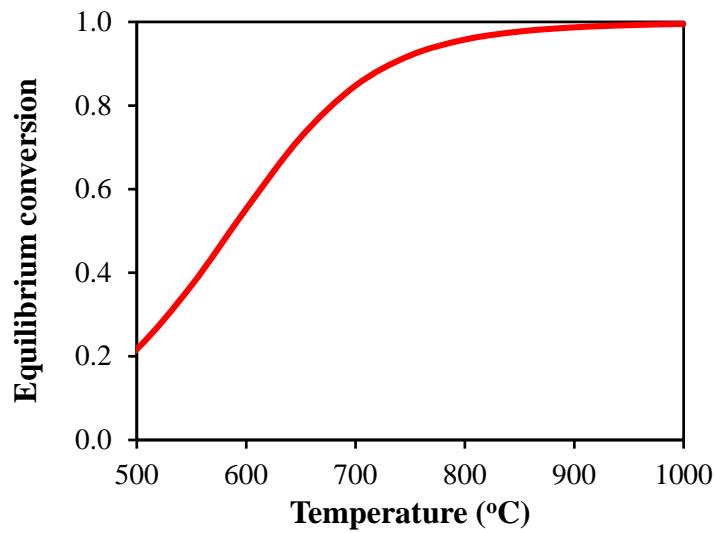


Figure 6. Equilibrium conversions of CH₄ and CO₂ for dry reforming of methane as a function of temperature at P=1 atm and CH₄/CO₂/Ar=1/1/3

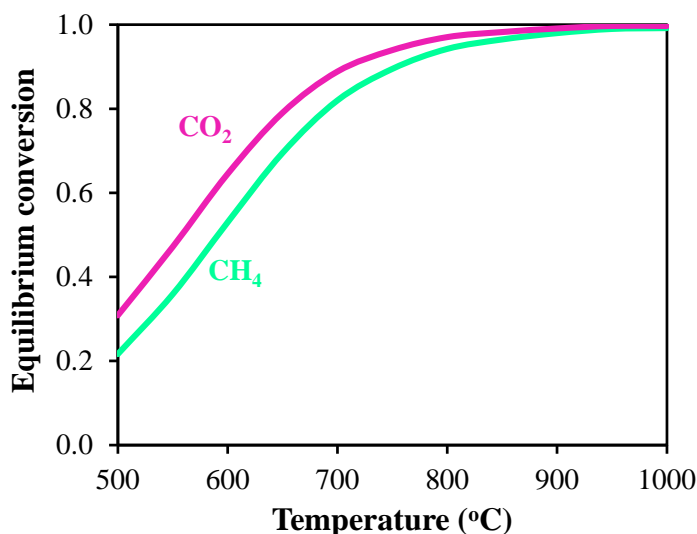


Figure 7. Equilibrium conversions of CH₄ and CO₂ for simultaneous dry reforming of methane and RWGS reaction as a function of temperature at P=1 atm and CH₄/CO₂/Ar=1/1/3

2.3.2 Mechanism of Carbon dioxide Reforming of Methane

The major problem in dry reforming of methane which is carbon formation has been regarded mainly originating from methane decomposition and carbon monoxide disproportionation [1,28]. While the former is favorable at high temperatures and low pressures, the latter is preferred at low temperatures and higher pressures [37]. An appropriate catalyst for dry reforming of methane reaction should exhibit not only high activity but also high stability. A basic factor for the selection of a catalyst is its capacity to kinetically impede coke deposition. For this aim, it is important to consider the mechanism of the target and side reactions on different catalytic systems [1].

The initial stage in dry reforming of methane reaction sequence is methane adsorption [1]. While the predominating mechanism for methane adsorption and desorption is precursor mediated at low temperatures, it is direct at high

temperatures. According to the results of the study on the interaction between methane and Ni(111) surface, it was proposed that for dissociation, methane has to be distorted from its tetrahedral configuration to make a trigonal pyramidal shape and then tunneling of a hydrogen atom takes place through the activation barrier [19,28 and references therein]. On the other hand, in an another study it was asserted that the activation barrier did not include molecular distortion for dissociation of methane on nickel and that it subjected solely to the tunneling of a hydrogen atom through the activation barrier for hydrogen abstraction [19,28 and references therein].

In general, methane adsorbs in a dissociated form on metals to generate H and CH_x species where the numerical value of x ranges between zero and four which depends on the metal substrate and temperature. When x is zero, this shows that coke formation takes place on surface of metal. Both hydrogen atoms and CH_x species are connected to the active metal sites. The great part of the adsorbed hydrogen atoms recombine and produce hydrogen molecules which afterwards desorbs into the gas phase [19 and references therein].

Methane activation was reported to be structure sensitive [1,28 and references therein]. Beebe et al. showed that methane dissociation on nickel surface took place with activity increasing in the order of Ni(111)<Ni(100)<Ni(110) [38]. Abild-Pedersen et al. showed that steps of Ni (111) surface exhibited better activity than the terraces in methane dissociation [39]. Based on the results of DFT calculations over a Ni(111) surface and a stepped Ni (211) surface, Bengaard et al. concluded that the step sites were more reactive than the close-packed surface in the activation of methane [40].

In general, carbon dioxide adsorption and dissociation on transition metal surfaces is considered to be controlled by electron transfer and necessitates the creation of an

anionic CO_2^- precursor. Carbon dioxide adsorption was also reported to be structure sensitive as in the case of methane activation (Table 1) [28 and references therein].

Table 1. Structure sensitivity of CO_2 adsorption [28]

Metal	Dissociative chemisorption	Nondissociative adsorption
Fe	(111), (100)	(110)
Ni	(110), (100)	(111), (100)
Cu	—	(110), (100)
Rh	(533), (711)	(111), (100)
Pd	—	(111), (100)
Ag	—	(110)
Re	(0001)	—
Pt	—	(111)

Solymosi [41] studied CO_2 adsorption on various metal surfaces. While CO_2 adsorbed weakly and molecularly on Pt at 100-300 K under UHV, the dissociation was very limited on Cu. CO_2 was reported to adsorb on Ni, Re, Fe, Mg and Al dissociatively [41]. Bartos et al. showed that carbon dioxide adsorption on Ni surface could take place through three various coordination geometries (Figure 8) [42].

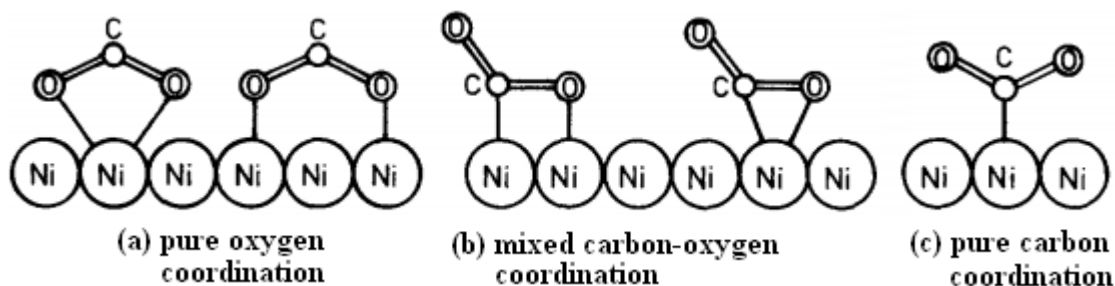


Figure 8. Possible coordination geometries of adsorbed CO_2^- [adapted from 42]

CO₂ can adsorb on metal oxides [43-46] which usually serve as catalyst support in dry reforming of methane [1]. Several spectroscopic studies showed that adsorption of CO₂ on metal oxide surfaces resulted in the formation of carbonates (bidentate, monodentate or bridged), bicarbonates, carboxylates, formates as well as bent CO₂ species [47 and references therein]. CO₂ binding energies on oxides are typically larger than those on metal surfaces [44].

Depending on the metal oxide employed as support, dissimilarities have been observed on CO₂ activation behavior for various catalytic systems: Ferreira-Aparicio et al. [48] proposed that CO₂ reforming of CH₄ took place via Langmuir–Hishelwood mechanism for SiO₂ supported Ru catalyst, where both of the reactants were activated on the metal (Table 2). On the other hand, a bifunctional mechanism was proposed for Al₂O₃ supported Ru (Table 3). For this catalyst, CH₄ was activated on metal, while CO₂ was hydrogenated on Al₂O₃ to produce formate species which were eventually decomposed to yield CO.

Table 2. Reaction steps for CO₂ reforming of CH₄ over Ru/SiO₂ [48]

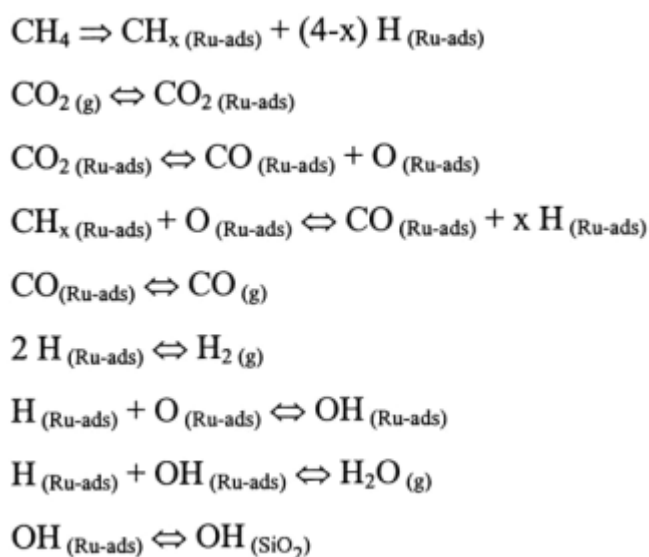
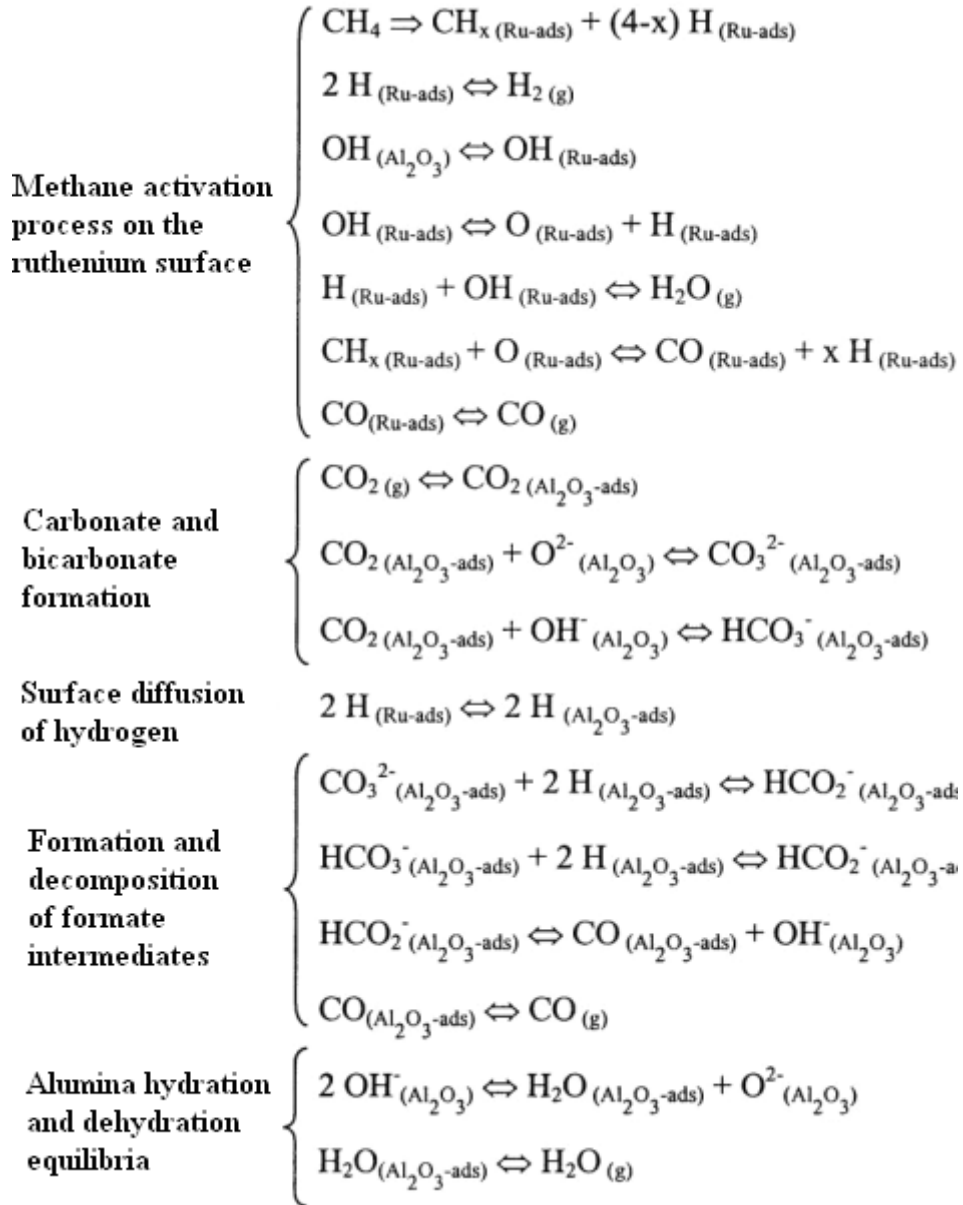


Table 3. Reaction steps for CO₂ reforming of CH₄ over Ru/Al₂O₃ [48]

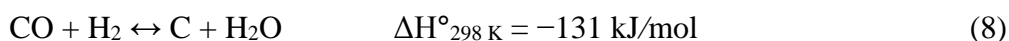
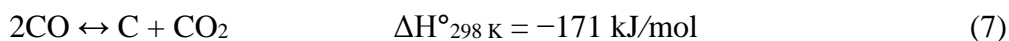
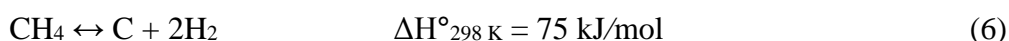


Nakamura et al. [49] observed that the activity of Rh/SiO₂ in dry reforming of methane reaction increased significantly with the addition of metal oxides such as TiO₂, MgO and Al₂O₃ to the support. This was ascribed to the improved CO₂ activation on the support, proposing a bifunctional mechanism where the support contributed to CO₂ activation.

Bitter et al. [50] proposed a bifunctional mechanism for dry reforming of methane on Pt/ZrO₂. They suggested that CH₄ was activated on the metal while CO₂ was activated on the support and the activated species might give a reaction with each other on the boundary of Pt-ZrO₂.

2.3.3 Deactivation due to Carbon Deposition

The major problem in dry reforming of methane is catalyst deactivation which can be due to carbon formation [1,28,29], sintering at high temperature [30,31] and oxidation of metallic sites [32,33]. Coke formation has been accepted as the primary reason of deactivation in dry reforming of methane [34]. It leads to loss in catalytic activity and insufficient heat transfer between the catalyst and the gas phase. When it becomes very severe, it blocks the open surface area resulting in an excessive pressure drop within the reactor. Furthermore it can also lead to localized hot spots which can cause runaway conditions for the reactor [51]. Carbon deposition during dry reforming of methane can happen by one or more of the following reactions:



In literature, carbon formation during dry reforming of methane has been regarded mainly originating from methane decomposition (Equation 6) and carbon monoxide disproportionation (Equation 7) [1,28].

Being the most ubiquitous form of catalyst deactivation, carbon deposition can happen through various mechanisms, depending on factors such as the nature of the hydrocarbon and the catalyst and reaction operating conditions [52]. Mechanisms of carbon deposition from CO and coke formation from hydrocarbons are shown in Figure 9 and Figure 10.

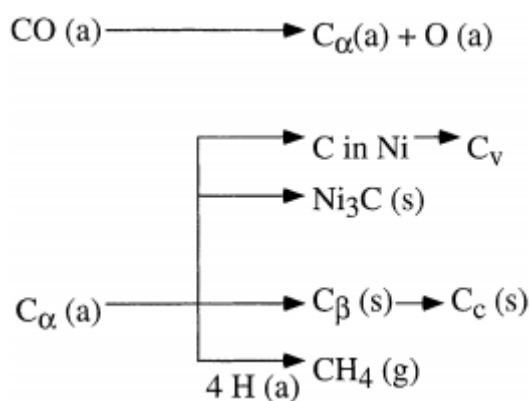


Figure 9. Formation, transformation and gasification of carbon on nickel (a:adsorbed, g:gaseous, s:solid) [53]

Various forms of coke and carbon varying in reactivity and morphology are formed in these reactions (Table 4). For instance, CO dissociation on metals results in formation of C_α , an adsorbed atomic carbon which can react to C_β , a polymeric carbon. The more reactive, amorphous types of carbon formed at low temperature transform into less reactive, graphitic form of carbon over a period of time at high temperature [53].

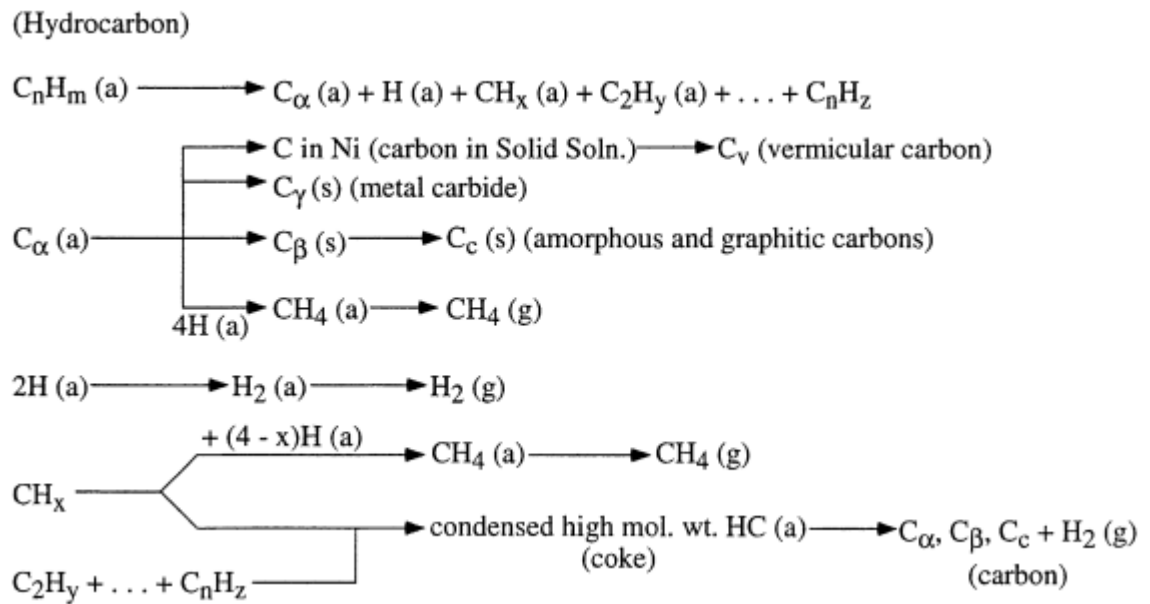


Figure 10. Formation and transformation of coke on metal surfaces (a:adsorbed, g:gaseous, s:solid) [53]

Table 4. Types and reactivities of carbon species formed by CO decomposition on nickel [53]

Structural type	Designation	Temperature of formation (°C)	Peak temperature (°C) for reaction with H ₂
Adsorbed, atomic (surface carbide)	C _α	200–400	200
Polymeric, amorphous films or filaments	C _β	250–500	400
Vermicular filaments, fibers, and/or whiskers	C _v	300–1000	400–600
Nickel carbide (bulk)	C _γ	150–250	275
Graphitic (crystalline) platelets or films	C _c	500–550	550–850

The carbon formed during CO₂ reforming of CH₄ is often in the form of filamentous whiskers [28 and references therein]. The carbon filaments do not deactivate the catalyst immediately, except after a massive carbon accumulation [54]. On nickel surfaces, whisker carbon can form by dissociation of hydrocarbons or carbon

monoxide [55]. According to the classical model, adsorbed carbon atoms dissolve in the bulk of the metal, then carbon diffuses through the bulk of the metal and nucleates into a fiber at the rear interface. The nickel crystal alters shape into a pear-like particle, abandoning tiny fragments of nickel behind in the whisker [56]. This mechanism was challenged recently by a study based on ab initio DFT calculations to investigate different diffusion processes that can take place in whisker carbon formation [57]. It was reasoned that carbon diffusion through the bulk nickel is very improbable. On the other hand, carbon transport could take place via surface or subsurface diffusion. They showed that nickel step edge sites behave as the favorable centers for the growth of graphene layers [57]. These conclusions are in accordance with the results obtained by Helveg et al. [58] who used in situ HRTEM to investigate the formation of carbon nanofiber growth from CH_4 decomposition over MgAl_2O_4 supported nickel nanocrystals (Figure 11)

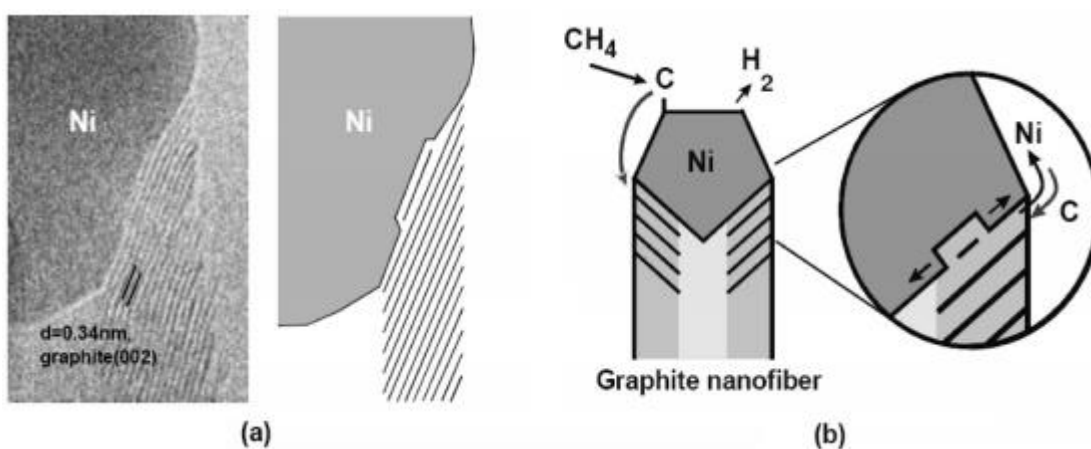


Figure 11. a) HRTEM of carbon nanofiber growth,
b) Illustration of growth mechanism [57]

CH₄ decomposition and CO disproportionation are reversible and the potential for carbon formation can be assessed by thermodynamics. Rostrup-Nielsen showed that ‘the principle of equilibrated gas’ can be applied which states that carbon will be formed if the gas exhibits affinity for carbon after the foundation of methane reforming and shift equilibrium [55]. This suggests that the composition used to compute the equilibrium corresponds to the composition after accounting for the reforming and shift equilibrium [59].

In a carbon limit diagram (Figure 12), atomic ratios of O/C are plotted in the abscissa and the atomic ratios of H/C are plotted in the ordinate. While the straight line increasing from H/C=4, O/C=0 (CH₄ component) represents all feed mixtures of steam-CH₄, the lower line represents all feed mixtures of CO₂-CH₄. The dotted lines exhibits conditions (O/C and H/C) resulting in the indicated H₂/CO ratio in the reformer exit gas [52].

The thermodynamic data for carbon are affected by the morphology of it formed on the catalyst [52]. Figure 12 shows the carbon limit curve for graphite (Curve 1) and whisker carbon (Curve 2). H₂/CO ratios correspond to equilibrated gas at the reformer outlet temperature of 900°C and pressure of 5 bar. For O/C and H/C ratios on the left side of the curves, there is thermodynamic potential for carbon formation [52].

As Rostrup-Nielsen indicated “the principle of equilibrated gas is no law of nature”. It is feasible to rupture the thermodynamic limit [55]. One solution is to perform the reaction over noble metal catalysts, which exhibit little tendency for carbon formation [60]. Another alternative for large scale applications is to use sulphur passivated catalysts as practiced in SPARG process [60]. This process solves carbon formation problem by "ensemble control" which purports that the active sites for carbon formation are blocked while adequate sites are preserved for the reforming reaction. This effect is acquired by the addition of sulphur to the process feed [52].

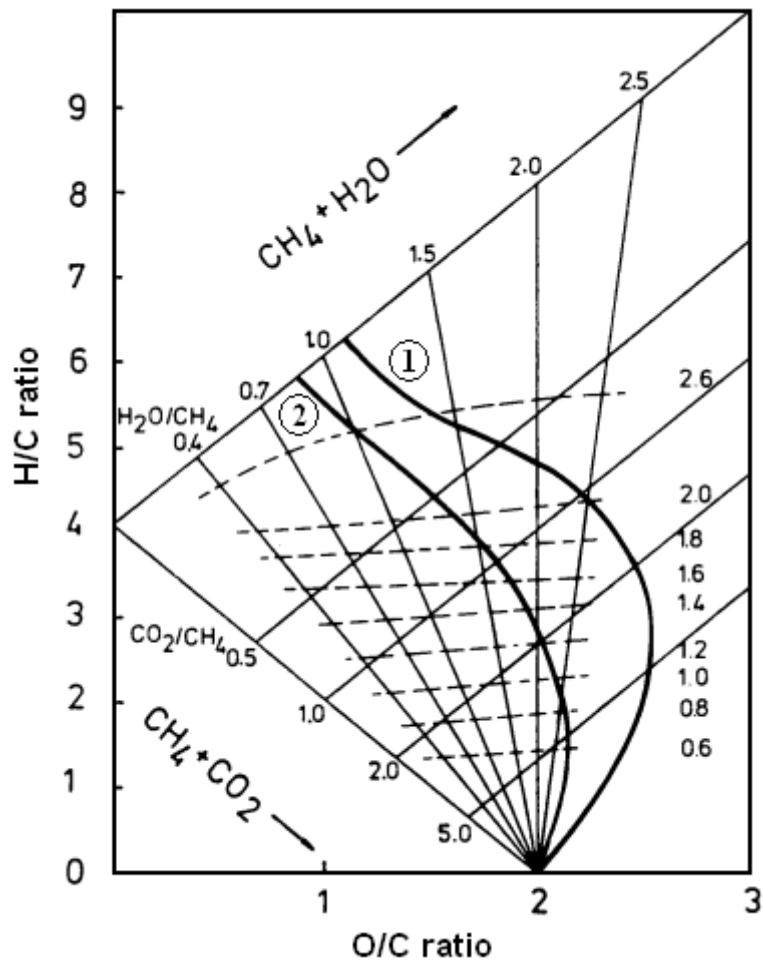


Figure 12. Carbon limit diagram (principle of equilibrated gas)
 Curve 1: graphite data, Curve 2: whisker carbon [adapted from 52]

CHAPTER 3

EXPERIMENTAL

3.1 Catalyst preparation

3.1.1 Preparation of Ni/Al₂O₃, Co/Al₂O₃ and Ni-Co/Al₂O₃ by incipient wetness impregnation method

γ -Al₂O₃ supported monometallic 8 wt % nickel and 8 wt % cobalt; bimetallic 8-4 wt % nickel-cobalt and 4-4 wt % nickel-cobalt catalysts were synthesized by incipient wetness impregnation technique. Commercial γ -Al₂O₃ supplied by Alfa Aesar was used as catalysts support, Ni(NO₃)₂·6H₂O (Merck) and Co(C₂H₃O₂)₂·4H₂O (Merck) were used as metal sources. The impregnation solution was prepared by dissolving required amount of Ni(NO₃)₂·6H₂O and Co(C₂H₃O₂)₂·4H₂O in deionized water (1-2 ml H₂O/g support). Ni and Co were loaded onto the γ -Al₂O₃ supports by impregnating the supports with metal precursor solution to bring about incipient wetness. Ni-Co bimetallic catalysts were prepared by co-impregnation method. The catalysts were dried overnight at room temperature and then for 30 minutes at 80°C. Finally, the catalysts were calcined at 700°C as well as 900°C for 5 hours to remove ligands from the nickel and cobalt precursors. The catalysts calcined at 700°C were denoted as Ni/Al₂O₃-I-700, Co/Al₂O₃-I-700 and Ni-Co/Al₂O₃-I-700. The catalysts calcined at 900°C were denoted as Ni/Al₂O₃-I-900, Co/Al₂O₃-I-900 and Ni-Co/Al₂O₃-I-900.

4-4 wt % Ni-Co/Al₂O₃ bimetallic catalyst was only used in DRIFTS experiments. The metal loading for the Al₂O₃ supported bimetallic catalyst is 8-4 wt % Ni-Co in all other parts.

3.1.2 Preparation of Ni/Al₂O₃ by polyol method

Ni(NO₃)₂·6H₂O (Merck) was dissolved in 100 mL ethylene glycol (Merck) to obtain a solution having 0.05M metal concentration. PVP (polyvinylpyrrolidone, Mw=40,000 g/mol, Merck) was added to this solution as the metal-protecting agent and mixed with a magnetic stirrer until obtaining a clear solution. Then required amount of Al₂O₃ (Alfa Aesar) was added under stirring to obtain 10 wt % (nominal) Ni/Al₂O₃ and mixed at room temperature for 20 hours. The pH of the solution was adjusted to 10-11 with dropwise addition of 1 M NaOH which was prepared by dissolution of sodium hydroxide in ethylene glycol. The abovementioned solution was heated to the boiling point of ethylene glycol (185-190°C) with a reflux condenser and it was kept at this temperature under magnetic stirring until the reduction of Ni²⁺ to metallic Ni was achieved. The progress of reduction was observed by the change of the color of solution. While the color was green at the beginning of heating, it turned to grey gradually with the start of reduction. It turned to black when the reduction finished. Then, the solution was quickly cooled down to room temperature in an ice-water bath. The catalyst was isolated via centrifuge, then washed with ethanol and centrifuged again. Subsequently, the catalyst loaded with metal was dried in a furnace at 80°C for 24 hour. No calcination procedure was applied. Three different catalysts were synthesized according to this procedure, changing the PVP/Ni ratio (weight /weight): 0.0, 2.5 and 5.0. The samples obtained in this work were denoted as Ni/Al₂O₃-without-PVP, Ni/Al₂O₃-PVP/Ni=2.5 and Ni/Al₂O₃-PVP/Ni=5.0 corresponding to the PVP/Ni(NO₃)₂·6H₂O ratio described before. To make a comparison, a sample was prepared without changing neither the pH nor adding PVP according exactly to the same procedure.

3.1.3 Preparation of Ni/CeO₂, Co/CeO₂ and Ni-Co/CeO₂ by incipient wetness impregnation method

CeO₂ supported monometallic 8 wt % nickel, 8 wt % cobalt and bimetallic 8-4 wt % nickel-cobalt catalysts were prepared by incipient wetness impregnation technique. Pure CeO₂ support was obtained by calcination of Ce(C₂H₃O₂).1.5H₂O at 700°C as well as 900°C for 3 hours. Ni(NO₃)₂·6H₂O (Merck) and Co(C₂H₃O₂)₂·4H₂O (Merck) were used as metal sources. The impregnation solution was prepared by dissolving required amount of Ni(NO₃)₂·6H₂O and Co(C₂H₃O₂)₂·4H₂O in deionized water. Ni and Co were loaded onto the CeO₂ supports by impregnating the supports with metal precursor solution to bring about incipient wetness. Ni-Co bimetallic catalysts were prepared by co-impregnation method. The catalysts were dried overnight at room temperature and then at 120°C for four hours. Finally, the resulting products were calcined at 700°C as well as 900°C for 5 hours to remove ligands from the nickel and cobalt precursors. The catalysts calcined at 700°C were denoted as Ni/CeO₂-I-700, Co/CeO₂-I-700 and Ni-Co/CeO₂-I-700. The catalysts calcined at 900°C were denoted as Ni/CeO₂-I-900, Co/CeO₂-I-900 and Ni-Co/CeO₂-I-900.

3.1.4 Preparation of CeO₂ by exotemplating method ¹

Ceria fibers were synthesized according to an exotemplating method using electrospun PMMA polymer fibers, followed by spray coating of an inorganic ceria sol [61]. A template solution of 15 wt % PMMA in a mixture of acetone and dimethyl formamide (60/40 wt %) was electrospun via a glass syringe (5 mL) with tip dimensions of 0.8x40 mm at an electrode distance of 20 cm and 26 kV to the copper counter electrode (15x15 cm²) (Figure 13).

1.37 g Cerium (IV) ammonium nitrate salt was dissolved in 40 mL distilled water. 0.65 mL of aqueous solution of ammonia (25 wt %) was added so as to increase the pH of the solution. This solution was kept under vigorous stirring for 30 minutes.

¹ Preparation of CeO₂ by exotemplating method was done at Technical University of Darmstadt.

About 1 gram of Pluronic P123 block copolymer was added as surfactant and the solution was mixed at 50°C for 5 hours. This solution was spray coated onto the prepared polymer fibers. The sol-gel transformation of the sample was accomplished in a furnace at 80°C overnight.

Oxygen plasma etching was done by using a Diener Electronics PS Tech, Femto machine for 18 h. Plasma was created by an inductively coupled RF generator with the frequency of 13.56 MHz and the output power of 200 W. The flow rate of oxygen sent to chamber was 4 mL/min. Finally, the sample was calcined at 350°C for 3 h.

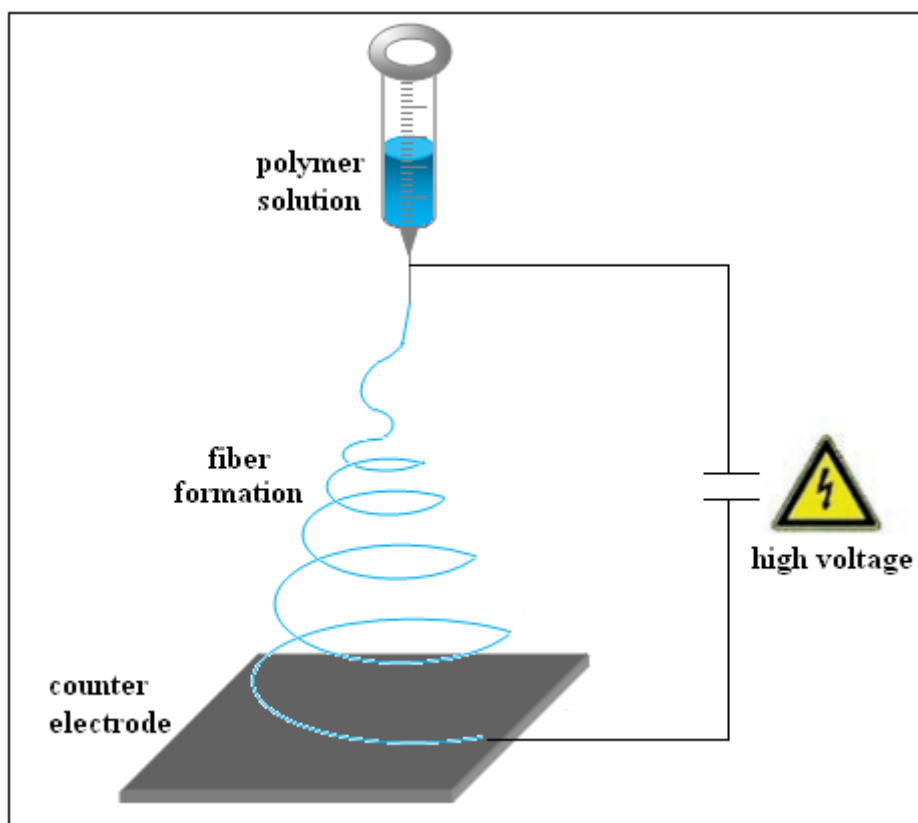


Figure 13. Electrospinning set-up

3.2 Catalyst Characterization

3.2.1 X-Ray Diffraction (XRD) Analysis

X-ray powder diffraction data were acquired with a Philips model PW1840 X-ray diffractometer using Ni-filtered Cu K α radiation source ($\lambda=0.1542$ nm) operated at 30kV and 24 mA. XRD patterns were measured between $2\theta=10^{\circ}$ - 100° at a scan rate of $0.01^{\circ}/\text{sec}$.

3.2.2 Surface Area, Pore Size Distribution and Adsorption-Desorption Isotherms

Micromeritics TriStar II surface area and porosity analyzer was utilized to measure the N₂ adsorption-desorption isotherms of the samples at 77K. The samples were degassed for 3 hours at 423K prior to measurements by means of Micromeritics VacPrep 061 Sample Degas System for removing the moisture and other adsorbed gases from the catalyst surface. The surface area was obtained from multipoint BET (Brunauer–Emmett–Teller) method. The pore volume and average pore diameter were estimated from adsorption branch of isotherms by the method of BJH (Barrett, Joyner and Halenda).

3.2.3 Temperature Programmed Reduction (TPR) Analysis

The reducibility of the samples was investigated by H₂ temperature programmed reduction study. TPR experiments were performed by a home built system using a fixed bed quartz reactor, the length of which was 35 cm and the inner diameter of which was 4 mm. The quartz reactor was placed into a temperature controlled tube oven. Gas flows were metered by mass flow controllers. 100 mg catalyst was heated from room temperature to 850°C using 40 sccm H₂:Ar (3:97) gas flow at a ramp rate of 5°C/min. The temperature was kept constant at 850°C for half an hour. The outlet

H₂ concentrations were recorded online by means of a Teledyne 2000 XTC model TCD detector.

3.2.4 DRIFTS

In order to determine the adsorbed species and to investigate how the species are adsorbed on the surface of the catalysts, DRIFTS experiments were performed. DRIFTS measurements were carried out using a Perkin Elmer FTIR (Spectrum 100 series) which was equipped with a drift cell (Pike) and MCT detector. All spectra were recorded with 4 cm⁻¹ resolution in the range of 4000-400 cm⁻¹ for a total scan count of 128.

Experimental set up of DRIFTS measurements is shown in Figure 14. Feed gas (H₂, CO₂ and CH₄) lines were connected to a gas manifold, the outflow of which was attached to the reaction cell. The feed gas was first accumulated in the manifold and then sent to the reaction cell.

Prior to the CO₂ and CH₄ adsorption experiments, the following pretreatment procedure was performed. First, the sample was outgassed at room temperature at a pressure of 10⁻⁶ Torr. Then, the temperature of the samples was increased from room temperature to 400°C incrementally. Reduction was done by sending 100 Torr H₂ four times at 400°C and between each H₂ treatment, the system was evacuated. Finally, the system was outgassed and cooled down to room temperature. After the pretreatment, background spectra was recorded and then the pressure of the adsorbate gas was set to 97.5, 300, 500 Torr respectively. DRIFTS spectra were recorded after the admission of each dosage of gas. Then the system was heated to 100, 200, 300 and 400°C incrementally in order to observe the change in adsorption pattern with an increase in temperature by recording the DRIFTS spectra.

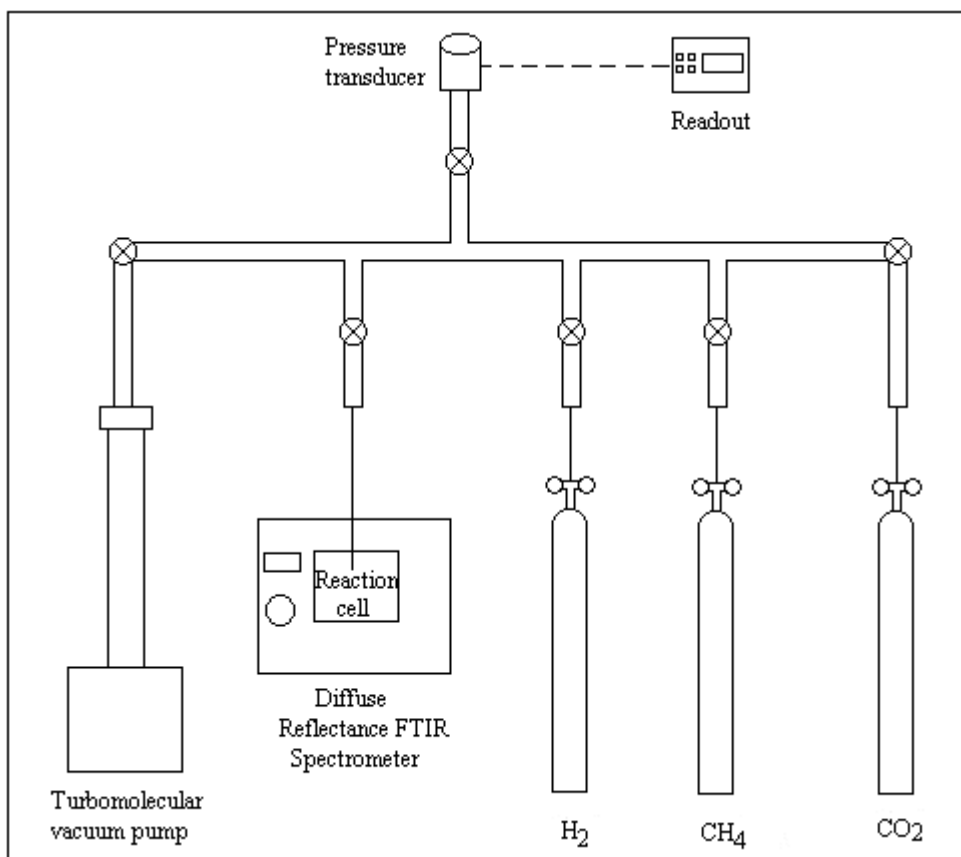


Figure 14. Experimental set up of DRIFTS measurements

3.2.5 Microcalorimetry

Microcalorimetric adsorption was used to study the energy of surface bonding for CO₂ adsorption on pure uncalcined Al₂O₃, calcined Al₂O₃, Ni/Al₂O₃, Co/Al₂O₃ and Ni-Co/Al₂O₃. Microcalorimetry studies were carried out at 50°C by using a Tian-Calvet type heat flow calorimeter (Seteram C-80) which was connected to a gas manifold. Experimental set up of microcalorimetry measurements is shown in Figure 15. The manifold employs a Baratron capacitance manometer in the range of 10⁻⁴-10 Torr and a Pfeifer turbo molecular pump. Pyrex tee was utilized to connect the sample cell and the reference cell to each other and to the manifold. 500 mg sample

was used for all experiments. The feed gas was first accumulated in the manifold and then sent to the reaction cell.

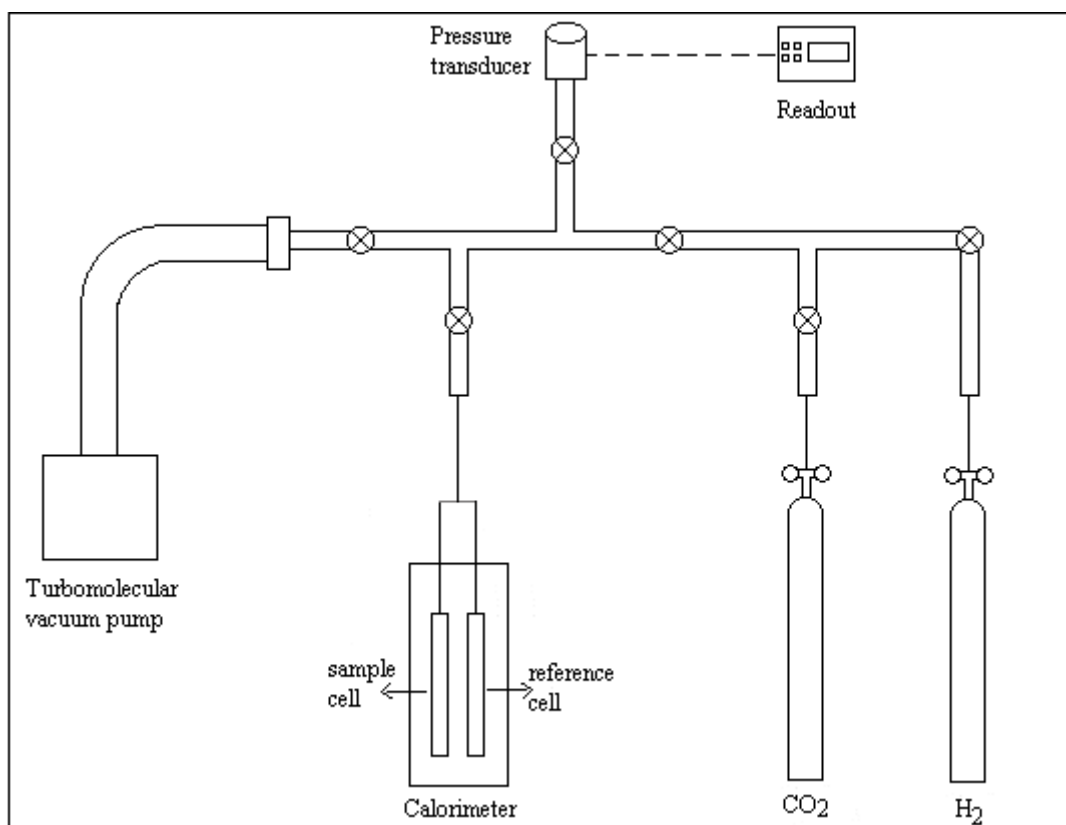


Figure 15. Experimental set up of microcalorimetry measurements

Prior to the CO₂ adsorption experiments, the following pretreatment procedure was performed. First, the catalyst was heated to 523K at a ramp rate of 2K/min and kept at this temperature under vacuum for 10 hours. After being cooled down to room temperature it was again heated up to 523K and reduced in situ at this temperature by repeatedly increasing the pressure to 10 torr of H₂, followed by evacuation. Finally, the system was outgassed and cooled down to 323 K. The differential heats of CO₂ measurements were performed at 323 K by sending subsequent doses of gas onto the samples. The heat response resulted from adsorption was recorded as a function of

time. The equilibrium pressure was recorded when thermal equilibrium was reached. The amount of adsorbed gas onto the sample was calculated volumetrically by using the initial dosage of gas and the equilibrium pressure. The integration of the heat curve yielded the heat evolved as a result of adsorption. The above procedure was repeated until the surface of the sample was saturated with the adsorbate gas.

3.2.6 Thermal Gravimetric Analysis (TGA)

TGA was carried out to determine the amount of coke deposition on the samples after being used in the CO₂ reforming of CH₄. In addition to this, TGA was also used to determine the amount of organics in the fresh samples prepared by polyol process. The analyses were performed using a Shimadzu DTG 60-H instrument, where each sample was introduced into an alumina microbalance pan that was heated to 1173 K at a rate of 10 K/min in an oxygen/nitrogen mixture (21:79 vol/vol with a total flow of 75 ml/min).

3.2.7 Transmission Electron Microscopy (TEM)

3.2.7.1 High Resolution Transmission Electron Microscopy (HRTEM)

The morphology of Al₂O₃ supported fresh samples which were prepared by incipient wetness impregnation method were characterized by Jeol 2100F HRTEM machine equipped with Orius SC1000 Model 832 11 Megapixel CCD camera. Before taking the micrographs, the catalysts were dispersed ultrasonically in alcohol and a drop of dispersion was deposited and dried on holey carbon film grid.

3.2.7.2 High Contrast Transmission Electron Microscopy (HCTEM)

The morphology of carbon deposited on the samples after dry reforming of methane reaction and the morphology of the fresh samples prepared by polyol method were

characterized by FEI Tecnai G² Spirit Bio (TWIN) HCTEM operated at 120 kV. Before taking the micrographs, the samples were dispersed ultrasonically in alcohol and a drop of dispersion was deposited and dried on a 400 mesh carbon-coated copper grid.

3.2.8 Scanning Electron Microscopy (SEM) ²

SEM was done by FEI XL30 FEG operating at a voltage of 25 kV to characterize the morphology of ceria sample prepared by an exotemplating method.

3.2.9 Nuclear Magnetic Resonance (NMR) ³

Room temperature ¹³C direct detection magic angle spinning (MAS) NMR spectroscopy experiments were acquired at 7.05T with a 4 mm Chemagnetics probe using a Tecmag Discovery Spectrometer and spinning speed of 10 kHz. The carbon channel of the probe was tuned to 75.39 MHz.

3.3 Dry Reforming Reaction Tests

Carbon dioxide reforming of methane reactions were performed in a home built reaction system. The reaction setup consists of a gas supply system, reaction part and analyzer as shown in Figure 16.

² SEM studies were done at Technical University of Darmstadt.

³ NMR measurements were done at UC Berkeley.

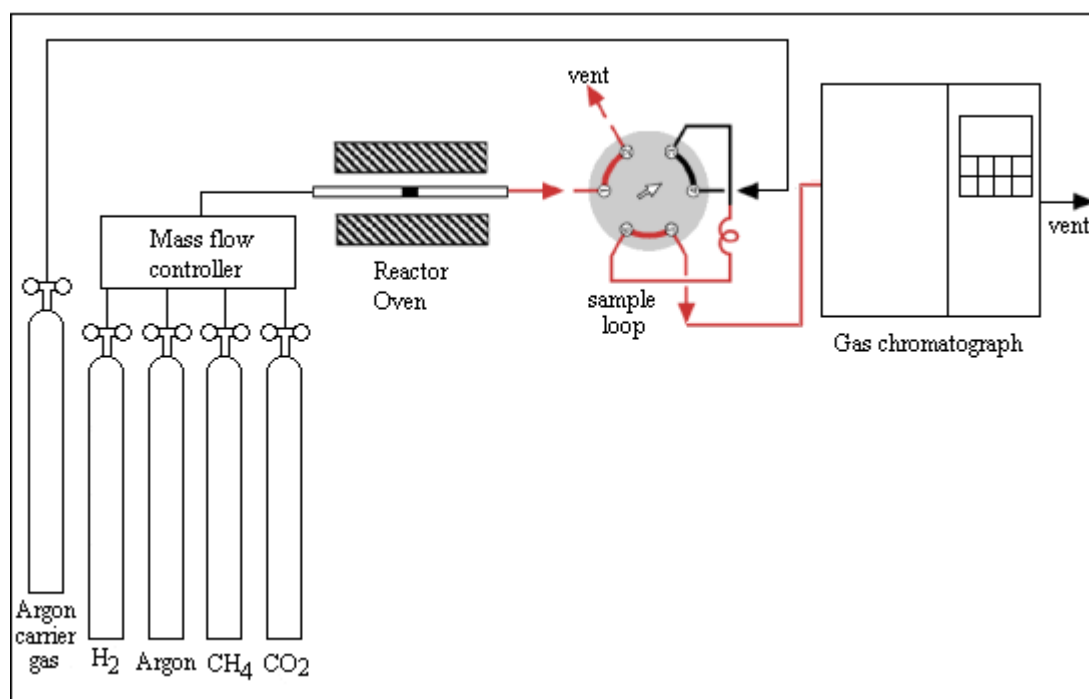


Figure 16. Experimental set up for the catalytic reaction tests

The gas supply system contains the feed gas cylinders (H_2 , Ar, CH_4 and CO_2) and mass flow controllers (MKS 1179 B). The flow of inlet gas streams were controlled by these mass flow controllers. The reaction part is composed of quartz reactor and a temperature controlled tube oven. The length and inner diameter of reactor are 35 cm and 4 mm, respectively. The temperature of the reaction was controlled by means of a thermocouple which was placed in the middle of tube oven. The product gases were sent to a gas chromatograph (HP 5890 Series II) by means of a 6 way valve (Vici valco) equipped with a $100\mu\text{L}$ sample loop. The gas chromatograph contains a thermal conductivity detector and a Carboxen 1010 Plot column. Before the analysis, the gas chromatograph was calibrated for H_2 , CO, CH_4 and CO_2 gases in order to analyze the outlet stream of the reaction quantitatively. The calibration curves were drawn as the volumetric flow rate of the gas (sccm) versus the corresponding area under the peak. The operating conditions of gas chromatograph are given in Table 5.

Table 5. Operating conditions of gas chromatograph

Column	Carboxen 1010 Plot, 30 m x 0.53 mm I.D.
Detector	Thermal conductivity detector (TCD)
Injection temperature	200°C
Detector temperature	210°C
Oven temperature	27°C (5.5 min) 30°C /min to 80°C (6 min) 30°C /min to 120°C (3 min)
Column pressure	100 kPa
Injection volume	100 µL valve injection
Reference gas	Argon

In the reaction tests, both powder and particles in the size range of 0.5-1.0 mm were used. For obtaining the particles in the size range of 0.5-1.0 mm, the powder catalysts were first pressed, then crushed and finally sieved to a size of 0.5-1.0 mm. The samples were placed in the center of the 4 mm-i.d. microreactor by quartz wool at both ends. The reactions were carried out at 600°C or 700°C with 50 sccm CH₄:CO₂:Ar (1:1:3) gas flow for 5 hours. Before the catalytic activity tests, the samples prepared by incipient wetness impregnation method were reduced in 50 sccm H₂:Ar (2:3) by heating from room temperature to 700°C with 10°C/min heating rate and kept at this temperature for one hour. 30 sccm pure Argon was sent to the reactor for half an hour before the reactant gases were sent. On the other hand, the catalysts prepared by polyol process were not reduced before the reaction tests. They were heated in 30 sccm Argon flow from room temperature to the reaction temperature (600°C or 700°C) with 10°C/min. 50 sccm CH₄:CO₂:Ar (1:1:3) were sent to the reactor immediately after reaching to the reaction temperature.

3.4 Redox Experiments on Ceria Samples ⁴

Ceria samples prepared by exotemplating (CeO₂-ESC), coprecipitation (CeO₂-CPC) and commercial ceria (CeO₂-COC) were first pressed, then crushed and finally sieved with a size of 250-355 mesh. 50 mg of sample was placed in the U-tube quartz reactor system. The product gases were analyzed by means of an on-line quadrupole mass spectrometer.

One redox experiment consisted of six steps. The first two steps were flow experiments and the remainings were transient pulse experiments while 500 μ L gas was introduced at a frequency of 1 minute. For the pulse experiments, computer-controlled switching valves were utilized. In each case, Helium was used as the major component of the gas mixture. The total flow rate was set to 100 sccm. The flow of the reactant gases CO and O₂ was adjusted to be 1 % of the total flow rate.

Step 1. The sample was oxidized under 100 sccm O₂/He by heating from room temperature to 600°C with 10°C/min. The temperature was kept at 600°C for 25 minutes. The sample was cooled down in He atmosphere.

Step 2. The sample was reduced under 100 sccm CO/He by heating from room temperature to 600°C with 10°C/min. The temperature was kept at 600°C for 25 minute. Then it was switched to He and kept under He atmosphere for 25 minutes.

Step 3. 100 sccm O₂/He was sent to the sample loop. 100 oxygen pulses were applied. After having finished oxygen pulses, the sample was kept under He for 25 minutes.

Step 4. 100 sccm CO/He was sent to the sample loop. 120 CO pulses were applied. After having finished CO pulses, the sample was kept under He for 25 minutes.

⁴ Redox experiments on ceria samples were done at Ruhr University Bochum.

Step 5. 100 sccm O₂/He was sent to the sample loop. 100 oxygen pulses were applied. After having finished oxygen pulses, the sample was kept under He for 25 minutes.

Step 6. 100 sccm CO/He was sent to the sample loop. 120 CO pulses were applied. After having finished CO pulses, the sample was kept under He for 25 minutes.

CHAPTER 4

DRY REFORMING OF METHANE ON Al_2O_3 SUPPORTED Ni, Co and Ni-Co CATALYSTS SYNTHESIZED BY INCIPIENT WETNESS IMPREGNATION METHOD

4.1 Introduction

Ni catalysts have taken great interest in dry reforming of CH_4 due to their high catalytic activity, wide availability and low cost [1,10,62]. However, the main restriction of Ni-based catalysts is the formation of carbon which brings about catalyst deactivation [1,10,62]. Several approaches have been proposed for decreasing the carbon formation tendency of Ni-based catalysts: employing appropriate catalyst preparation methods, using metal oxides as supports or promoters, addition of a second metal to form bimetallic system, sulfur passivation, introducing steam, changing reaction conditions [1,11,63,64].

The addition of a second metal is one of the methods applied for dry reforming process with the objective of developing carbon resistance of Ni-based catalysts. There are studies reported on the beneficial effect of noble metal addition such as Rh [65,66], Pt [67,68], Pd [68] and Ru [69] to the Ni-based catalyst. From an economic point of view, the addition of a non-noble metal is more preferable. In this respect cobalt is of great interest.

Xu et al. [11] prepared Ni monometallic, Co monometallic and Ni-Co bimetallic catalysts with varying compositions which were supported on commercial $\gamma\text{-Al}_2\text{O}_3$ doped with La_2O_3 for biogas reforming. For bimetallic samples, the ratio of nickel and cobalt was changed by keeping the total metal loading at 10 % by weight. The monometallic 10 Co/LaAl sample exhibited the lowest catalytic activity. On the other hand, the monometallic 10 Ni/LaAl sample showed high activity. The

incorporation of cobalt to the nickel catalyst influenced the catalytic activity. The catalyst having Ni/Co ratio of 7/3 exhibited the highest CH₄ and CO₂ conversion. Nevertheless, the catalytic activity decreased considerably if the amount of cobalt was increased further. Bimetallic catalysts having a Ni/Co ratio of 5/5 and 3/7 exhibited lower activity than monometallic Ni catalyst. The authors proposed that the adjustment of nickel to cobalt ratio could enhance pore textural properties and metal dispersion and hence improve the catalytic activity and resistance against carbon formation.

Zhang et al. [36] prepared Ni–Me–Al–Mg–O catalysts by using coprecipitation method where Me was cobalt, iron, copper or manganese. Ni–Co sample exhibited excellent activity and stability compared to the other bimetallic catalysts in dry reforming of methane. The CH₄ conversion was in the order of Ni–Co > Ni–Mn > Ni–Fe > Ni–Cu. Cobalt incorporated nickel sample was also shown to be the best one due to its lowest coke deposition rate. By decreasing the nickel and cobalt loading to approximately half of their initial amounts, coke formation was eliminated for up to 250 hours which was attributed to better metal dispersion and smaller particle size. The authors suggested that “The high activity and excellent stability of Ni–Co catalyst was closely related to its high metal dispersion, strong metal–support interaction, and formation of stable solid solutions.”

Takanabe et al. [70] compared the catalytic activities of TiO₂ supported Ni, Co and Ni–Co catalysts for CO₂ reforming of CH₄. The monometallic Co/TiO₂ sample didn't exhibit any activity when the temperature was lower than 750°C which was ascribed to the oxidation of metallic Co. Although this catalyst started to exhibit activity above 850°C, it was still less than the activity of Ni/TiO₂ and Ni–Co/TiO₂. When the temperature was between 600°C and 750°C, CH₄ conversion was approximately same for Ni/TiO₂ and Ni–Co(50–50)/TiO₂. On the other hand, the activity of Ni/TiO₂ in terms of CH₄ conversion was higher than that of Ni–Co(50–50)/TiO₂ when the temperature was higher than 750°C. While Ni/TiO₂ sample

deposited considerable amount of coking particularly at lower temperatures, Co/TiO₂ sample exhibited tendency to be oxidized during dry reforming. On the other hand, the combination of Ni-Co catalyst showed both high catalytic activity and resistance to coke formation during the reaction. The authors suggested that the composition of bimetallic Ni-Co catalyst could be adjusted to alter its catalytic performance for dry reforming of methane.

Nagaoka et al. [32] studied the effect of replacing cobalt by nickel in a TiO₂ supported Co catalyst for CO₂ reforming of CH₄. When cobalt was replaced by a small quantity of nickel, the catalytic stability of Co/TiO₂ improved. On the hand, the catalytic stability decreased if cobalt was replaced by an excess amount of nickel. Deactivation was attributed to metal oxidation when cobalt amount was too high, whereas it was attributed to carbon deposition when nickel amount was too high. As a result, replacement of cobalt by nickel aided to the retardation of metallic cobalt oxidation; but, excess nickel caused carbon deposition. Co:Ni ratio of 90:10 was shown to be optimum presenting high stability with an unimportant amount of carbon formation.

San-Jose'-Alonso et al. [10] prepared Al₂O₃ supported Ni, Co and Ni-Co catalysts (having 9 % nominal metal content by weight) for CO₂ reforming of CH₄. The catalysts containing the highest amount of cobalt (Co(9) and NiCo(1-8)) exhibited the highest activity and stability. However, they produced much higher amount of coke. Their higher activity was attributed to the higher activity of cobalt for CH₄ decomposition. Their noteworthy stable behavior was ascribed to the existence of big particles taking place in long-term conversion and producing non-deactivating carbonaceous deposit. In this study, carbon deposition increased with increasing Co content, while it decreased with increasing Ni content.

The literature indicates that there are discrepancies between the outcomes of different researches dealing with Ni-Co supported bimetallic catalysts. In this part, a

comprehensive investigation on the effect of cobalt addition to the alumina supported nickel catalysts for CO₂ reforming of CH₄ was carried out by studying Ni/Al₂O₃, Co/Al₂O₃ and Ni-Co/Al₂O₃ catalysts comparatively. In order to see the effect of calcination temperature on the activity of the catalyst during carbon dioxide reforming of methane, they were calcined at two different temperatures, 700°C and 900°C.

The catalyst deactivation during dry reforming of methane is caused by carbon formation [1,28,29], sintering at high temperature [30,31] and oxidation of metallic sites [32,33]. Although in literature it is agreed that the primary cause of catalyst deactivation is carbon formation, there are disagreements existing on the origin of coke which can come from CH₄ and CO₂.

Wang and Lu [71] investigated how coking rate depended on partial pressures of CO₂ and CH₄ over γ -Al₂O₃ supported nickel catalyst during dry reforming of methane at 600°C. While coke formation had a positive relationship with CH₄ partial pressure, it had a negative relationship with CO₂ partial pressure, indicating that CO₂ in the feed inhibited coke formation. Therefore, the authors concluded that decomposition of CH₄ was the dominating way of coke formation in dry reforming of methane reaction over Ni/ γ -Al₂O₃.

Yang and Papp [72] used CO₂-temperature programmed surface reaction (TPSR) to determine the source of carbon deposition during dry reforming of methane. They exposed fresh Pt/MgO catalyst to a mixture of CH₄/N₂ and CO/N₂ separately at 800°C for 10 minutes. CO₂-TPSR resulted in two CO peaks (one is at 820°C, another is higher than 900°C) for the catalyst exposed to CH₄/N₂ mixture, indicating two types of carbon deposition from methane decomposition. On the other hand, no CO peak was detected for the catalyst exposed to CO/N₂ mixture, indicating that CO disproportionation did not occur under the applied reaction condition. CO₂-TPSR profile of the spent catalyst in severe dry reforming conditions also resulted in two CO peaks where the main peak coincided very well with the high temperature peak

observed in the TPSR profile of the catalyst exposed to CH₄/N₂ mixture. The authors concluded that carbon deposition in dry reforming reaction was resulted mainly from methane decomposition.

Verykios [73] showed that dry reforming of methane over Rh/Al₂O₃ catalyst resulted in the formation of three types of carbon species by using TPH and TPO techniques. The relative and the total amounts of various kinds of carbonaceous species were shown to depend on period of exposure and temperature. To investigate the source of carbon species, Verykios conducted reaction experiments with ¹³CH₄ and ¹²CO₂ (¹³CH₄/¹²CO₂/He = 0.2/0.2/0.6) for 10 minutes over Rh/Al₂O₃ at 650°C. TPO results of the spent catalyst revealed that the carbon deposited over Rh/Al₂O₃ mainly originated from CO₂ molecule with a little contribution of CH₄ molecule.

Lemonideu et al. [74] investigated the source of carbon species deposited during dry reforming of methane at 750°C by conducting isotopic experiments on 5 weight % Ni loaded calcium aluminate. They performed TPO experiments after conducting the reaction at 750°C for 5 minutes by using ¹²CO₂/¹³CH₄/He=0.2/0.2/0.6 feed mixture. TPO results indicated the formation of two types of carbonaceous species which exhibited different reactivities towards oxidation. The coke was found to originate from both reactants where the proportion of it resulting from carbon dioxide as opposed to methane was found to be 2.1.

Kroll et al. [75] performed TPO experiments over 24.6 mg Ni/SiO₂ after a 10 minute reaction at 700°C by using ¹²CO₂ and ¹³CH₄ feed mixture (¹²CO₂/¹³CH₄/He=9.5/9.5/81) with a flow rate of 3 L/hour. Two kinds of carbonaceous deposits were observed: a sharp oxidation peak at around 500°C and a broad oxidation peak having a maximum at around 650°C. The low temperature oxidation peak was mainly formed of ¹³Carbon (76%). On the other hand, the broad high temperature oxidation peak exhibited a higher concentration in ¹²Carbon (60%). The carbon species which could be oxidised easily were attributed to the reaction

intermediates. The less easily oxidised carbon deposits were attributed to slowly depositing species which would convert progressively into carbon whiskers and carbon veils with time-on stream. The authors concluded that these less reactive carbon species could arise from both CO₂ and CH₄ activation on the catalyst.

Tsipouriari and Verykios [5] conducted isothermal oxidation followed by isothermal hydrogenation of the carbon deposits accumulated on 17 wt % Ni/La₂O₃ and 17 wt % Ni/Al₂O₃ after 0.5 hour dry reforming reaction with 30 ml/min CO₂/¹³CH₄/He (20/20/60 vol %) at 750°C. The results of isothermal oxidation and isothermal hydrogenation together showed that most of the carbon deposited over Ni/La₂O₃ was originated from the reaction pathway of methane rather than from carbon dioxide. Approximately 80% of the coke was originated from methane cracking over Ni/La₂O₃ catalyst. On the other hand, the majority of the carbon deposited over Ni/Al₂O₃ was shown to come from carbon dioxide dissociation. While approximately 85% of the deposited carbon derived from carbon dioxide dissociation, only 15% of it came from methane cracking.

Recently, McFarlane et al. [76] performed reaction testing measurements over 10 mg Ni/Al₂O₃ (26 wt %) catalyst at 625°C for 90 minutes in the micro-reactor where 5.6 sccm/min ¹³CO₂ and 5.6 sccm/min ¹²CH₄ diluted in 40 sccm/min He were used as reactants. The post reaction TPO profiles revealed that in the addition to the ¹²CO₂ peak centered at 617°C, there was also a significant ¹³CO₂ feature at the same temperature. This result made the authors to conclude that both CH₄ and CO₂ contributed to carbon deposition over the catalyst surface during dry reforming process, methane being the greater contributor.

The clarification of this issue is necessary in terms of understanding the mechanism of carbon formation with the aim of reactor design and catalyst design which can prevent accumulation of coke. For this aim, reaction tests were carried out with ¹³CO₂ over Ni/Al₂O₃ and the used catalyst was characterized by solid ¹³C solid state

NMR spectrometer. This is the first study to the authors knowledge of characterizing the spent catalyst by ^{13}C solid state NMR to determine the coke origin in dry reforming of methane reaction.

4.2 Results and Discussion

4.2.1 Characterization of commercial Al_2O_3

4.2.1.1 X-Ray Diffraction (XRD) Analysis

$\gamma\text{-Al}_2\text{O}_3$ powder from Alfa Aesar was used as support. Alumina has the property of existing in different kinds of metastable structures, so-called transition aluminas (such as κ , γ , δ , θ) and also its stable $\alpha\text{-Al}_2\text{O}_3$ phase [77]. When boehmite (AlOOH) is heated up, all OH are eliminated and it transforms into different transition aluminas with the sequence of $\gamma \rightarrow \delta \rightarrow \theta \rightarrow \alpha\text{-Al}_2\text{O}_3$ [77,78].

This polymorphism could be sorted according to the oxygen sublattice structure and the distribution into this sublattice of aluminum ions in tetrahedral and octahedral interstitial sites. In $\alpha\text{-Al}_2\text{O}_3$, the oxygen sublattice is hexagonal-close-packed structured with 2/3 of octahedral sites filled with cations. On the other hand, κ , γ , δ , θ phases have face-centered-cubic structure of oxygen atoms and cations existing in different proportions in both octahedral and tetrahedral sites [77].

Le Coz et al. suggested the below mechanisms of dehydration and crystallisation according to the TGA, DTA and XRD results [78].



In the XRD pattern of the as received alumina powder (Figure 17) it is demonstrated that boehmite, γ -Al₂O₃ and δ -Al₂O₃ phases coexist simultaneously by considering the reference XRD patterns (Boehmite: 21-1307 JCPDS file, γ -Al₂O₃: 50-741 JCPDS file, δ -Al₂O₃: 46-1215 JCPDS file).

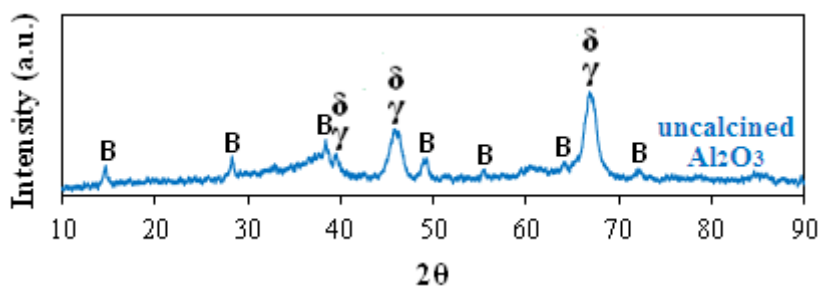


Figure 17. XRD pattern of commercial Al₂O₃ powder

4.2.1.2 Surface Area, Pore Size Distribution and Adsorption-Desorption Isotherms

Properties of commercial Al₂O₃ powder obtained from nitrogen physisorption data is summarized in Table 6.

Table 6. Textural properties of commercial Al₂O₃ powder

Sample	BET Surface area (m ² /g)	Pore volume (cm ³ /g)	Average pore diameter (nm)
commercial Al ₂ O ₃	73.19	0.37	19.69

N₂ adsorption-desorption isotherm and pore size distribution of pure alumina is shown in Figure 18 and Figure 19 respectively. According to the IUPAC classification commercial pure Al₂O₃ exhibits type II adsorption isotherm which is

characteristic of macroporous materials and the H3-shape hysteresis loop of the sample shows the presence of mesopores [79]. The presence of H3 hysteresis loop indicates a broad pore size distribution (Figure 19) [80]. Pore size distribution of the sample indicates that it is mainly composed of macropores (pore diameter >50 nm in diameter) in addition to the mesopores (2nm < pore diameter < 50 nm).

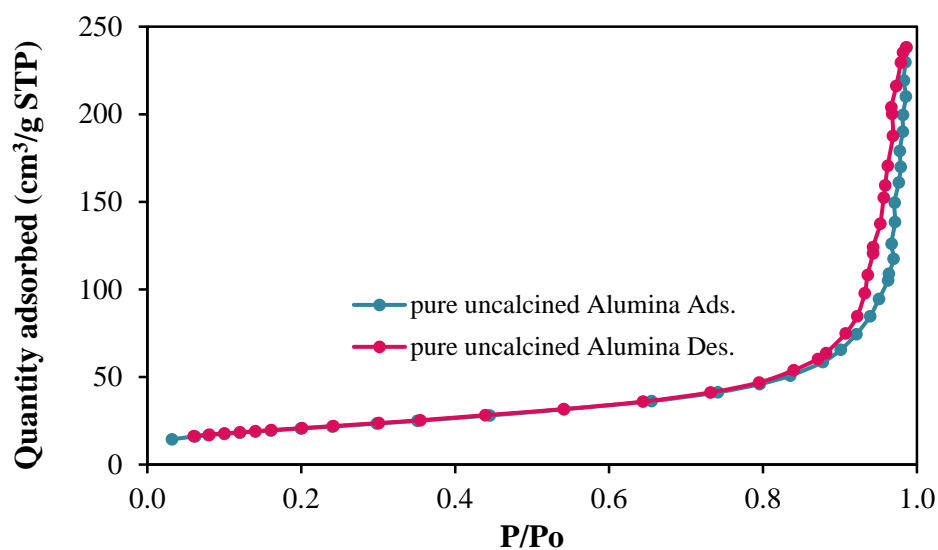


Figure 18. Nitrogen adsorption-desorption isotherms of commercial Al₂O₃ powder

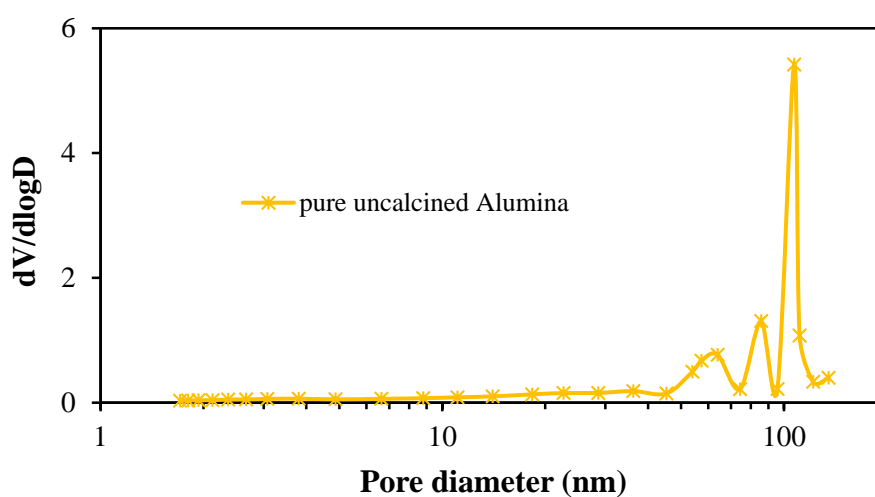


Figure 19. BJH pore size distribution of commercial Al₂O₃ powder

4.2.2 Characterization of fresh catalysts

4.2.2.1 X-Ray Diffraction (XRD) Analysis

To see the influence of calcination temperature on dry reforming of methane reaction, Al₂O₃ supported Ni, Co and Ni-Co catalyst were prepared by calcining at both 700°C and 900°C. XRD patterns of pure Al₂O₃, Ni/Al₂O₃, Co/Al₂O₃ and Ni-Co/Al₂O₃ calcined at 700°C and 900°C are given in Figure 20 and Figure 21 respectively.

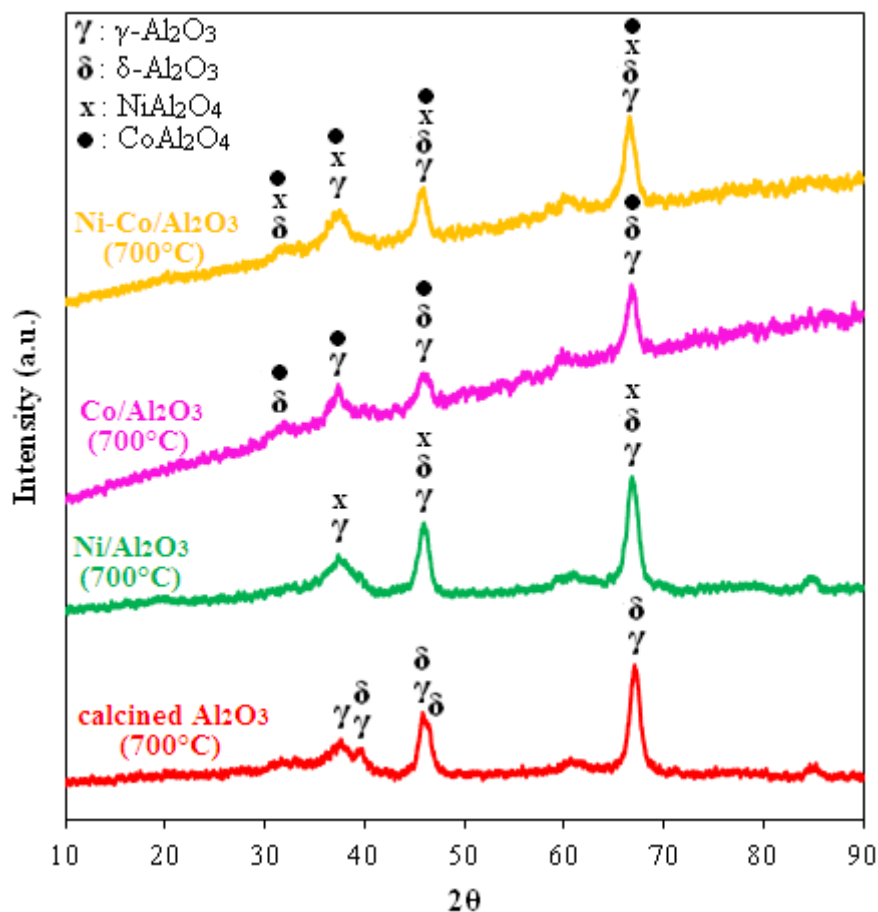


Figure 20. XRD pattern of pure Al₂O₃, Ni/Al₂O₃, Co/Al₂O₃ and Ni-Co/Al₂O₃ calcined at 700°C

Bulk phase property of the catalysts were identified by means of XRD. The species generated during calcination were strongly dependent on calcination temperature. As remembered, the diffraction peaks of boehmite, γ - Al_2O_3 and δ - Al_2O_3 were observed in commercial pure alumina powder (Figure 17). When this alumina was calcined at 700°C and 900°C for 5 hours, boehmite diffraction peaks disappeared and peaks due to δ - Al_2O_3 and γ - Al_2O_3 became more dominant (Figure 20 and Figure 21).

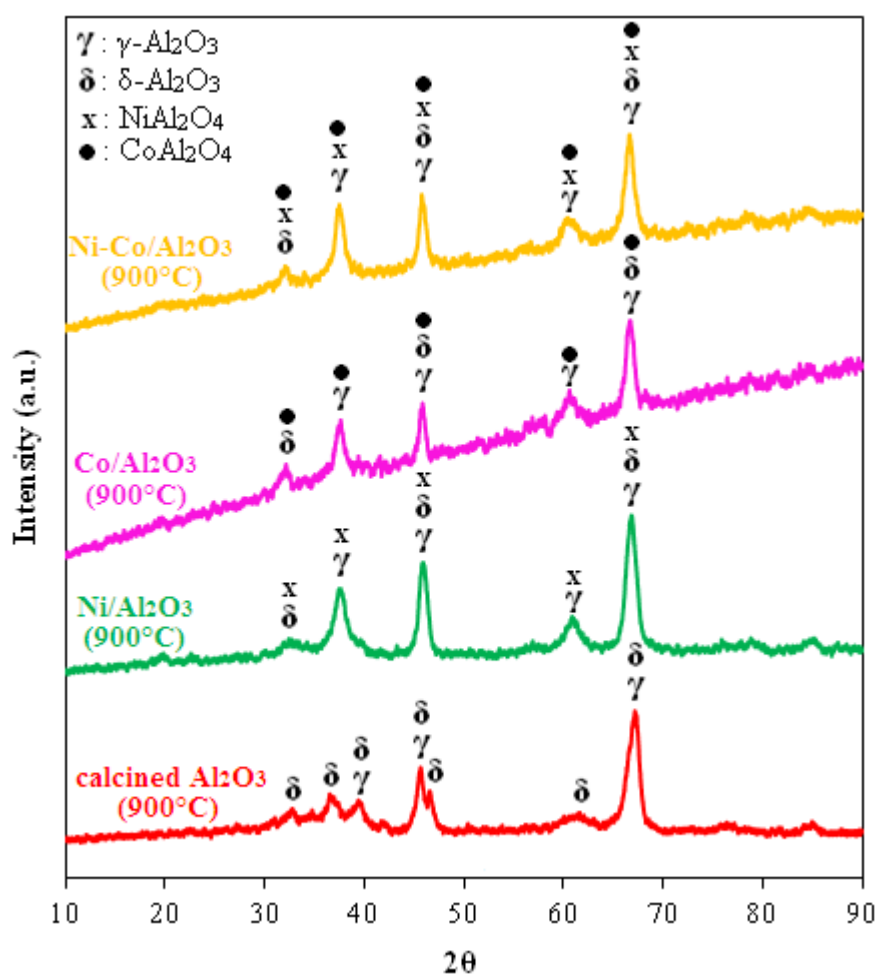


Figure 21. XRD pattern of pure Al_2O_3 , Ni/ Al_2O_3 , Co/ Al_2O_3 and Ni-Co/ Al_2O_3 calcined at 900°C

Due to the decomposition of the nitrates and subsequent oxidation, the following oxides can be formed during calcination step [81]:



NiAl_2O_4 , CoAl_2O_4 and NiCo_2O_4 spinel compounds might have been formed during the high temperature calcination step [11,81]. From the diffractograms it is difficult to make a discrimination between the distinct species due to the overlap of the reflections of these phases. It is also hard to distinguish monometallic and bimetallic catalysts from each other because of their similar morphology and characteristic peaks. Ni^{2+} , Co^{2+} , Mg^{2+} and Al^{3+} were thought to pertain to the identical lattice in Ni/Co/Al/Mg composite catalyst [82]. Characteristic peaks of NiO were not observed in the XRD patterns which indicated that the active metal species were embodied into the spinel structure [83 and references therein].

When Figure 20 and Figure 21 is compared with each other, it is seen that the intensity of the peaks which are considered to correspond to the spinel phases become stronger with increasing temperature, suggesting an increased degree of crystallization and particle size.

4.2.2.2 Surface Area, Pore Size Distribution and Adsorption-Desorption Isotherms

BET surface area, pore volume and pore diameter of commercial pure Al_2O_3 were 73.19 m^2/g , 0.37 cm^3/g and 19.69 nm respectively (Table 6). When this Al_2O_3 was calcined at 700°C and 900°C, its surface area, pore volume and pore diameter decreased significantly as shown in Table 7 and 8. This could be attributed to the sintering of the particles with increasing calcination temperature.

Table 7. Textural properties of pure Al₂O₃, Ni/Al₂O₃, Co/Al₂O₃ and Ni-Co/Al₂O₃ calcined at 700°C

Catalyst	BET surface area (m ² /g)	Pore volume (cm ³ /g)	Average pore diameter (nm)
Pure Al ₂ O ₃ calc. at 700°C	57.26	0.23	15.29
Ni/Al ₂ O ₃	48.86	0.35	26.92
Co/Al ₂ O ₃	49.50	0.31	23.66
Ni-Co/Al ₂ O ₃	46.42	0.28	22.99

Table 8. Textural properties of pure Al₂O₃, Ni/Al₂O₃, Co/Al₂O₃ and Ni-Co/Al₂O₃ calcined at 900°C

Catalyst	BET surface area (m ² /g)	Pore volume (cm ³ /g)	Average pore diameter (nm)
Pure Al ₂ O ₃ calc. at 900°C	51.15	0.21	16.67
Ni/Al ₂ O ₃	45.45	0.34	27.74
Co/Al ₂ O ₃	42.91	0.31	27.71
Ni-Co/Al ₂ O ₃	40.84	0.30	27.87

At a given metal loading (Ni, Co or Ni-Co), the surface area decreased with an increase in calcination temperature. The particles agglomerate more with increasing temperature which result in progressive reduction in surface area. While the total pore volume of all catalysts were lower than that of the as received support (0.37 cm³/g), their average pore diameter were higher than that of the as received support (19.69 nm).

N₂ adsorption-desorption isotherms of the pure Al₂O₃, Ni/Al₂O₃, Co/Al₂O₃ and Ni-Co/Al₂O₃ calcined at 700°C and 900°C are shown in Figure 22 and Figure 23 respectively. All samples exhibit type II adsorption isotherm which is characteristic of macroporous materials. H3-shape hysteresis loop of the samples indicate the existence of mesopores [79]. Broad pore size distribution of the catalysts mainly dominated by macropores are shown in Figure 24 and 25. Mesoporosity is also seen clearly for all the catalysts except Co/Al₂O₃ calcined at 900°C.

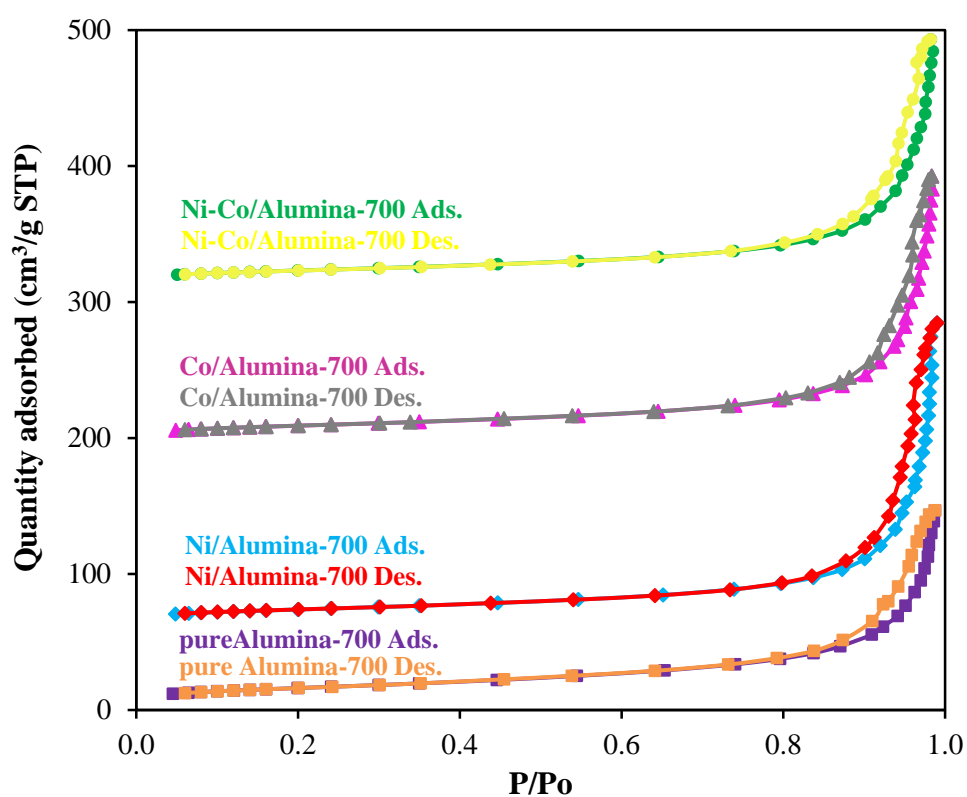


Figure 22. Nitrogen adsorption-desorption isotherms of pure Al₂O₃, Ni/Al₂O₃, Co/Al₂O₃ and Ni-Co/Al₂O₃ calcined at 700°C

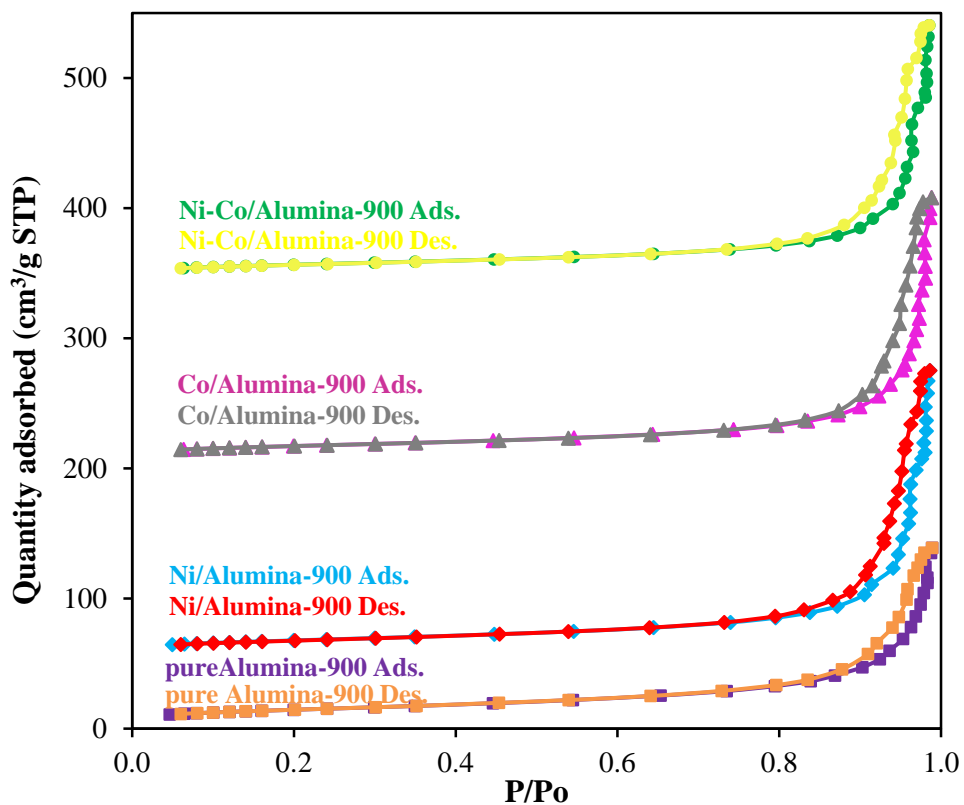


Figure 23. Nitrogen adsorption-desorption isotherms of pure Al₂O₃, Ni/Al₂O₃, Co/Al₂O₃ and Ni-Co/Al₂O₃ calcined at 900°C

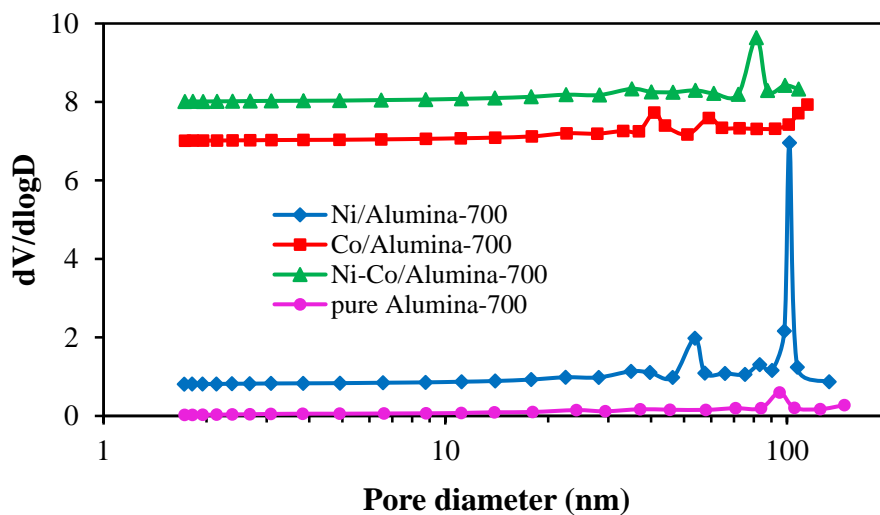


Figure 24. BJH pore size distribution of pure Al₂O₃, Ni/Al₂O₃, Co/Al₂O₃ and Ni-Co/Al₂O₃ calcined at 700°C

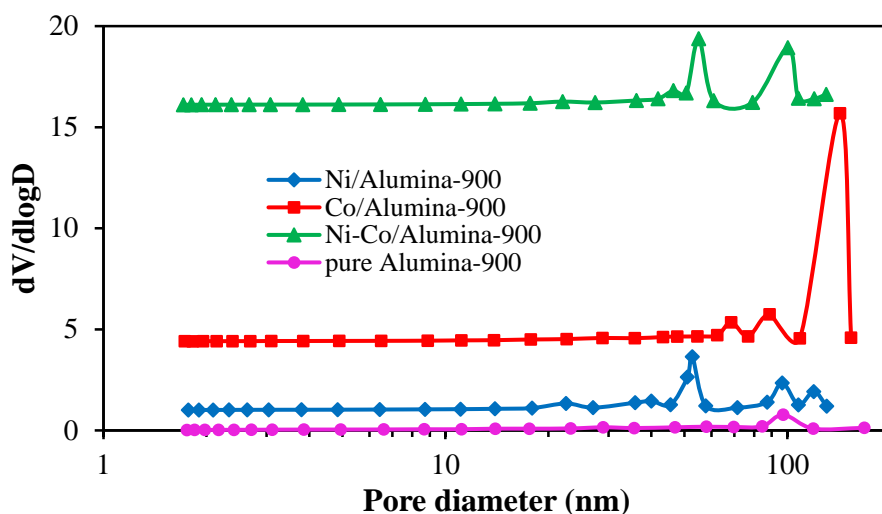


Figure 25. BJH pore size distribution of pure Al_2O_3 , $\text{Ni}/\text{Al}_2\text{O}_3$, $\text{Co}/\text{Al}_2\text{O}_3$ and $\text{Ni-Co}/\text{Al}_2\text{O}_3$ calcined at 900°C

4.2.2.3 High Resolution Transmission Electron Microscopy (HRTEM)

HRTEM was performed to examine the morphologies of the fresh catalysts. HRTEM images of fresh $\text{Ni}/\text{Al}_2\text{O}_3$ -I-900 and $\text{Ni-Co}/\text{Al}_2\text{O}_3$ -I-900 are given in Figure 26 and Figure 27, respectively. The dark spots scattering in the lighter zone reveal the nickel particles and alumina support, respectively [84]. In addition to the spherical and rod-like particles, the TEM analysis shows that most of the particles have an irregular shape. The nickel or cobalt particles are seen to be located over the alumina support. Neither TEM nor XRD data could reveal any morphological difference between $\text{Ni}/\text{Al}_2\text{O}_3$ and $\text{Ni-Co}/\text{Al}_2\text{O}_3$ catalysts.

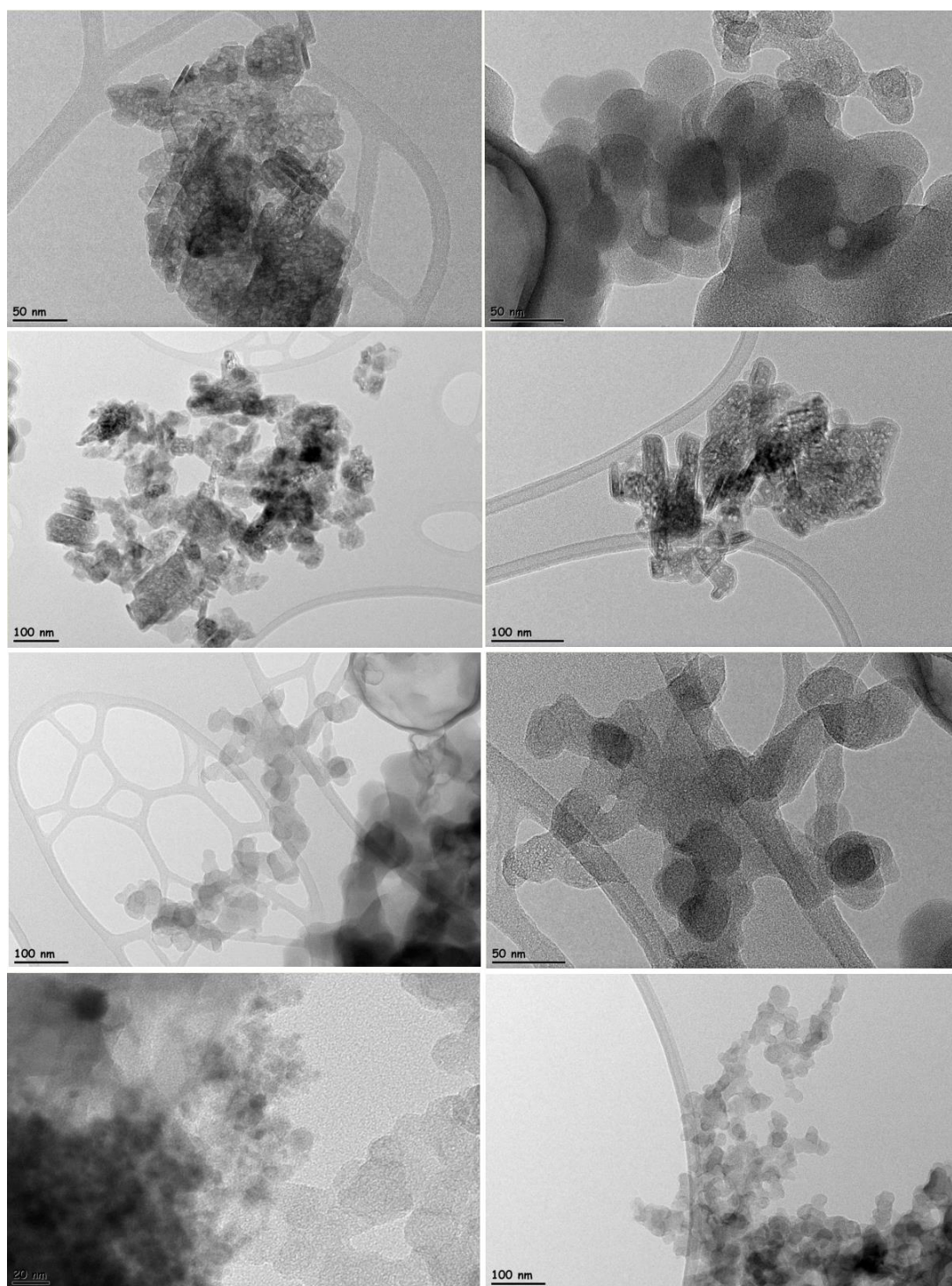


Figure 26. HRTEM images of fresh Ni/Al₂O₃-I-900

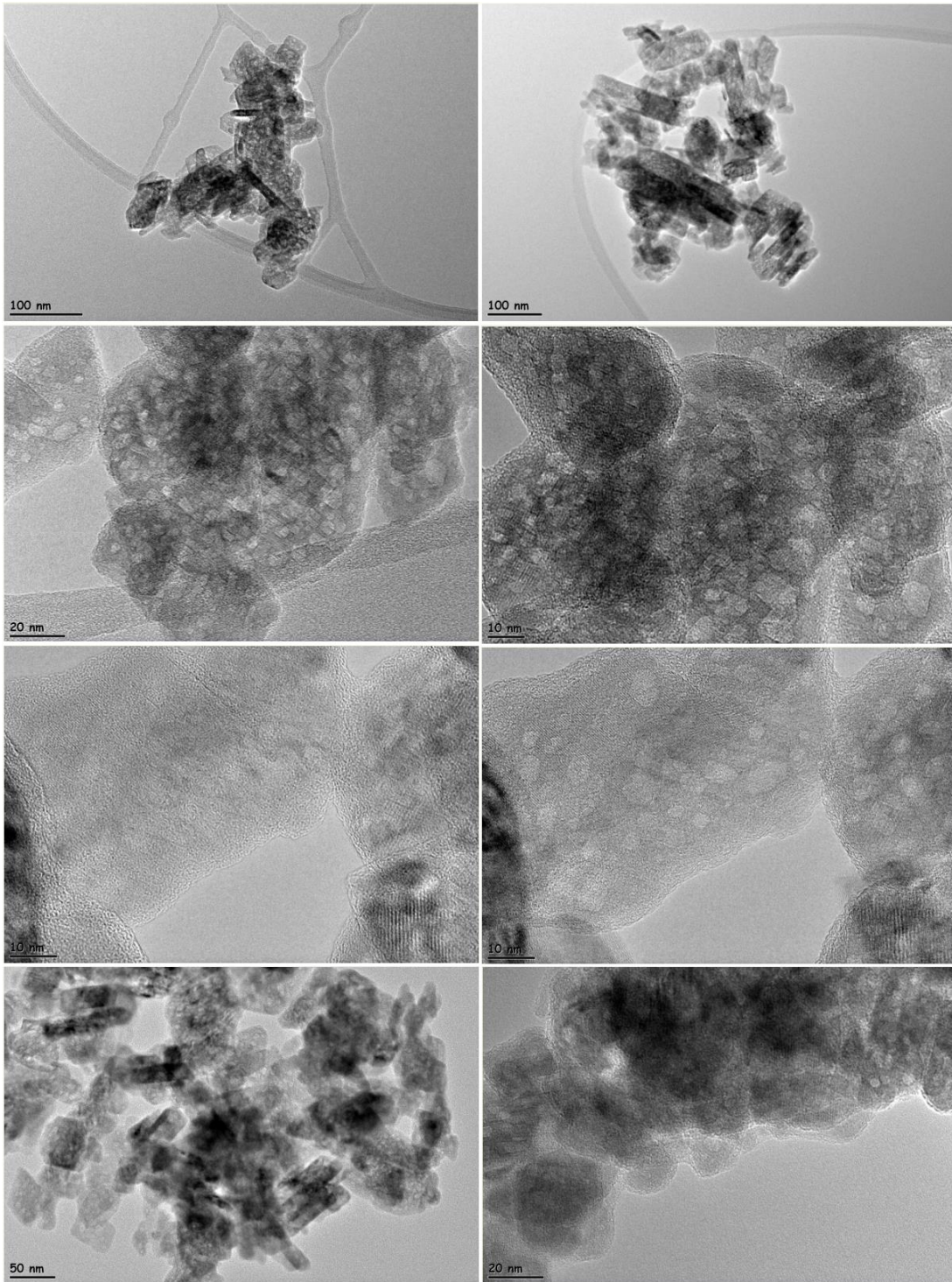


Figure 27. HRTEM images of fresh Ni-Co/Al₂O₃-I-900

4.2.2.4 Temperature Programmed Reduction (TPR) Analysis

Reducibility of the catalysts was investigated by TPR which can be discussed in terms of two main subjects. The first one is the effect of calcination temperature and the second one is the effect of Co addition to the Ni based catalysts.

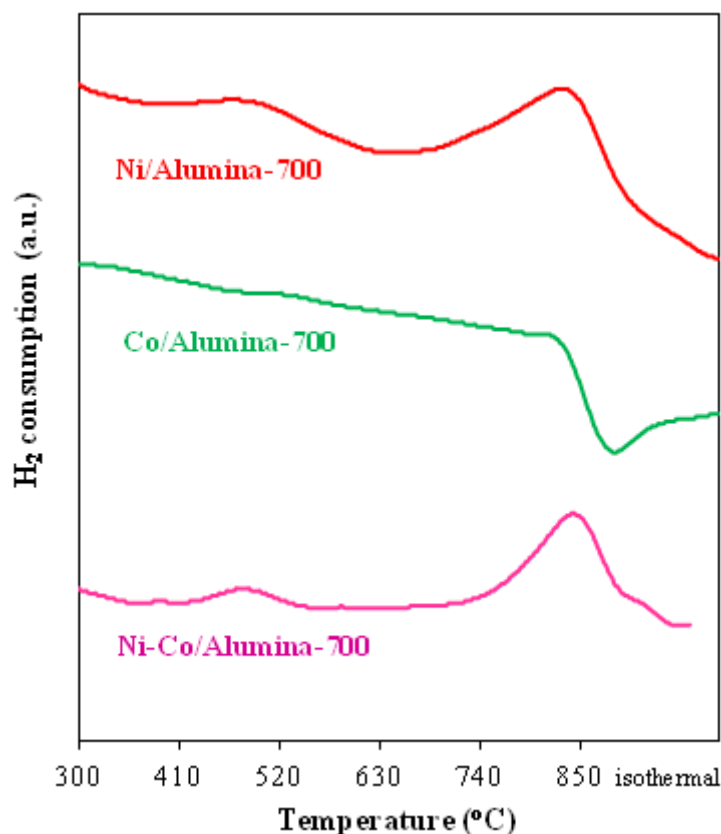


Figure 28. TPR profiles of Ni/Al₂O₃, Co/Al₂O₃ and Ni-Co/Al₂O₃ calcined at 700°C

When Figure 28 and Figure 29 are compared with each other, it is seen that while the catalysts calcined at 700°C have two reduction peaks, the ones calcined at 900°C have only one peak. The small peaks appearing in the low temperature region, 465°C for Ni/Al₂O₃-I-700 and 480°C for Ni-Co/Al₂O₃-I-700 were attributed to the reduction of NiO [85] and Co₃O₄ (or CoO) [86-87] respectively. The high

temperature reduction peaks for both the catalysts calcined at 700°C and 900°C were attributed to the reduction of spinel oxides which could be NiAl_2O_4 , CoAl_2O_4 and NiCo_2O_4 [11,85-86,88-89]. While the high temperature reduction peak of $\text{Ni}/\text{Al}_2\text{O}_3$ was 828°C when it was calcined at 700°C, it increased to 840°C with the calcination at 900°C. Similarly, the high temperature reduction peak of $\text{Ni-Co}/\text{Al}_2\text{O}_3$ increased from 842°C to 850°C when the calcination temperature was increased from 700°C to 900°C. It was concluded that increasing the calcination temperature from 700°C to 900°C, caused an increase in the reduction temperature of $\text{Ni}/\text{Al}_2\text{O}_3$ and $\text{Ni-Co}/\text{Al}_2\text{O}_3$ catalysts.

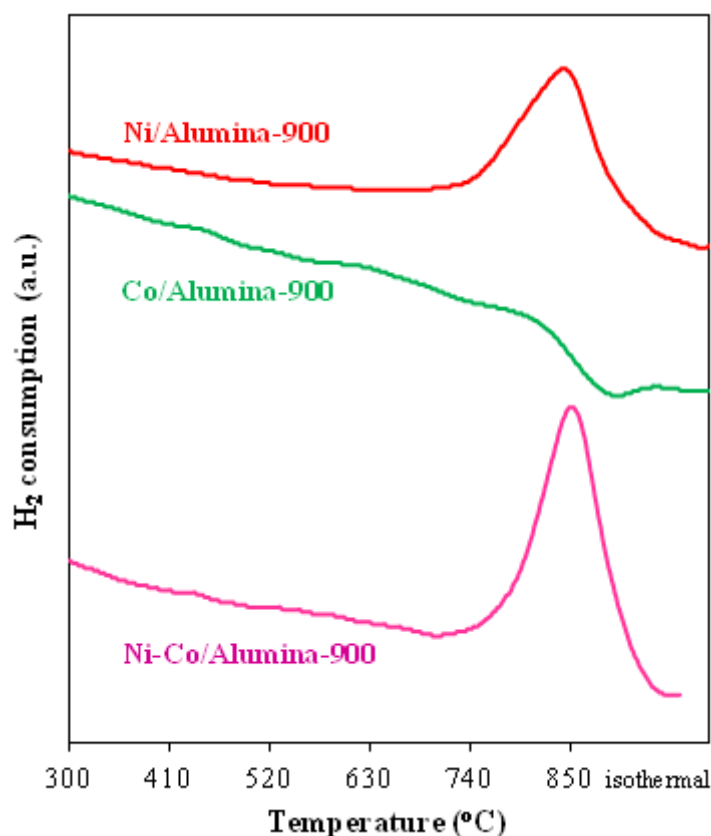


Figure 29. TPR profiles of $\text{Ni}/\text{Al}_2\text{O}_3$, $\text{Co}/\text{Al}_2\text{O}_3$ and $\text{Ni-Co}/\text{Al}_2\text{O}_3$ calcined at 900°C

The effect of Co addition to the Ni based catalyst on the reduction temperature can be discussed by taking into consideration the shifts in the peak positions. The position of the peak shifted towards higher temperature from Ni/Al₂O₃ to Ni-Co/Al₂O₃ for both calcination temperatures, from 827°C to 842°C when calcination was carried out at 700°C and from 840°C to 850°C when calcination was done at 900°C. This suggested the increased metal-support interaction with the addition of cobalt. Similar trend was also observed for Co-Ni aerogel catalysts having 10 weight % MgO and 10 weight % active metal with the Cobalt/Nickel ratio of 0:10, 3:7, 5:5, 7:3 and 10:0 where the reduction temperature increased with increasing the cobalt amount in the catalyst [83]. Contrary to our results, Zhang et al. showed that the reduction peak maximum of bimetallic nickel-cobalt catalyst occurred at a lower temperature (850°C) than those of monometallic nickel (868°C) and monometallic cobalt catalyst (896°C) [36]. They attributed this decrease to the creation of nickel and cobalt oxide species which were more easily approachable on the surface of the bimetallic combination than those in the bulk structures. Furthermore, they interpreted the presence of a single reduction peak at lower temperatures was due to the formation of nickel-cobalt alloy during reduction.

One of the most striking results in TPR profiles was about monometallic Co catalysts. They did not show any reduction peak. On the other hand, they exhibited negative peak, beginning to occur at 815°C for Co/Al₂O₃-I-700 and 798°C for Co/Al₂O₃-I-900 catalyst. Firstly, it was thought that this could be attributed to the oxygen release ability of cobalt oxide. For this reason, thermogravimetric analysis of Co/Al₂O₃-I-700 and Co/Al₂O₃-I-900 was done under inert gas (nitrogen) from room temperature to 1100°C. As shown in Figure 30 below, there was not seen a significant weight loss at around 800°C for both of the catalysts. The negative peak might be ascribed to the evolution of hydrogen, resulting from the desorption of hydrogen stored by the solid.

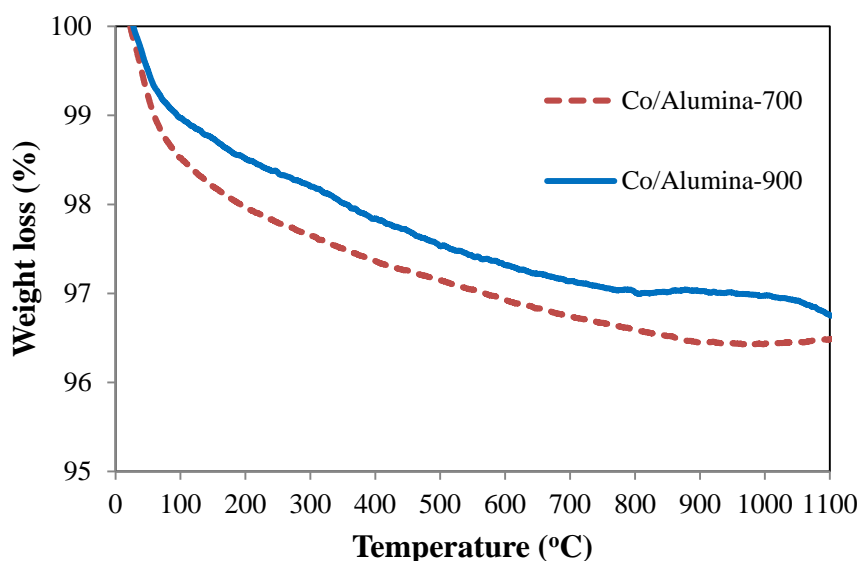


Figure 30. TGA profiles of Co/Al₂O₃-I-700 And Co/Al₂O₃-I-900 under N₂ environment

Ewbank et al. [87] reported that the Co/Al₂O₃ catalyst prepared by dry impregnation and calcined at 500°C for 3 hours exhibited a reduction peak centered at 850°C which was ascribed to the reduction of CoAl₂O₄ species. Kim Nga and Kim Chi [90] prepared CoAl₂O₄ spinels by sol-gel method with citric acid. When they calcined the catalyst at 700°C, the TPR profile exhibited one main peak centered at 870°C which was ascribed to the reduction of Co²⁺ ions in the lattice, except for a small peak at 540°C due to reduction of an impurity. Wang and Ruckenstein [88] investigated the reducibility of γ -Al₂O₃-supported Co catalysts as a function of calcination temperature using TPR. While Co₃O₄ was generated as a major phase at a calcination temperature of 500°C, Co₂AlO₄ and CoAl₂O₄ were formed at 1000°C calcination temperature. The peak temperatures observed during TPR were as followings. For Co(O)/ γ -Al₂O₃(700°C), two peaks, at 460°C and 830°C were identified. For Co(O)/ γ -Al₂O₃(800°C), three peaks at 485°C, 810°C and 1045°C were noted. For Co(O)/ γ -Al₂O₃(900°C), three peaks, at 480°C, 860°C and >1000°C were observed.

4.2.2.5 DRIFTS

In order to better comprehend the activation of reactants on the Al_2O_3 catalysts, CO_2 and CH_4 adsorption were studied in-situ using DRIFTS.

Prior to sending the reactant gases, the catalysts were reduced by sending 100 torr H_2 four times at 400°C . After the pretreatment, the pressure of CO_2 was set to 97.5, 300, 500 torr respectively. DRIFTS spectra were recorded after the admission of each dose of gas (Figure 31).

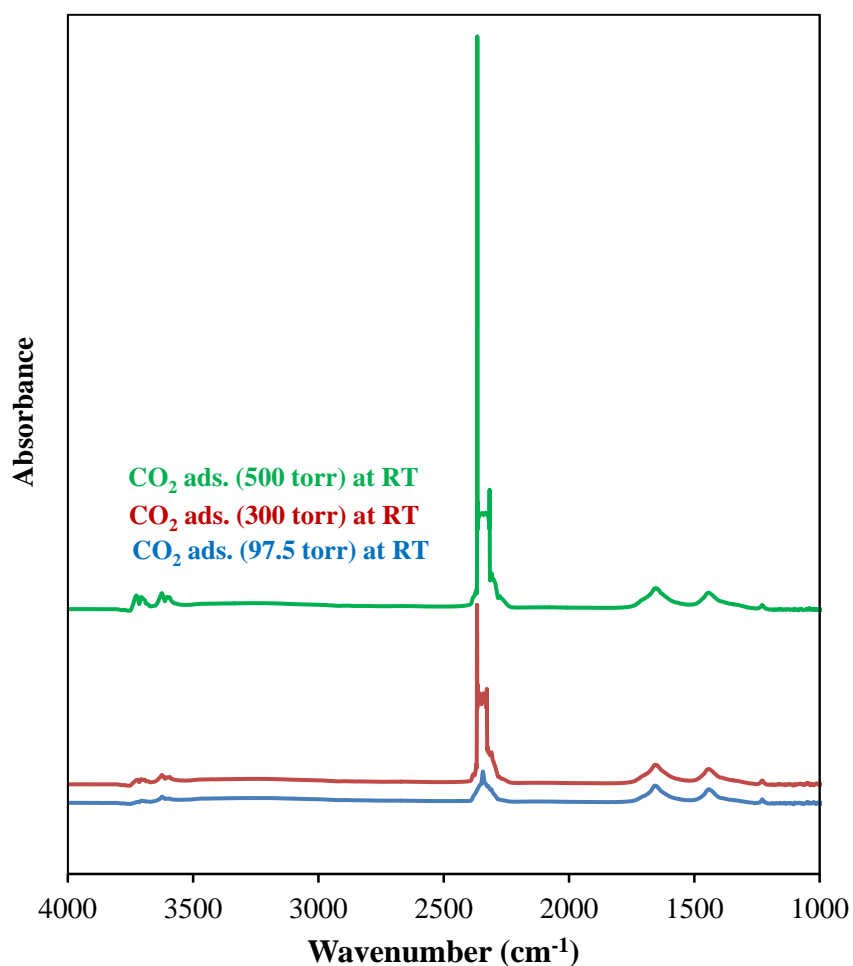


Figure 31. DRIFT spectra of CO_2 adsorption on $\text{Ni}/\text{Al}_2\text{O}_3\text{-900}$ with increasing CO_2 dosage

When Ni/Al₂O₃-900 was exposed to CO₂ at room temperature, the spectra showed a strong band at 2344 which was attributed to physically adsorbed CO₂ on alumina, the intensity of which increased with increasing CO₂ pressure. This agrees substantially with the ones already reported in literature. Gregg and Ramsay studied the infrared spectra of CO₂ adsorption on an alumina prepared by calcination of gibbsite (aluminum trihydrate) [91]. They attributed the band at 2365 cm⁻¹ to the physically adsorbed CO₂. Machado et al. studied adsorption of CO₂ on γ -alumina by carrying out volumetric and microcalorimetric measurements [92]. They assigned the bands at 2358 and 2344 cm⁻¹ to weakly adsorbed CO₂. Ferreira-Aparicio et al. attributed the band at 2349 cm⁻¹ to gas phase CO₂ upon the adsorption of CO₂ on Ru/Al₂O₃ at 723 K [48].

The bands seen at 1229, 1444, 1654 were attributed to chemically adsorbed CO₂. These bands are characteristic of the formation of adsorbed bicarbonate, HCO₃⁻ and are attributed to the bending ($\delta_4(\text{COH})$), symmetric stretching ($\nu_3(\text{OCO})^s$) and asymmetric stretching ($\nu_2(\text{OCO})^a$) vibrational modes on γ -alumina [93]. Baltrusaitis et al. studied FTIR spectroscopy of CO₂ reaction with surface hydroxyl groups on γ -Al₂O₃ [93]. They assigned the bands at 1231, 1438 and 1648 cm⁻¹ to bicarbonate. The infrared results of CO₂ adsorption on γ -Al₂O₃ exhibited bands at 1652, 1446-1450, and 1230 cm⁻¹ which were attributed to surface bicarbonates by Machado et al. [92]. Alumina, being an amphoteric oxide, not only possesses acidic sites but also basic sites. CO₂ adsorption on basic sites usually forms carbonate species, and CO₂ adsorption on comparatively acidic sites forms bicarbonate species [94 and references therein]. In the region 3750-3600 cm⁻¹, bands due to the O-H stretching mode of alumina hydroxyls are seen [95].

The changes in the adsorption profile of CO₂ adsorption on Ni/Al₂O₃-900 with increasing temperature at 500 torr was monitored via DRIFTS. As shown in Figure 32, the intensity of physisorbed CO₂ decreased dramatically when the temperature was increased to 200°C and then decreased slightly in intensity with an increasing temperature up to 400°C.

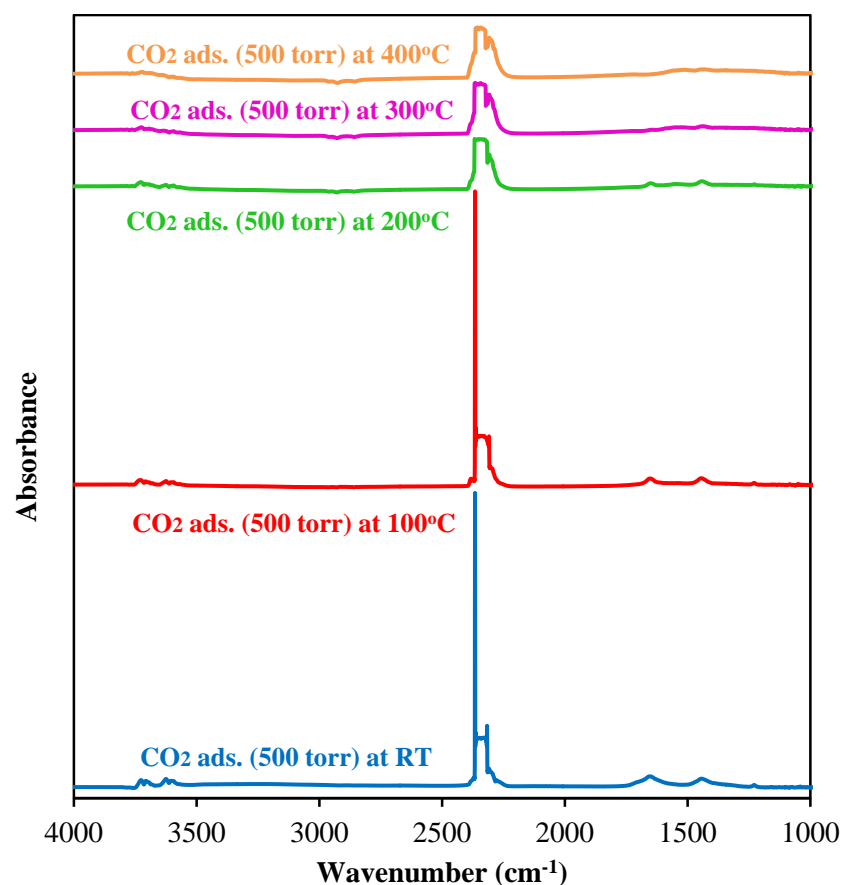


Figure 32. DRIFT spectra of CO₂ adsorption on Ni/Al₂O₃-900 with increasing temperature at 500 torr

Same CO₂ adsorption experiments were carried out with 4-4 wt% Ni-Co/Al₂O₃-900⁵ catalyst in order to see the effect of cobalt loading. Same adsorption behaviors were observed as shown in Figure 33, suggesting that the type of metal loaded on the catalyst did not show any significant effect on the CO₂ adsorption behavior. It was concluded that CO₂ adsorbed mainly on the support of Ni/Al₂O₃-900 and Ni-Co/Al₂O₃-900 catalysts prepared by incipient wetness impregnation.

⁵ 4-4 wt % Ni-Co/Al₂O₃ bimetallic catalyst was only used in the DRIFTS experiments. The metal loading for the Al₂O₃ supported bimetallic catalyst is 8-4 wt % Ni-Co in all other parts.

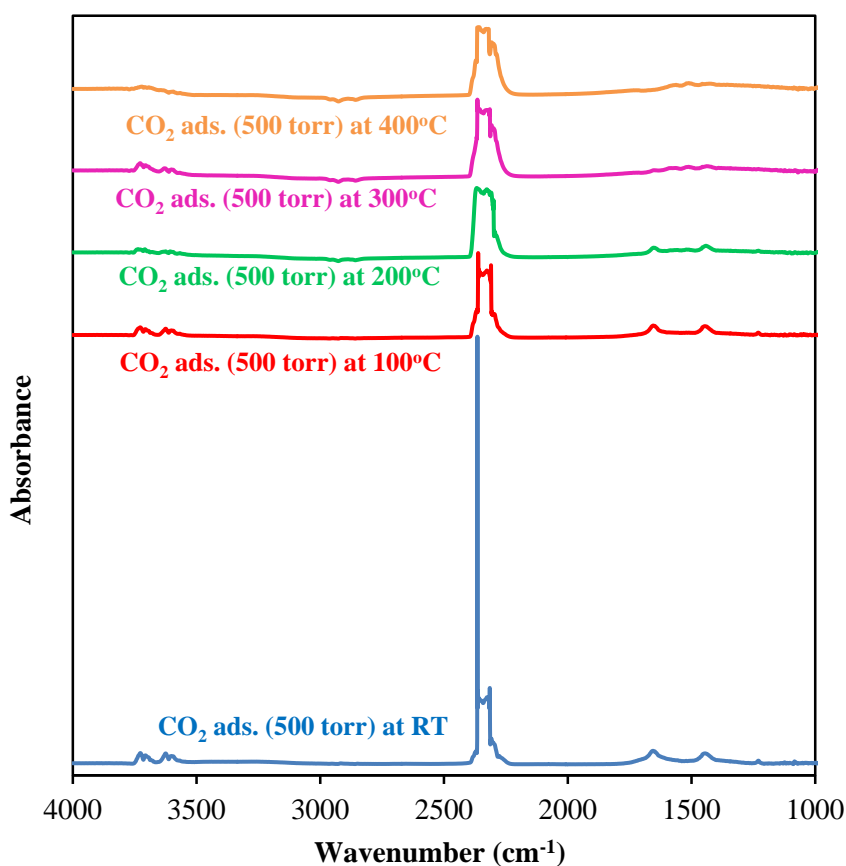


Figure 33. DRIFT spectra of CO₂ adsorption on Ni-Co/Al₂O₃-900 with increasing temperature at 500 torr

DRIFT spectra of CO₂ adsorption on Ni/Al₂O₃-900 and Ni-Co/Al₂O₃-900 at 500 torr with increasing temperature are given in larger scale in Figure 34 to better understand the influence of temperature. As shown in the Figure, the intensity of all bicarbonates (seen between 1228-1655 cm⁻¹) decreased with increasing temperature. When temperature reached to 400°C, the bands at 1229 cm⁻¹ and 1654 cm⁻¹ had almost disappeared. On the other hand, the band at 1444 cm⁻¹ was still much in evidence. This suggests that the bands at 1229 and 1654 cm⁻¹ corresponds to a weaker form of bonding than the band at 1444 cm⁻¹ which is in agreement with the literature reported before [91].

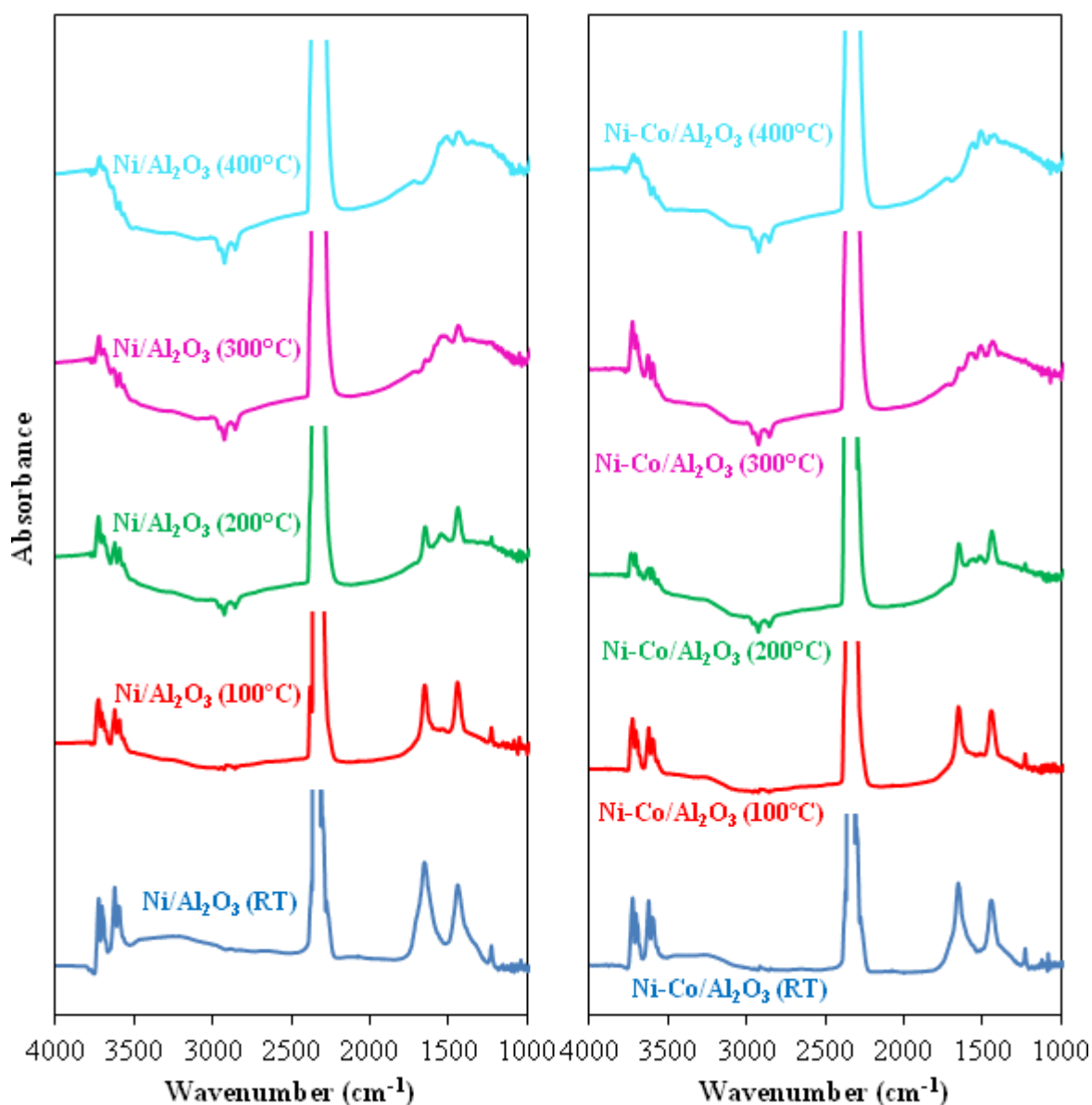


Figure 34. Comparison between the DRIFT spectra of CO₂ adsorption on Ni/Al₂O₃-900 and Ni-Co/Al₂O₃-900 at 500 torr

One interesting result seen in Figure 34 is about the peaks at 2858, 2928 and 2960 cm⁻¹. Their positive intensity is barely seen at room temperature in the larger scale sketch. On the other hand, their negative peaks become visible at 100°C and more prominent with increasing temperature.

Rege and Yang studied the adsorption of H₂O on γ -Al₂O₃ [96]. They observed a broad band in the region of 2800–3500 cm⁻¹ and assigned as hydrogen-bonded OH stretching vibrations. The nature of isolated OH groups on low index planes of transition aluminas has been investigated by infrared spectroscopy in the past [97]. Casarin et al. [97] classified them as the followings by utilizing these studies: “(i) OH groups coordinated to a single tetrahedral Al³⁺ site; (ii) OH groups coordinated to a single octahedral Al³⁺ site; (iii) OH groups bridging a tetrahedral and an octahedral site; (iv) OH groups bridging two octahedral sites; (v) capped OH groups, that is, contemporary bridging three octahedral sites.” By taking into consideration these studies, the peaks seen at 2858, 2928 and 2960 cm⁻¹ were also attributed to OH stretching vibrations of Al₂O₃. Since there are different kinds of surface OH groups, their vibrations can also be seen at different wavenumbers.

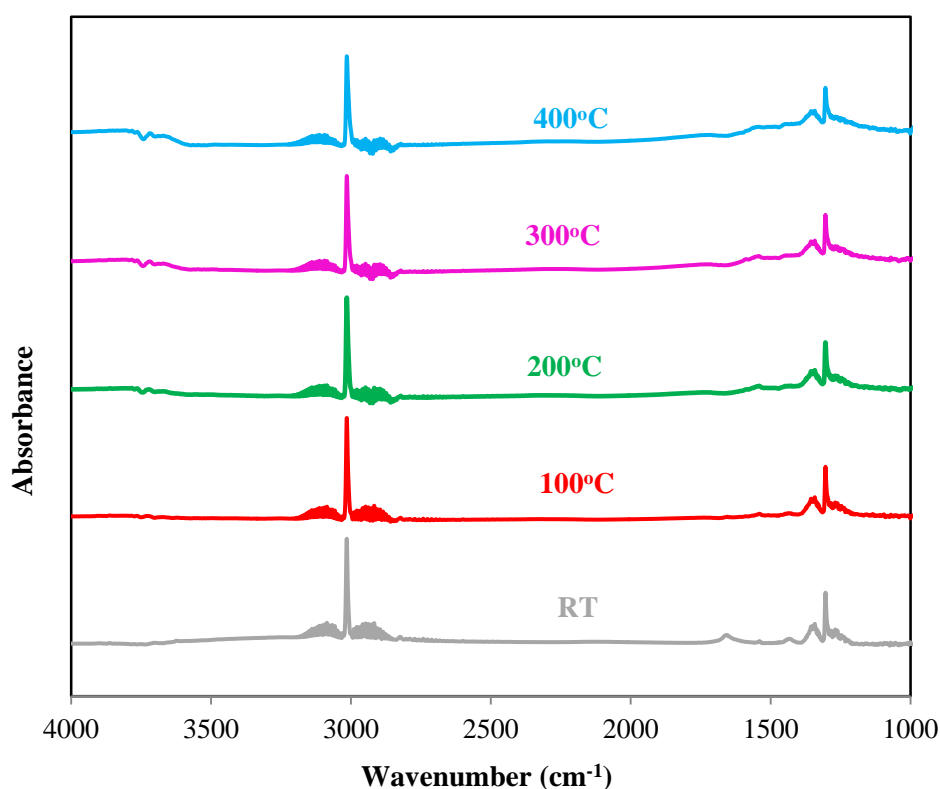


Figure 35. DRIFT spectra of CH₄ adsorption on Ni/Al₂O₃-900 with increasing temperature at 500 torr

DRIFTS study of CH₄ adsorption on Ni/Al₂O₃-900 resulted in the spectra belonging to only gas phase CH₄ contribution centered at 1305 and 3015 cm⁻¹ (Figure 35) [48,98]. This was due to the fact that the catalyst could not be reduced at 400°C. CH₄ can be activated as long as the active component is in metallic state. Takenaka et al. made a comparison between the performances of nickel catalysts supported on various supports, such as SiO₂, TiO₂, MgO/SiO₂, MgO, SiO₂/Al₂O₃, Al₂O₃ and graphite in methane catalytic decomposition [99]. While SiO₂, TiO₂ and graphite supported catalysts exhibited high activity and stability, Al₂O₃, MgO and SiO₂-MgO supported ones were not active under the same conditions. They proved further by means of XRD and Ni K-edge XANES/EXAFS that nickel was present in metallic state in the active catalysts, while it formed oxide compounds with the components of the support in the inactive catalysts.

4.2.2.6 Microcalorimetry

The energetics of carbon dioxide adsorption on commercial Al₂O₃, Al₂O₃-900, Ni/Al₂O₃-900 and Ni-Co/Al₂O₃-900 was studied by means of microcalorimetry. As shown in Figure 36, CO₂ was strongly adsorbed on all of the samples. The adsorption characteristics were not influenced by the metals indicating that CO₂ adsorbed on alumina. Differential heat of CO₂ adsorption displayed a sharp decrease which could be ascribed to the saturation of high energy sites. Further differential heat of carbon dioxide was observed until reaching the saturation coverage. Rosynek assigned the surface of γ -Al₂O₃ to be heterogeneous in its interaction with CO₂ which was shown by a decline in its heat of adsorption with increasing coverage and by conformity of CO₂ adsorption isotherms to the Freundlich equation at low coverages [100]. The carbon dioxide adsorption capacity of commercial alumina was higher than that of Al₂O₃-900, Ni/Al₂O₃-900 and Ni-Co/Al₂O₃-900 as seen in Figure 36 and 37. High temperature heat treatment resulted in a decrease in carbon dioxide adsorption capacity.

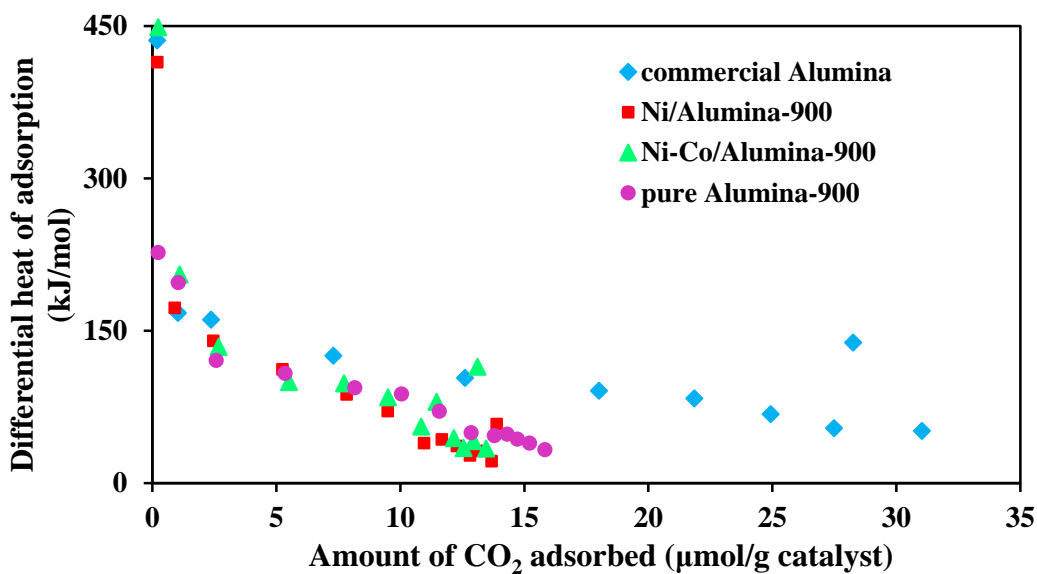


Figure 36. Differential heat of CO₂ adsorption on commercial Al₂O₃, Al₂O₃-900, Ni/Al₂O₃-900 and Ni-Co/Al₂O₃-900

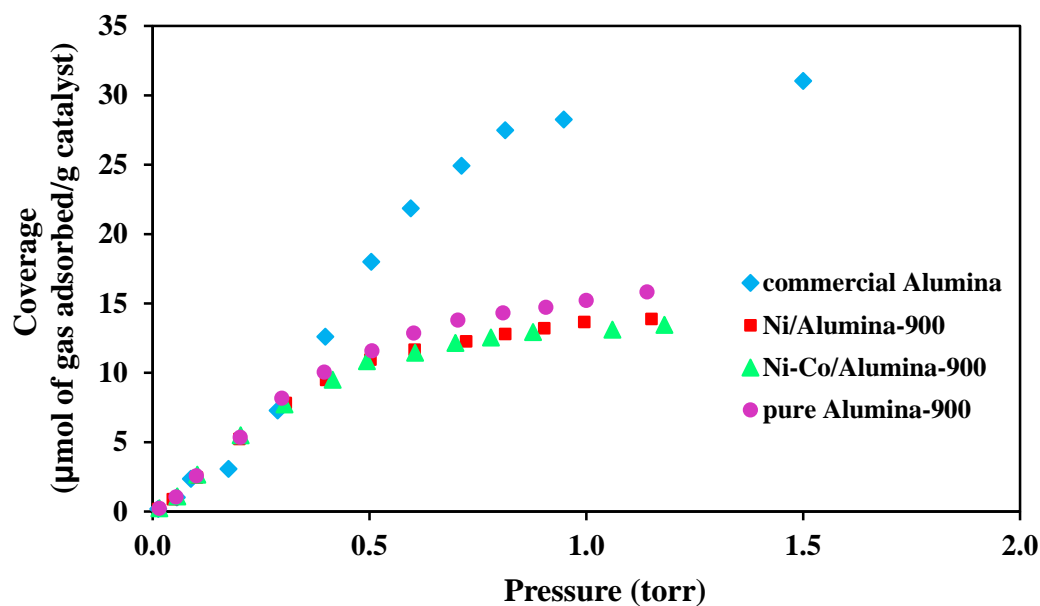


Figure 37. Coverage as a function of pressure for CO₂ adsorption on commercial Al₂O₃, Al₂O₃-900, Ni/Al₂O₃-900 and Ni-Co/Al₂O₃-900

4.2.3 Dry reforming reaction results

Dry reforming of methane was performed with the synthesized catalysts as described in Section 3.1.1. CO₂ conversion, CH₄ conversion, H₂ yield and CO yield were examined by using the following equations.

$$\text{CH}_4 \text{ conversion: } X_{\text{CH}_4} = \frac{\text{CH}_4 \text{ in} - \text{CH}_4 \text{ out}}{\text{CH}_4 \text{ in}} \quad (19)$$

$$\text{CO}_2 \text{ conversion: } X_{\text{CO}_2} = \frac{\text{CO}_2 \text{ in} - \text{CO}_2 \text{ out}}{\text{CO}_2 \text{ in}} \quad (20)$$

$$\text{H}_2 \text{ yield: } Y_{\text{H}_2} = \frac{\text{H}_2 \text{ out}}{2 \times \text{CH}_4 \text{ in}} \quad (21)$$

$$\text{CO yield: } Y_{\text{CO}} = \frac{\text{CO out}}{\text{CO}_2 \text{ in} + \text{CH}_4 \text{ in}} \quad (22)$$

Comparison of CH₄ and CO₂ conversion over the catalysts calcined at 700°C are given in Figure 38. While Ni/Al₂O₃-I-700-pellet and Ni-Co/Al₂O₃-I-700-pellet provided comparable activities during the first 90 minutes of the reaction, Ni-Co/Al₂O₃-I-700-pellet started to lose its activity after then. On the other hand, Ni/Al₂O₃-I-700-pellet preserved its stability during the five hour reaction period. The activity of Co/Al₂O₃-I-700-pellet was lower than the other two catalysts. Although a reduction peak for Co/Al₂O₃-I-700 could not be seen in TPR profile, it showed quite a high activity and preserved its stability. As remembered, there was a negative baseline shift in TPR profiles of all the samples investigated. There could have been a small H₂ consumption peak for Co/Al₂O₃-I-700 which could be suppressed due to the negative baseline shift.

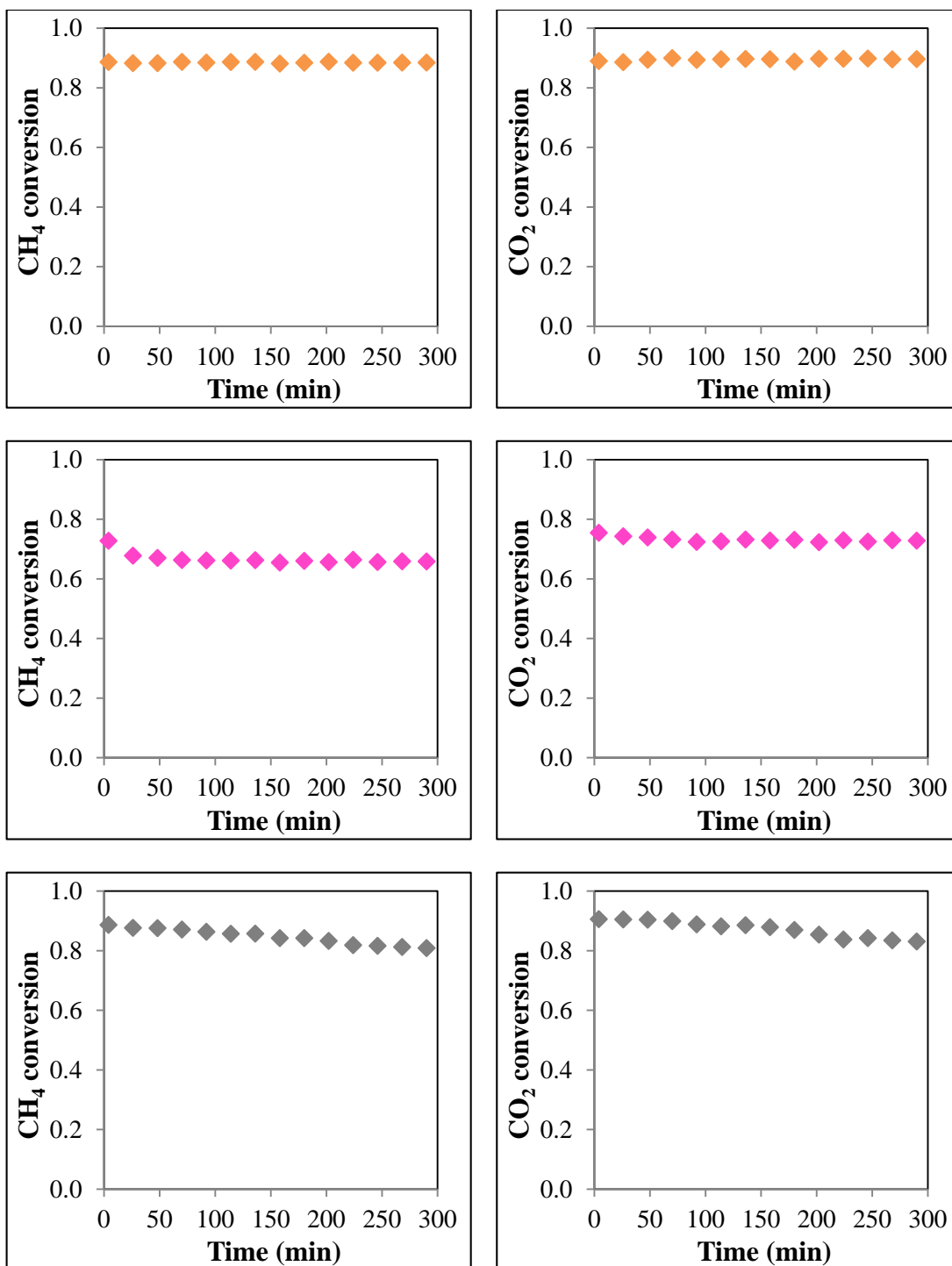


Figure 38. Comparison of CH₄ and CO₂ conversion versus time on stream over the catalysts calcined at 700°C, Ni/Al₂O₃-I-700-pellet ◆, Co/Al₂O₃-I-700-pellet ◆, Ni-Co/Al₂O₃-I-700-pellet ◆, (Reaction conditions: 700°C, 1 atm)

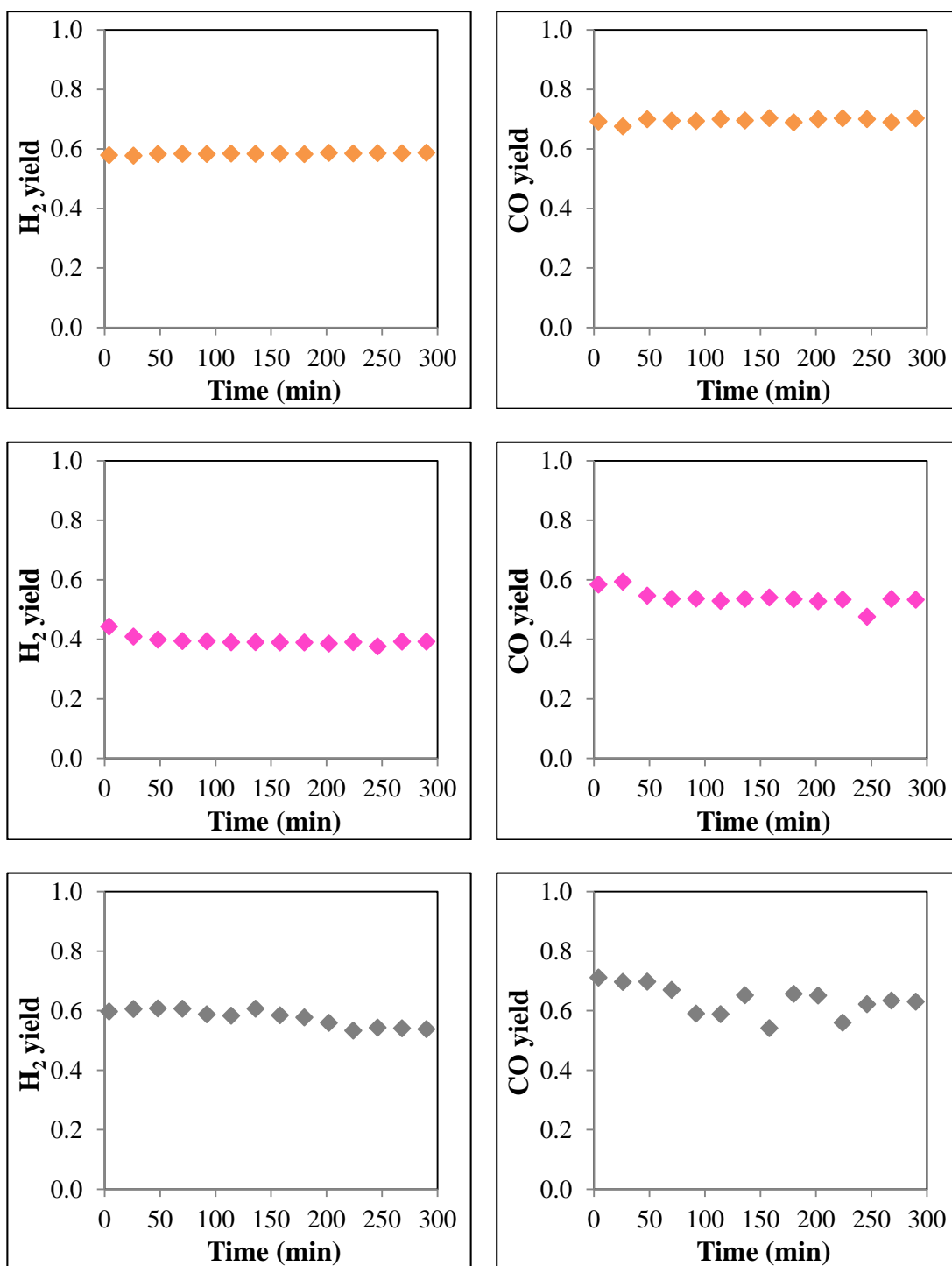


Figure 39. Comparison of H₂ and CO yield versus time on stream over the catalysts calcined at 700°C, Ni/Al₂O₃-I-700-pellet ◆, Co/Al₂O₃-I-700-pellet ◆, Ni-Co/Al₂O₃-I-700-pellet ◆, (Reaction conditions: 700°C, 1 atm)

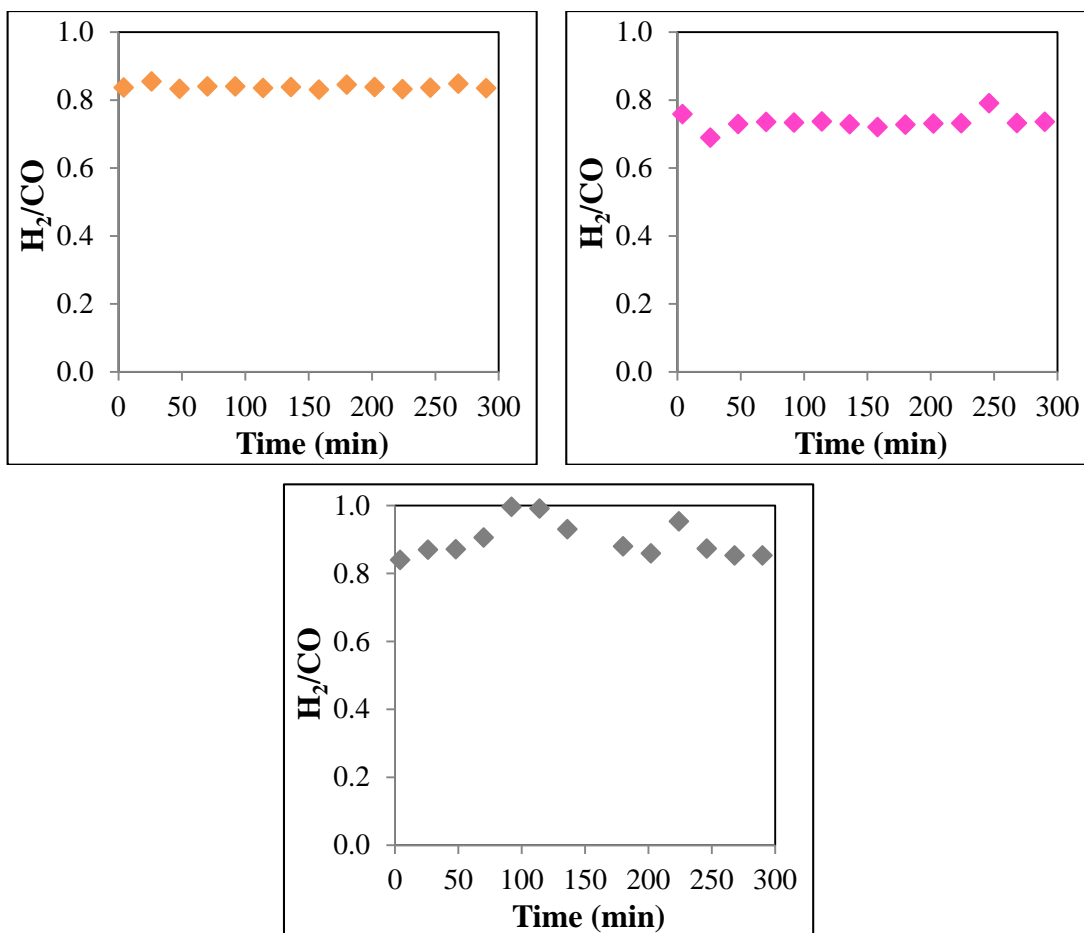


Figure 40. Comparison of H₂/CO ratio versus time on stream over the catalysts calcined at 700°C, Ni/Al₂O₃-I-700-pellet ◆, Co/Al₂O₃-I-700-pellet ◆, Ni-Co/Al₂O₃-I-700-pellet ◆, (Reaction conditions: 700°C, 1 atm)

The time dependent H₂ and CO yield of the catalysts calcined at 700°C are given in Figure 39. Carbon monoxide yield was higher than hydrogen yield for all the catalysts because of the RWGS reaction. While the H₂ yield was comparable for Ni/Al₂O₃-I-700-pellet and Ni-Co/Al₂O₃-I-700-pellet for the first 200 minutes of the reaction, the latter started to lose performance after then. In terms of CO yield, Ni/Al₂O₃-I-700-pellet showed the best performance and stability, while Ni-Co/Al₂O₃-I-700-pellet exhibited a diminishing performance with some deviations. As in the case of conversions, Co/Al₂O₃-I-700-pellet yielded lowest amount of H₂ and CO.

As for H₂/CO ratio Ni/Al₂O₃-I-700-pellet exhibited the most stable performance. Ni-Co/Al₂O₃-I-700-pellet also exhibited comparable behavior with the nickel loaded catalyst except for the some higher points which resulted from the deviations seen in the CO yield profile. H₂/CO ratio was the lowest for Co/Al₂O₃-I-700-pellet as seen in Figure 40. While H₂/CO ratio was higher than 0.8 for Ni/Al₂O₃-I-700-pellet and Ni-Co/Al₂O₃-I-700-pellet, it was lower than 0.8 for Co/Al₂O₃-I-700-pellet catalyst.

In order to understand the effect of calcination temperature, performances of the catalysts calcined at 900°C were also investigated. The time dependent CH₄ and CO₂ conversion over the catalysts calcined at 900°C are given in Figure 41. Ni/Al₂O₃-I-900-pellet exhibited the best performance in terms of CH₄ and CO₂ conversion amongst the catalysts calcined at 900°C. While Ni-Co/Al₂O₃-I-900-pellet showed almost the same stability with Ni/Al₂O₃-I-900-pellet during the first 70 minute of reaction, it exhibited a decrease after then, but preserved its stability up to the end of the reaction. Co/Al₂O₃-I-900-pellet was almost inactive in carbon dioxide reforming of methane reaction and the production of H₂ and CO was insignificant. The reducibility of the γ -Al₂O₃-supported Co catalysts decreased with increasing calcination temperature due to the formation of the less reducible Co₂AlO₄ and CoAl₂O₄ [88]. It was concluded that Co/Al₂O₃-I-900 was mostly in the form of Co₂AlO₄ and CoAl₂O₄ which could not be reduced at the reduction temperature and hence did not show activity in CO₂ reforming of CH₄ reaction. CO yield was higher than that of H₂ as in the case of 700°C calcination temperature which was again due to the simultaneous RWGS reaction (Figure 42). As a result H₂/CO ratio was below one for Ni/Al₂O₃-I-900 and Ni-Co/Al₂O₃-I-900 (Figure 43). Except for Co/Al₂O₃-I, Ni/Al₂O₃-I and Ni-Co/Al₂O₃-I catalysts provided comparable activities during the entire period of study irrespective of the calcination temperature.

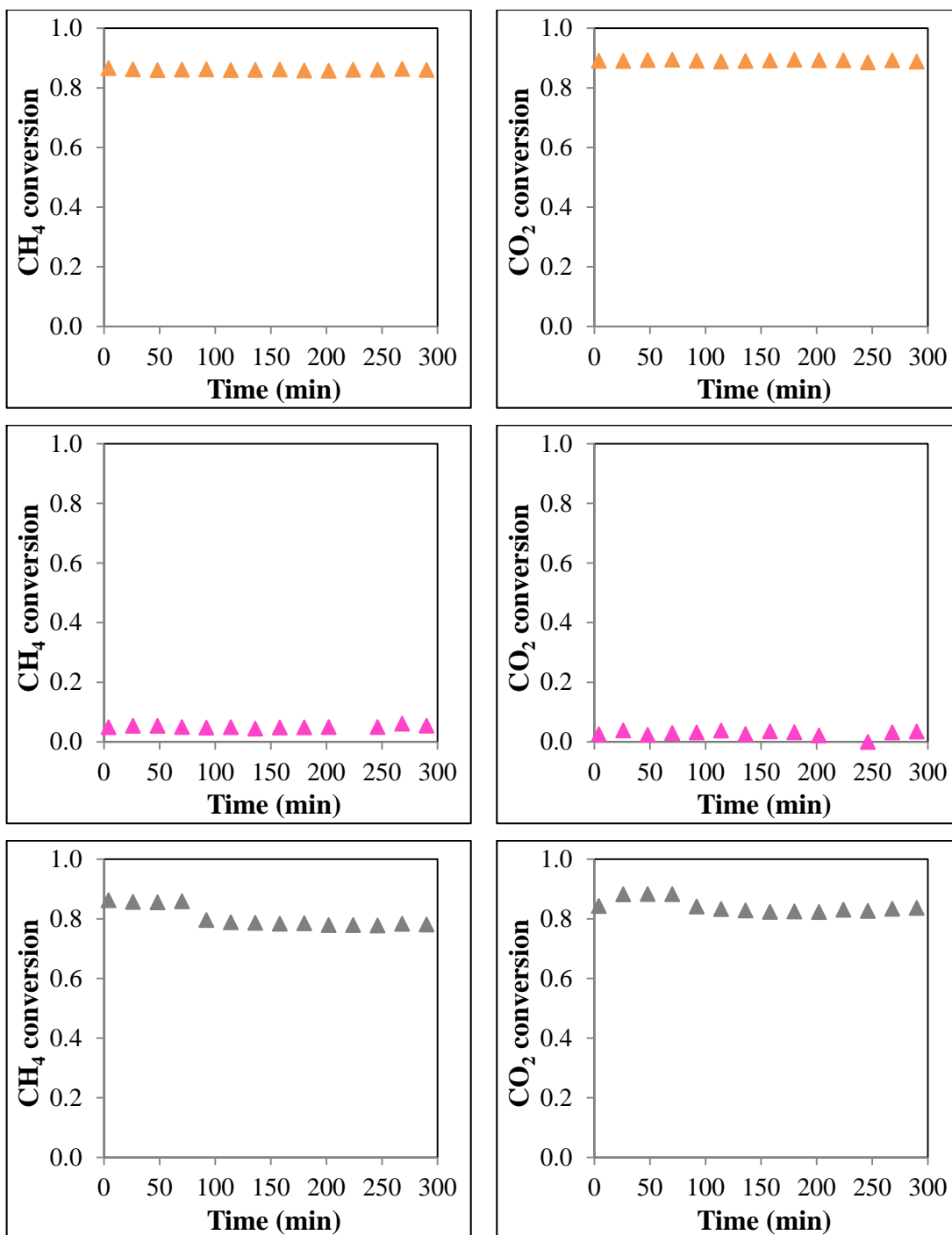


Figure 41. Comparison of CH₄ and CO₂ conversion versus time on stream over the catalysts calcined at 900°C, Ni/Al₂O₃-I-900-pellet ▲, Co/Al₂O₃-I-900-pellet ▲, Ni-Co/Al₂O₃-I-900-pellet ▲, (Reaction conditions: 700°C, 1 atm)

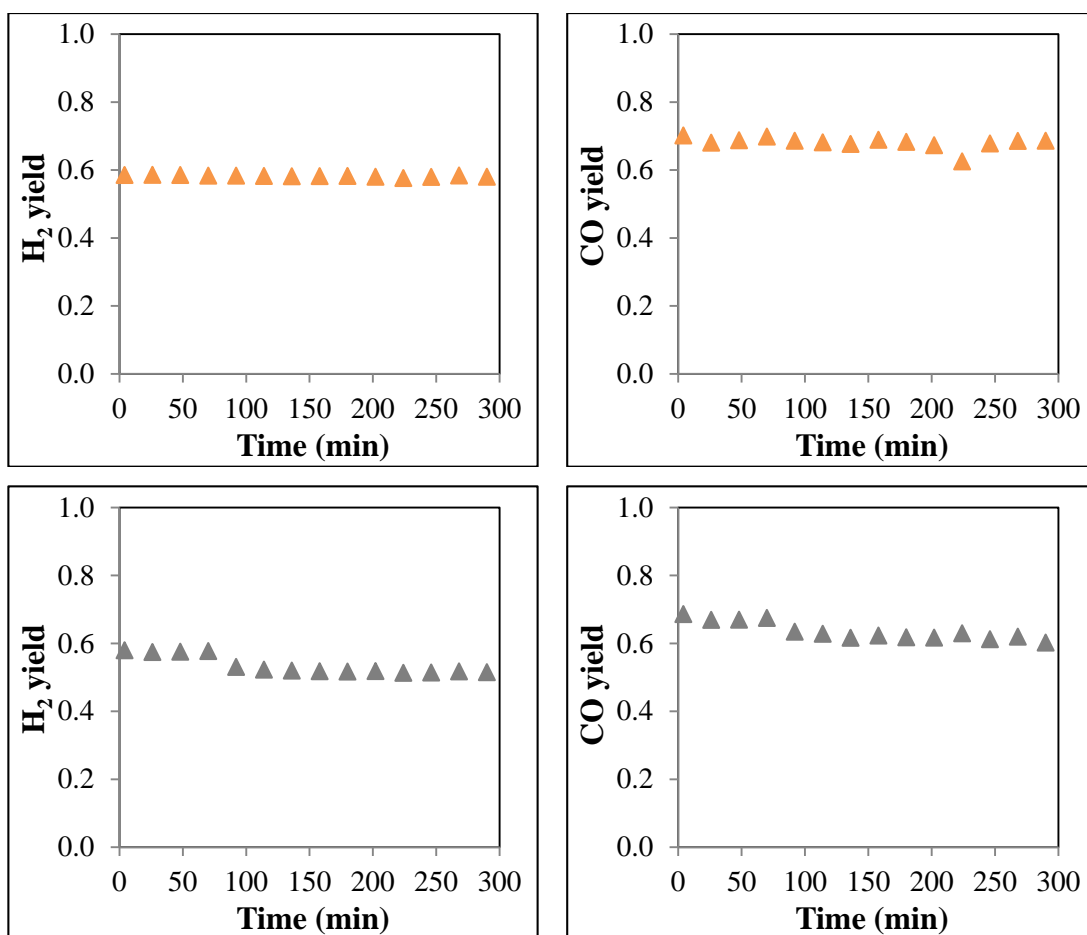


Figure 42. Comparison of H₂ and CO yield versus time on stream over Ni/Al₂O₃-I-900- pellet ▲ and Ni-Co/Al₂O₃-I-900-pellet ▲, (Reaction conditions: 700°C, 1 atm)

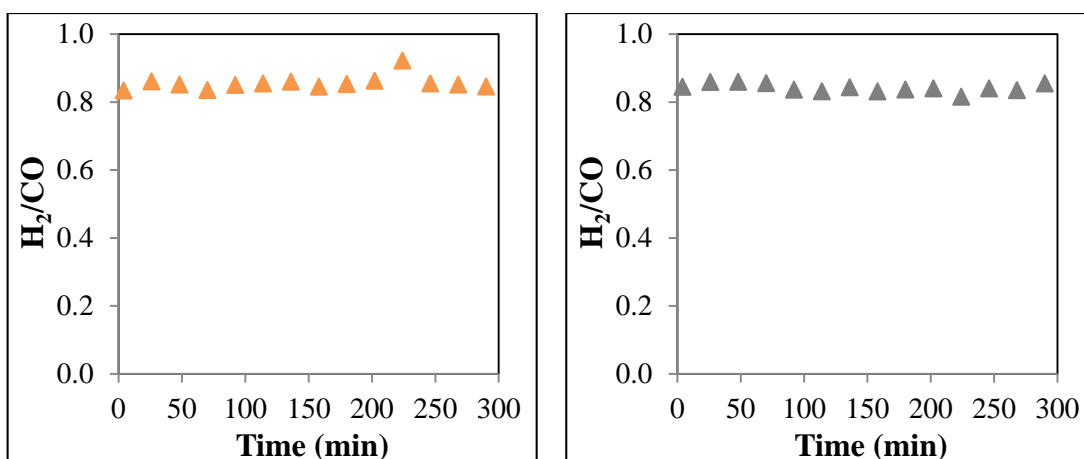


Figure 43. Comparison of H₂/CO ratio versus time on stream over Ni/Al₂O₃-I-700-pellet ▲ and Ni-Co/Al₂O₃-I-700-pellet ▲ (Reaction conditions: 700°C, 1 atm)

In addition to the pellet form, the catalysts in powder form were also investigated in dry reforming of methane reaction. Powder form of the catalysts calcined at 900°C exhibited very high CH₄ and CO₂ conversion (Figure 44). Accordingly the H₂ yield and CO yield were very high, being the CO amount slightly higher than H₂ amount due to the RWGS reaction (Figure 45 and Figure 46). Although the catalysts were in powder form, no instability or clogging were observed for the catalysts calcined at 900°C.

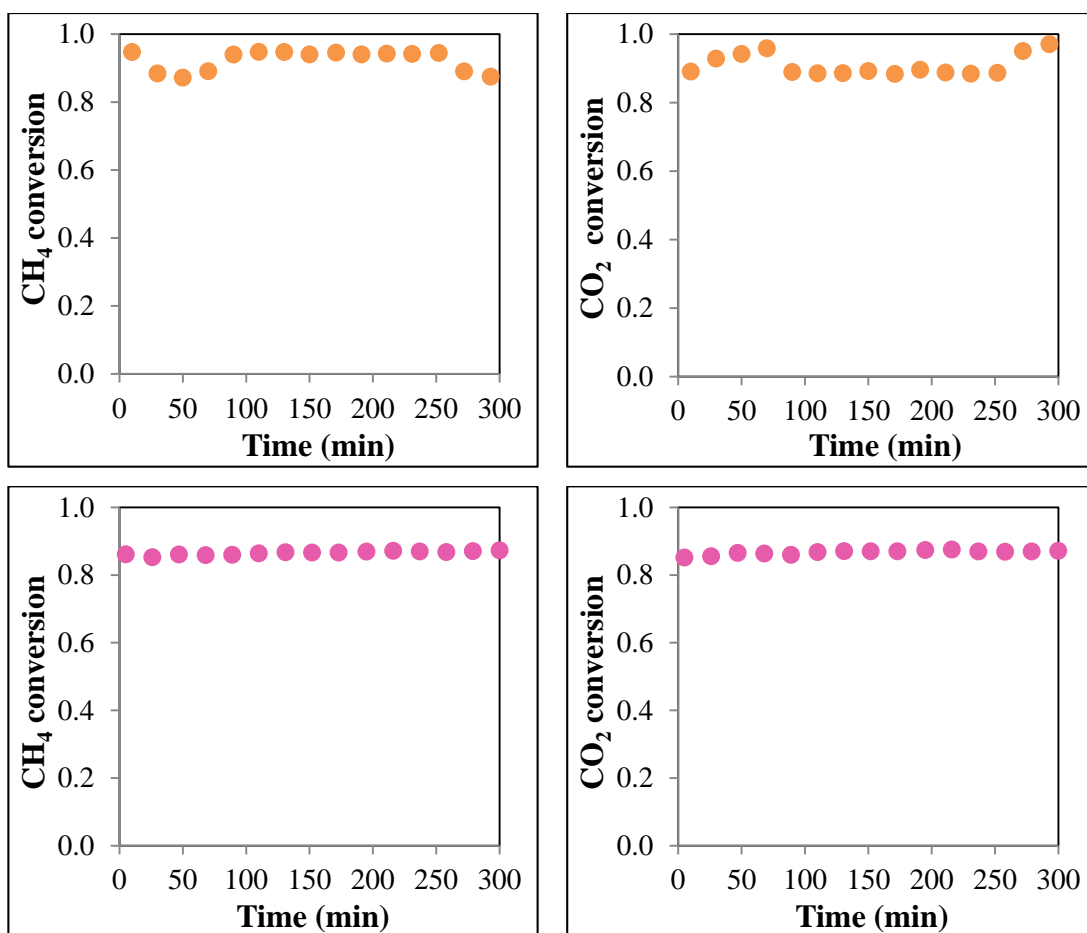


Figure 44. Comparison of CH₄ and CO₂ conversion versus time on stream over the catalysts calcined at 900°C, Ni/Al₂O₃-I-900-powder ●, Ni-Co/Al₂O₃-I-900-powder ●, (Reaction conditions: 700°C, 1 atm)

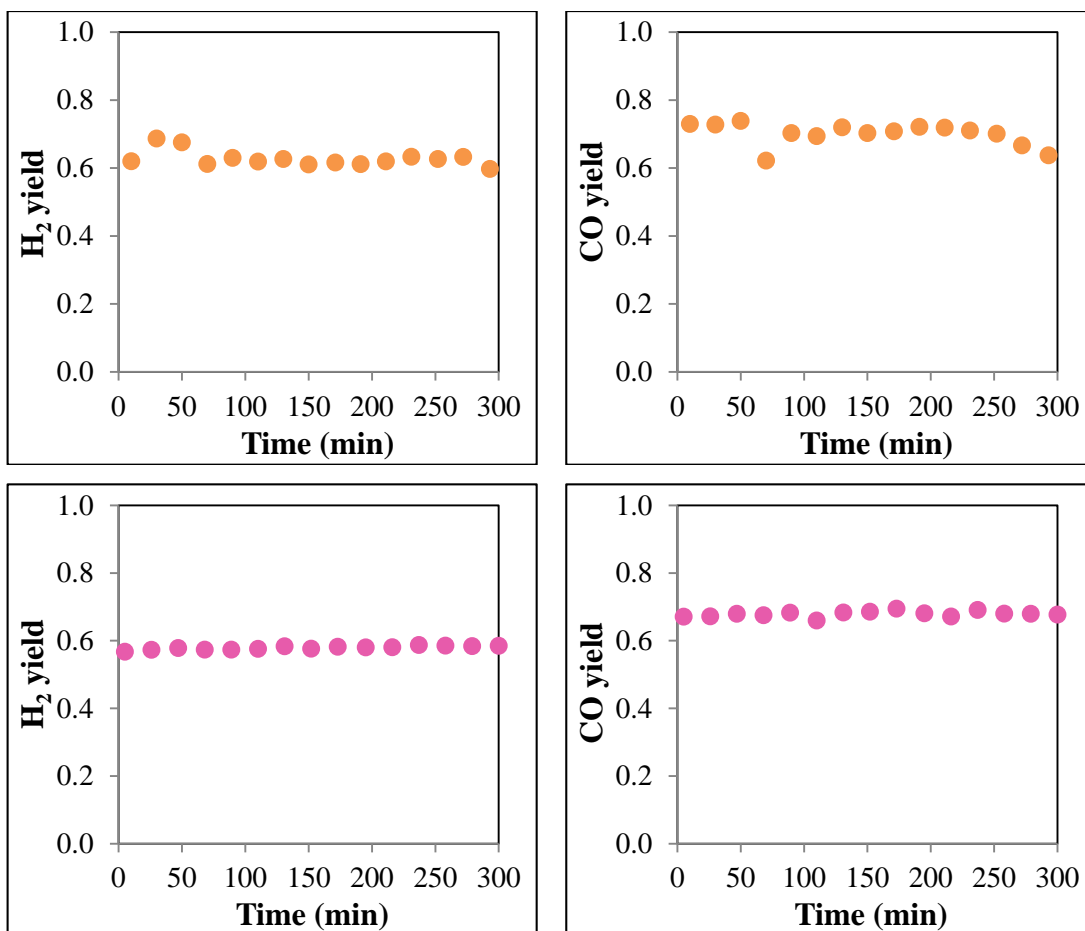


Figure 45. Comparison of H₂ and CO yield versus time on stream over Ni/Al₂O₃-I-900-powder ●, Ni-Co/Al₂O₃-I-900-powder ●, (Reaction conditions: 700°C, 1 atm)

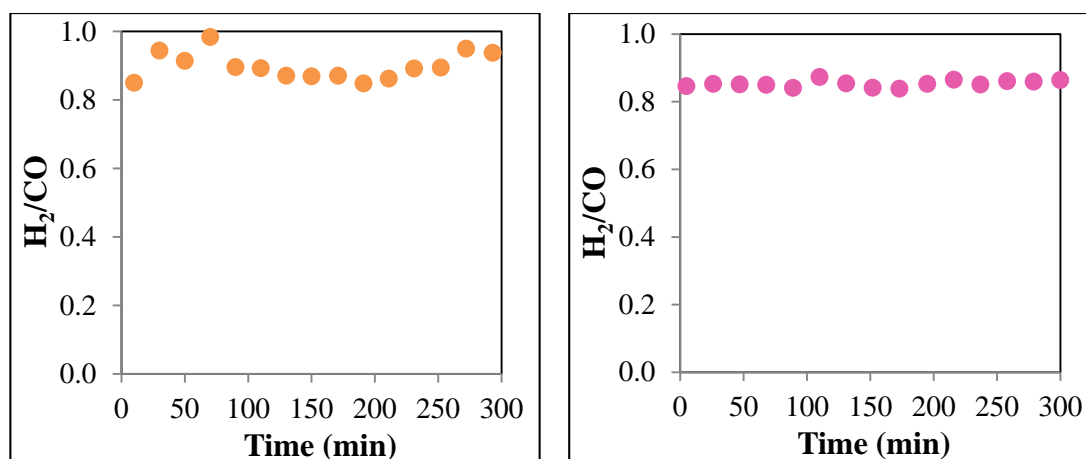


Figure 46. Comparison of H_2/CO ratio versus time on stream over Ni/ Al_2O_3 -I-900-powder ●, Ni-Co/ Al_2O_3 -I-900-powder ●, (Reaction conditions: 700°C, 1 atm)

In addition to the powder form of the catalysts calcined at 900°C, the powder catalysts calcined at 700°C were also investigated in carbon dioxide reforming of methane reaction. Ni/ Al_2O_3 -I-700-powder exhibited very high and stable performance during the entire period of the study which was almost same with the corresponding one in pellet form (Figure 38 and Figure 47).

Although Ni-Co/ Al_2O_3 -I-700-powder exhibited very high conversion in the first half period of the study, clogging occurred and a decrease in the flow rates of the reactants were observed after 150 min. The CH_4 and CO_2 conversion could not be calculated after the onset of clogging, because they were no longer the specified inlet flow rates.

As remembered from Figure 44, both Ni/ Al_2O_3 -I and Ni-Co/ Al_2O_3 -I exhibited stable behavior in powder form when they were calcined at 900°C. Figure 47 proved that while Ni/ Al_2O_3 -I again preserved its stability during the entire period of reaction, Ni-Co/ Al_2O_3 -I lost its stability when it was calcined at 700°C.

As it was remembered from Figures 38, the pellet form of the Ni-Co/Al₂O₃-I catalyst exhibited a slight decrease in its activity when the calcination was done at 700°C. These results suggested that when the calcination was done at 700°C, Ni-Co/Al₂O₃-I catalyst might more prone to carbon formation than Ni/Al₂O₃-I in the long term reaction test.

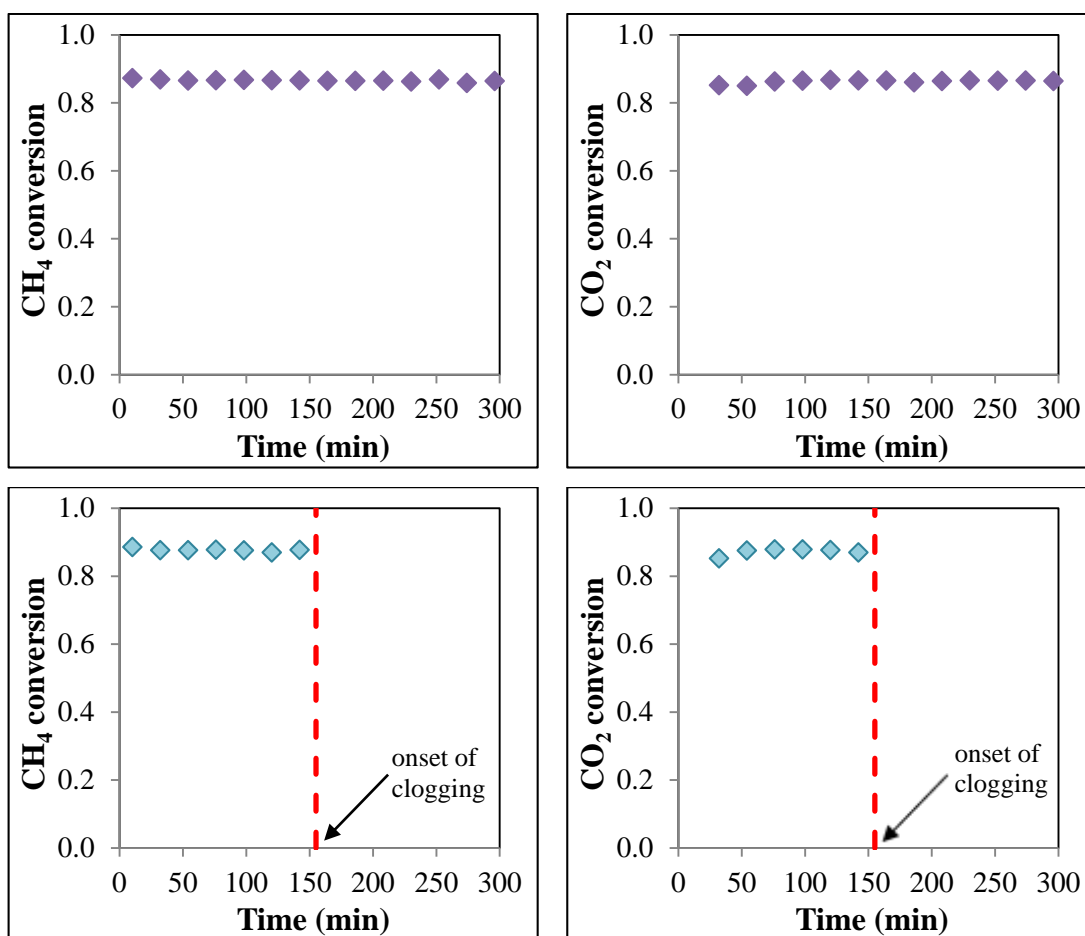


Figure 47. Comparison of CH₄ and CO₂ conversion versus time on stream over the catalysts calcined at 700°C, Ni/Al₂O₃-I-700-powder \blacklozenge , Ni-Co/Al₂O₃-I-700-powder \blacklozenge , (Reaction conditions: 700°C, 1 atm)

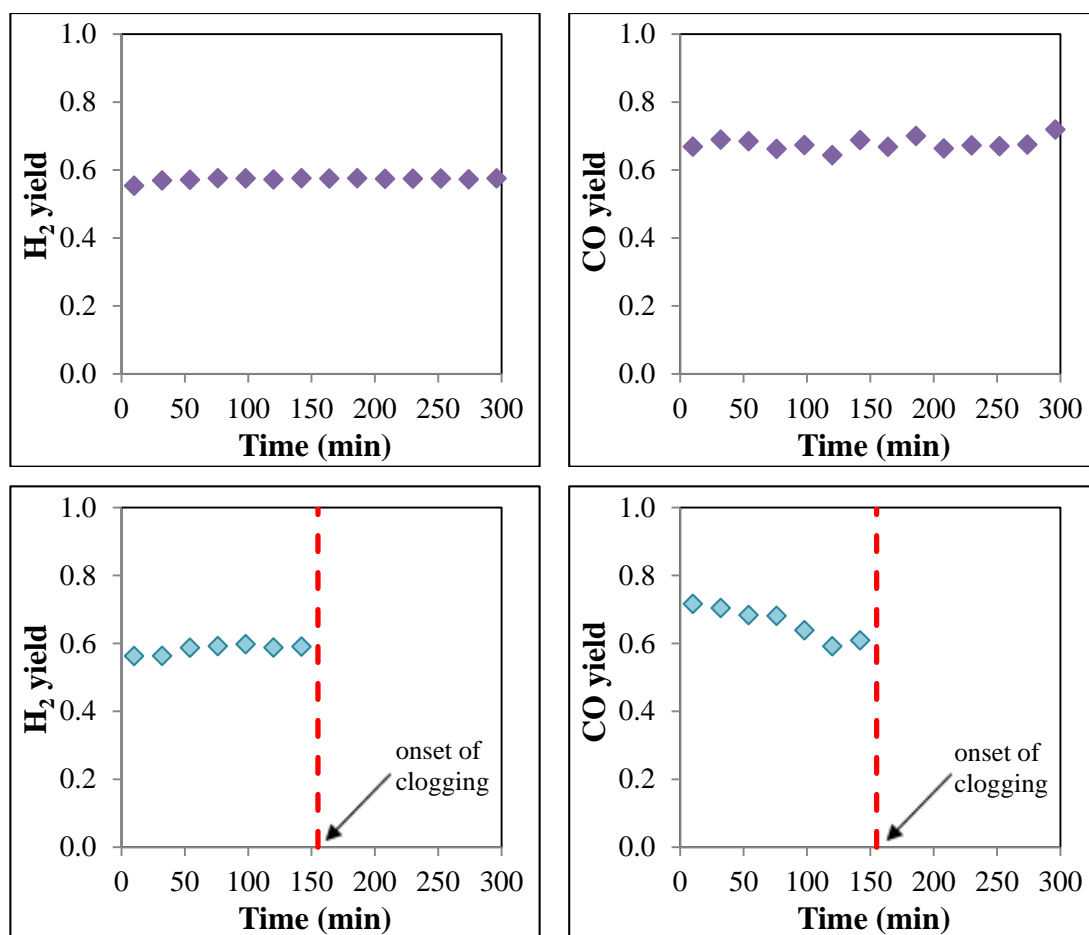


Figure 48. Comparison of H₂ and CO yield versus time on stream over the catalysts calcined at 700°C, Ni/Al₂O₃-I-700-powder \blacklozenge , Ni-Co/Al₂O₃-I-700-powder \blacklozenge , (Reaction conditions: 700°C, 1 atm)

Dry reforming of methane reaction is a highly endothermic reaction. Some reactions were also carried out at 600°C to see the effect of temperature. The conversion decreased with a decrease in temperature over Ni/Al₂O₃-I-900-powder and Ni-Co/Al₂O₃-I-900-powder as expected (Figure 49). It is also important to mention here that the repeat experiments deviated by $\pm 10\%$ conversion at 600°C reaction temperature. This is interpreted as the large sensitivity to minor deviations in reaction or pretreatment conditions. As in the case of conversion, H₂ yield and CO yield were also decreased with decreasing temperature (Figure 50). H₂/CO ratio was below one at 600°C again due to the RWGS reaction (Figure 51).

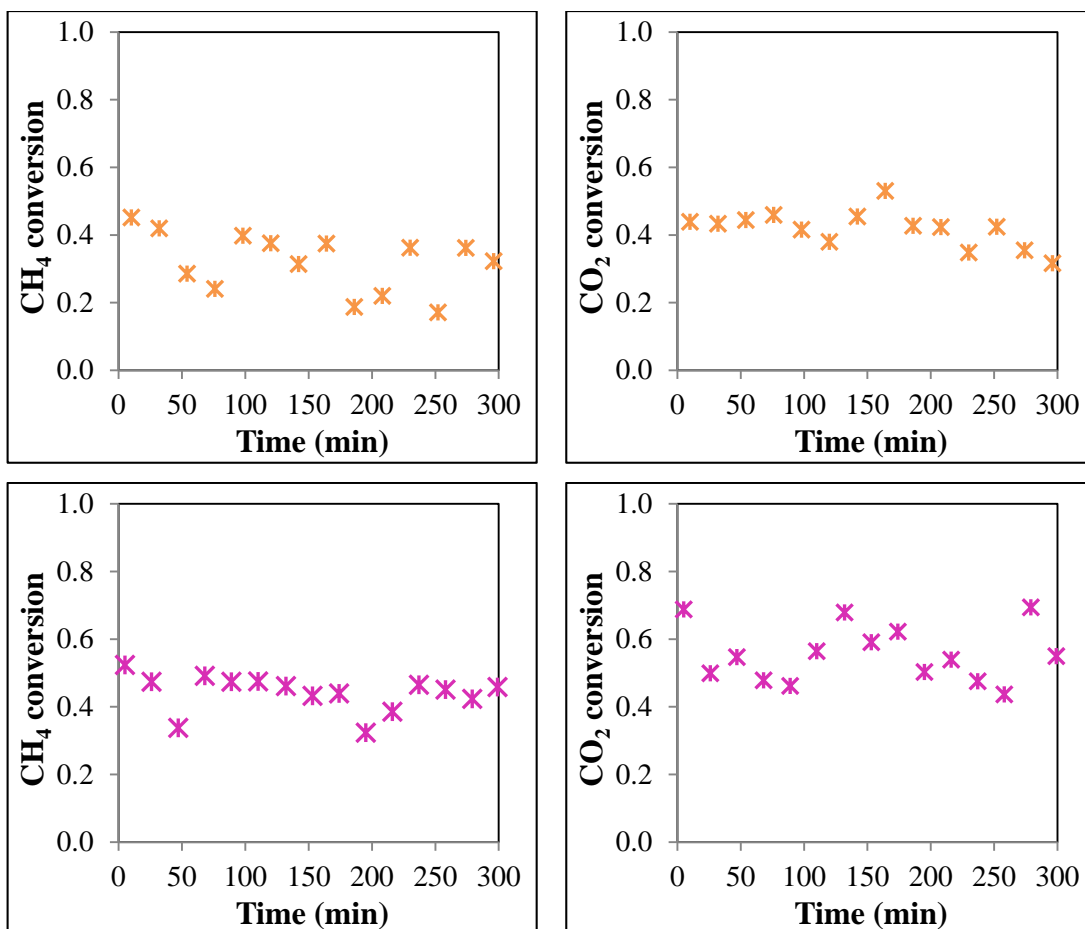


Figure 49. Comparison of CH₄ and CO₂ conversion versus time on stream over the catalysts calcined at 900°C, Ni/Al₂O₃-I-900-powder **x**, Ni-Co/Al₂O₃-I-900-powder **x**, (Reaction conditions: 600°C, 1 atm)

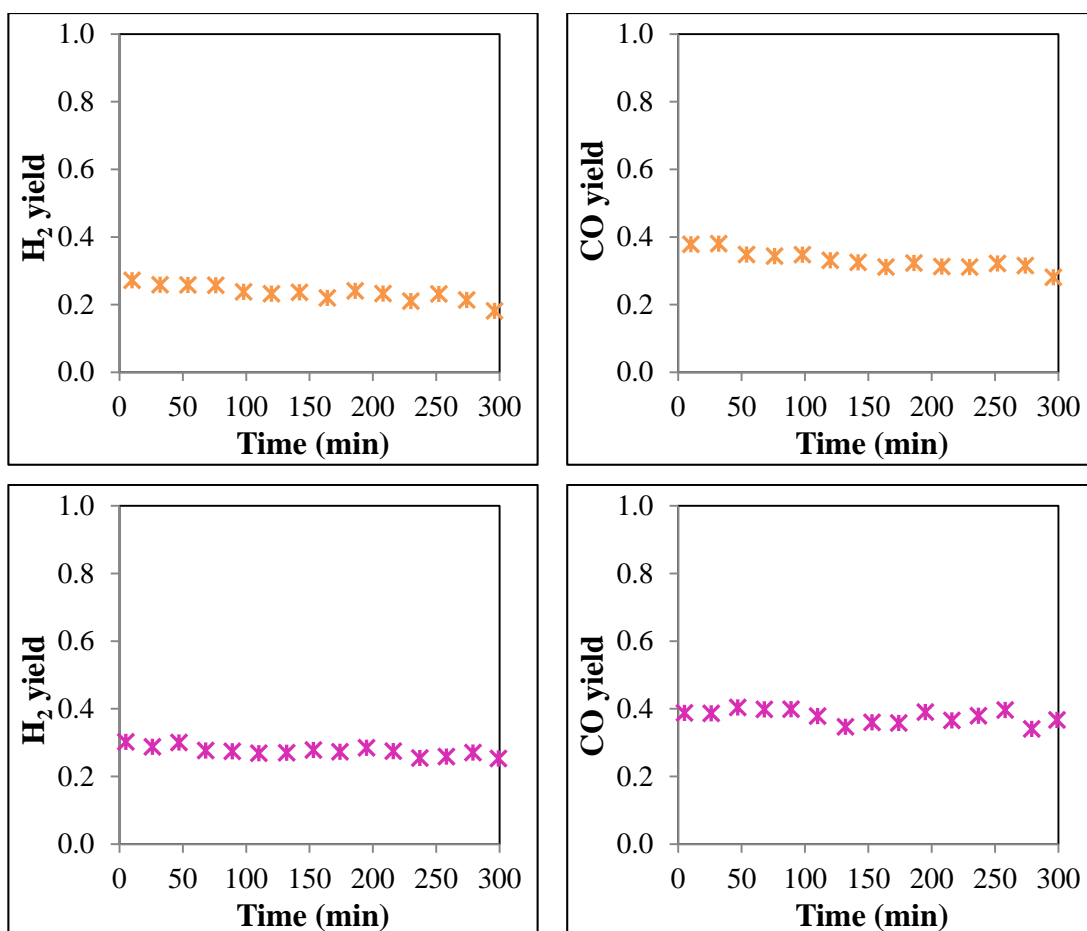


Figure 50. Comparison of H₂ and CO yield versus time on stream over the catalysts calcined at 900°C, Ni/Al₂O₃-I-900-powder \times , Ni-Co/Al₂O₃-I-900-powder \times , (Reaction conditions: 600°C, 1 atm)

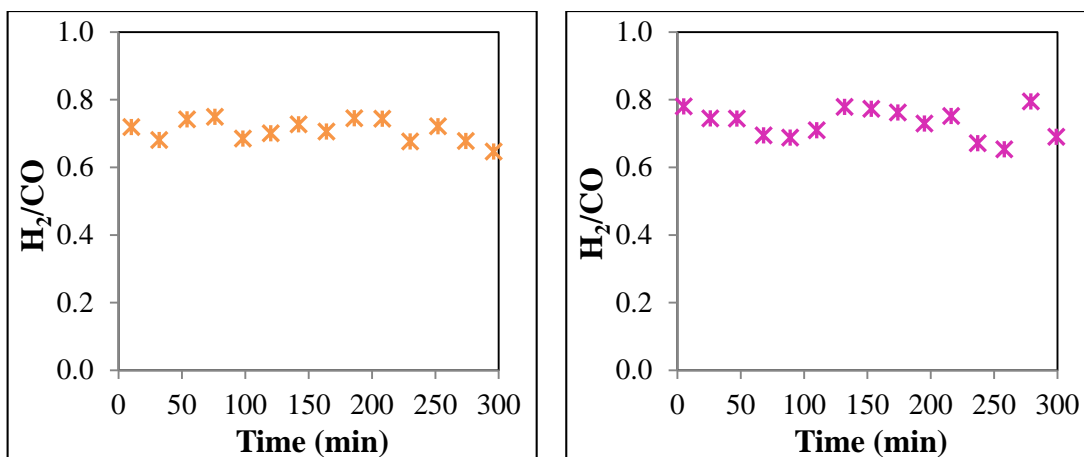


Figure 51. Comparison of H₂/CO ratio versus time on stream over Ni/Al₂O₃-I-900-powder \times , Ni-Co/Al₂O₃-I-900-powder \times , (Reaction conditions: 600°C, 1 atm)

4.2.4 Characterization of spent catalysts

4.2.4.1 Thermal Gravimetric Analysis (TGA)

The amount of carbon deposited on the pellet-samples after being used in CO₂ reforming of CH₄ for five hour reaction period was determined by TGA. More carbon was deposited when the calcination was done at 700°C.

Both Ni and Ni-Co catalysts had almost same amount of carbon deposition when they were calcined at 900°C. On the other hand, much higher amount of coke was deposited on Ni-Co than Ni catalyst when they were calcined at 700°C.

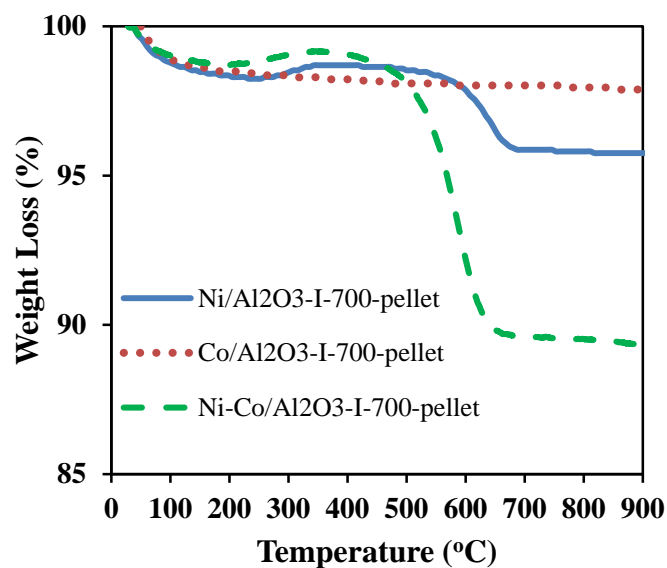


Figure 52. TGA curves in air atmosphere for Ni/Al₂O₃-I-700-pellet, Co/Al₂O₃-I-700-pellet and Ni-Co/Al₂O₃-I-700-pellet after being used in reaction at 700°C for 5 hours

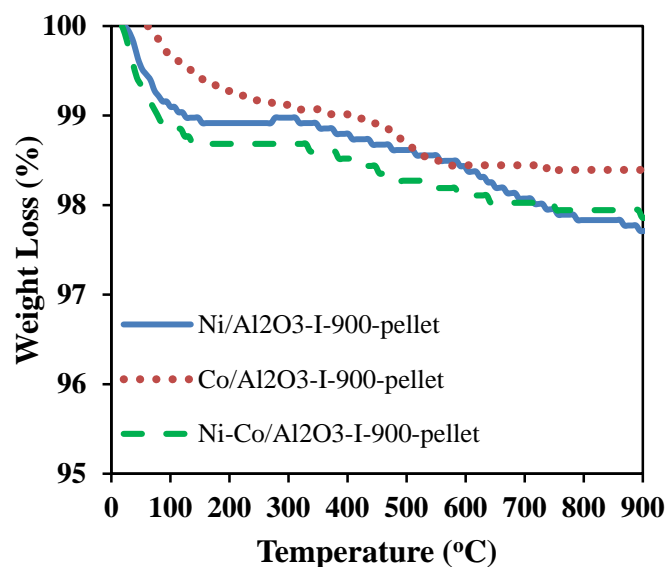


Figure 53. TGA curves in air atmosphere for Ni/Al₂O₃-I-900-pellet, Co/Al₂O₃-I-900-pellet and Ni-Co/Al₂O₃-I-900-pellet after being used in reaction at 700°C for 5 hours

4.2.4.2 High Contrast Transmission Electron Microscopy (HCTEM)

The morphology of carbon formed on the surface of the catalysts after five hour reaction at 600°C was investigated by CTEM. The electron micrographs of carbon deposits over Ni/Al₂O₃-I-900 powder are shown in Figure 54. Octopus carbon structure, where several fibers are growing from one nickel crystal are seen on large nickel particles. Although very scarce, octopus type carbon formation was reported in literature before. Bernardo et al. [101] reported that carbon formation on Ni-Cu/SiO₂ catalyst during methane decomposition was mostly in the form of whisker. Copper content did not alter the form of carbon up to a threshold value, corresponded to 80 %. On the other hand, the carbon deposited on 80% copper sample showed an unusual structure having a variety of amorphous carbon filaments connected to the identical metal particle which were called as octopus carbon. Rostrup-Nielsen [102] also observed octopus carbon on Ni catalysts with high sulphur coverage after being exposed to CH₄/H₂ mixtures. Ermakova [103] reported octopus carbon nanotube growth formed on Fe/Al₂O₃ catalyst upon exposure to high purity methane. Pham-Huu et al. [104] observed octopus-like formation of carbon nanofibers over Ni catalyst supported on graphite microfibers upon decomposition of ethane/hydrogen mixture. Rass-Hansen et al. [105] observed that large particles around 100 nm in K-doped Ni/MgAl₂O₄ catalyst resulted in octopus carbon structure during ethanol steam reforming. In addition to the octopus type of carbon, filamentous carbon in the form of carbon nanotubes are seen on the small nickel particles (Figure 54).

Figure 55 shows the filamentous carbons of nanotubes and nanofibers with varying diameters over Ni-Co/Al₂O₃ catalyst. No octopus carbon was observed over this catalyst. The surface properties and thus the catalytic performance of bimetallic catalysts can be explained in terms of a change of the surface ensemble structures [106]. The presence of cobalt may suppress octopus carbon growth by breaking nickel ensembles.

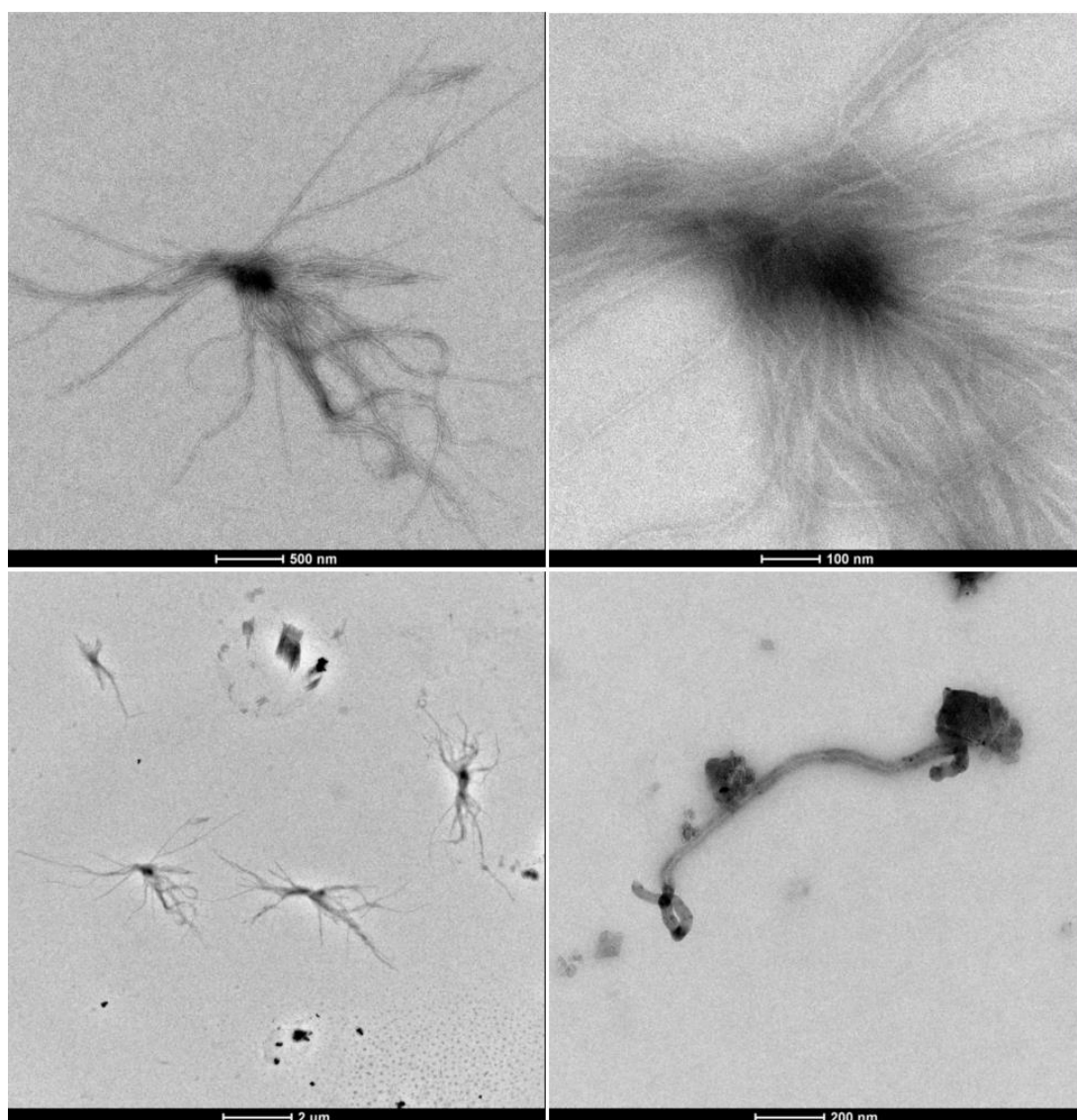


Figure 54. HCTEM of Ni/Al₂O₃-I-900-powder after being used in reaction at 600°C for 5 hours

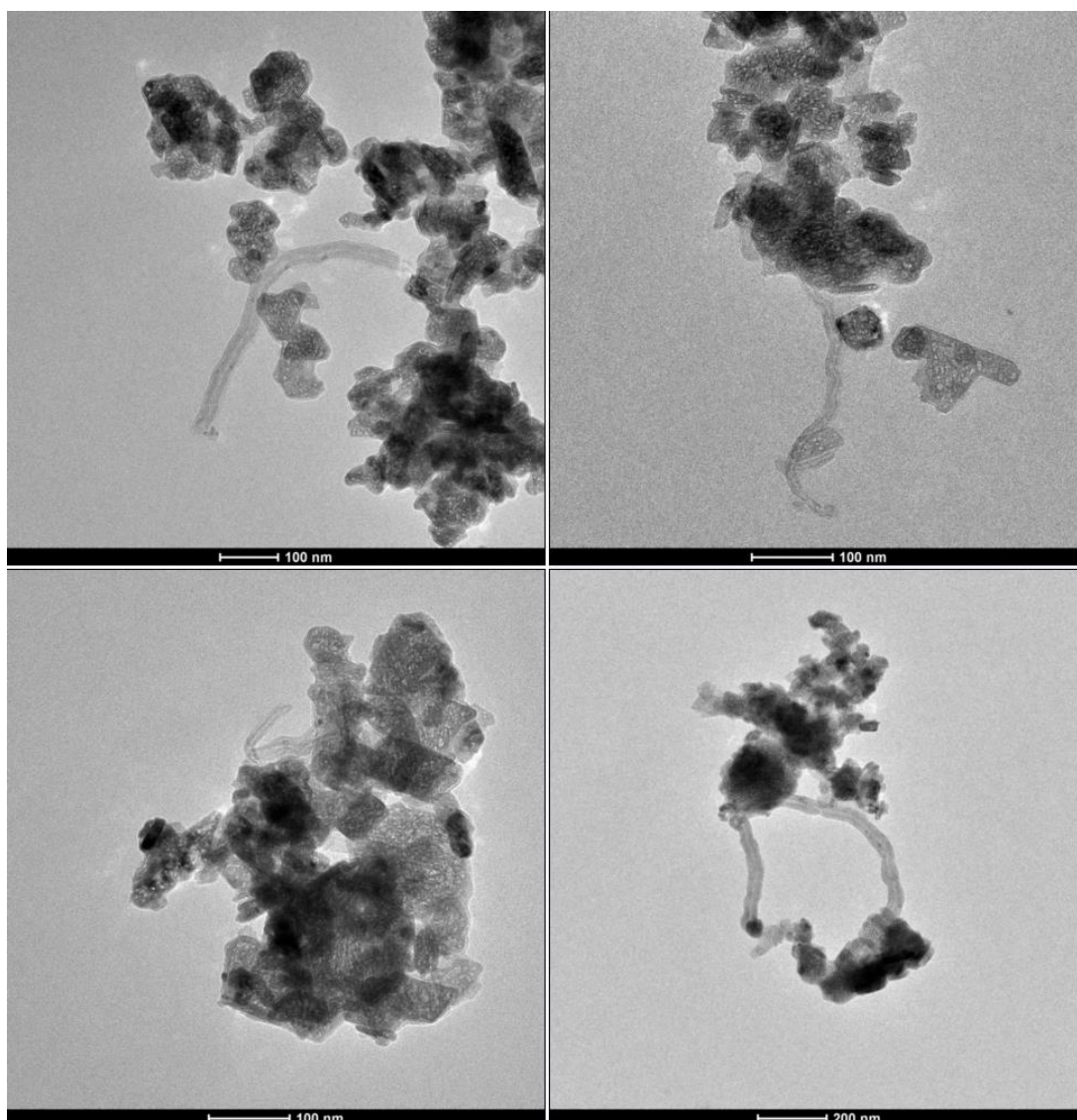


Figure 55. HCTEM of Ni-Co/Al₂O₃-I-900-powder after being used in reaction at 600°C for 5 hours

4.2.5 Source of Coke Determination Reactions and Characterization Results

As mentioned before, the catalyst deactivation during dry reforming of methane is caused by carbon formation [1,28,29], sintering at high temperature [30,31] and oxidation of metallic sites [32,33]. Although in literature it is agreed that the primary cause of catalyst deactivation is carbon formation, there are disagreements existing on the origin of coke which can come from CH₄ and CO₂.

The clarification of this issue is necessary in terms of understanding the mechanism of carbon formation with the aim of reactor design and catalyst design which can prevent the accumulation of coke. For this aim, reaction tests were carried out with ¹³CO₂ and ¹²CH₄ over Ni/Al₂O₃-I-powder catalysts and the used catalyst was characterized by ¹³C solid state NMR spectrometer. To the best of our knowledge, there has been no study on the characterization of the used catalyst by ¹³C solid state NMR for the determination of coke origin in dry reforming of methane reaction.

Since ¹³CO₂ was limited, reaction conditions were first prepared with ¹²CO₂ and ¹²CH₄ to deposit carbon in short time. Before the reaction, the samples were reduced with flowing 50 sccm H₂/Argon (2/3) mixture at 700°C for 1h. The weight gain of the catalysts after 10 minutes reaction at 600°C under 10 sccm CO₂ and 10 sccm CH₄ diluted in 30 sccm Ar was determined as 1.9% for Ni/Al₂O₃-I-900-powder and 2.6% for Ni/Al₂O₃-I-700-powder. Since these quantities are low, it is difficult to detect them in NMR. For this reason it was decided to change the flow rate of the reactants which could result in considerable amount of coke in a small period of reaction. This time the reaction was carried out at 600°C for 10 minutes under 30 sccm CO₂ and 30 sccm CH₄ without using diluting gas. The weight gain of the Al₂O₃ supported catalysts after 10 minutes reactions at 600°C under 30 sccm CO₂ and 30 sccm CH₄ without using diluting gas are given in Table 9. It was determined to continue with the catalysts calcined at 700°C in coke determination reactions due to their higher carbon depositing tendency.

Table 9. The weight gain of Al₂O₃ supported powder catalysts after being used in the reaction at 600°C for 10 minutes under 30 sccm CO₂ and 30 sccm CH₄

Catalyst	Weight gain (%)
Ni/Al ₂ O ₃ -I-900-powder	3.5
Ni-Co/Al ₂ O ₃ -I-900-powder	1.1
Ni/Al ₂ O ₃ -I-700-powder	11.7
Ni-Co/Al ₂ O ₃ -I-700-powder	8.4

Reaction tests were done over Ni/Al₂O₃-I-700-powder catalyst with varying CH₄/CO₂ ratios so as to determine the source of carbon. The carbon amount increased with increasing CH₄ ratio as seen in Figure 56, indicating that CH₄ could be the main source of carbon formation in dry reforming of methane reaction.

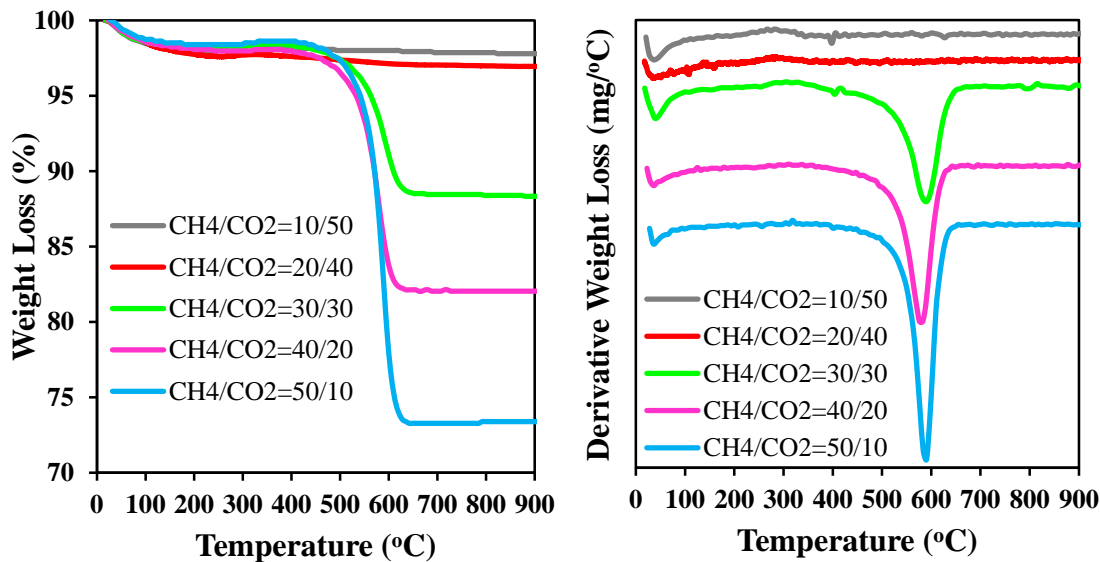


Figure 56. The effect of CH₄/CO₂ ratio in the input stream on a) amount of carbon deposition b) type of carbon deposition over Ni/Al₂O₃-700-powder after being used in the reaction at 600°C for 10 minutes

The stoichiometry of dry reforming reaction is 1 to 1 for CO₂ and CH₄. A high CH₄/CO₂ ratio in the feed mixture is regarded as a harsh state for this reaction. When this ratio is higher than 1.0, CH₄ becomes excess. If the reaction mixture does not have sufficient oxidant (CO₂), the produced carbon will deposit on the catalyst surface and lead to deactivation. As a result, the higher the methane/carbon dioxide ratio, the harsher the reaction conditions for dry reforming [72]. Yang and Papp studied dry reforming of CH₄ at 800°C over Pt/MgO with a feed ratio of CH₄/CO₂ 1.0 and 2.0. Both the ESCA and the CO₂-TPSR results of the spent catalysts indicated that more carbon was formed on the catalyst having the higher CH₄/CO₂ ratio [72].

Amongst the potential coke depositing reactions, methane decomposition and carbon monoxide disproportionation have generally been regarded as carbon deposition reactions in literature. Methane decomposition is endothermic whereas carbon monoxide disproportionation is exothermic. In the review article of Papadopoulou [1], CH₄ decomposition is reported to be predominating at temperatures higher than 700°C and CO disproportionation at temperatures lower than 600°C. The extent of their contribution to carbon formation depends on operating conditions and catalyst composition [1].

York et al. [2] studied the rate of carbon deposition from pure methane and carbon monoxide over a supported nickel catalyst at different temperatures, showing that both CO disproportionation and CH₄ decomposition are catalysed by nickel, but to changing extents depending on the reaction temperature.

Although the TGA results give the impression that CH₄ decomposition is the primary reason of carbon formation, the thermodynamics indicate that CO disproportionation should also have an impact on carbon deposition at 600°C. The methane conversion and H₂/CO ratio were also calculated at the fifth minute of reaction as shown in Figure 57.

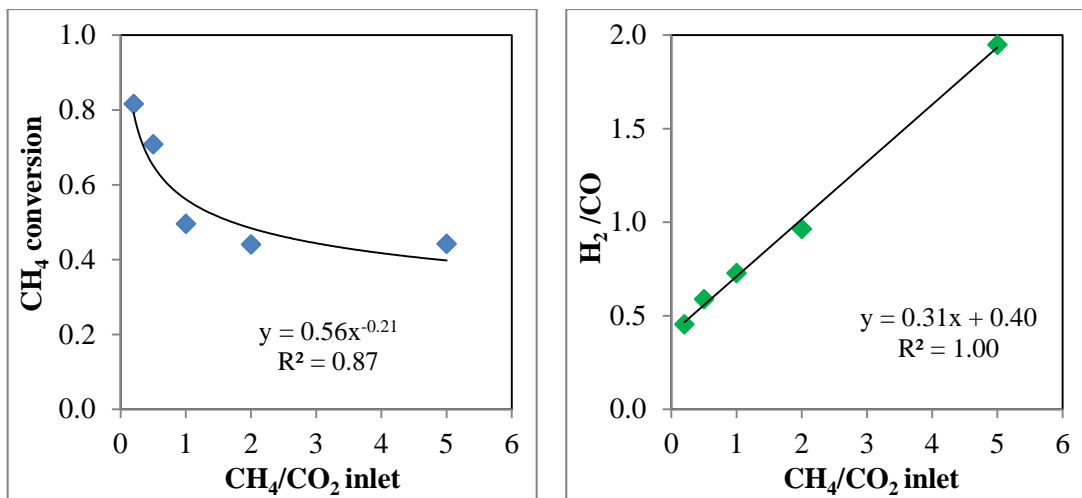


Figure 57. Effect of the CH₄/CO₂ ratio in the input stream on a) CH₄ conversion and b) H₂/CO ratio

It was observed that while methane conversion decreased steeply at CH₄/CO₂<1, it did not change considerably at CH₄/CO₂>1 where CO₂ is the limiting reactant. If CH₄ was the sole source of carbon by its decomposition, the conversion of CH₄ would have increased steadily, but it did not. This gave the clue that CH₄ was not only component responsible for carbon formation.

In their thermodynamic equilibrium study on the multi-reaction system for CO₂ reforming of CH₄ regarding the reactions taking place in carbon formation based on direct minimization of Gibbs free energy method, Nikoo and Amin [107] showed that CH₄ conversion increases with CO₂/CH₄ ratio suggesting that CO₂ gas being a soft oxidant has a beneficial influence on CH₄ conversion in the temperature range of interest. This beneficial influence is more noticeable at temperatures lower than 700°C; hence, addition of more CO₂ to CH₄ results in a higher activity for CH₄ molecules.

Braga et al. [108] investigated the effect of CH₄/CO₂ molar ratio (0.25, 2.125 and 4.0) on dry reforming of methane by using Ni/SiO₂. While CH₄ conversion decreased with an increase in CH₄/CO₂ ratio at 700°C and 800°C, a maximum was observed at a CH₄/CO₂ ratio of 2.125 at 600°C reaction temperature.

Although TGA results showed that the carbon deposition increased with an increase in CH₄, the reaction tests were carried out over Ni/Al₂O₃-700 with ¹³CO₂ with the idea of CO₂ could also have a role in coke formation by taking into consideration the CH₄ conversion and the thermodynamics. The deposited coke was characterized by solid state NMR in UC Berkeley, Department of Chemical and Biomolecular Engineering. As shown in Figure 58, the deposited coke not only comes from CH₄, but CO₂ has also a significant role in carbon formation.

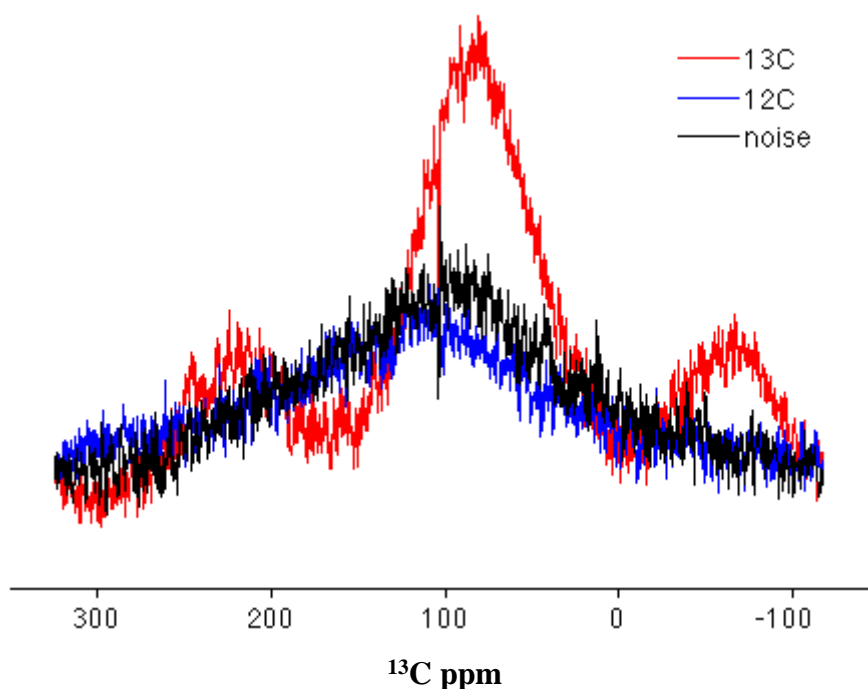


Figure 58. ¹³C NMR spectra of the coke deposited on Ni/Al₂O₃-I-700-powder after being used in the reaction at 600°C for 10 minutes under 30 sccm ¹³CO₂ and 30 sccm CH₄

Our conclusion is consistent with the deductions made by Tsipouriari and Verykios [5], Lemonideu et al. [74], Kroll et. al. [75], and McFarlane et al. [76] in terms of showing that both reactants take place in carbon formation during dry reforming of methane. Further NMR studies are in progress to exhibit the quantitative role of CO₂ in coke deposition over Ni/Al₂O₃-I-700-powder catalysts which were used in dry reforming reaction with varying CH₄/¹³CO₂ ratios.

The effect of CH₄/CO₂ ratio on the morphology of the spent catalysts was investigated by HCTEM. Figure 59, 60 and 61 shows the HCTEM of Ni/Al₂O₃-700 catalyst after being used in the reaction at 600°C for 10 minutes with ¹³CO₂/¹²CH₄ ratios of 10/50, 30/30 and 50/10 respectively. Besides scarce amount of long straight filaments with elongated nickel particles inside, most of the deposited carbon is in the form of short and thick filaments (thicker-walled tubes with narrow inner channels) which are rolled up into shapeless tangles in Figure 59 where the CH₄ ratio was highest. Carbon filaments entangled one another are again seen in Figure 60 but the intensity of which decreased compared to the ones seen in Figure 59. No carbon filaments were observed over the sample treated with the lowest CH₄ ratio (Figure 61). Some carbon in the form of encapsulating type was detected in that case.

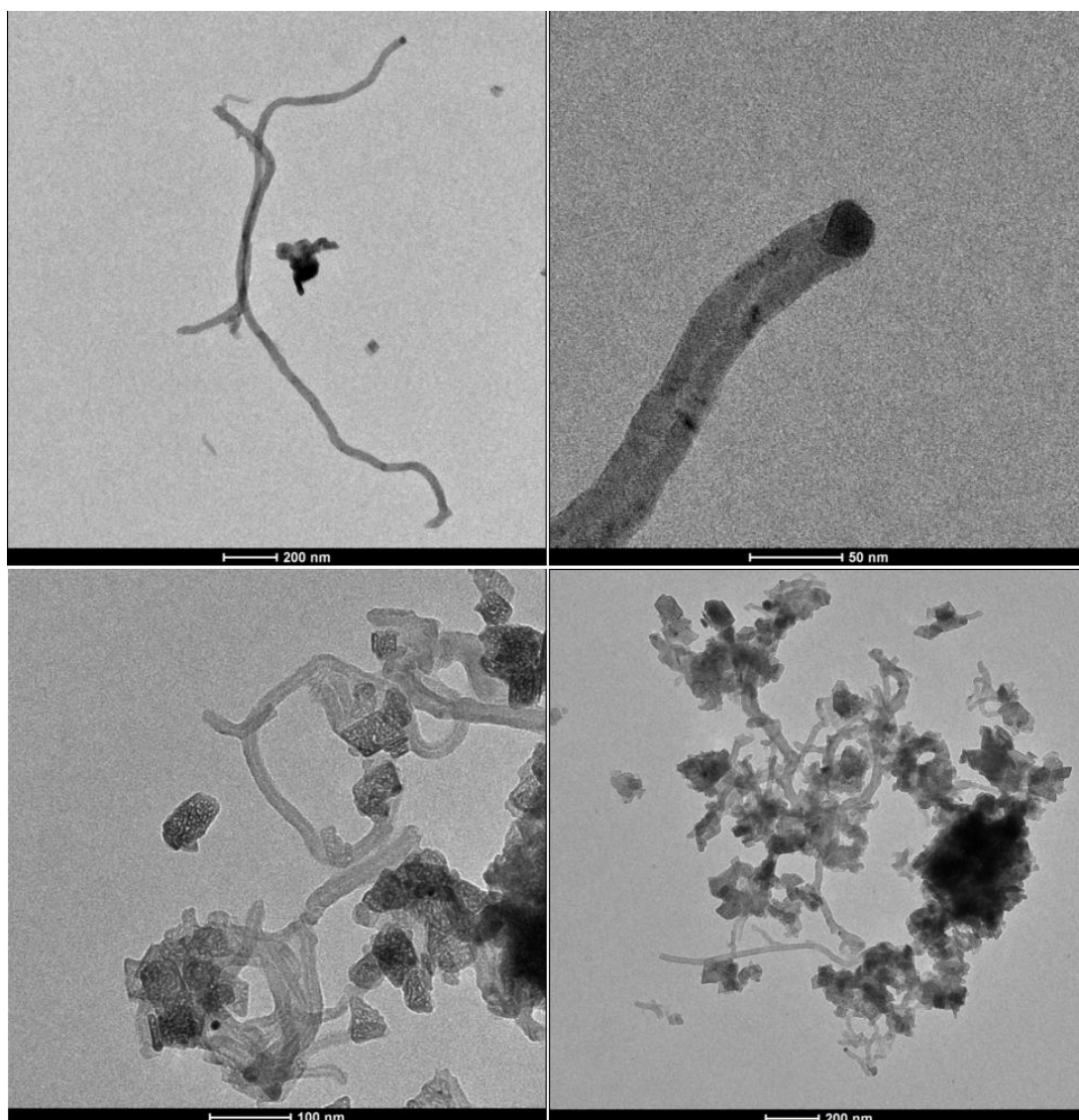


Figure 59. HCTEM of Ni/Al₂O₃-I-700-powder catalyst after being used in the reaction at 600°C for 10 minutes with ¹³CO₂/¹²CH₄ ratio of 10/50

As remembered, the electron micrographs of carbon deposits obtained after the reaction at 600°C for 5 hours exhibited octopus carbon structure. On the other hand, no octopus carbon was observed on any of the samples after 10 minutes reaction.

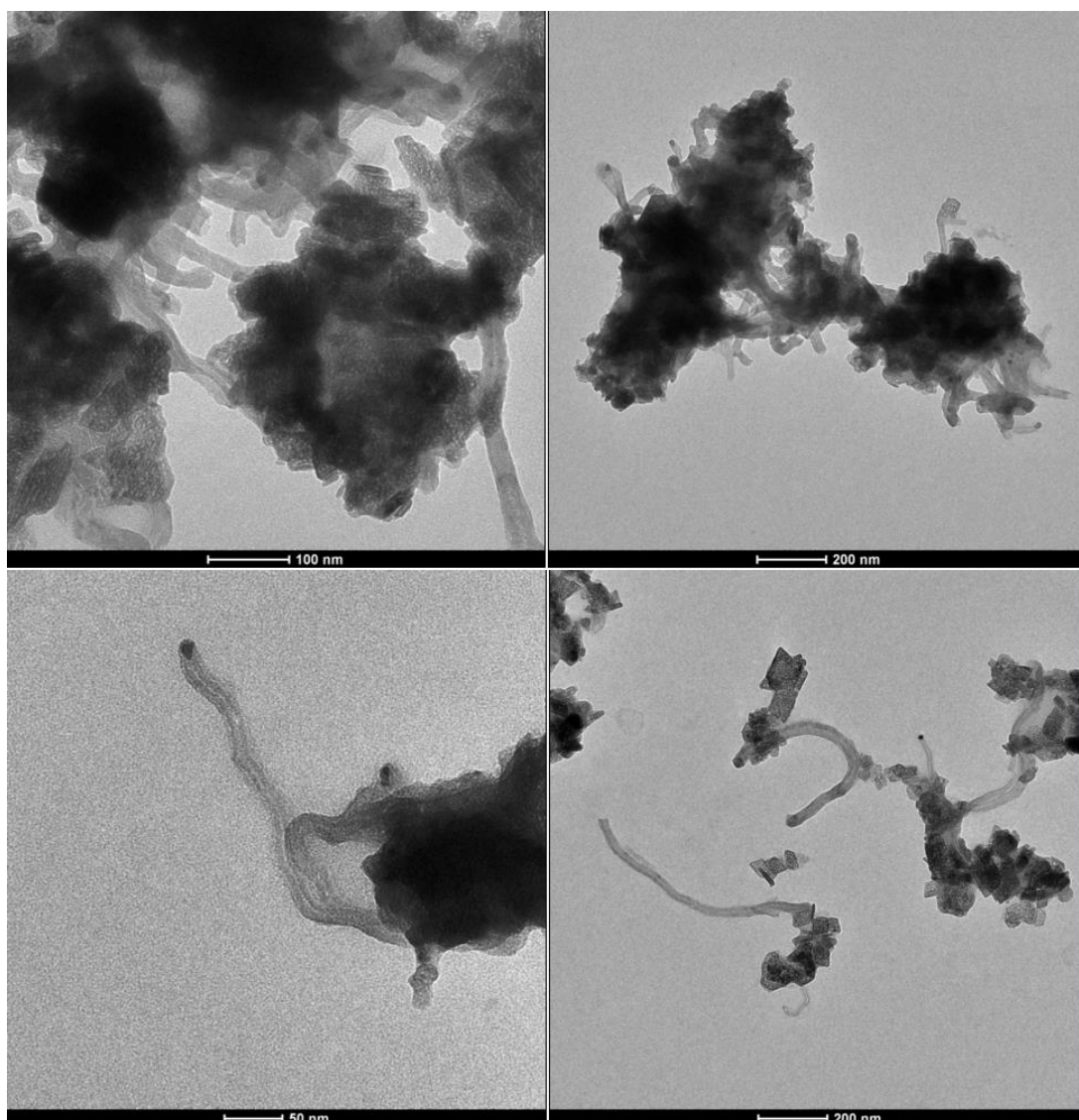


Figure 60. HCTEM of Ni/Al₂O₃-I-700-powder catalyst after being used in the reaction at 600°C for 10 minutes with ¹³CO₂/¹²CH₄ ratio of 30/30

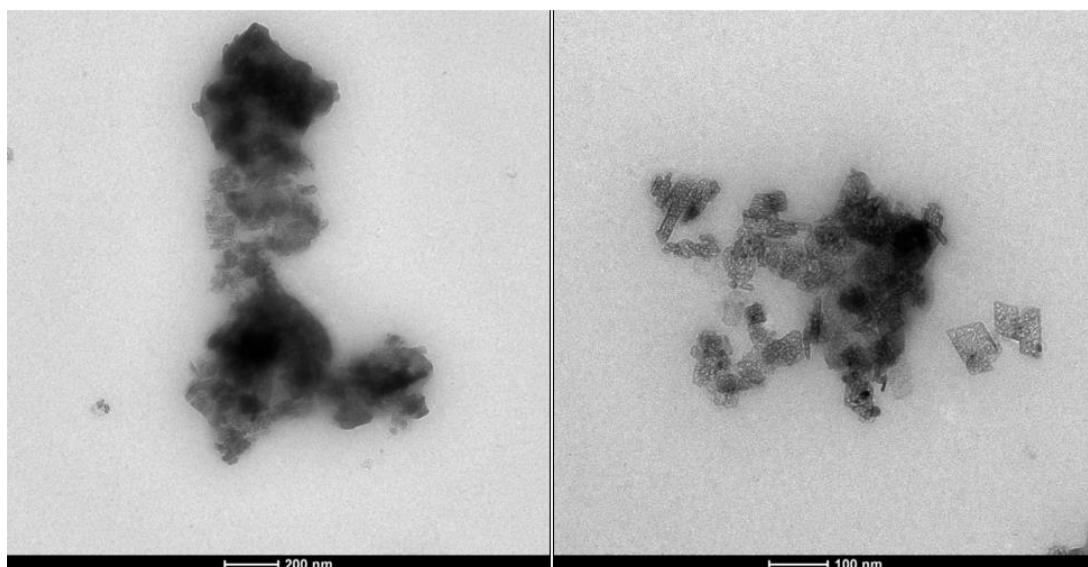


Figure 61. HCTEM of Ni/Al₂O₃-I-700-powder catalyst after being used in the reaction at 600°C for 10 minutes with ¹³CO₂/¹²CH₄ ratio of 50/10

4.3 Conclusions

Al₂O₃ supported Ni, Co and Ni-Co catalysts were synthesized via incipient wetness impregnation method for dry reforming of methane reaction. To see the influence of calcination temperature, the catalysts were prepared by calcining at two different temperatures, 700°C and 900°C. Addition of Co to the Ni-based catalyst resulted in the increased metal-support interaction.

In situ-DRIFTS study of CO₂ adsorption on the catalysts resulted in bicarbonate formation and were assigned to the bending, symmetric stretching and asymmetric stretching vibrational modes on γ -alumina. The energetics of carbon dioxide adsorption was studied by means of microcalorimetry. The adsorption characteristics were not influenced by the metals indicating that CO₂ adsorbed on alumina.

Catalytic tests were conducted at 600°C and 700°C. The activity of Co/Al₂O₃-I was lower than those of Ni/Al₂O₃-I and Ni-Co/Al₂O₃-I catalyst. While doing the

calcination at 700°C or 900°C did not really affect the catalytic performance of Ni/Al₂O₃-I and Ni-Co/Al₂O₃-I catalysts, it had significant influence on the performance of Co/Al₂O₃-I catalyst. Ni/Al₂O₃-I and Ni-Co/Al₂O₃-I catalysts provided comparable activities. Both Ni and Ni-Co catalysts had almost same amount of carbon deposition when they were calcined at 900°C. On the other hand, much higher amount of coke was deposited on Ni-Co than Ni catalyst when they were calcined at 700°C.

The electron micrographs of carbon deposits over Ni/Al₂O₃-I-900 exhibited octopus carbon structure, where several fibers are growing from one nickel crystal. No octopus carbon was observed over Ni-Co/Al₂O₃-I-900 catalyst. The presence of cobalt may suppress octopus carbon growth by breaking nickel ensembles.

¹³C NMR characterization of the deposited coke revealed that coke not only came from CH₄, but CO₂ had also significant role in carbon formation.

CHAPTER 5

DRY REFORMING OF METHANE ON Al_2O_3 SUPPORTED Ni CATALYSTS PREPARED BY POLYOL METHOD

5.1 Introduction

Polyol method has gained great attention recently in preparation of Ni nanoparticles [109-113]. It is an efficient, easy and cheap method for the reduction of a huge amount of metallic powder with a uniform shape and size [111 and references therein]. This process uses poly-alcohol as both solvent and reducing agent for the production of nanoparticles from the metallic precursor [113 and references therein]. Different polyols, such as ethylene glycol, diethylene glycol, tetraethylene glycol, propylene glycol, trimethylene glycol and butylene glycol can be used to achieve the reduction process [111-112]. There are several factors affecting the properties of nanoparticles acquired by the polyol method, as the type of precursor [111], the type of polyol [112], the reaction time [110] and temperature [114], pH [115,116], the presence of protective agent [113,117] and the utilization of an extra-reducing agent [113].

Noble metals such as Au, Ag and Pd can be synthesized by polyol method under neutral or even acidic conditions. On the other hand, enough alkalinity is required for reducing Ni^{2+} because of its lower oxidation potential [115]. Bai et al. showed the great effect of alkalinity on the morphology of the resulting Ni powders in polyol process by obtaining metallic nickel powders with various morphologies including microspheres, icosahedra and flowerlike clusters at different pHs [115].

Carroll et al. [112] studied the effect of polyol type in the nucleation and growth of copper and nickel nanoparticles. The reduction of nickel and copper salt precursors (acetate, hydroxide and chloride salts) dissolved in different polyols (propylene

glycol, ethylene glycol, tetraethylene glycol, diethylene glycol, and butylene glycol) under both refluxing and distillation conditions were studied. With the exception of NiCl₂ in EG, the product was elemental nickel for all the nickel precursors under distillation and refluxing conditions. NiCl₂ could not be totally reduced to elemental nickel even after 36 h at reflux which was most probably because of the improved stability of Ni(EG)₃ hydrated intermediate complex.

Ung et al. [118] synthesized Co-Ni and Co nanoparticles by reducing nickel and cobalt acetate mixtures in NaOH solution in 1,2-propanediol. Co-Ni composition and the basicity of the medium are shown to be two important parameters on which the particle shape depended strongly. For the samples abundant in cobalt, agglomerated rods, nanowires and platelets were seen when sodium hydroxide concentration was increased in the range 0-0.2 M. For Co₅₀Ni₅₀ composition and sodium hydroxide concentration in the range 0.1-0.18 M, nanodumbbells were formed the shape of which strongly depended on the basicity. While long dumbbells were observed for the lowest sodium hydroxide concentration, short dumbbells and diabolos were obtained for the highest sodium hydroxide concentration

Couto et al. [113] synthesized nickel nanoparticles in air by a modified polyol process, using nickel chloride as precursor, PVP as protective agent and sodium borohydride as reducing agent. The presence of PVP was shown to be necessary to inhibit the aggregation and growth of nanoparticles. High homogeneous and stable dispersions of PVP-coated nickel nanoparticles were acquired by using ethylene glycol.

Singh et al. [119] synthesized almost spherical nickel nanoparticles in non-aqueous environment using PVP as a surfactant and hydrazine hydrate as reducing agent. The nickel particles were fcc in their crystal structure and monodisperse within the PVP matrix with an average size about three nm. The synthesized nickel nanoparticles showed superparamagnetism behavior.

Chou and Huang [114] investigated the synthesis of nanosized nickel colloids by using nickel chloride as precursor, hydrazine as reducing agent and palladium as nucleation agent. Nickel with a high purity could be acquired when the temperature was higher than 80°C. On the other hand, nickel hydroxide was also present in its precipitate form at a lower temperature. The starting concentration of nickel ion was shown to be the most important element influencing the crystallite size of precipitates. On the other hand, the quantity of PVP and the reaction temperature had only negligible effects. The presence of PVP could not prevent agglomeration of Ni particles into micron sizes. However, if polyacrylic acid was supplemented instantly after the reaction, nickel colloids could be stabilized in the nanometer range.

Viau et al. [120] synthesized $\text{Co}_x\text{Ni}_{100-x}$ particles with tailored morphological characteristics by reduction from metallic salts dissolved in 1,2-propanediol. Heterogeneous nucleation using Pt^{II} as nucleating agent enabled them to synthesize spherical, non agglomerated particles in the submicrometer to nanometer-size range with a narrow size distribution. In the 200–500nm range, the XRD pattern of $\text{Co}_x\text{Ni}_{100-x}$ particles only depended on composition: a fcc phase was always observed either as a single phase for $x < 35$ or as the main phase with a second hcp phase for $x > 35$.

Nouneh et al. [121] synthesized nickel nanoparticles successfully and attached them on indium tin oxide substrate by two separate routes: from solution reduction method by using NaBH_4 as reducing agent in the presence of PVP as stabilizing and protective agent and by polyol method under ethylene glycol as a solvent. While the samples synthesized in aqueous solution exhibited the formation of fcc metallic nickel nanoparticles with a medium diameter of ~31nm and good size dispersion, the ones prepared in ethylene glycol displayed big size ~150 nm.

Roselina et al. [110] presented an easy and quick synthesis way of nickel nanoparticles at nearly 180°C in a mixture containing ethylene glycol and hydrazine as reducing agent. They studied the effect of reaction time on the Ni nanoparticles that was produced with advantages of facile and rapid synthesis without using any other protective agent such as polyvinylpyrrolidone, polyvinyl alcohol, oleic acid and cetyltrimethyl ammonium bromide. XRD showed that the reduction of Ni²⁺ to metallic Ni could be accomplished completely in 15 minutes. XRD also exhibited that the synthesized nanoparticles were purely metallic nickel with fcc crystal structure. Reaction time was shown to have a critical role in changing particle size. Particles with a mean size ranging between 1 and 175 nm could be synthesized by controlling the reaction time.

Instead of traditional methods requiring high calcination temperatures Bayrakdar et al. [117] proposed an alternative way for the synthesis of nanosized Ni/Al₂O₃ catalysts. They prepared stable PVP-protected Ni/Al₂O₃ catalysts having nickel amount ranging between 5.4 and 7.4 wt. % without doing calcination. Metallic nickel was acquired with peaks at 44.3° (111), 51.6° (200), 76.4° (220). Any peaks of NiO, NiAl₂O₄ or Ni(OH)₂ were detected among the synthesized catalysts.

In this part of the study, polyol process as an alternative to conventional preparation methods was employed to obtain 10 wt % (nominal) Ni/Al₂O₃ catalysts in the presence of PVP (polyvinylpyrrolidone) as stabilizer and ethylene glycol as both solvent and reducing agent. Catalysts with different PVP/Ni ratios were acquired. Since literature survey showed that metallic nickel could be obtained during the synthesis in polyol process, the performances of the as-prepared catalysts were evaluated for carbon dioxide reforming of methane at 600°C and 700°C without making a reduction step before the reaction.

5.2 Results and Discussion

5.2.1 Characterization of fresh catalysts

5.2.1.1 X-Ray Diffraction (XRD) Analysis

γ -Al₂O₃ powder from Alfa Aesar was used as support. As discussed in Section 4.2.1.1 XRD pattern of the as received alumina powder (Figure 17) demonstrates that boehmite, γ -Al₂O₃ and δ -Al₂O₃ phases coexist simultaneously by considering the reference XRD patterns (Boehmite: 21-1307 JCPDS file, γ -Al₂O₃: 50-741 JCPDS file, δ -Al₂O₃: 46-1215 JCPDS file).

X-ray diffraction patterns of the synthesized catalysts show the formation of metallic Ni as long as alkaline condition is provided regardless of the PVP amount used. Alkalinity is not only necessary for Ni reduction, it has also great effect on both purity and the morphology of the resulting Ni powders [115,122]. XRD pattern shown in Figure 62 exhibits four characteristic peaks at 44.6°, 51.8°, 76.4° and 93.1° corresponding to (111), (200), (220) and (311) Miller index planes of fcc nickel. Although nickel can easily oxidise, peaks belonging to the oxide phase were not seen, which may be due to the fact that the reaction was performed at appropriate temperature and pH [119].

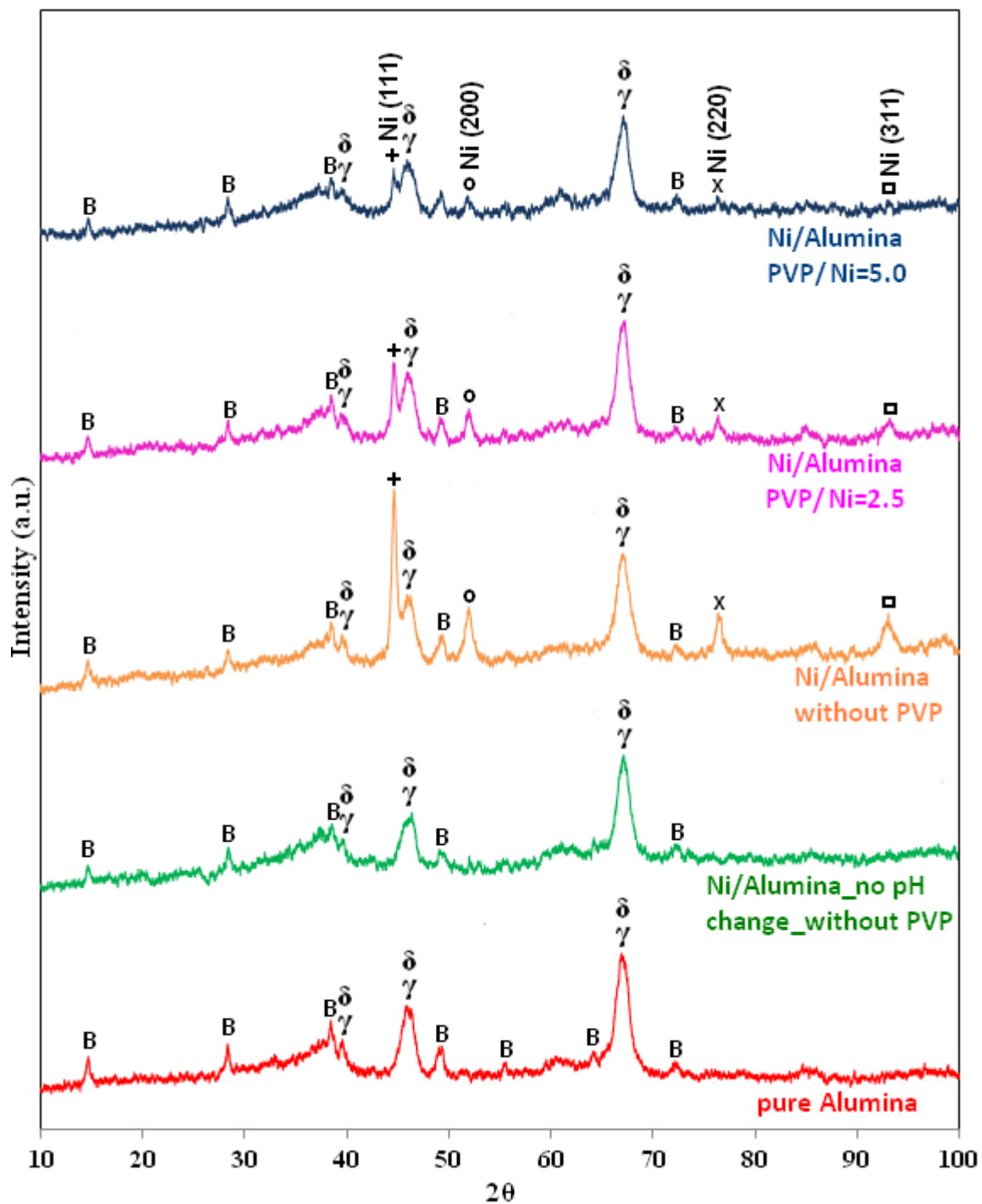


Figure 62. Comparison of the XRD pattern of pure alumina with those of catalysts prepared by polyol method

5.2.1.2 Surface Area, Pore Size Distribution and Adsorption-Desorption Isotherms

The surface area of all the catalysts was reduced significantly compared to that of the parent pure alumina support (Table 10). While the pore volume of Ni/Al₂O₃-without-PVP and Ni/Al₂O₃-PVP/Ni=2.5 catalysts was similar to that of pure alumina, pore volume of Ni/Al₂O₃-PVP/Ni=5.0 catalyst was considerably lower which might be due to its highest PVP content.

Table 10. Comparison of textural properties of pure Al₂O₃ with the catalysts prepared by polyol method

Catalyst	BET Surface area (m ² /g)	Pore volume (cm ³ /g)	Average pore diameter (nm)
Pure Al ₂ O ₃	73.2	0.37	19.7
Ni/Al ₂ O ₃ without PVP	46.5	0.35	28.2
Ni/Al ₂ O ₃ PVP/Ni=2.5	54.3	0.40	27.5
Ni/Al ₂ O ₃ PVP/Ni=5.0	50.7	0.28	19.5

The nitrogen adsorption/desorption isotherm and pore size distribution of the pure Al₂O₃ and the synthesized catalysts are shown in Figure 63 and Figure 64. According to the IUPAC classification all samples exhibited type II adsorption isotherm which is characteristic of macroporous materials and the H3-shape hysteresis loop of the samples shows the presence of mesopores [79]. Pore size distribution of the samples exhibits that they are mainly composed of macropores (pore diameter > 50 nm in diameter) in addition to the mesopores (2 nm < pore diameter < 50 nm).

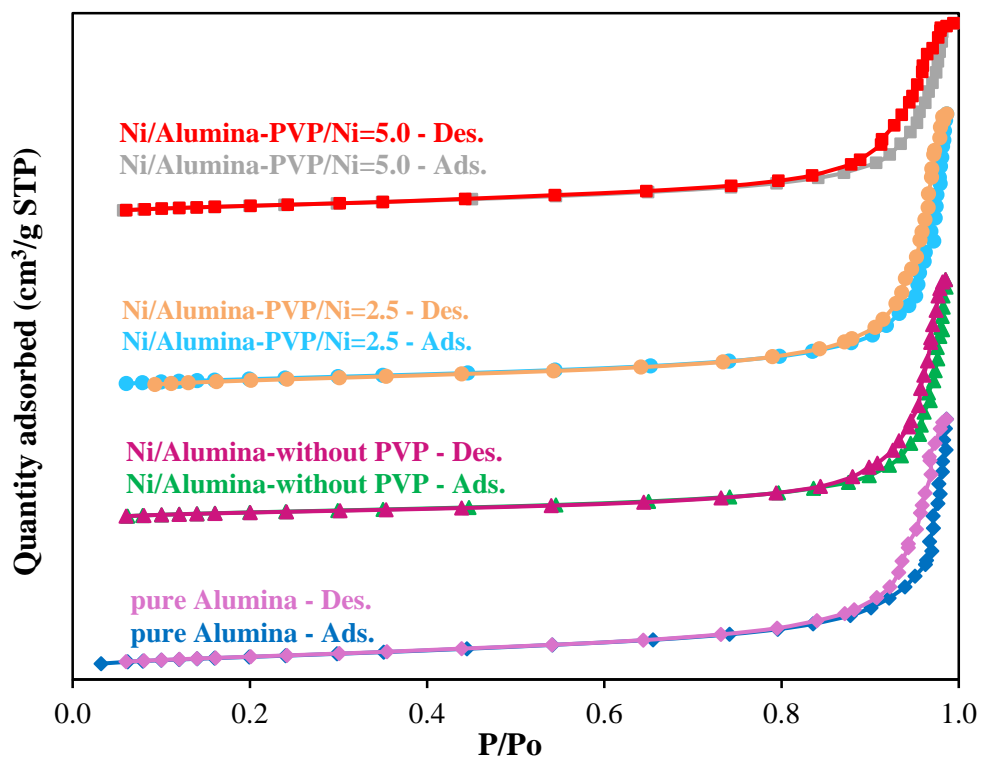


Figure 63. Comparison of nitrogen adsorption-desorption isotherms of pure Al₂O₃ with the catalysts prepared by polyol method

5.2.1.3 Thermal Gravimetric Analysis (TGA)

The thermal analysis was performed to investigate the presence of organics on the nanoparticles. The TGA analysis of pure ethylene glycol, pure PVP and synthesized catalyst is shown in Figure 65. The weight loss is approximately 5%, 11% and 19% for the catalysts Ni/Alumina-without PVP, Ni/Alumina-PVP/Ni=2.5 and Ni/Alumina-PVP/Ni=5.0, respectively. As PVP amount was increased, the weight loss also increased as expected.

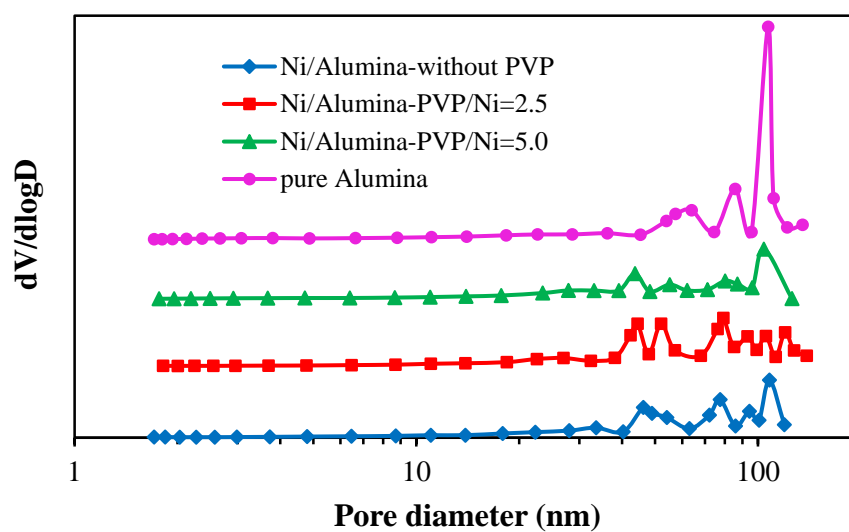


Figure 64. Comparison of BJH pore size distribution of pure Al₂O₃ with the catalysts prepared by polyol method

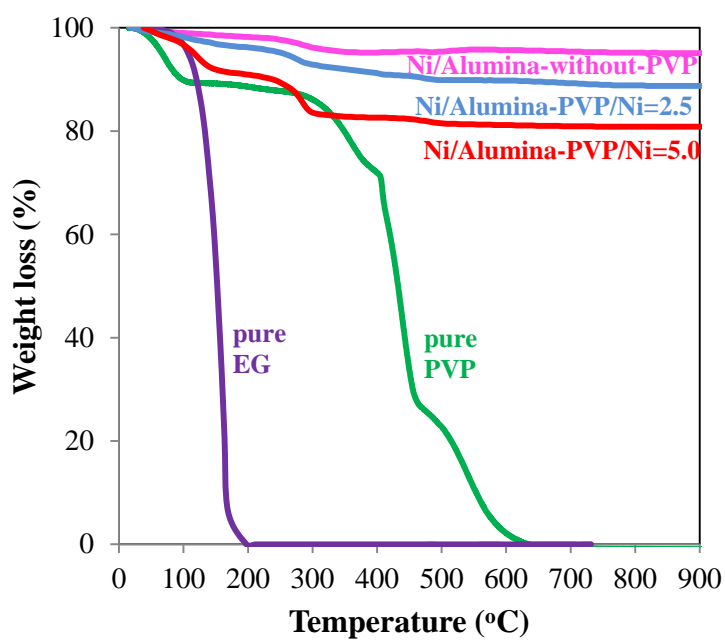


Figure 65. TG analysis of pure ethylene glycol, pure PVP and the catalysts prepared by polyol method

The derivative weight loss analysis of pure ethylene glycol, pure PVP and the catalysts prepared by polyol method is given in Figure 66, giving idea about the presence and quantity of PVP and ethylene glycol on the synthesized samples. Shifts are observed in the synthesized catalysts compared to the pure PVP and pure ethylene glycol which are attributed to the interaction between the PVP molecules and the Ni particles; between ethylene glycol molecules and the Ni particles.

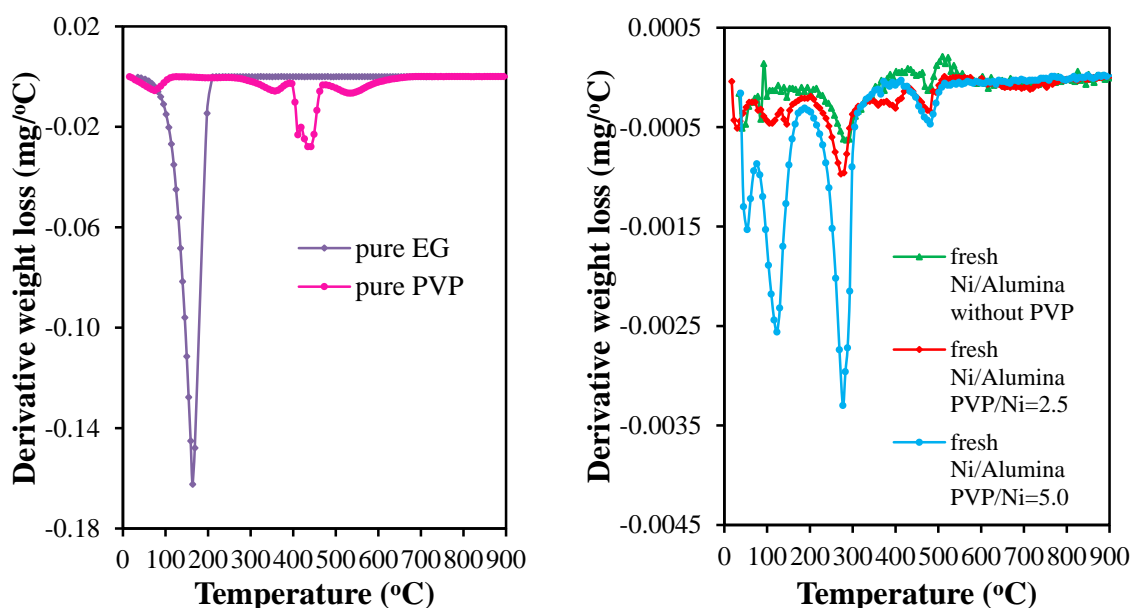


Figure 66. Derivative weight loss analysis of pure ethylene glycol, pure PVP and the catalysts prepared by polyol method

5.2.1.4 High Contrast Transmission Electron Microscopy (HCTEM)

The morphology and size of the synthesized catalysts were studied in more detail by means of high contrast transmission electron microscopy. While the size and shape of the Ni/Al₂O₃-without-PVP and Ni/Al₂O₃-PVP/Ni=2.5 are comparable to each other, the size of Ni/Al₂O₃-PVP/Ni=5.0 is smaller than these two.

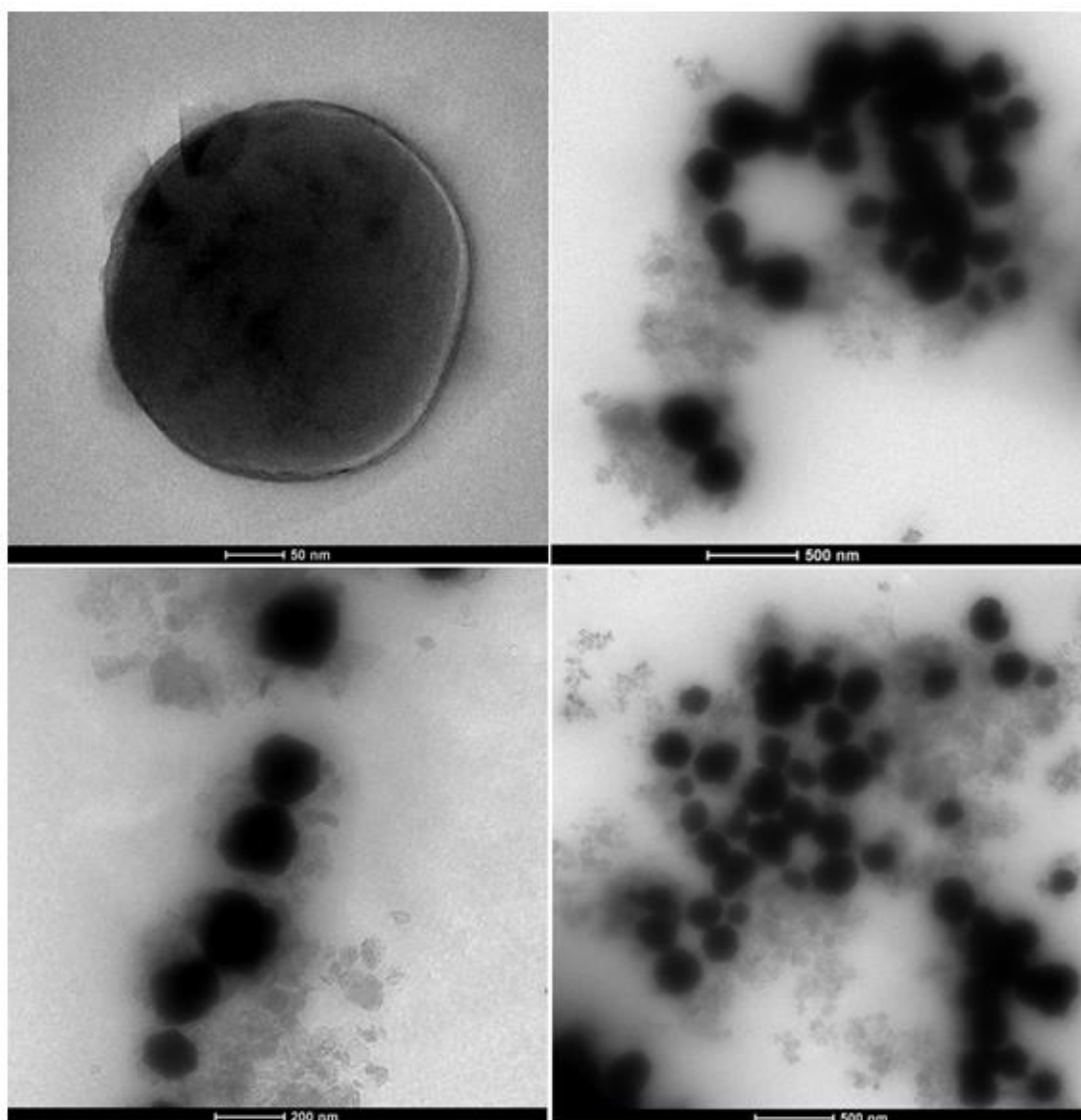


Figure 67. TEM of fresh Ni/Alumina-without-PVP catalyst

There are studies in literature concerning the effect of PVP on the particle size. Dinç et al. [123] synthesized water soluble polymer stabilized Fe^0 nanoclusters from the reduction of Fe(III) chloride by ammonia borane and sodium borohydride mixture in the presence of polyethylene glycol (PEG) as stabilizer and ethylene

glycol as solvent. They showed that increasing the amount of PEG stabilizer resulted in the formation of bigger particles embedded in the polymer matrix.

Bayrakdar et al. [117] synthesized PVP-protected Ni nanoparticles supported on γ - Al_2O_3 by polyol method in ethylene glycol environment. They observed that particle size decreased with increasing PVP/Ni ratio.

Couto et al. [113] reported that particle size decreased with increasing amount of PVP for the samples prepared according to a modified polyol route, using nickel chloride as precursor, sodium borohydride as reducing agent and PVP as protective agent. In that study, the system was maintained at 140°C for 2 hour specified time after NaBH_4 was added. On the other hand, in our study each solution was kept at the boiling point of ethylene glycol until total reduction was accomplished by observing the color change.

Chou and Huang [114] reported that with the addition of PVP to the system, the reduction of $\text{Ni}(\text{OH})_2$ to Ni metal took more time, implying that PVP molecules could interact with nickel precursors

Reduction period is another crucial parameter in tuning the size of the particles. Nik Roselina et al. [110] studied the effect of reaction time on the growth of Ni nanoparticles when all the conditions except for the reaction time were kept constant. They concluded that particle size increased significantly with prolong of the reaction time.

In our study, since increasing PVP ratio made the reduction process difficult, both PVP amount and the reduction period increased at the same time. For this reason, it is not possible to make a conclusion about the sole effect of PVP amount on the particle size.

As shown in Figure 67 and Figure 68, the Ni/ Al_2O_3 -without-PVP and Ni/ Al_2O_3 -PVP/Ni=2.5 sample consist of spherical and cubooctahedral particles the size of which range between 110-320 nm and 150-450 nm respectively.

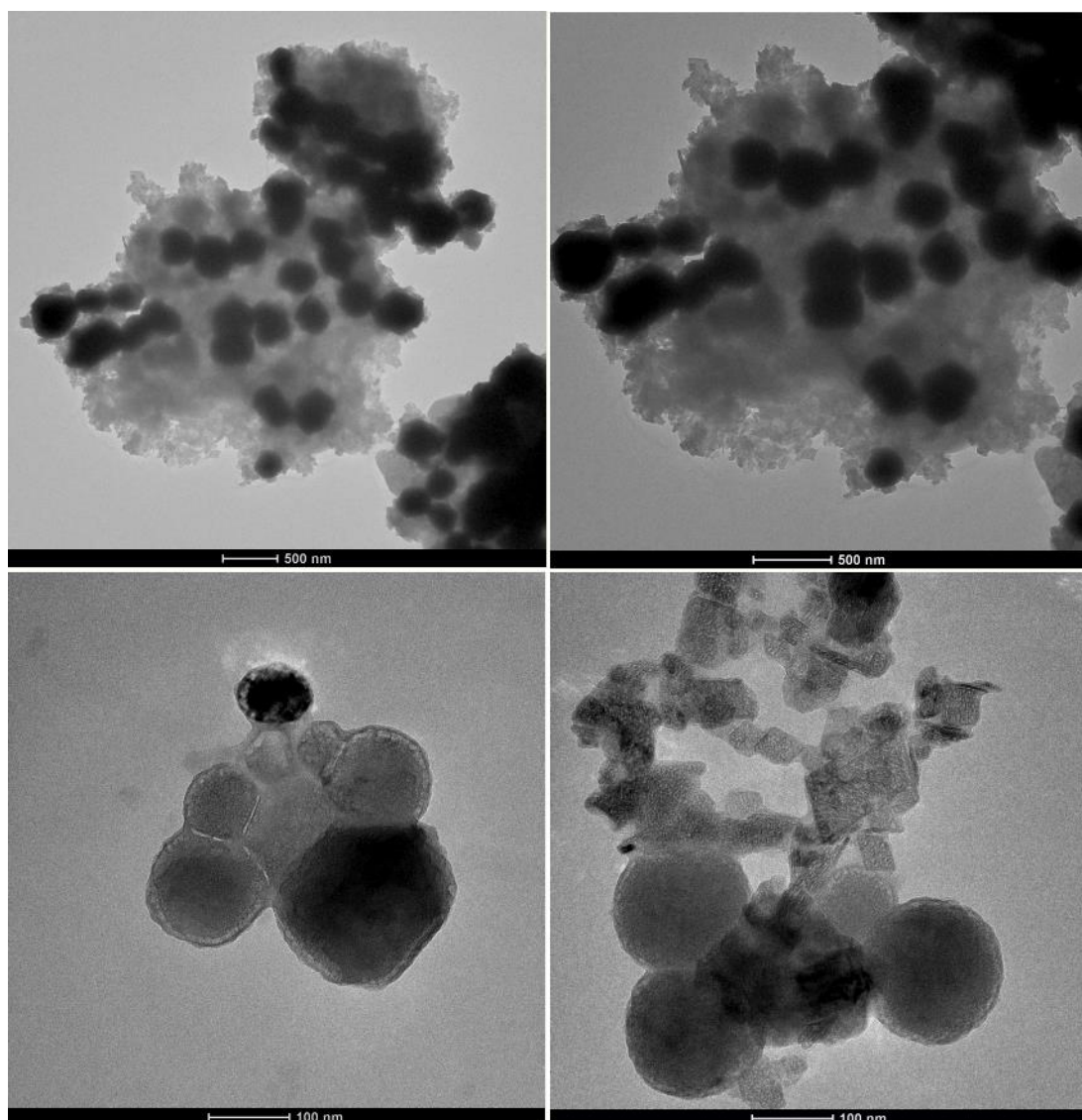


Figure 68. TEM of fresh Ni/Alumina-PVP/Ni=2.5 catalyst

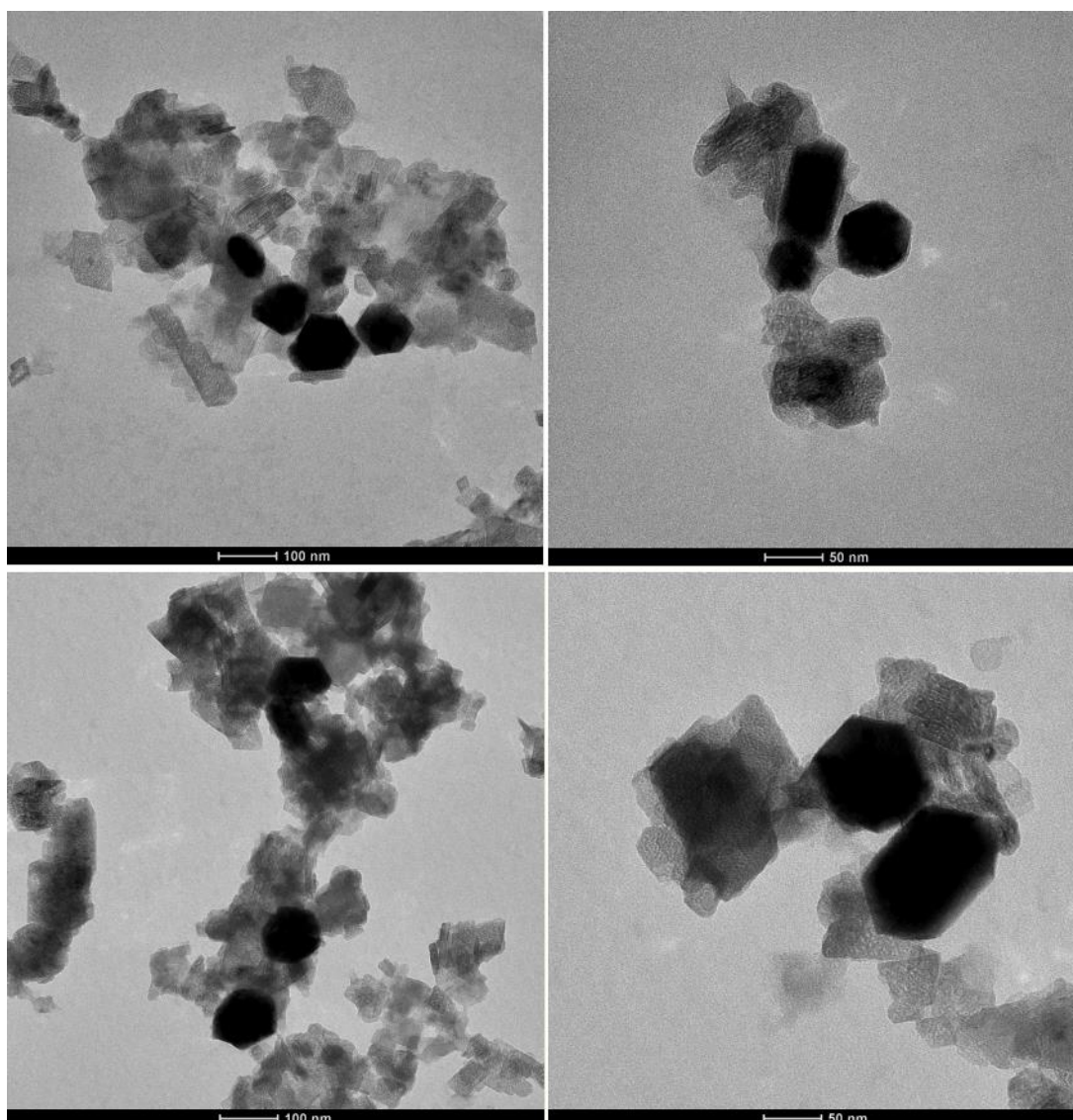


Figure 69. TEM of fresh Ni/Alumina-PVP/Ni=5.0 catalyst

The catalysts having the highest amount of PVP and longest reduction time has the smallest particle size ranging between 40-120 nm. The morphology of the products revealed that in addition to the cubooctahedral particles, Ni/Alumina-PVP/Ni=5.0 catalyst also contains rod-shaped particles (Figure 69).

5.2.2 Dry reforming reaction results

Dry reforming of methane reaction was tested over Ni/Al₂O₃-without-PVP, Ni/Al₂O₃-PVP/Ni=2.5 and Ni/Al₂O₃-PVP/Ni=5.0 without making a reduction step before the reaction. In Figure 70, comparison of time dependent CH₄ and CO₂ conversions at 700°C over the catalysts synthesized by polyol method are given. Ni/Al₂O₃-PVP/Ni=5.0 catalyst showed superior initial catalytic performance to Ni/Al₂O₃-without-PVP and Ni/Al₂O₃-PVP/Ni=2.5 catalyst. On the other hand it deactivated fastest as seen in Figure 70. The PVP polymer in high concentration may cover the particle surface and lead to a decrease in total pore volume of Ni/Alumina-PVP/Ni=5.0. As dry reforming reaction proceeds, carbon deposits and may block the pores and active sites on the surface resulting in the deactivation of the catalyst.

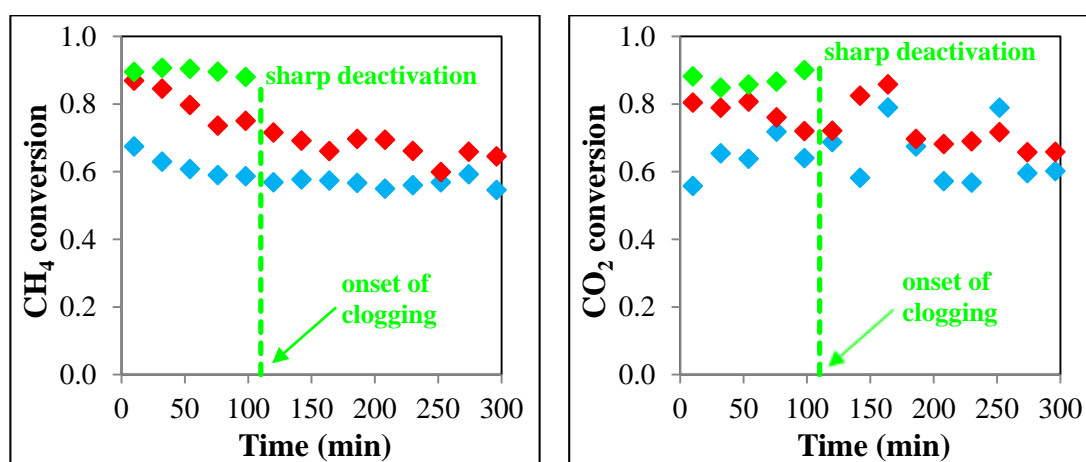


Figure 70. Comparison of CH₄ and CO₂ conversion versus time on stream over the catalysts prepared by polyol method, Ni/Al₂O₃-without PVP \blacklozenge , Ni/Al₂O₃-PVP/Ni=2.5 \blacklozenge , Ni/Al₂O₃-PVP/Ni=5.0 \blacklozenge , (Reaction conditions: 700°C, 1 atm, no reduction)

Ni/Al₂O₃-without-PVP and Ni/Al₂O₃-PVP/Ni=2.5 showed a small decrease in their activities in terms of CH₄ conversion at the initial period of reaction, but exhibited quite high performance during the whole reaction period.

The time dependent H₂ and CO yield of the catalysts during the reaction at 700°C are given in Figure 71. CO yield was higher than H₂ yield for all the catalysts due to the RWGS reaction. The H₂ and CO yield also exhibited same behaviors as in the case of conversion. Since CO yield was higher than H₂ yield, the H₂/CO ratio was lower than one for all the catalysts examined (Figure 72).

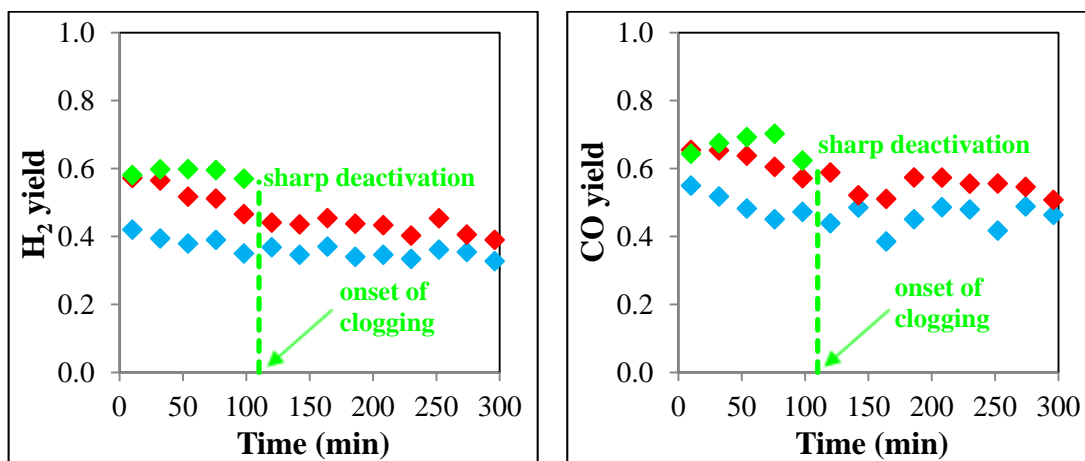


Figure 71. Comparison of H₂ and CO yield versus time on stream over the catalysts prepared by polyol method, Ni/Al₂O₃-without PVP ♦, Ni/Al₂O₃-PVP/Ni=2.5 ♦, Ni/Al₂O₃-PVP/Ni=5.0 ♦, (Reaction conditions: 700°C, 1 atm, no reduction)

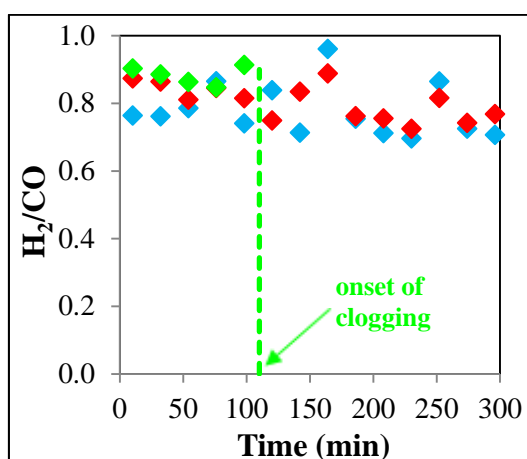


Figure 72. Comparison of H₂/CO ratio versus time on stream over the catalysts prepared by polyol method, Ni/Al₂O₃-without PVP \blacklozenge , Ni/Al₂O₃-PVP/Ni=2.5 \blacklozenge , Ni/Al₂O₃-PVP/Ni=5.0 \blacklozenge , (Reaction conditions: 700°C, 1 atm, no reduction)

As mentioned before, dry reforming of methane reaction is an endothermic reaction. The reactions were carried out also at 600°C to see the effect of temperature. The conversion of CH₄ and CO₂ decreased with a decrease in temperature, as expected (Figure 73).

One of the most striking difference between the reaction results of 600°C and 700°C was seen for Ni/Al₂O₃-PVP/Ni=5.0 catalyst. The severe deactivation of it started much earlier at 600°C reaction temperature. As mentioned before, CH₄ decomposition and CO disproportionation have been regarded as main coke deposition reactions during dry reforming of methane. Being exothermic, the equilibrium constant of CO disproportionation decreases with an increase in temperature. On the other hand, being endothermic, the equilibrium constant of CH₄ decomposition increases with an increase in temperature (Figure 4). The earlier severe deactivation of the catalyst at 600°C suggests that the main contribution to coke formation comes from CO disproportionation.

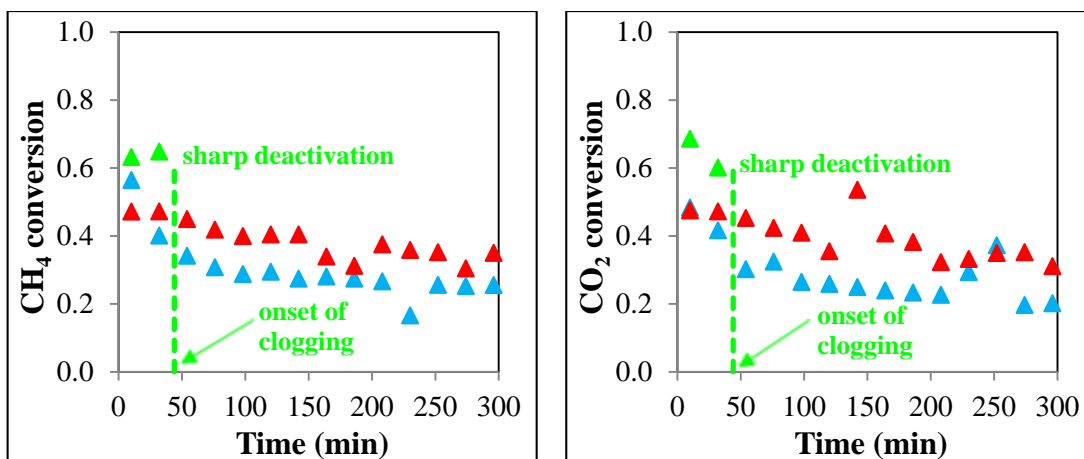


Figure 73. Comparison of CH₄ and CO₂ conversion versus time on stream over the catalysts prepared by polyol method, Ni/Al₂O₃-without PVP ▲, Ni/Al₂O₃-PVP/Ni=2.5 ▲, Ni/Al₂O₃-PVP/Ni=5.0 ▲, (Reaction conditions: 600°C, 1 atm, no reduction)

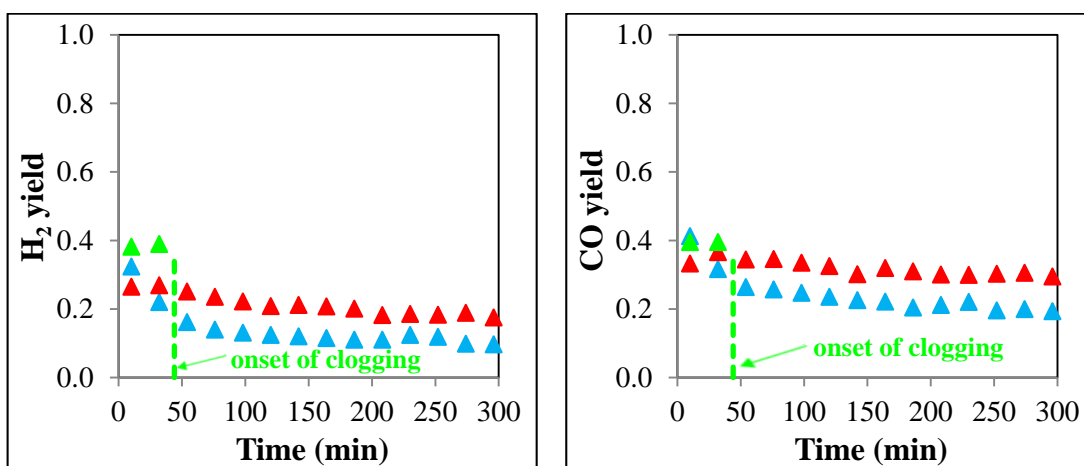


Figure 74. Comparison of H₂ and CO yield versus time on stream over the catalysts prepared by polyol method, Ni/Al₂O₃-without PVP ▲, Ni/Al₂O₃-PVP/Ni=2.5 ▲, Ni/Al₂O₃-PVP/Ni=5.0 ▲, (Reaction conditions: 600°C, 1 atm, no reduction)

H₂ yield and CO yield also decreased with decreasing temperature from 700°C to 600°C (Figure 74), as expected.

H₂/CO ratio was below one at 600°C again due to the RWGS reaction (Figure 75).

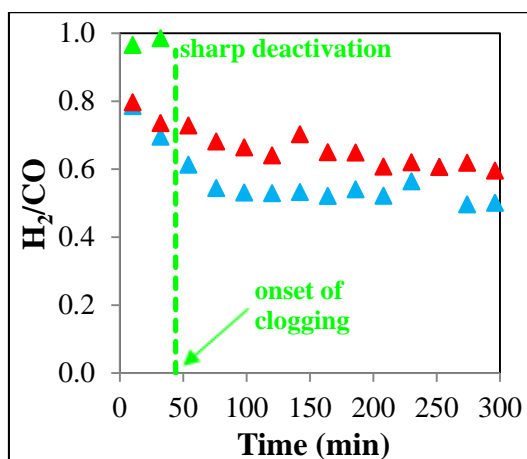


Figure 75. Comparison of time dependent H₂/CO ratio over the catalysts prepared by polyol method, Ni/Al₂O₃-without PVP ▲, Ni/Al₂O₃-PVP/Ni=2.5 ▲, Ni/Al₂O₃-PVP/Ni=5.0 ▲, (Reaction conditions: 600°C, 1 atm, no reduction)

5.2.3 Characterization of spent catalysts

5.2.3.1 Thermal Gravimetric Analysis (TGA)

Thermal analysis of the fresh and spent catalysts after five hour reaction at 600°C and 700°C is shown comparatively in Figure 76. More coke was deposited on the catalysts when the reaction was carried out at 600°C, suggesting that the major contributor to coke formation is CO disproportionation. For both Ni/Al₂O₃-without-PVP and Ni/Al₂O₃-PVP/Ni=2.5 catalysts, while the weight loss of the spent catalyst at 600°C was higher than that of the fresh one, the weight loss of the spent catalyst at 700°C was lower than that of the fresh one.

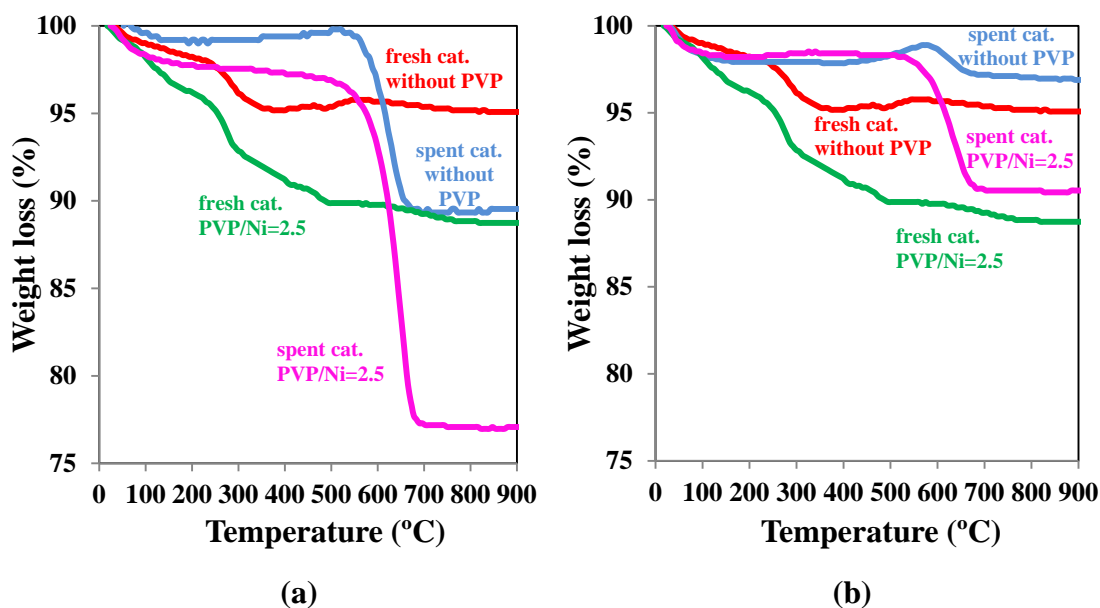


Figure 76. Comparison of weight losses between the fresh and the used polyol catalysts in the reaction at a) 600°C and b) 700°C

The comparison of derivative weight losses between the fresh and the used polyol catalysts in the reaction at 600°C and 700°C (Figure 77) shows that the weight loss of the spent catalysts comes from oxidation of carbon deposits, the peak temperature of which take place in a temperature range of 626 and 645°C. The presence of PVP makes the oxidation of carbon deposits more difficult as understood from the positive shift in the oxidation peak temperature of the spent catalyst containing PVP compared to the ones without PVP (Figure 77-b).

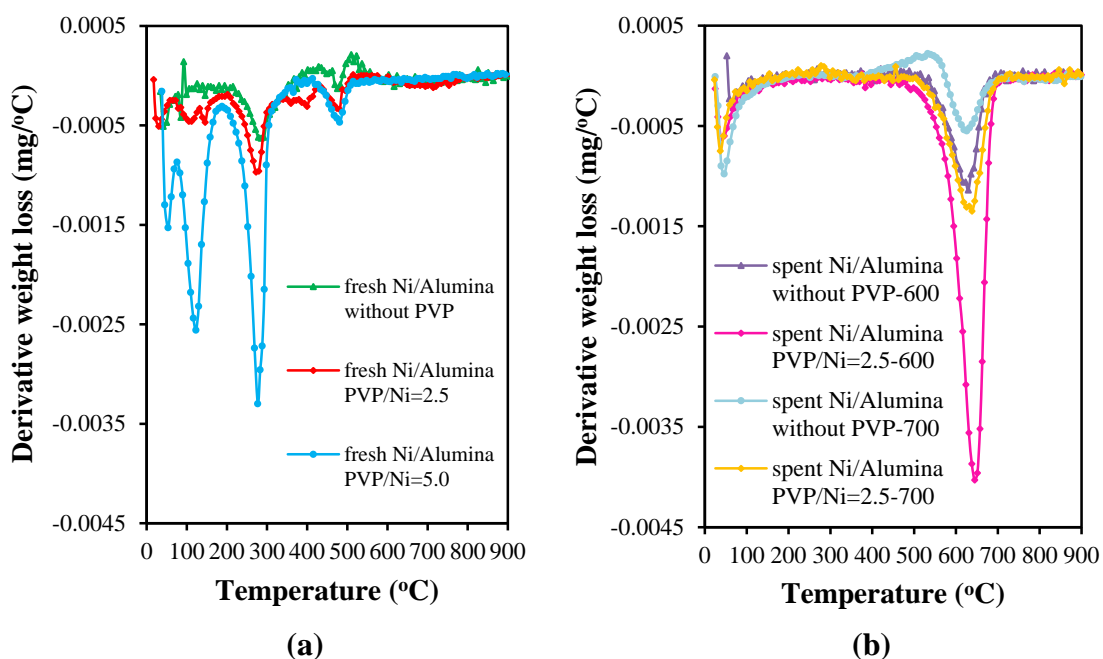


Figure 77. Comparison of derivative weight losses between the fresh and the used polyol catalysts in the reaction at 600°C and 700°C

5.2.3.2 High Contrast Transmission Electron Microscopy (HCTEM)

The TEM images of spent Ni/Al₂O₃-without PVP and Ni/Al₂O₃-PVP/Ni=2.5 catalysts after five hour reaction at 600°C show abundant filamentous carbon growing with varying dimensions (Figure 78 and 79). In addition to carbon nanotubes and carbon nanofibers having hollow structure, there are some fibers which do not have hollow inside them.

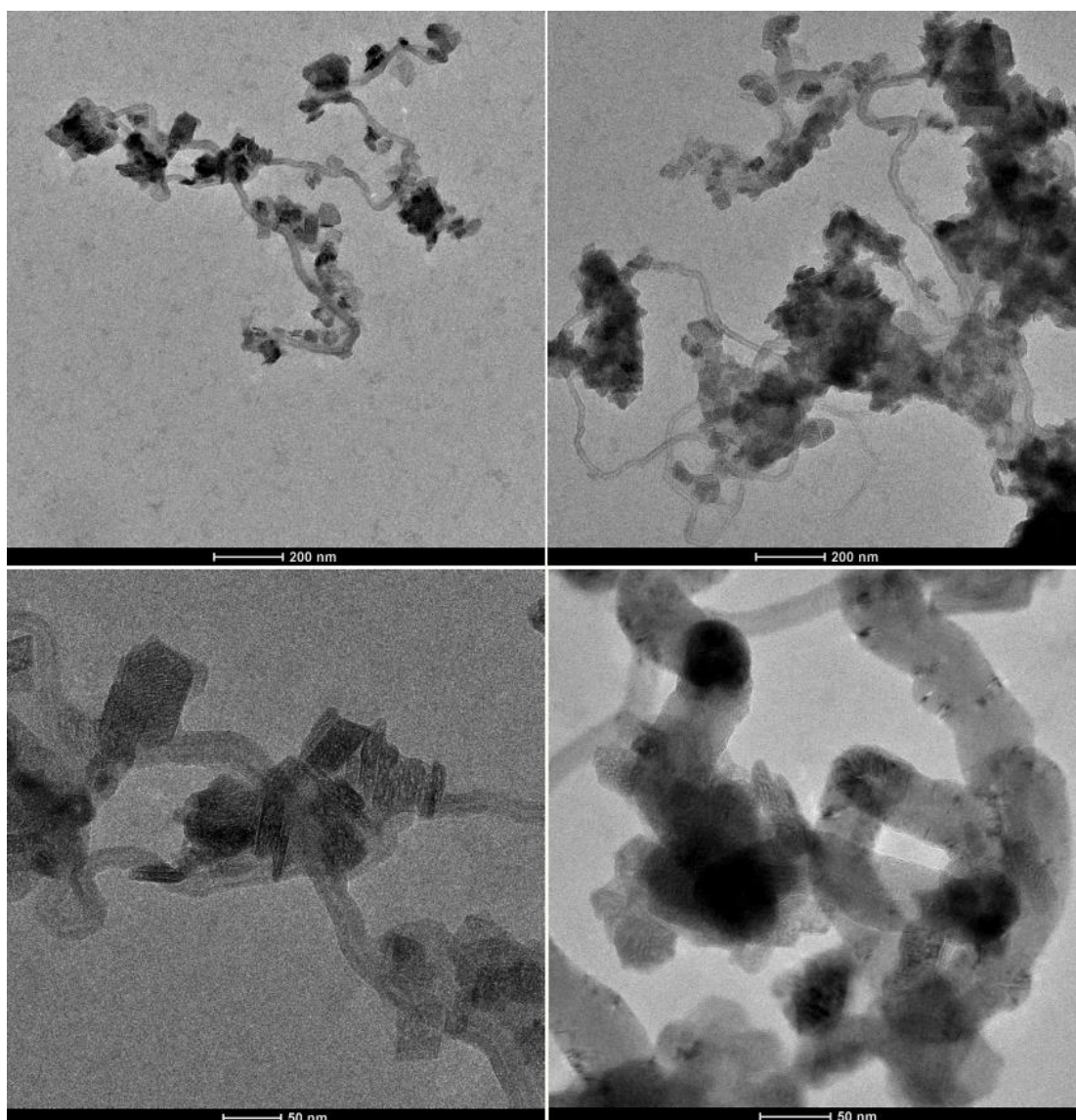


Figure 78. HCTEM of Ni/Al₂O₃-without PVP catalyst after being used in reaction at 600°C for 5 hours

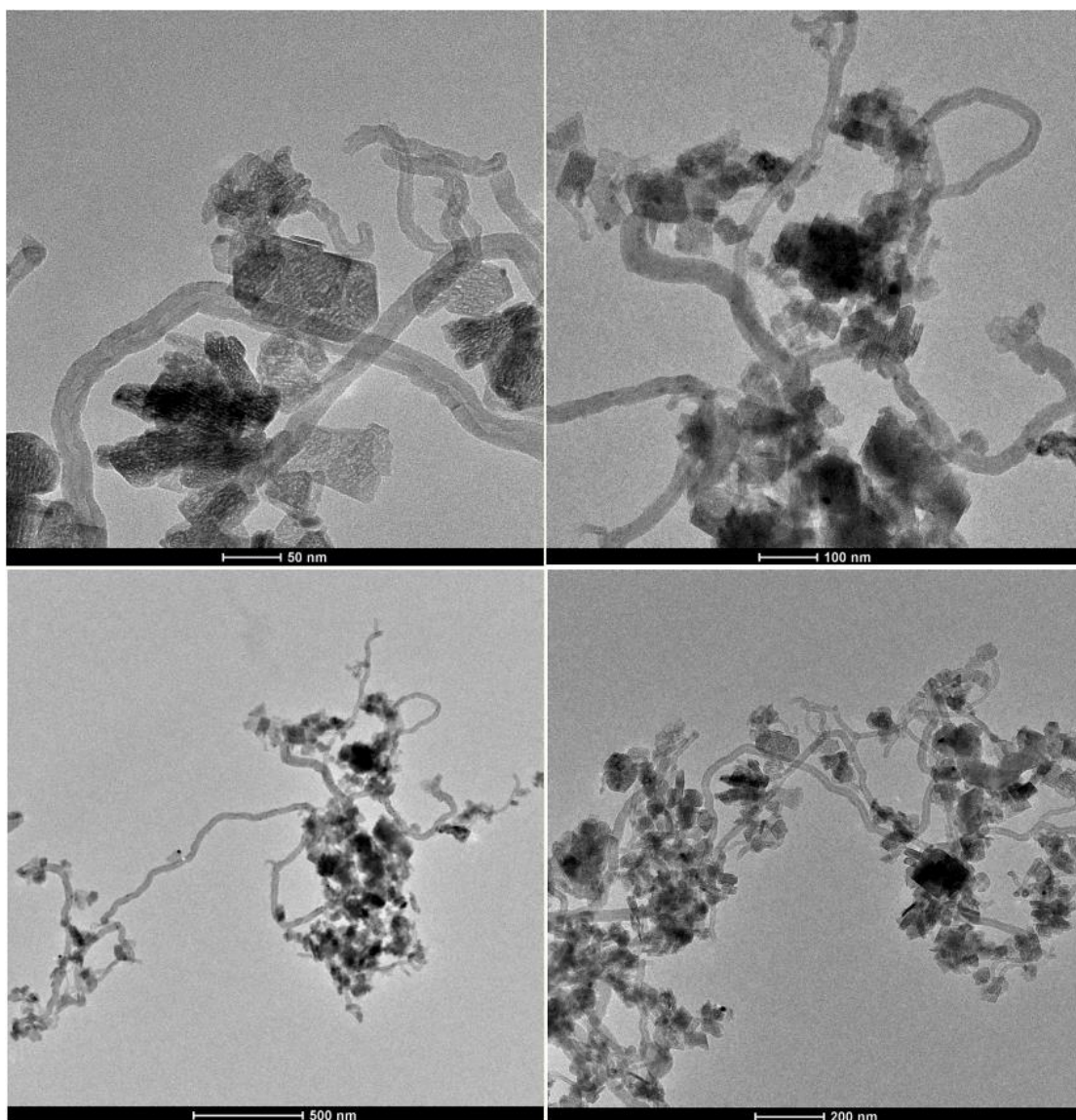


Figure 79. HCTEM of Ni/Al₂O₃-PVP/Ni=2.5 catalyst after being used in reaction at 600°C for 5 hours

5.3 Conclusions

Polyol process was employed to obtain 10 wt % (nominal) Ni/Al₂O₃ catalysts in the presence of PVP (polyvinylpyrrolidone) as stabilizer and ethylene glycol as both solvent and reducing agent. Samples with varying PVP/Ni ratios were obtained. The as-prepared products were characterized by XRD, TEM, BET and TGA. The activities of the catalysts were evaluated for carbon dioxide reforming of methane.

X-ray diffraction patterns of the synthesized catalysts showed the formation of metallic Ni as long as alkaline condition was provided regardless of the PVP amount used. XRD pattern exhibited four characteristic peaks at 44.6°, 51.8°, 76.4° and 93.1° corresponding to (111), (200), (220) and (311) Miller index planes of fcc nickel.

Dry reforming of methane reaction was carried at 600°C and 700°C without making a reduction step before the reaction. Ni/Al₂O₃-PVP/Ni=5.0 catalyst showed superior initial catalytic performance to Ni/Al₂O₃-without-PVP and Ni/Al₂O₃-PVP/Ni=2.5 catalyst. On the other hand it deactivated fastest, which was attributed to the highest PVP content of it. Ni/Al₂O₃-without-PVP and Ni/Al₂O₃-PVP/Ni=2.5 showed a small decrease in their activities at the initial period of reaction, but exhibited quite high performance during the whole reaction period.

The TEM images of spent Ni/Al₂O₃-without-PVP and Ni/Al₂O₃-PVP/Ni=2.5 catalysts after five hour reaction at 600°C show abundant filamentous carbon growing with varying dimensions. In addition to carbon nanotubes and carbon nanofibers having hollow structure, there are some fibers which do not have hollow inside them.

CHAPTER 6

DRY REFORMING OF METHANE ON CeO₂ SUPPORTED Ni, Co and Ni-Co CATALYSTS PREPARED BY INCIPIENT WETNESS IMPREGNATION METHOD

6.1 Introduction

CeO₂ has mostly been used as an additive promoter on Ni/Al₂O₃ catalysts in dry reforming of methane reaction. These catalyst were found to provide considerably higher catalytic activity and resistance to carbon formation compared to the conventional Ni/Al₂O₃ [62,124-126]. These improvements are mainly due to the redox property of ceria [127]. While it is able to release oxygen under oxygen deficient medium, it can rapidly reoxidize under oxygen abundant medium [128].

Under dry reforming of methane conditions, the catalytic behavior of ceria is the result of a complex series of surface reactions [1 and references therein]. CO₂ adsorption and activation occurs on Ce³⁺ sites with formation of CO followed by oxidation of Ce³⁺ to Ce⁴⁺, while the presence of bulk oxygen vacancies creates additional driving force for the reduction of CO₂ to CO [129]. Furthermore, ceria has the ability of chemisorbing huge amounts of H₂ to CO where the quantity depends on physicochemical properties and thermal treatment conditions [1 and references therein]. “In general, the redox properties of CeO₂ are very sensitive to the textural, structural, and morphological properties of the catalytic system, brought about by the preparation method, the presence of metals or metal oxide additives and the pretreatment.” [1 and references therein]

The following reactions between ceria and feed are probable during dry reforming of methane process [130].



As mentioned before, carbon can be formed due to the decomposition of CH_4 and CO disproportionation. Being a lattice oxygen supplier, CeO_2 might oxidize the solid carbon as in the following reaction [130].



The presence of CeO_2 can cause oxidation of Ni according to the below reaction.



To investigate the probability of the above reactions, standard Gibbs-free energy changes (ΔG°) were calculated and shown in Figure 80 as a function of temperature.

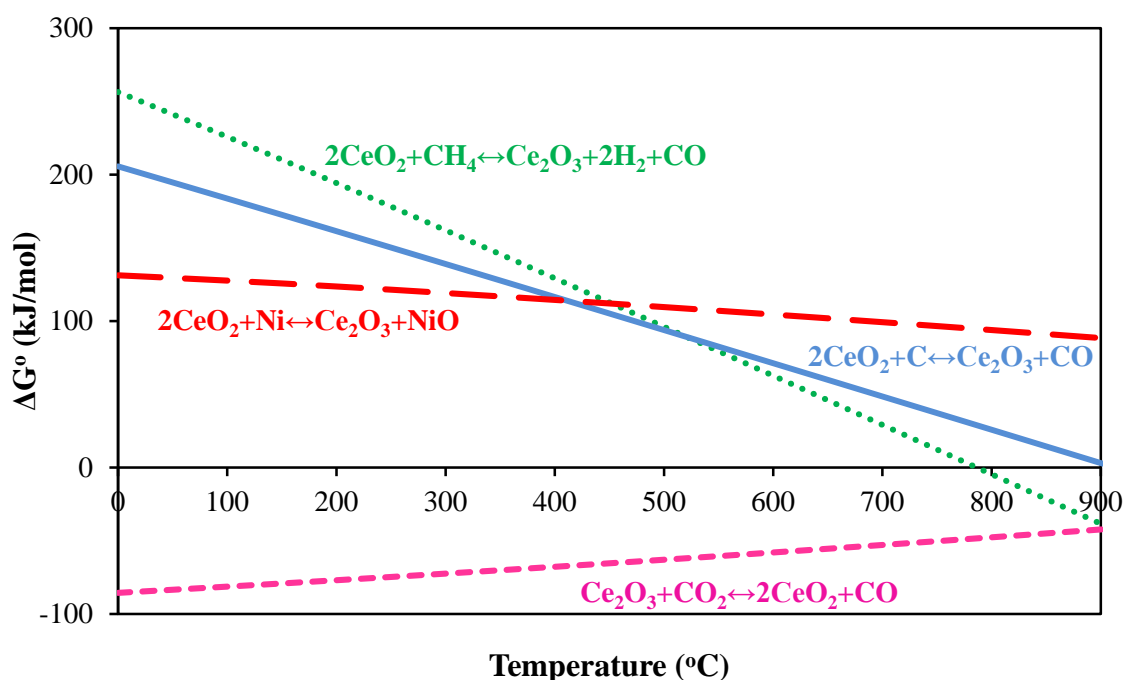


Figure 80. Standard Gibbs free energy as a function of temperature for CeO_2 based nickel catalyst

Since the gasification of solid carbon is thermodynamically favorable at temperatures higher than 900°C, the existence of CeO₂ can suppress carbon formation throughout dry reforming process. Furthermore, it is not probable that CeO₂ oxidizes Ni to NiO which is less active than Ni species. On the other hand, Ce₂O₃ probably reduces NiO to Ni, keeping Ni active for dry reforming of methane [130].

Pure ceria was shown to be a promising candidate for CO₂ reforming of CH₄ due to its resistance to deactivation [131]. While methane conversion was approximately 15 % for low surface area ceria (55 m²/g), it was about 30 % for high surface area ceria (105 m²/g) at 900°C reaction temperature. The utilization of high surface area ceria importantly decreased the extent of deactivation by thermal sintering when compared to low surface area ceria.

Wang and Lu [132] tested nickel catalysts which were supported on γ -Al₂O₃, CeO₂ and CeO₂+Al₂O for carbon dioxide reforming of methane. Ni/CeO₂ exhibited considerably different catalytic behaviour from Ni/Al₂O₃ at 500-800°C temperature range. While CH₄ conversion of CeO₂ supported catalyst was higher than that of Al₂O₃ supported catalyst before 600°C, opposite behavior was observed after 600°C. Using CeO₂ as a support for nickel catalysts caused a strong metal-support interaction, which decreased the catalytic activity and carbon deposition. Nevertheless, adding CeO₂ into Ni/ γ -Al₂O₃ catalyst increased catalytic activity and stability and also inhibited coke formation. Because CeO₂ improved the dispersion of nickel and the reactivities of carbon deposits

Asami et al. [133] examined CO₂ reforming of CH₄ over nickel, cobalt, and iron catalysts supported on cerium oxide. Ni/CeO₂ was the most effective catalyst with 95% methane conversion at 850°C. Co/CeO₂ showed an activity approximately equal to that of Ni/CeO₂ when reduced sufficient enough, whereas Fe/CeO₂ exhibited a poor performance. Although being highly active at 850°C, Ni/CeO₂

deactivated rapidly at low temperature of 700°C. They found that high temperature heat treatment played a key role in attaining high activity. Even though the influence of high temperature treatment was not yet clear, the intimate contact between nickel and CeO₂ or the variation in the number of the active sites was proposed to be the probable reasons of high activity.

Gonzalez-Delacruz et al. [134] prepared Ni–CeO₂ catalysts, in a wide range of nickel loadings (7–26%) by using combustion synthesis method for dry reforming of methane. This new synthesis method was shown to be an easy, efficient and trusty way of preparing catalysts with a narrow size distribution and homogeneous dispersion over the support. The reducer/oxidizer ratio was shown to affect the number of nickel particles and hence activity. Higher activities were obtained with decreasing ratios of this parameter. Even though the catalyst preserved its activity and stability even after more than two weeks, severe coke formation in the form of narrow and long nano-fibers was observed.

Odedairo et al. [135] prepared ceria supported nickel particles under microwave plasma. A totally different material was obtained under microwave plasma compared with the catalyst synthesized using conventional thermal calcinations. The HRTEM images of the plasma treated sample revealed that the majority of the nickel particles were arranged in an orderly way on support surface and not within the support, resulting in a clean metal–support interface. On the other hand, the HRTEM images of the ceria sample prepared by conventional thermal method exhibited that nickel particles were dispersed within the ceria support. The sample treated with plasma displayed higher activity and excellent stability than the thermally calcined catalyst in CO₂ reforming of CH₄ reaction. The clean metal–support interface created by the microwave plasma treatment was reported to be the reason of higher catalytic activity and very good stability.

Wang et al. [136] studied CO₂ reforming of CH₄ over novel fibrous NiO/CeO₂ catalysts to find out the effects of NiO content, crystallization temperature and gas flow rate on coke formation. The influence of crystallization temperature and NiO content could be ascribed to its effect on the interaction between the CeO₂ support and NiO which importantly determined coke formation over the fibrous samples during CO₂ reforming of CH₄. As the interaction became stronger, the amount of carbon formation became lower. When the gas flow rate was increased, coke formation rate was reduced by a large amount which was ascribed to the enhanced radical desorption and low conversion of CH₄ at high gas flow rates.

Du et al. [137] studied the morphology dependence of Ni/CeO₂ nanomaterials for dry reforming of methane reaction. Ni/CeO₂ nanorods exhibited much better catalytic activity and coking resistance compared with Ni/CeO₂ nanopolyhedras. The predominately exposed planes were the extraordinary reactive {110} and {100} planes in the CeO₂ nanorods rather than the stable {111} plane in the CeO₂ nanopolyhedra. The {110} and {100} planes exhibited big supremacy for anchoring the nickel nanoparticles resulting in the presence of strong metal–support interaction effect. This effect could be useful to inhibit the sintering of nickel particles benefiting to decrease the deactivation of the catalyst.

Luisetto et al. [138] prepared Ni/CeO₂, Co/CeO₂ and Co-Ni/CeO₂ by surfactant assisted co-precipitation method for CO₂ reforming of CH₄ in the temperature range of 600-800°C. The bimetallic catalyst exhibited higher CH₄ conversion in comparison with the monometallic catalysts in the whole temperature range. While H₂/CO selectivity was highest for Co-Ni/CeO₂, it was lowest for Co/CeO₂. They suggested that catalytic activity was mainly related to an intrinsic feature of the cobalt-nickel alloy. Carbon deposition resistance of Co-Ni/CeO₂ and Co/CeO₂ was substantially higher than that of Ni/CeO₂.

As understood from the above literature survey, there are some studies over CeO₂ supported Ni for dry reforming of methane. On the other hand, CeO₂ supported Co and Ni-Co catalysts have not been investigated in detail. In this part, a comprehensive study on the role of cerium oxide as a support in Ni/CeO₂, Co/CeO₂ and Ni-Co/CeO₂ was conducted for dry reforming of methane. In order to see the effect of calcination temperature, the catalysts were calcined at 700°C and 900°C.

6.2 Results and Discussion

6.2.1 Characterization of fresh catalysts

6.2.1.1 X-Ray Diffraction (XRD) Analysis

XRD was used for the identification of bulk phase feature of the catalysts. Figure 81 and 82 shows the XRD patterns of the ceria-based catalysts calcined at 700 and 900°C, respectively. The pure ceria and the ceria supported catalysts contain CeO₂ fluorite structure (JCPDS 34-0394), corresponding to the (111), (200), (220), (311), (222) and 400) planes. As can be seen, with the increasing temperature from 700 to 900°C, a remarkable increase in the intensity of the lines due to better crystallization of CeO₂ could be noted.

Ni/CeO₂-I-700 and Ni/CeO₂-I-900 exhibit NiO, corresponding to (111), (200) and (220) planes. Co/CeO₂-I-700 and Co/CeO₂-I-900 exhibit the diffraction peaks of Co₃O₄, corresponding to (311), (400) and (440) planes.

Ni-Co/CeO₂-I-700 and Ni-Co/CeO₂-I-900 show a diffraction peak in 37-38° region between NiO (111) and Co₃O₄ (311), suggesting the formation of a nickel-cobalt alloy.

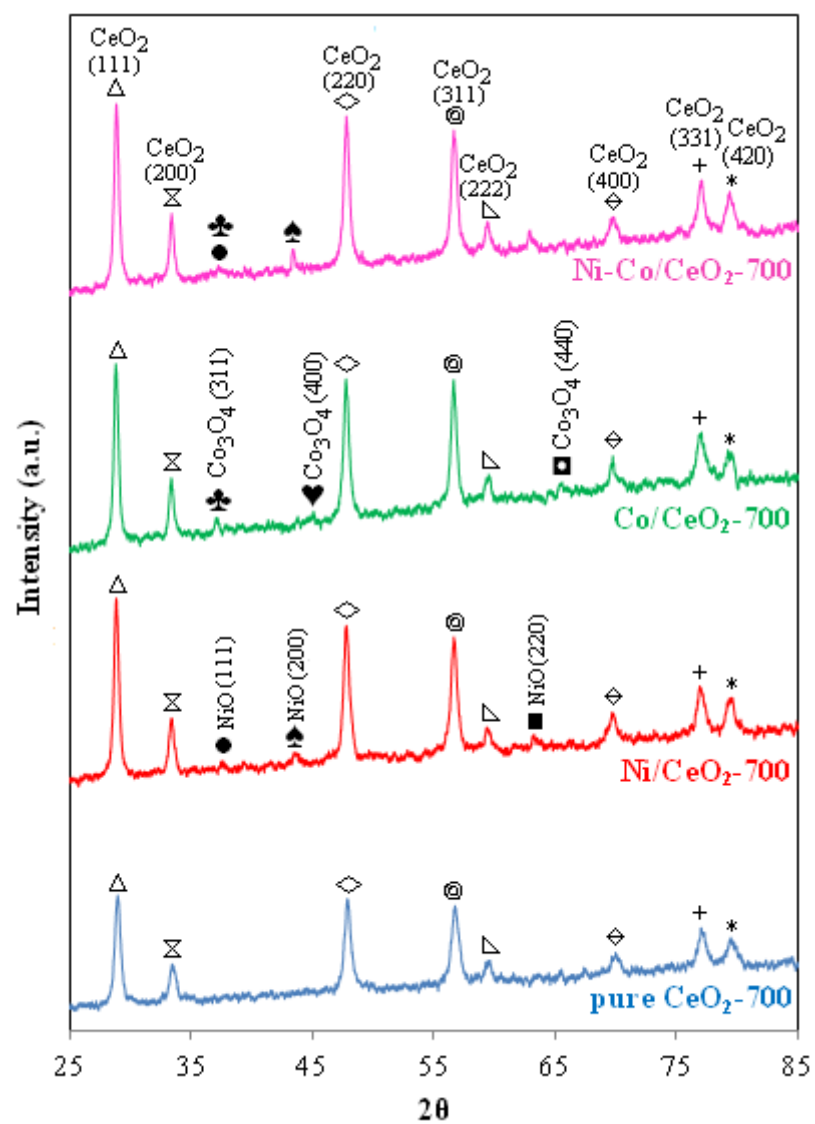


Figure 81. XRD pattern of pure CeO₂, Ni/CeO₂, Co/CeO₂ and Ni-Co/CeO₂ calcined at 700°C

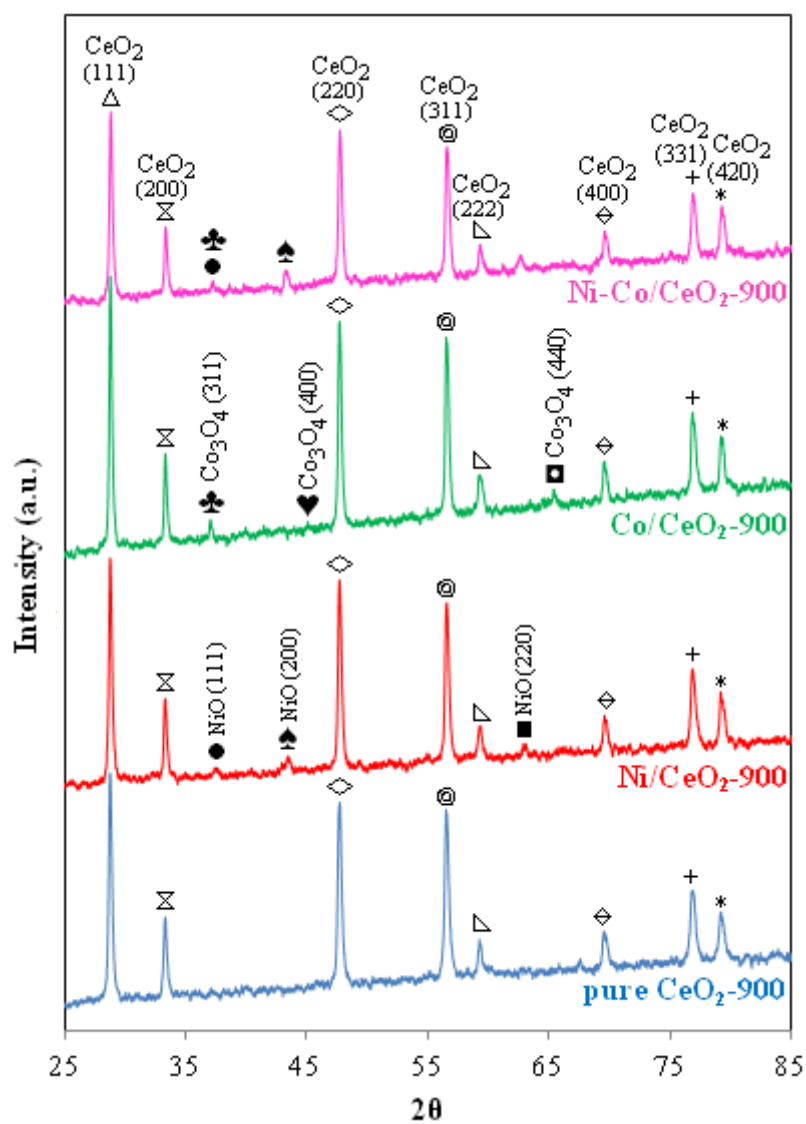


Figure 82. XRD pattern of pure CeO₂, Ni/CeO₂, Co/CeO₂ and Ni-Co/CeO₂ calcined at 900°C

6.2.1.2 Surface Area, Pore Size Distribution and Adsorption-Desorption Isotherms

Textural properties of the samples calcined at 700°C and 900°C are given in Table 11 and 12 respectively.

Table 11. Textural properties of pure CeO₂, Ni/CeO₂, Co/CeO₂ and Ni-Co/CeO₂ calcined at 700°C

Catalyst	BET Surface area (m ² /g)	Pore volume (cm ³ /g)	Average pore diameter (nm)
Pure CeO ₂ calc. at 700°C	40.47	0.16	13.49
Ni/CeO ₂	23.78	0.12	17.35
Co/CeO ₂	18.92	0.10	17.80
Ni-Co/CeO ₂	18.27	0.10	20.31

Table 12. Textural properties of pure CeO₂, Ni/CeO₂, Co/CeO₂ and Ni-Co/CeO₂ calcined at 900°C

Catalyst	BET Surface area (m ² /g)	Pore volume (cm ³ /g)	Average pore diameter (nm)
Pure CeO ₂ calc. at 900°C	14.41	0.09	19.74
Ni/CeO ₂	7.86	0.04	19.77
Co/CeO ₂	4.32	0.02	14.77
Ni-Co/CeO ₂	5.76	0.02	16.62

As it was remembered pure CeO₂ support was obtained by calcination of Ce(C₂H₃O₂).1.5H₂O at 700°C as well as 900°C for 3 hours. The surface area of the CeO₂ obtained by calcination cerium acetate at 900°C was much lower than the one obtained by calcination of cerium acetate at 900°C. Thermal treatment at higher temperature brings about gradual sintering and crystallite growth resulting in the loss of surface area [139]. When Ni, Co or Ni-Co was added to the support, the surface area and the total pore volume decreased significantly.

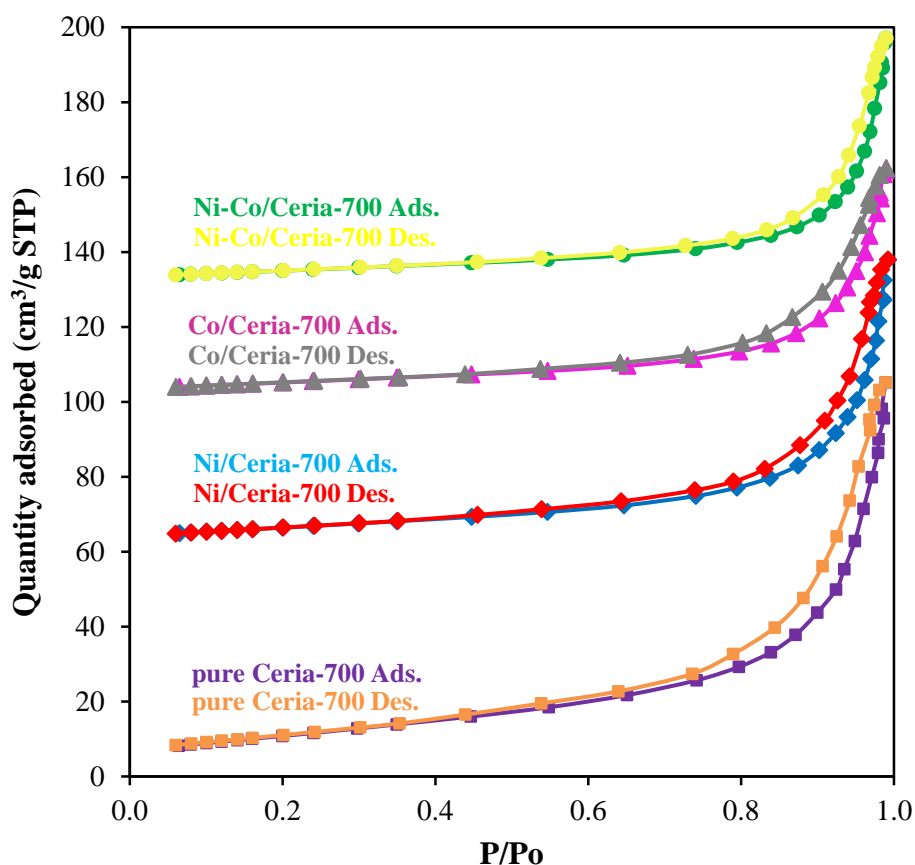


Figure 83. Nitrogen adsorption-desorption isotherms of pure CeO₂, Ni/CeO₂, Co/CeO₂ and Ni-Co/CeO₂ calcined at 700°C

The N₂ adsorption/desorption isotherm of the samples calcined at 700°C and 900°C are given in Figure 83 and 84 respectively. According to the IUPAC classification all samples exhibited type II adsorption isotherm which is characteristic of macroporous materials and the H3-shape hysteresis loops show the presence of mesopores [79]. Pore size distribution of the samples exhibits that they are mainly composed of macropores (pore diameter > 50 nm in diameter) in addition to the mesopores (2 nm < pore diameter < 50 nm) (Figure 85 and Figure 86).

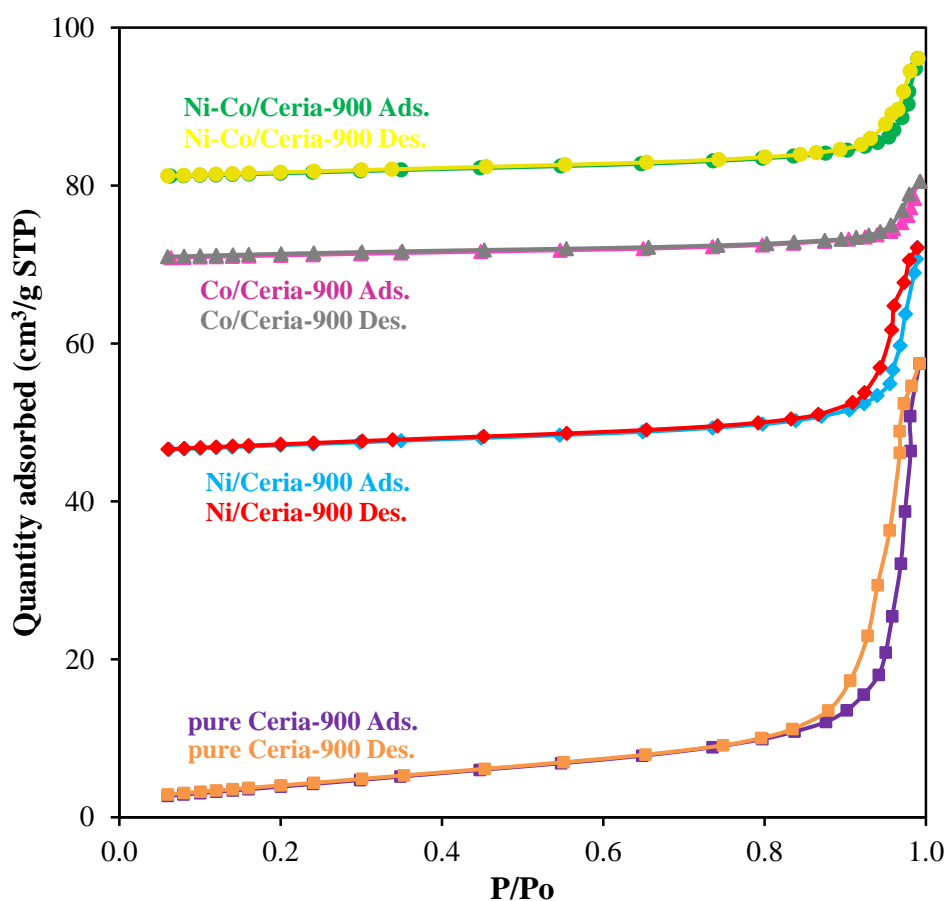


Figure 84. Nitrogen adsorption-desorption isotherms of pure CeO₂, Ni/CeO₂, Co/CeO₂ and Ni-Co/CeO₂ calcined at 900°C

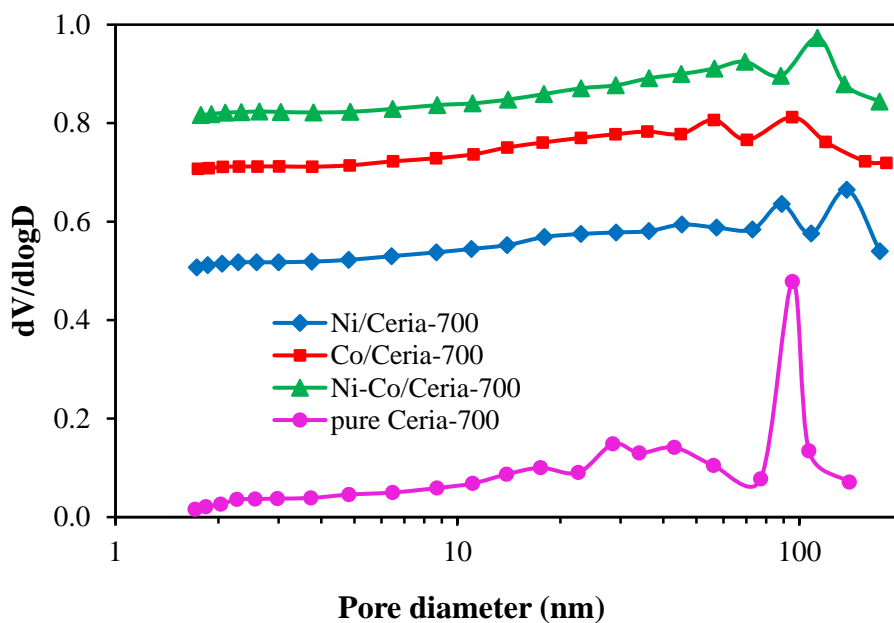


Figure 85. BJH pore size distribution of pure CeO₂, Ni/CeO₂, Co/CeO₂ and Ni-Co/CeO₂ calcined at 700°C

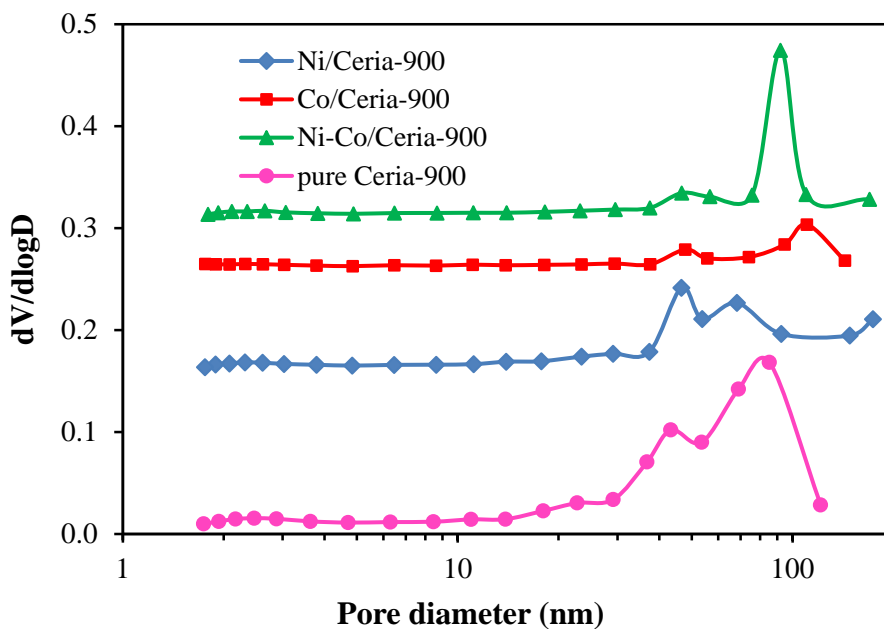


Figure 86. BJH pore size distribution of pure CeO₂, Ni/CeO₂, Co/CeO₂ and Ni-Co/CeO₂ calcined at 900°C

6.2.1.3 Temperature Programmed Reduction (TPR) Analysis

The reducibility of the samples was investigated by TPR. Pure CeO₂ showed a broad Ce⁴⁺ → Ce³⁺ reduction peak with a maximum at 450°C attributed to the surface reduction. The second reduction peak with a maximum at 812°C was ascribed to the bulk reduction [140,141] (Figure 87).

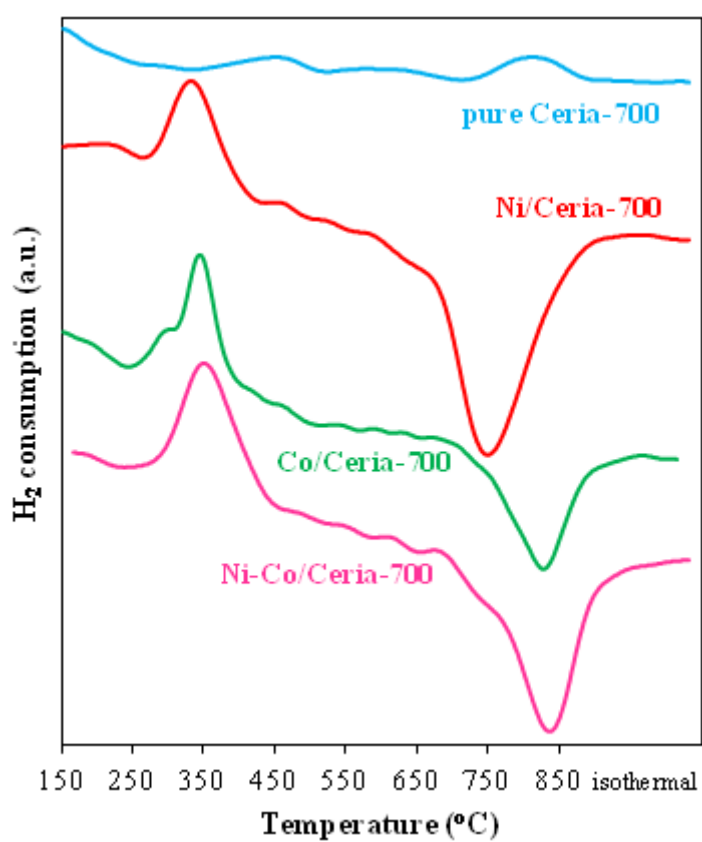


Figure 87. TPR profiles of pure CeO₂, Ni/CeO₂, Co/CeO₂ and Ni-Co/CeO₂ calcined at 700°C

The reduction of CeO₂ happens by means of direct dissociative chemisorption of H₂ on surface site resulting in the formation of H₂O via hydroxyl groups followed by the formation of surface oxygen vacancies and reduction of Ce⁴⁺ to Ce³⁺. This can be shown as [141]



where \square is a surface oxygen vacancy. The diffusion of surface anion vacancies into the bulk ceria happens at comparatively high temperatures making a contribution to slow bulk reduction [141].

The first peak for the metal loaded samples corresponded to the reduction of metal oxides. There was only one peak for bimetallic catalyst, suggesting the formation of nickel-cobalt alloy. The ease of reducibility was in the order of Ni/CeO₂ < Co/CeO₂ < Ni-Co/CeO₂ for the catalysts calcined at 700°C. While there was only one peak for NiO reduction, there was a two-step reduction process for Co₃O₄ which was attributed to Co₃O₄ → CoO → Co⁰.

The most striking results seen in the TPR profiles of CeO₂ supported catalysts calcined at 700°C was the negative peak.

Laachir et al. [142] observed a negative peak in the hydrogen TPR of ceria sample which was obtained by calcination of CeO₂ (Rhône Poulenc) at 400°C. Prior to reduction, the sample was standardised for 1 h at 400°C under oxygen flow and then treated for 1 hour at the same temperature either under vacuum or rare gas before cooling to room temperature. They attributed the negative peak at 617°C to the release of CO which could originate from the reduction of carbonates existing in the bulk of the ceria and not removed by the standardisation process at 400°C.

Rogemond et al. [143] also observed negative peaks in the hydrogen TPR profiles of pure CeO₂, Rh/CeO₂, Pt/CeO₂ and Rh-Pt/CeO₂ obtained after calcination at 500°C. They concluded that the negative peak could be ascribed to the evolution of H₂, CO, and CO₂ in the gas phase, originating from the desorption of hydrogen stored by the solid (metal and reduced ceria) and from the reduction or decomposition of

carbonate species existing in the bulk ceria and not removed in the course of the pretreatment.

By taking into consideration the above studies, the negative peak might be attributed to the desorption of fixed hydrogen by the solid during TPR.

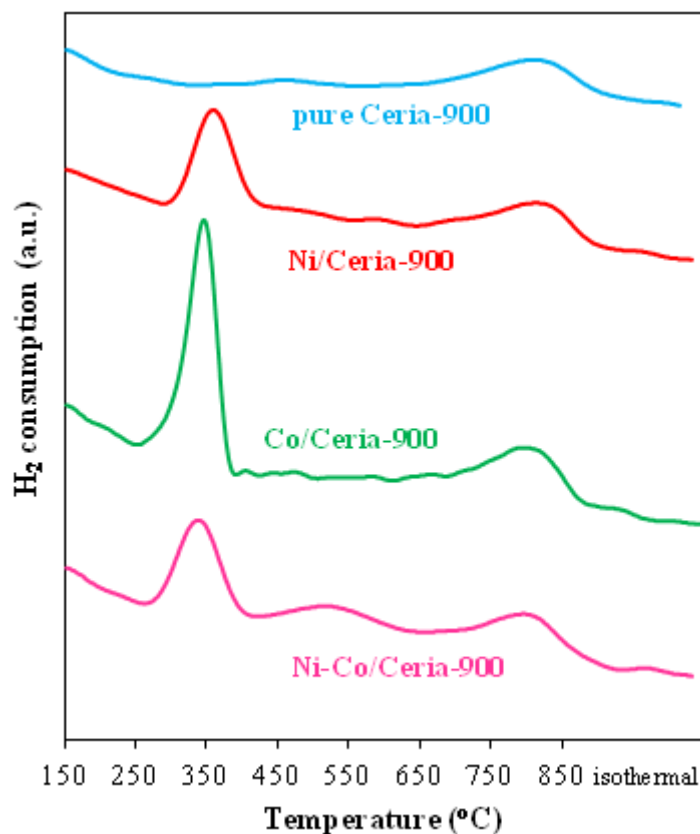


Figure 88. TPR profiles of pure CeO₂, Ni/CeO₂, Co/CeO₂ and Ni-Co/CeO₂ calcined at 900°C

The TPR profiles of the samples calcined at 900°C are given in Figure 88. The first peak at about 350°C was again ascribed to the reduction of metal oxides, the ease of which was in the order of Ni-Co/CeO₂ < Co/CeO₂ < Ni/CeO₂. The second broad peak, the peak temperature of which was around 800°C, was attributed to the reduction of bulk ceria.

The reducibility order was different for the catalysts calcined at 700°C and 900°C. While Ni catalyst was reduced easiest at 700°C calcination temperature, its reduction was most difficult at 900°C calcination temperature. Similarly, while the reduction of Ni-Co bimetallic catalyst was achieved at the lowest temperature when the calcination was carried out at 900°C, its reduction peak was observed at the highest temperature when the calcination was carried out at 700°C. These results made us to conclude that the interaction of the metals with ceria changed with calcination temperature.

6.2.2 Dry reforming reaction results

The time dependent CH₄ and CO₂ conversion over the catalysts calcined at 700°C are given in Figure 89. While Ni/CeO₂-I-700-pellet and Ni-Co/CeO₂-I-700-pellet provided comparable high activities, Co/CeO₂-I-700-pellet exhibited very low performance. Although showing a slight decrease in activity in the first period of reaction, Ni/CeO₂-I-700-pellet and Ni-Co/CeO₂-I-700-pellet preserved their performance up to the end of the reaction. Wang and Lu [132] reported that an initial quick (non-linear) deactivation took place over Ni/CeO₂ catalyst at 700°C. After five hour a linear deactivation rate was seen. Asami et al. [133] also observed such deactivation at that temperature. In their work, the initial conversion of CH₄ at 700°C was only 30%, and it fell rapidly to only several percentage points for 2–3 hour. We also observed such an initial deactivation in the CH₄ and CO₂ conversions at 700°C reaction temperature (Figure 89), but not that much severe.

The time dependent H₂ and CO yield of the catalysts calcined at 700°C are given in Figure 90. CO yield was higher than H₂ yield for all the catalysts due to the occurrence of the RWGS reaction. Since CO yield was higher than H₂ yield, the H₂/CO ratio was lower than 1.0 for all the catalysts examined (Figure 91).

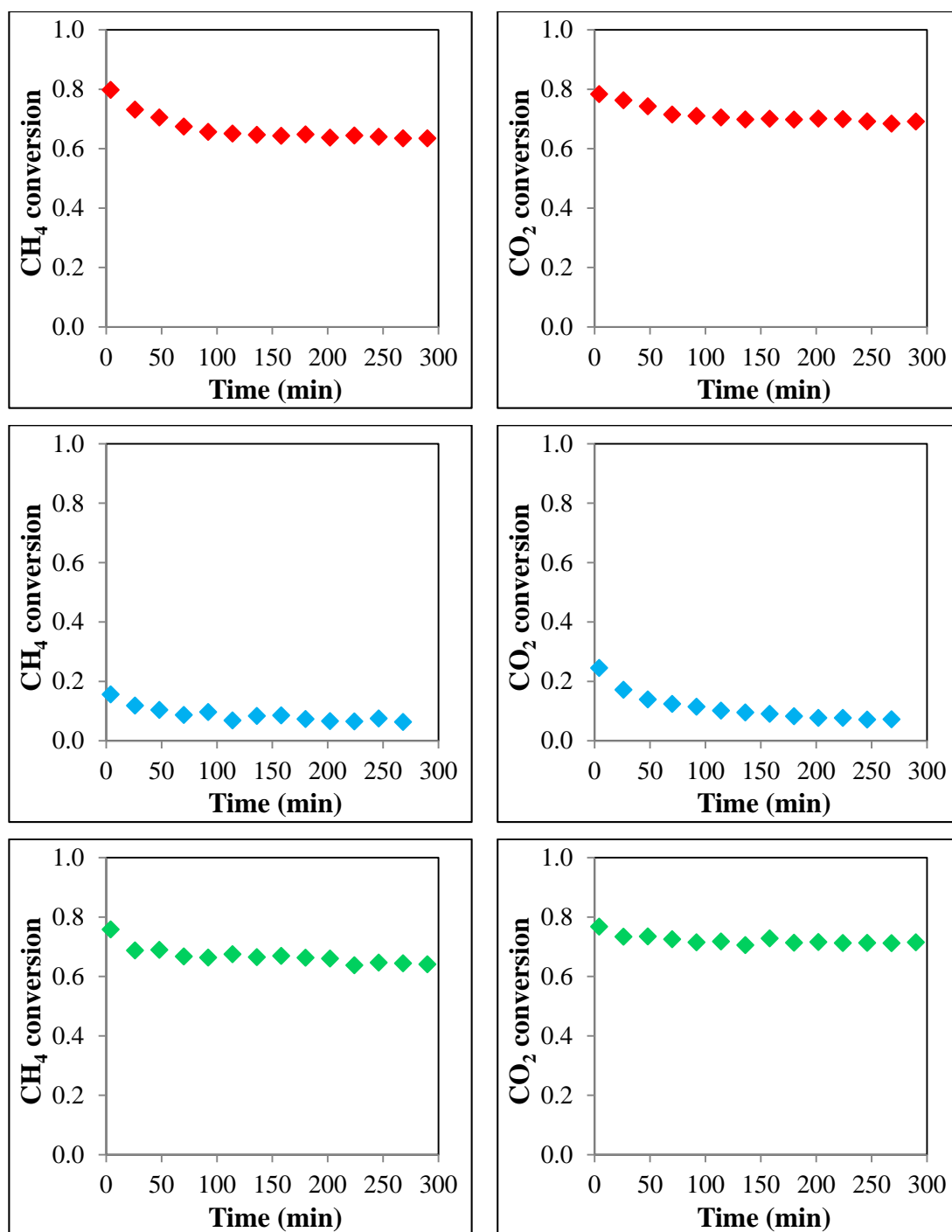


Figure 89. Comparison of CH₄ and CO₂ conversion versus time on stream over the catalysts calcined at 700°C, Ni/CeO₂-I-700-pellet ◆, Co/CeO₂-I-700-pellet ◆, Ni-Co/CeO₂-I-700-pellet ◆, (Reaction conditions: 700°C, 1 atm)

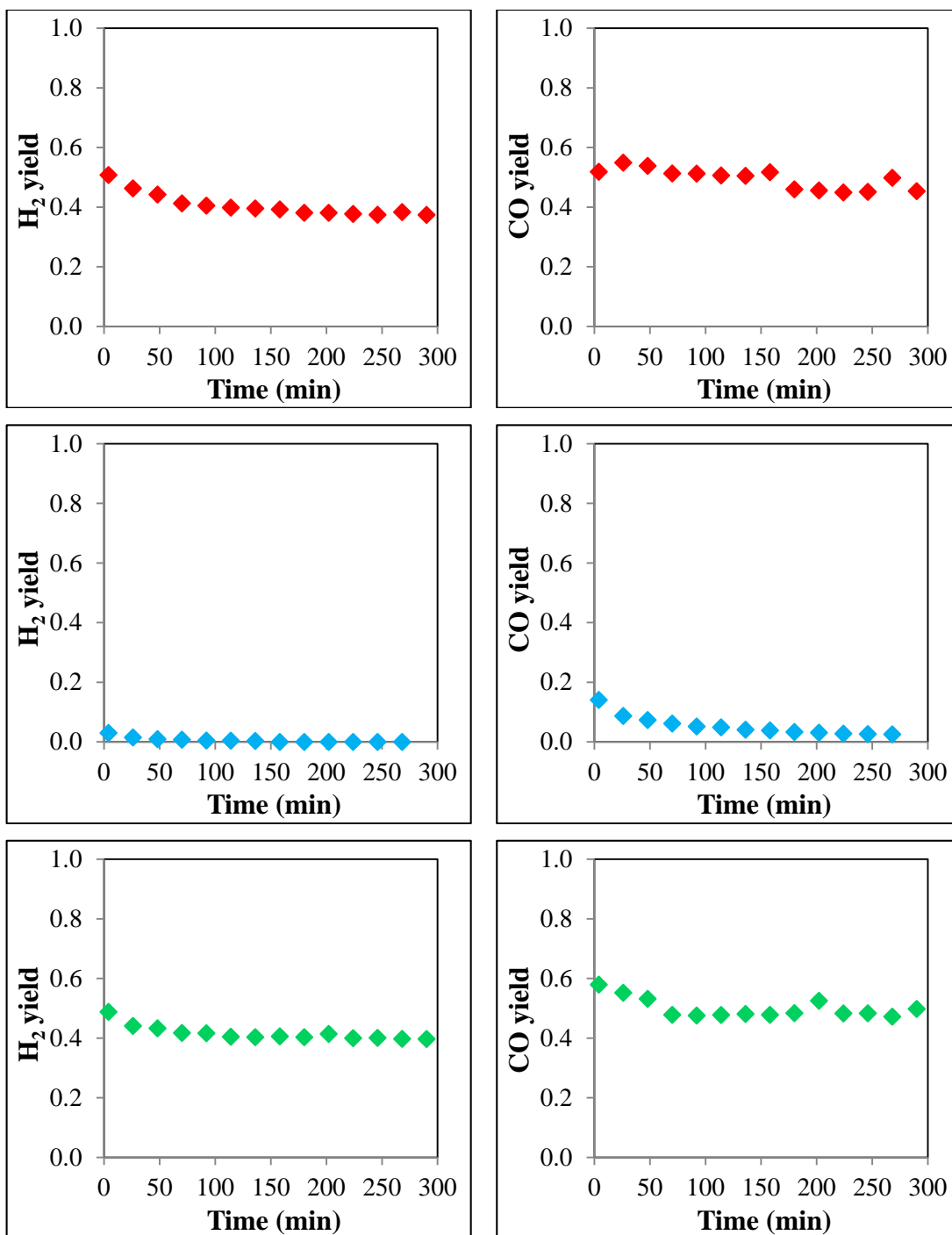


Figure 90. Comparison of H₂ and CO yield versus time on stream over the catalysts calcined at 700°C, Ni/CeO₂-I-700-pellet ◆, Co/CeO₂-I-700-pellet ◆, Ni-Co/CeO₂-I-700-pellet ◆, (Reaction conditions: 700°C, 1 atm)

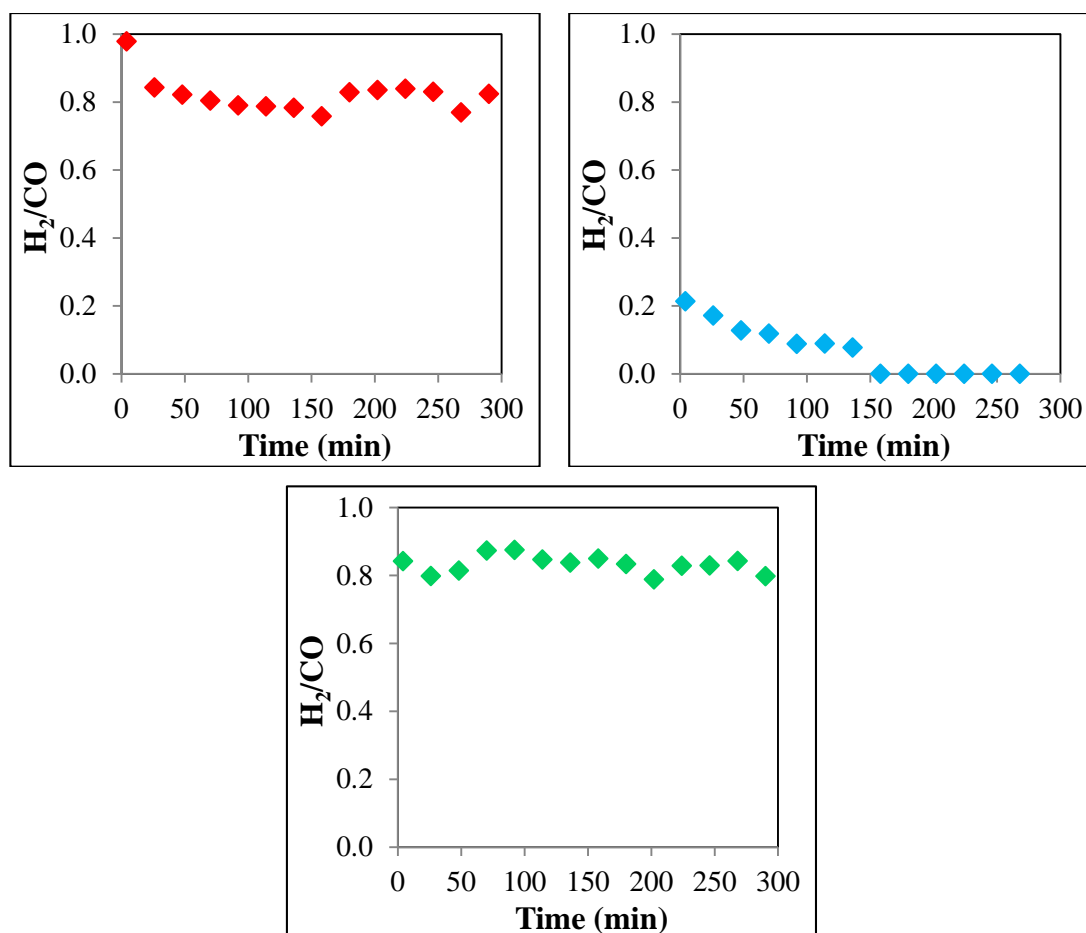


Figure 91. Comparison of H₂/CO ratio versus time on stream over the catalysts calcined at 700°C, Ni/CeO₂-I-700-pellet ♦, Co/CeO₂-I-700-pellet ♦, Ni-Co/CeO₂-I-700-pellet ♦, (Reaction conditions: 700°C, 1 atm)

In order to understand the effect of calcination temperature, the activity of the catalysts calcined at 900°C were also investigated for dry reforming of methane. CH₄ and CO₂ conversions versus time on stream over the catalysts calcined at 900°C are given in Figure 92. When Figure 89 and Figure 92 are compared with each other, it is seen that conversion of CH₄ and CO₂ decreased with the increase of calcination temperature from 700°C to 900°C. The initial deactivation was more severe in the case of 900°C calcination temperature.

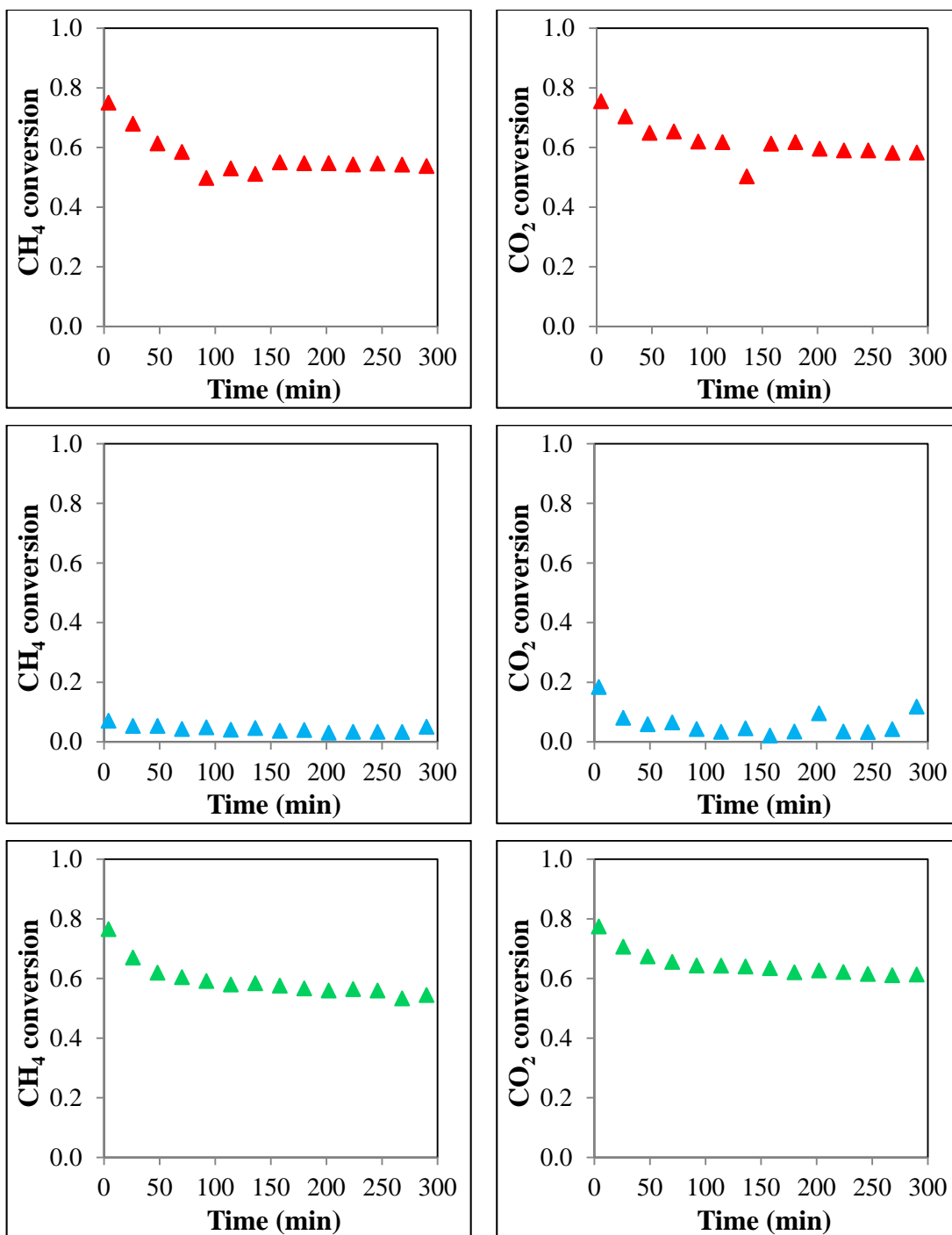


Figure 92. Comparison of CH₄ and CO₂ conversion versus time on stream over the catalysts calcined at 900°C, Ni/CeO₂-I-900-pellet ▲, Co/CeO₂-I-900-pellet ▲, Ni-Co/CeO₂-I-900-pellet ▲, (Reaction conditions: 700°C, 1 atm)

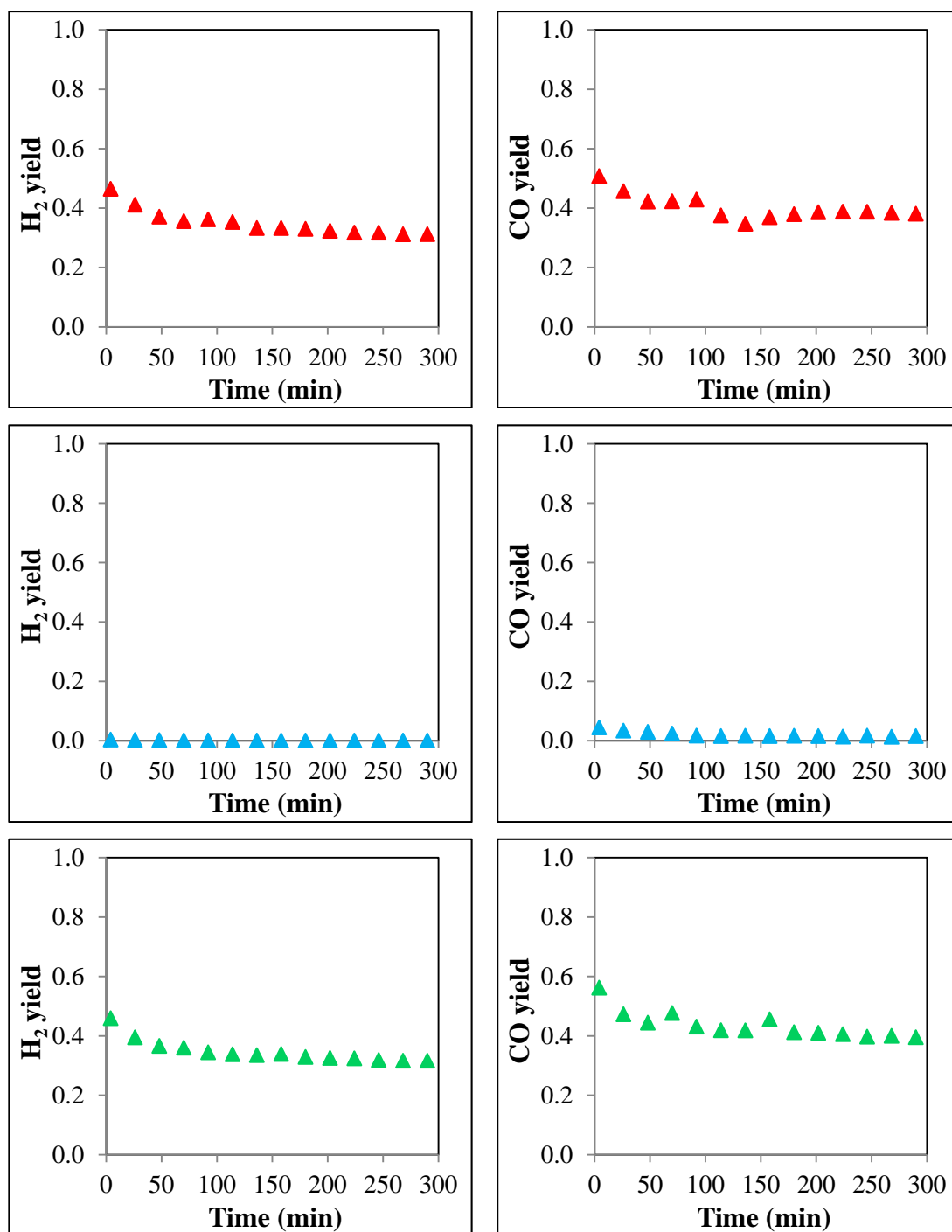


Figure 93. Comparison of H₂ and CO yield versus time on stream over the catalysts calcined at 900°C, Ni/CeO₂-I-900-pellet ▲, Co/CeO₂-I-900-pellet ▲, Ni-Co/CeO₂-I-900-pellet ▲, (Reaction conditions: 700°C, 1 atm)

The performance of Ni-Co/CeO₂-I-900-pellet was slightly higher than that of Ni/CeO₂-I-900-pellet. Although relatively lower than the performance of their corresponding ones calcined in 700°C, Ni/CeO₂-I-900-pellet and Ni-Co/CeO₂-I-900 exhibited quite high activity. On the other hand Co/CeO₂-I-900-pellet did not show any activity.

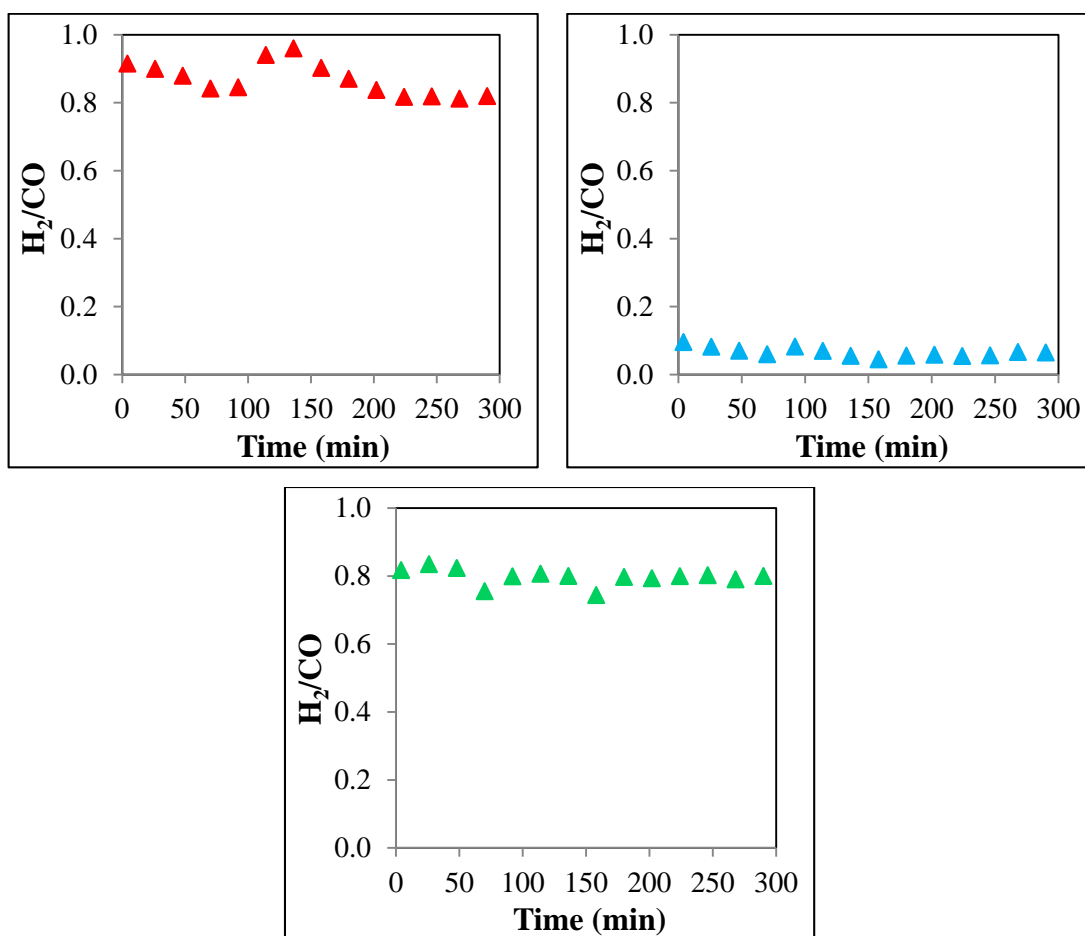


Figure 94. Comparison of H₂/CO ratio versus time on stream over the catalysts calcined at 900°C, Ni/CeO₂-I-900-pellet ▲, Co/CeO₂-I-900-pellet ▲, Ni-Co/CeO₂-I-900-pellet ▲, (Reaction conditions: 700°C, 1 atm)

CO yield was again higher than H₂ yield as in the case of 700°C calcination temperature which was again due to the RWGS reaction (Figure 93). When Figure 90 and Figure 93 are compared with each other, it is seen that yield of CO and H₂ decreased with the increase of calcination temperature from 700°C to 900°C. H₂/CO ratio was below 1.0 for the catalysts calcined at 900°C because of RWGS reaction (Figure 94).

6.2.3 Characterization of spent catalysts

6.2.3.1 Thermal Gravimetric Analysis (TGA)

The amount of carbon deposited on the samples after being used in CO₂ reforming of CH₄ was determined by TGA. The weight loss and derivative weight loss of the spent catalysts are given in Figure 95 and Figure 96, respectively.

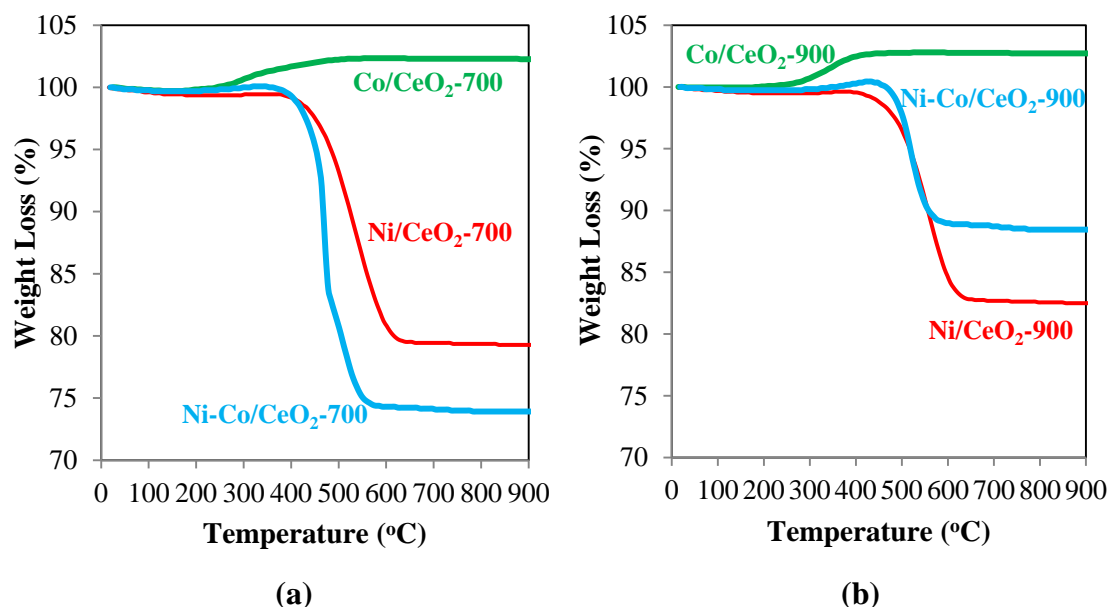


Figure 95. TGA curves in air atmosphere after being used in reaction at 700°C for 5 hours for the catalysts calcined at a) 700°C, b) 900°C

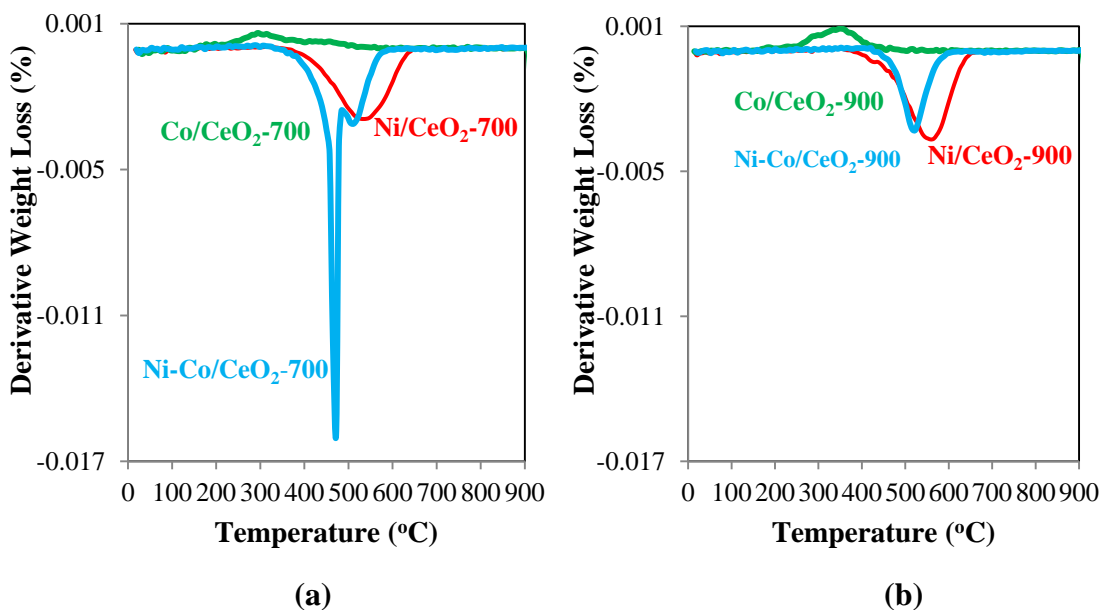


Figure 96. Derivative weight losses after being used in reaction at 700°C for 5 hours for the catalysts calcined at a) 700°C, b) 900°C

Although their catalytic performances were comparable, their behavior in terms of coke deposition was different. Higher amount of coke deposited on Ni-Co/CeO₂ when the calcination was done at 700°C. On the other hand, deposited amount of coke was higher on Ni/CeO₂ when the calcination was carried out at 900°C. The presence of two oxidation peaks in the derivative weight loss of Ni-Co/CeO₂-I-700 indicates the formation of two types of carbon formation.

6.2.3.2 High Contrast Transmission Electron Microscopy (HCTEM)

The morphology of deposited carbon on the spent catalysts were determined by HCTEM and shown in Figure 97 and Figure 98 for Ni/CeO₂-I-700 catalyst and Ni-Co/CeO₂-I-700 catalyst, respectively. Abundant filamentous carbon growing with varying dimensions are seen.

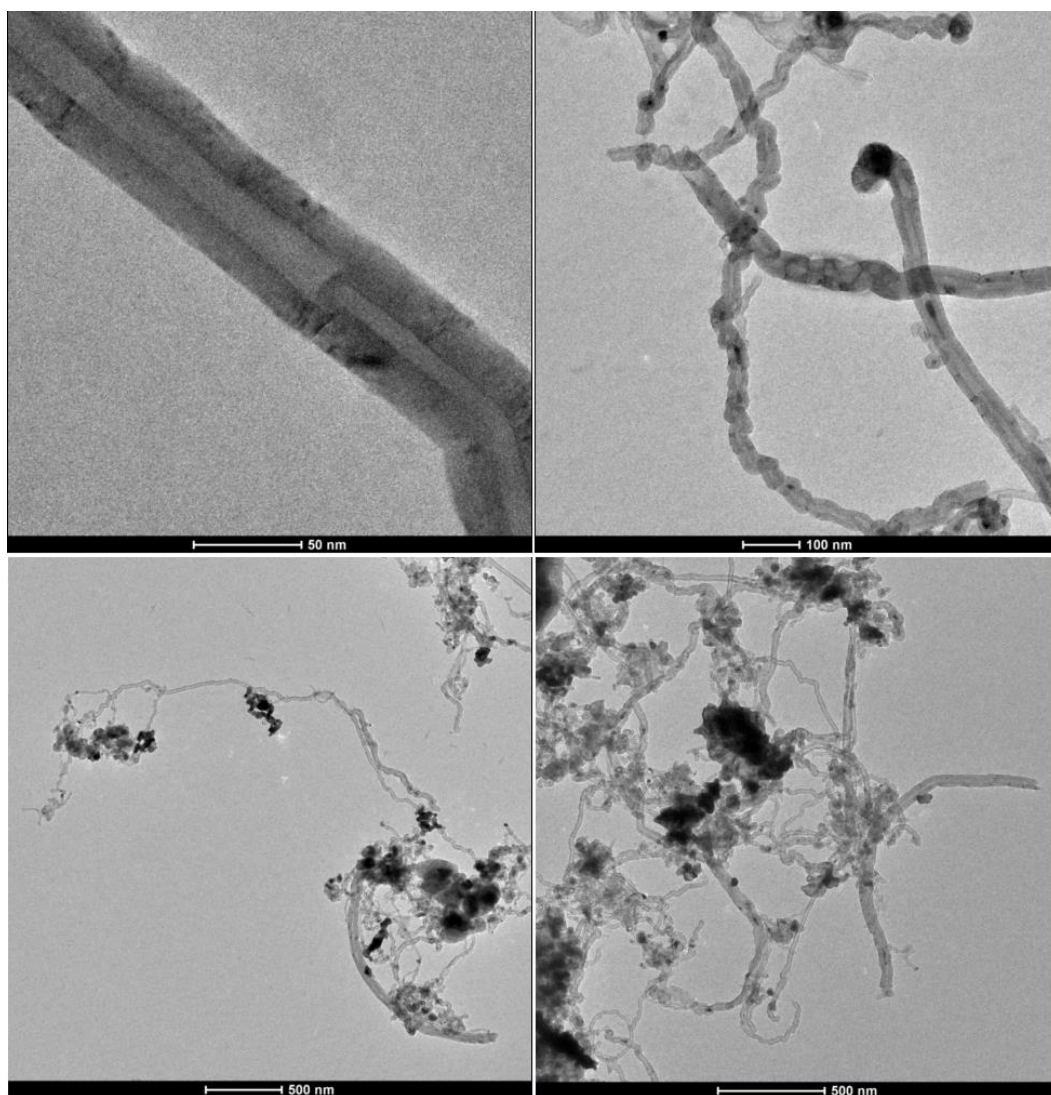


Figure 97. HCTEM of Ni/CeO₂-I-700 catalyst after being used in reaction at 700°C for 5 hour

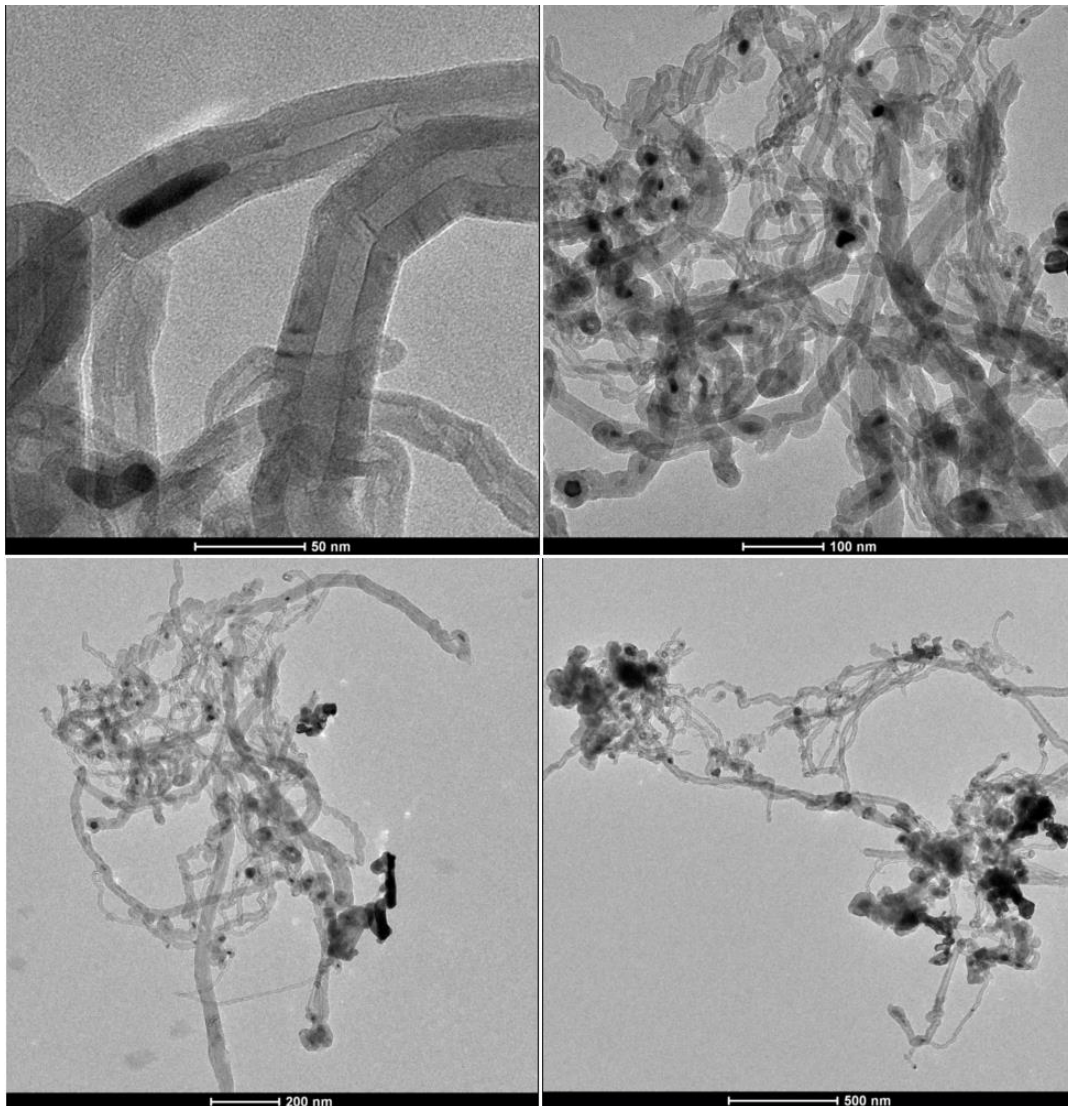


Figure 98. HCTEM of Ni-Co/CeO₂-I-700 catalyst after being used in reaction at 700°C for 5 hours

As seen in Figure above, the metal particle was encapsulated within the filament for Ni-Co/CeO₂-I-700 catalyst resulting in deactivation of the active surface.

6.3 Conclusions

Ceria supported Ni, Co monometallic and Ni-Co bimetallic catalysts were prepared by incipient wetness impregnation method at two different calcination temperatures (700 and 900°C) for dry reforming of methane.

TPR results showed that the interaction of metals with ceria changed with calcination temperature.

The activities of ceria-based catalysts decreased obviously with increasing calcination temperature. The initial deactivation was more severe in the case of 900°C calcination temperature. Although showing a decrease in activity in the first period of reaction, Ni and Ni-Co catalyst exhibited comparable high activities at both calcination temperatures. On the other hand ceria supported Co catalysts was shown to be inactive for dry reforming of methane at studied reaction conditions.

Higher amount of coke deposited on Ni-Co/CeO₂ when the calcination was done at 700°C. On the other hand, deposited amount of coke was higher on Ni/CeO₂ when the calcination was carried out at 900°C. Filamentous carbon growing with varying dimensions were seen on the spent catalysts after being used in the reaction. The deactivation of the catalysts was attributed to the encapsulation of active metal particles within the carbon filaments.

CHAPTER 7

MORPHOLOGY DEPENDENT REDOX PROPERTIES OF CeO₂⁶

7.1 Introduction

Cerium oxide and CeO₂-containing materials have been investigated intensively for the past several years as a result of their potential applications in the fields of electrochemistry, optics and catalysis [144-153]. Ceria is extensively employed in three way catalysts for eliminating the toxic auto-exhaust gases [144-146]. Catalyst based on CeO₂ have been reported to be very promising for water gas shift reaction [147-149]. Ceria is an excellent catalyst for fuel cell anodes [150-151]. Due to its strong absorption in the UV range, CeO₂ is used as UV blocking and shielding materials [152-153].

The broad range applications of ceria is mostly due to its unique redox properties and remarkable oxygen storage capacities [154-156]. Ceria has very good redox properties due to the very quick reduction of Ce⁴⁺ to Ce³⁺ associated with the creation of oxygen vacancies [157]. It can release oxygen under reducing atmosphere and store oxygen by filling oxygen vacancies under oxidizing environment [158 and references therein].

Various approaches have recently been proposed to increase the redox properties of ceria including the development of novel methodologies of preparation with enhanced textural properties [155,159,160] and addition of small amount of dopant metal to ceria [141,145,161,162].

⁶ This study comprises the work done in Technical University of Darmstadt and Ruhr University Bochum in the context of TUBITAK Inten-C project with reference number 107M447.

Surface area has a major role on the redox properties and hence OSC of CeO₂ [145,163].

The reduction of ceria occurs mainly in two temperature regions. The first region is 300°C-600°C and attributed to surface reduction [145 and references therein]. The second region is 700°C-1000°C and ascribed to bulk reduction [145 and references therein]. A linear correlation was found between the surface area and the hydrogen consumption at the low temperature region, indicating that reduction of ceria takes place first on the surface and then progressively affects the bulk [163 and references therein].

Morphology has also strong influence on the redox properties of ceria. [154,155,156,159,160]. Ceria in different morphologies such as nanotubes [160], nanowires [156], nanorods [154], microspheres [155], nanoflowers [154] and nanocubes [159] have been synthesized and tested for different catalytic reactions.

Wu and Wang [155] synthesized novel 3D-like CeO₂ microflowers and microspheres and tested them for CO oxidation. 3D-like ceria exhibited great superiority for favoring creation of oxygen vacancies, which in turn resulted in higher oxygen mobility and reducibility. The catalytic activity and thermal stability of 3D-like ceria were much better than that of CeO₂ nanoparticles. They proposed that highly active CeO₂ could be acquired by turning their shapes with a high concentration of oxygen vacancies.

Tana et al. [156] studied the redox properties and catalytic activities of ceria nanorods, nanoparticles and nanorods for CO oxidation comparatively. While ceria nanoparticles predominantly exposed stable {111} plane on the surface, the rod-shaped structures mainly exposed the reactive {100} and {111} planes, resulting in higher OSC and catalytic activity for CO oxidation. Although both the ceria nanorods and nanowires predominately exposed the reactive {100} and {111}

planes, ceria nanowires exhibited much higher catalytic activity than the nanorods due to favoring to expose a big portion of these reactive planes on the surface.

Mai et al. [159] synthesized CeO₂ nanorods, nanocubes and nanopolyhedras via hydrothermal method by altering the NaOH concentration and temperature. The synthesized samples exhibited various exposed crystal planes: {110} and {100} for nanorods; {100} for nanocubes; {111} and {100} for nanopolyhedra. OSC tests done at 400°C showed that while oxygen storage occurred both at the surface and in the bulk for nanocubes and nanorods, it was limited at the surface for the nanopolyhedra just like its bulk counterpart, because of exposure of more reactive (100)/(110) planes for the former two catalysts.

Meher and Rao [154] prepared highly uniform CeO₂ nanoflowers and nanorods by non-hydrothermal homogeneous precipitation method. Compared to the nanoflower sample, CeO₂ nanorod was shown to be easily and highly reducible. The OSC of nanorod was higher than that of nanoflower. CeO₂ nanorod exhibited better soot oxidation activity due to the larger CeO₂/soot interface than CeO₂ nanoflower.

The relationship between the oxygen storage capacity and the surface structure associated with a specific crystalline shape for CeO₂ nanomaterials lasts to be a subject of vivid investigation and discussion [159]. In present work, a comparative study was performed on the redox features of different kinds of ceria samples, including commercial ceria (COC) from Sigma Aldrich (54481-25G), coprecipitated ceria⁷ (CPC) and ceria fiber mats (ESC) obtained by a template directed synthesis using electrospun PMMA polymer fibers, followed by spray coating of an inorganic ceria sol.

⁷ The coprecipitated ceria sample was synthesized by a master student in Ruhr University Bochum .

7.2 Results and Discussion

7.2.1 Characterization of fresh catalysts

The BET surface areas of ESC, CPC and COC were measured as 77.4, 91.4 and 103.1 m²/g respectively. For ESC, this corresponds to the surface area after calcination at 350°C. For CPC and COC, these are the surface areas measured after calcination at 500°C.

The SEM images of ESC sample show mats of ceria tubes (Figure 99). The addition of Pluronic P123 not only facilitates the formation of 1D ceria tubes, it also provides the formation of 2D ceria film interconnecting the ceria tubes and hence generating a network structure [61]. As it is seen in the SEM images, the dimensions of the ceria tubes which was obtained by using electrospun PMMA fibers as templates are varying. The shapes and dimensions of the fibers formed during electrospinning depend upon several variables [164]. In their detailed study, Greiner and Wendorf [164] reported these parameters as “the properties of the polymer itself (such as molecular weight, molecular-weight distribution, glass-transition temperature, and solubility), as well the properties of the polymer solution (such as viscosity, viscoelasticity, concentration, surface tension, and electrical conductivity).” In addition, vapor pressure of the solvent, relative humidity of the environment, the features of the substrate, feeding rate of the solution, the field strength and the geometry of the electrodes were reported to have an important effect on fiber formation [164].

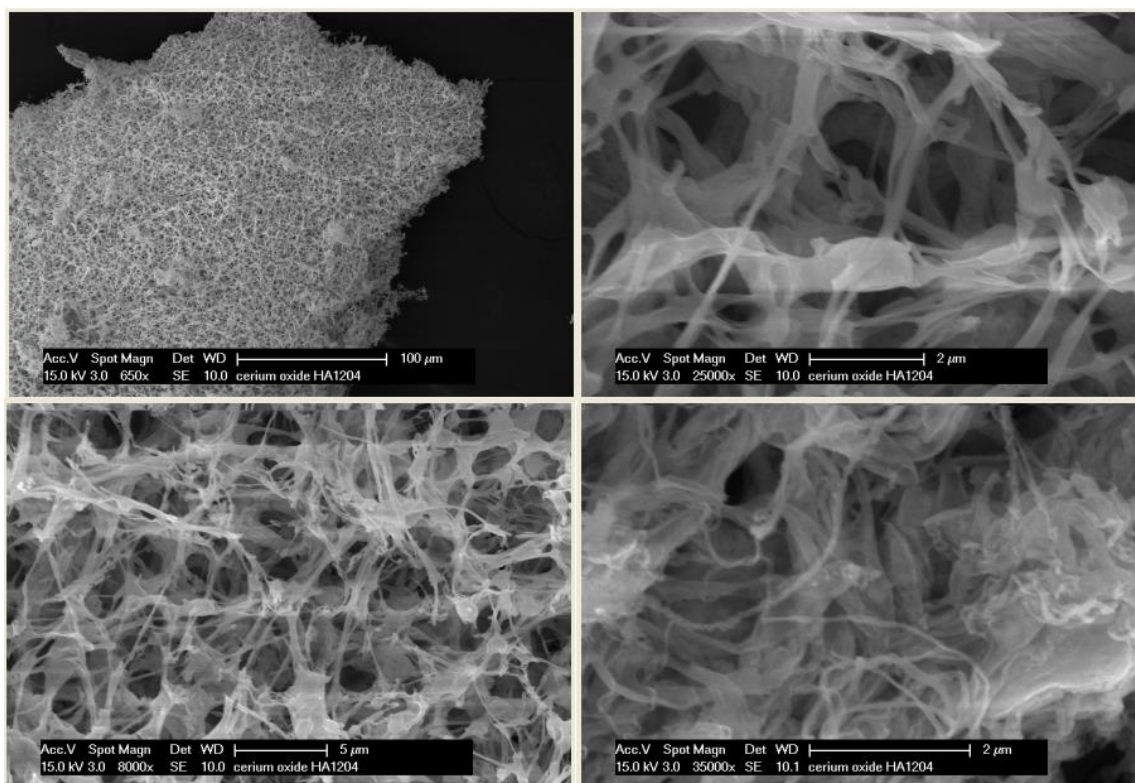


Figure 99. Scanning electron micrographs of ceria fiber mats

7.2.2 Redox Properties of CeO₂ samples

Redox experiments were performed in order to get information about the oxygen release/storage ability of different kinds of ceria samples.

Step 1 and Step 2 were carried out to obtain a defined state. The actual OSC measurement started with Step 3. 100 pulses of oxygen were done in Step 3.



The equation shows the process of oxygen storage from gas oxygen to lattice oxygen on the reduced ceria. O₂ uptake values for each sample were sketched in Figure 100 and tabulated in Table 13.

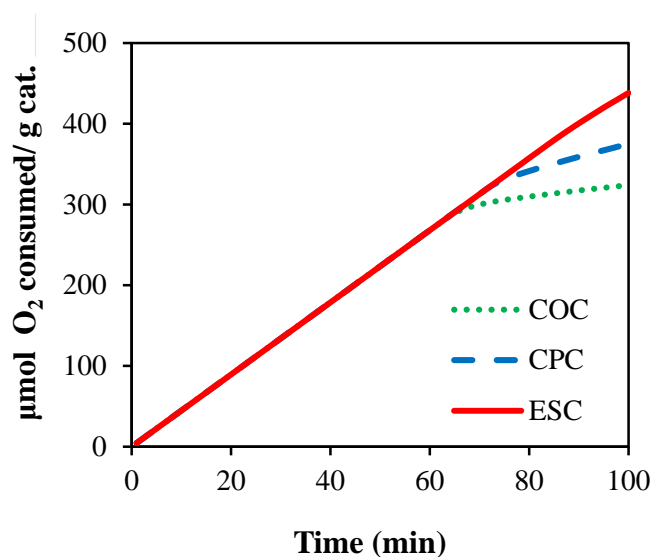


Figure 100. O₂ consumption during Step 3

Table 13. Oxygen storage of ceria samples at 600°C during Step 3

Sample	COC	ESC	CPC
O ₂ consumed (μmol/g cat.)	324	438	375

As it is seen, the oxygen uptake is in the order of ESC > CPC > COC. The mats of ceria fibers with the lowest surface area had the highest oxygen uptake value. This phenomenon demonstrated that the OSC of the CeO₂ samples depended strongly on the morphology.

120 pulses of CO were done in Step 4.



The above equation shows the ability of the sample to release oxygen in the absence of gaseous O₂. CO uptake and CO₂ production values upon CO pulses were sketched in Figure 101 and Figure 102 respectively.

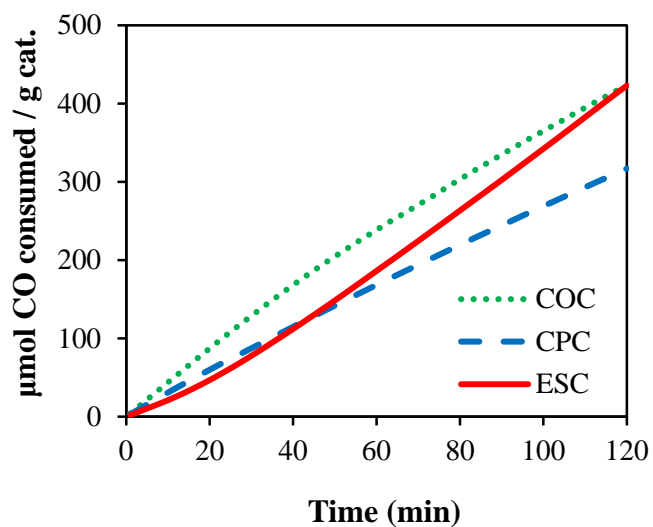


Figure 101. CO consumption during Step 4

There is a difference between CO uptake and CO₂ production on all of the catalysts examined (Table 14), which is called ‘carbon residual’ [161,165]. ESC is the best catalyst in terms of CO₂ production and prevention of carbon residual.

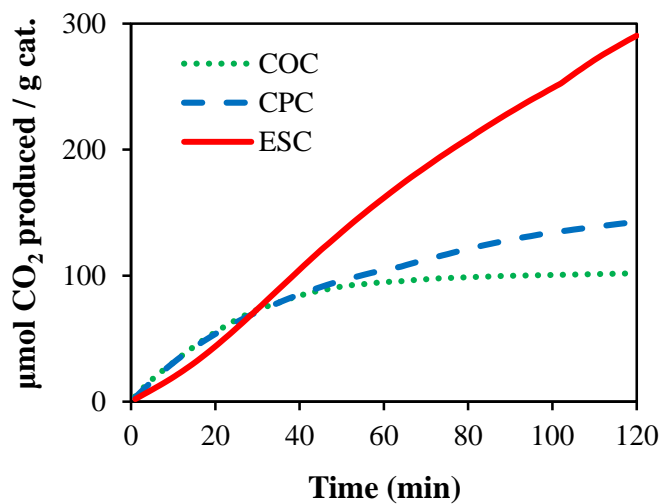


Figure 102. CO₂ production during Step 4

Table 14. Oxygen release of ceria samples at 600°C during Step 4

Sample	CO consumed ($\mu\text{mol/g cat.}$)	CO ₂ produced ($\mu\text{mol/g cat.}$)	Carbon residual ($\mu\text{mol/g cat.}$)
COC	424	102	322
ESC	423	290	132
CPC	317	143	174

CO adsorption on ceria is a complex process during which different events can occur:

- CO reacts with oxygen of ceria to form CO₂ [165].
- The produced CO₂ might desorb, or it may stay adsorbed on the ceria surface in a carbonate like species [165].
- CO may react with OH to produce H₂ and CO₂ [165].



- CO may react with itself in the CO disproportionation reaction, producing C and CO₂ [165].



Since the redox experiments were done at 600°C, hypothesis c can be excluded in our case. If CO reacted with itself in the CO disproportionation reaction, there would be CO₂ production in the next reoxidation (Step 5). But no CO₂ production was detected in the next reoxidation Step. It was concluded that carbon residual species on ceria was in the form of carbonates. The assumption seems reasonable due to the fact that the removal of surface carbonates does not normally consume any oxygen [165].

Having done the reduction of the catalysts in Step 4, the samples were reoxidized in Step 5 with again 100 O₂ pulses. O₂ uptake values for each sample were sketched in Figure 103 and tabulated in Table 15.

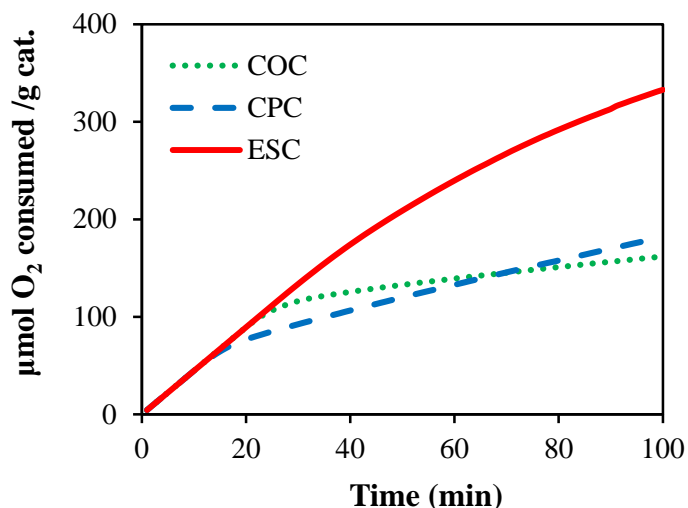


Figure 103. O₂ consumption during Step 5

Table 15. Oxygen storage of ceria samples at 600°C during Step 5

Sample	COC	ESC	CPC
O ₂ consumed (μmol/g cat.)	162	333	182

As it is seen the oxygen uptake is in the order of ESC > CPC > COC in Step 5 which is the case for Step 3, but with a decreased amount.

In order to test the reproducibility of the reduction cycle, 120 pulses of CO was again sent to the samples in Step 6 after the reoxidation (Step 5). CO uptake and

CO₂ production values upon CO pulses in Step 6 were sketched in Figure 104 and Figure 105 respectively.

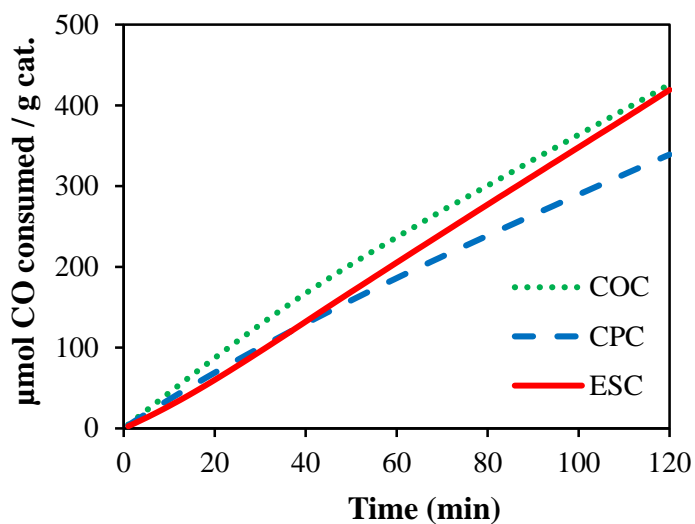


Figure 104. CO consumption during Step 6

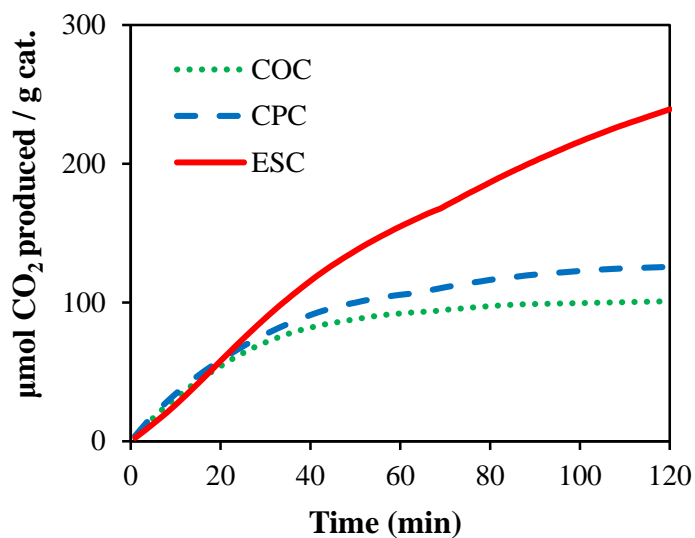


Figure 105. CO₂ production during Step 6

CO uptake and CO₂ production values were tabulated in Table 16 upon CO pulse in Step 6.

Table 16. Oxygen release of ceria samples at 600°C during Step 6

Sample	CO consumed ($\mu\text{mol/g cat.}$)	CO ₂ produced ($\mu\text{mol/g cat.}$)	Carbon residual ($\mu\text{mol/g cat.}$)
COC	426	101	325
ESC	419	239	180
CPC	339	126	213

Comparison of the values in Table 14 and Table 16 demonstrates the reversibility of the reduction cycle on the ceria samples. The difference between Step 4 and Step 6 can be explained by the uncertainty in the ability to calculate the areas under the peaks.

7.3. Conclusions

Fibers of ceria (ESC) were successfully prepared by a template directed synthesis method using electrospun PMMA polymer fibers, followed by spray coating of an inorganic ceria sol.

O₂, CO pulse experiments were performed to get information about redox properties of different kinds of ceria samples, including commercial ceria (COC), coprecipitated ceria (CPC) and ceria fibers (ESC). The oxygen storage capacities of the ceria samples were in the order of ESC > CPC > COC. The ceria fibers having the lowest surface area had the highest oxygen uptake value. This phenomenon demonstrated that the oxygen storage capacity of the CeO₂ samples depended

strongly on the morphology. A difference was observed between the CO uptake and CO₂ production on all of the samples examined, which was called carbon residual. ESC has shown the best performance in terms of least amount of carbon residual.

CHAPTER 8

CONCLUSIONS

Al₂O₃ supported Ni, Co and Ni-Co catalysts were prepared via incipient wetness impregnation method. Effect of calcination temperature was studied. Metal-support interaction of Ni-based catalyst increased with addition of cobalt. While doing the calcination at 700°C or 900°C did not really affect the catalytic performance of Ni/Al₂O₃-I and Ni-Co/Al₂O₃-I catalysts, it had significant influence on the performance of Co/Al₂O₃-I catalyst. Carrying out the calcination temperature at higher temperatures was found to be more preferable in terms of carbon deposition, especially for Ni-Co/Al₂O₃-I catalyst. Octopus carbon structure was observed on the spent Ni/Al₂O₃-I-900 catalyst. DRIFTS and microcalorimetry studies showed that CO₂ activation took place on Al₂O₃ for both Ni/Al₂O₃ and Ni-Co/Al₂O₃ catalysts. ¹³C NMR characterization of the deposited coke revealed that coke not only came from CH₄, but CO₂ had also significant role in carbon formation.

Polyol process was shown to be a good catalyst preparation method for dry reforming of methane reaction. The catalysts exhibited quite high performance at 600°C and 700°C without making a reduction step before the reaction. Abundant filamentous carbon growing with varying dimensions were observed on the TEM images of the spent catalysts.

CeO₂ supported Ni, Co and Ni-Co catalysts were prepared via incipient method at two different calcination temperatures. The interaction of metals with ceria changed significantly with calcination temperature. For the same sample calcined at different temperatures (700 and 900°C), the activities decreased obviously with increasing calcination temperature. Ni/CeO₂ and Ni-Co/CeO₂ catalyst exhibited comparable high activities. On the other hand ceria supported Co/CeO₂ was shown to be an

inactive catalyst for dry reforming of methane at our operating conditions. Abundant filamentous carbon growing with varying dimensions were seen on the TEM images of the spent catalysts after being used in the reaction. Deactivation was attributed to the encapsulation of active metal particles within the carbon filaments.

O₂, CO pulse experiments were done to get information about redox properties of different kinds of ceria samples, including commercial ceria (COC), coprecipitated ceria (CPC) and mats of ceria fibers (ESC). The oxygen storage capacities of the ceria samples were in the order of ESC > CPC > COC. The ceria fibers having the lowest surface area had the highest oxygen uptake value. Morphology was shown to be the main parameter that determined the redox properties of ceria.

REFERENCES

- [1] C. Papadopoulou, H. Matralis, and X. Verykios, Utilization of biogas as a renewable carbon source: Dry reforming of methane, in: L. Guzzi and A. Erd helyi (Eds.), *Catalysis for alternative energy generation*, Springer Science+Business Media, New York (2012) 57–127
- [2] A.P.E. York, T.C. Xiao, M.L.H. Green, J.B. Claridge, Methane oxyforming for synthesis gas production, *Catalysis Reviews* 49(4) (2007) 511–560
- [3] K. Otsuka, Y. Wang, E. Sunada, and I. Yamanaka, Direct partial oxidation of methane to synthesis gas by cerium oxide, *Journal of Catalysis* 175 (1998) 152-160
- [4] The magic of syngas-the link from feedstock to synthetic product, retrieved from http://www.chemrec.se/Syngas_the_link_from_feedstock_to_synthetic_product.aspx (last accessed June, 2014)
- [5] V.A. Tsipouriari and X.E. Verykios, Carbon and oxygen reaction pathways of CO₂ reforming of methane over Ni/La₂O₃ and Ni/Al₂O₃ catalysts studied by isotopic tracing techniques, *Journal of Catalysis* 187 (1999) 85–94
- [6] B. Beşergil, *Petrol, Petrol Kimyası, Bölüm 6, Doğal Gaz*, Ege Üniversitesi Yayını, İzmir (2009)
- [7] A.S.K. Raju, C.S. Park, J.M. Norbeck, Synthesis gas production using steam hydrogasification and steam reforming, *Fuel Processing Technology* 90(2) (2009) 330–336
- [8] L.A. Arkatova, The deposition of coke during carbon dioxide reforming of methane over intermetallides, *Catalysis Today* 157 (2010) 170-176

- [9] Ş. Özkara-Aydınoglu, E. Özensoy, A.E. Aksoylu, The effect of impregnation strategy on methane dry reforming activity of Ce promoted Pt/ZrO₂, *International Journal of Hydrogen Energy* 34 (2009) 9711-9722
- [10] D. San-José-Alonso, J. Juan-Juan, M.J. Illán-Gómez, M.C. Román-Martínez, Ni, Co and bimetallic Ni-Co catalysts for the dry reforming of methane, *Applied Catalysis A: General* 371 (2009) 54-59
- [11] J. Xu, W. Zhou, Z. Li, J. Wang, J. Ma, Biogas reforming for hydrogen production over nickel and cobalt bimetallic catalysts, *International Journal of Hydrogen Energy* 34 (2009) 6646-6654
- [12] WMO Greenhouse Gas Bulletin, The State of Greenhouse Gases in the Atmosphere Based on Global Observations through 2012, No 9, 6 November 2013, retrieved from http://www.wmo.int/pages/prog/arep/gaw/ghg/documents/GHG_Bulletin_No.9_en.pdf (last accessed May, 2014)
- [13] A.E.C. Luna, M.E. Iriarte, Carbon dioxide reforming of methane over a metal modified Ni-Al₂O₃ catalyst, *Applied Catalysis A: General* 343 (2008) 10–15
- [14] Z.F. Yan, R.G. Ding, L.H. Song, and L. Qian, Mechanistic study of carbon dioxide reforming with methane over supported nickel catalysts, *Energy Fuels* 12(6) (1998) 1114–1120
- [15] D. Liu, X.Y. Quek, W.N.E. Cheo, R. Lau, A. Borgna, Y. Yang, MCM-41 supported nickel-based bimetallic catalysts with superior stability during carbon dioxide reforming of methane: Effect of strong metal–support interaction, *Journal of Catalysis* 266 (2009) 380–390

- [16] E.V. Kondratenko, M. Baerns, Synthesis Gas Generation by Heterogeneous Catalysis, in: I. Horvath (Ed.), Encyclopedia of Catalysis, John Wiley and Sons, New Jersey, 6 (2003) 424-456
- [17] B. Fidalgo, J.A. Menéndez, Syngas production by CO₂ reforming of CH₄ under microwave heating—Challenges and opportunities, in: A. Indarto and J. Palgunadi (Eds), Syngas: Production, Applications and Environmental Impact, Nova Science Publishers Inc., New York (2011) 121-149
- [18] S. Tang, J. Lin and K.L. Tan, Pulse-MS studies on CH₄/CD₄ isotope effect in the partial oxidation of methane to syngas over Pt/ α -Al₂O₃, Catalysis Letters 55 (1998) 83–86
- [19] M.S. Fan, A.Z. Abdullah, and S. Bhatia, Catalytic technology for carbon dioxide reforming of methane to synthesis Gas, ChemCatChem 1 (2009) 192 – 208
- [20] M.A. Pena, J.P. Gómez, J.L.G. Fierro, New catalytic routes for syngas and hydrogen production, Applied Catalysis A: General 144 (1996) 7-57
- [21] A.P.E. York, T. Xiao, and M.L.H. Green, Brief overview of the partial oxidation of methane to synthesis gas, Topics in Catalysis 22 (2003) 345-358
- [22] A.C.W. Koh, L. Chen, W.K. Leong, B.F.G. Johnson, T. Khimyak, J. Lin, Hydrogen or synthesis gas production via the partial oxidation of methane over supported nickel–cobalt catalysts, International Journal of Hydrogen Energy 32 (2007) 725–730
- [23] Y. Qu, A.M. Sutherland, and T. Guo, Carbon Dioxide Reforming of Methane by Ni/Co Nanoparticle Catalysts Immobilized on Single-Walled Carbon Nanotubes, Energy & Fuels 22 (2008) 2183–2187

- [24] 2010 National Energy Technology Laboratory (NETL) Accomplishments Report, retrieved from <http://www.netl.doe.gov/File%20Library/newsroom/accomp10.pdf> (last accessed April, 2014)
- [25] Y.N. Chun, Y.C. Yang, K. Yoshikawa, Hydrogen generation from biogas reforming using a gliding arc plasma-catalyst reformer, *Catalysis Today* 148 (2009) 283–289
- [26] B.C. Murray, C.S. Galik and T. Vegh, Biogas in the United States, An Assessment of Market Potential in a Carbon-Constrained Future, Nicholas Institute for Environmental Policy Solutions, Duke University, (2014)
- [27] Sino-Danish, Renewable Energy Development Programme (RED), Report on the Development Status of Chinese Biogas Industry, Environmental Protection Research Institute of Light Industry, April, 2011, Beijing-China
- [28] M.C.J. Bradford and M.A. Vannice, CO₂ Reforming of CH₄, *Catalysis Reviews: Science and Engineering* 41(1) (1999) 1-42
- [29] J.R. Rostrup-Neilsen, J.H. Bak-Hansen, CO₂-Reforming of Methane over Transition Metals, *Journal of Catalysis* 144 (1993) 38-49
- [30] Z.L. Zhang, V.A. Tsipouriari, A.M. Efstathiou, X.E. Verykios, Reforming of methane with carbon dioxide to synthesis gas over supported rhodium catalysts. I. Effects of support and metal crystallite size on reaction activity and deactivation characteristics, *Journal of Catalysis* 158 (1996) 51–63.
- [31] J. Guo, H. Lou, H. Zhao, D. Chai, X. Zheng, Dry reforming of methane over nickel catalysts supported on magnesium aluminate spinels, *Applied Catalysis A: General* 273 (2004) 75–82

- [32] K. Nagaoka, K. Takanahe, K.I. Aika, Modification of Co/TiO₂ for dry reforming of methane at 2MPa by Pt, Ru or Ni, *Applied Catalysis A: General* 268 (2004) 151–158
- [33] E. Ruckenstein and H.Y. Wang, Carbon Deposition and Catalytic Deactivation during CO₂ Reforming of CH₄ over Co/ γ -Al₂O₃ Catalysts, *Journal of Catalysis* 205 (2002) 289–293
- [34] K. Nagaoka, K. Seshan, J.A. Lercher and K.I. Aika, Activation mechanism of methane-derived coke (CH_x) by CO₂ during dry reforming of methane—comparison for Pt/Al₂O₃ and Pt/ZrO₂, *Catalysis Letters* 70 (2000) 109–116
- [35] E. Ruckenstein, H.Y. Wang, Carbon dioxide reforming of methane to synthesis gas over supported cobalt catalysts, *Applied Catalysis A: General* 204 (2000) 257–263
- [36] J. Zhang, H. Wang, A.K. Dalai, Development of stable bimetallic catalysts for carbon dioxide reforming of methane, *Journal of Catalysis* 249 (2007) 300–310
- [37] B.S. Liu, C.T. Au, Carbon deposition and catalyst stability over La₂NiO₄/ γ -Al₂O₃ during CO₂ reforming of methane to syngas, *Applied Catalysis A: General* 244 (2003) 181–195
- [38] T.P. Beebe Jr., D.W. Goodman, B.D. Kay and J.T. Yates Jr., Kinetics of the activated dissociative adsorption of methane on the low index planes of nickel single crystal surfaces, *Journal of Chemical Physics* 87 (1987) 2305
- [39] F. Abild-Pedersen, O. Lytken, J. Engbæk, G. Nielsen, I. Chorkendorff, J.K. Nørskov, Methane activation on Ni(111): Effects of poisons and step defects, *Surface Science* 590 (2005) 127–137

- [40] H.S. Benggaard, J.K. Nørskov, J. Sehested, B.S. Clausen, L.P. Nielsen, A.M. Molenbroek, and J.R. Rostrup-Nielsen, Steam Reforming and Graphite Formation on Ni Catalysts, *Journal of Catalysis* 209 (2002) 365–384
- [41] F. Solymosi, The bonding, structure and reactions of CO₂ adsorbed on clean and promoted metal surfaces, *Journal of Molecular Catalysis*, 65 (1991) 337-358
- [42] B. Bartos, H.J. Freund, H. Kuhlenbeck, M. Neumann, H. Lindner, K. Müller, Adsorption and reaction of CO₂ and CO₂/O co-adsorption on Ni(100): Angle resolved photoemission (ARUPS) and electron energy loss (HREELS) studies, *Surface Science* 179 (1987) 59-89
- [43] H.J. Freund, M.W. Roberts, Surface chemistry of carbon dioxide, *Surface Science Reports* 25 (1996) 225-273
- [44] U. Burghaus, Surface science perspective of carbon dioxide chemistry-Adsorption kinetics and dynamics of CO₂ on selected model surfaces, *Catalysis Today* 148 (2009) 212–220
- [45] A. Cimino, F.S. Stone, Oxide solid solutions as catalysts. *Advances in Catalysis* 47 (2002) 141–306
- [46] S. Bennici and A. Auroux, Thermal Analysis and Calorimetric Methods, in: S.D. Jackson and J.S.J. Hargreaves (Eds), *Metal Oxide Catalysis*, Wiley-VCH Verlag GmbH & Co.KGaA, Weinheim (2009) 391-441
- [47] J. Baltrusaitis, Experimental and theoretical studies of the adsorption of atmospherically relevant gases on metal oxide and carbonate surfaces, Ph.D. Thesis, University of Iowa (2007)

- [48] P. Ferreira-Aparicio, I. Rodríguez-Ramos, J.A. Anderson, A. Guerrero-Ruiz, Mechanistic aspects of the dry reforming of methane over ruthenium catalysts, *Applied Catalysis A: General* 202 (2000) 183–196
- [49] J. Nakamura, K. Aikawa, K. Sato, T. Uchijima, Role of support in reforming of CH₄ with CO₂ over Rh catalysts, *Catalysis Letters* 25(3-4) (1994) 265-270
- [50] J. H. Bitter, K. Seshan, and J. A. Lercher, The State of Zirconia Supported Platinum Catalysts for CO₂/CH₄ Reforming, *Journal of Catalysis* 171 (1997) 279-286
- [51] Y.T. Shah, Steam Gasification and Reforming Technologies, in: *Water for Energy and Fuel Production*, CRC Press, Taylor & Francis Group, Boca Raton (2014) 47-112
- [52] C.A. Bernardo, The fouling of catalysts by deposition of filamentous carbon, in: L.F. Melo, T.R. Bott, C.A. Bernardo (Eds), *Fouling Science and Technology*, Kluwer Academic Publishers, Dordrecht, the Netherlands (1988) 369-389
- [53] C.H. Bartholomew, Mechanisms of catalyst deactivation, *Applied Catalysis A: General* 212 (2001) 17–60
- [54] V.C.H. Kroll, H.M. Swaan and C. Mirodatos, Methane reforming reaction with carbon dioxide over Ni/SiO₂ catalysts. I. Deactivation studies, *Journal of Catalysis* 161 (1996) 409-422
- [55] J.R. Rostrup-Nielsen and L.J. Christiansen, *Concepts in Syngas Manufacture*, Imperial College Press, London (2011)
- [56] J.R. Rostrup-Nielsen and J. Sehested, Whisker Carbon Revisited, *Studies in Surface Science and Catalysis*, 139 (2001) 1-12

- [57] F. Abild-Pedersen and J.K. Nørskov, J.R. Rostrup-Nielsen, J. Sehested, and S. Helveg, Mechanisms for catalytic carbon nanofiber growth studied by ab initio density functional theory calculations, *Physical Review B* 73 (2006) 115419(1-13)
- [58] S. Helveg, C. Lopez-Cartes, J. Sehested, P. L. Hansen, B. S. Clausen, J.R. Rostrup-Nielsen, F. Abild-Pedersen, J.K. Nørskov, Atomic-scale imaging of carbon nanofibre growth, *Nature* 427 (2004) 426-429
- [59] J.R. Rostrup-Nielsen, J.B. Hansen, Steam Reforming for Fuel Cells, in: D. Shekhawat, J.J. Spivey, D.A. Berry (Eds), *Fuel Cells: Technologies for Fuel Processing*, Elsevier, Amsterdam (2011) 49-71
- [60] J.R. Rostrup-Nielsen, I. Dybkjaer, L.J. Christiansen, Steam Reforming Opportunities and Limits of the Technology, in: H.I. de Lasa, G. Doğu, A. Ravella (Eds), *Chemical Reactor Technology for Environmentally Safe Reactors and Products*, Kluwer Academic Publishers, Dordrecht, the Netherlands (1992) 249-281
- [61] J.J. Schneider, M. Naumann, C. Schäfer, A. Brandner, H.J. Hofmann, and P. Claus, Template-assisted formation of microsized nanocrystalline CeO₂ tubes and their catalytic performance in the carboxylation of methanol, *Beilstein Journal of Nanotechnology* 2 (2011) 776–784
- [62] N. Wang, W. Chu, T. Zhang, X.S. Zhao, Synthesis, characterization and catalytic performances of Ce-SBA-15 supported nickel catalysts for methane dry reforming to hydrogen and syngas, *International Journal of Hydrogen Energy* 37 (2012) 19-30
- [63] D. Chen, R. Lødeng, A. Anundska, O. Olsvik, A. Holmen, Deactivation during carbon dioxide reforming of methane over Ni catalyst: microkinetic analysis, *Chemical Engineering Science* 56 (2001) 1371-1379

- [64] N.A. Pechimuthu, K.K. Pant and S.C. Dhingra, Deactivation Studies over Ni-K/CeO₂-Al₂O₃ Catalyst for Dry Reforming of Methane, *Industrial & Engineering Chemistry Research* 46 (2007) 1731-1736
- [65] A. Becerra, M.E. Iriarte, M. Dimitrijewits, A. Castro-Luna, Promoting effects of rhodium on supported nickel catalysts in the dry reforming of methane, *Boetín de la Sociedad Chilena de Química* 47(4) (2002) 385-392
- [66] H. Arbag, S. Yasyerli, N. Yasyerli, G. Dogu, Activity and stability enhancement of Ni-MCM-41 catalysts by Rh incorporation for hydrogen from dry reforming of methane. *International Journal of Hydrogen Energy* 35 (2010) 2296–2304
- [67] M. García-Diéguez, I.S. Pieta, M.C. Herrera, M.A. Larrubia, L.J. Alemany, Improved Pt-Ni nanocatalysts for dry reforming of methane, *Applied Catalysis A: General* 377 (2010) 191–199
- [68] Y. Chen, K. Tomishige, K. Yokohama, K. Fujimoto, Promoting effect of Pt, Pd and Rh noble metals to the Ni_{0.03}Mg_{0.97}O solid solution catalysts for the reforming of CH₄ with CO₂, *Applied Catalysis A: General* 165 (1997) 335–347
- [69] C. Crisafulli, S. Scirè, S. Minicò, L. Solarino, Ni–Ru bimetallic catalysts for the CO₂ reforming of methane, *Applied Catalysis A: General* 225 (2002) 1–9
- [70] K. Takanabe, K. Nagaoka and K.I. Aika, Improved resistance against coke deposition of titania supported cobalt and nickel bimetallic catalysts for carbon dioxide reforming of methane, *Catalysis Letters* 102 (2005) 153-157
- [71] S. Wang and G.Q. Lu, Thermogravimetric Analysis of Carbon Deposition over Ni/ γ -Al₂O₃ Catalysts in Carbon Dioxide Reforming of Methane, *Energy Fuels* 12(6) (1998) 1235–1240

- [72] M. Yang, H. Papp, CO₂ reforming of methane to syngas over highly active and stable Pt/MgO catalysts, *Catalysis Today* 115 (2006) 199–204
- [73] X.E. Verykios, Mechanistic aspects of the reaction of CO₂ reforming of methane over Rh/Al₂O₃ catalyst, *Applied Catalysis A: General* 255 (2003) 101–111
- [74] A.A. Lemonidou, M.A. Goula, I.A. Vasalos, Carbon dioxide reforming of methane over 5 wt.% nickel calcium aluminate catalysts-effect of preparation method, *Catalysis Today* 46 (1998) 175-183
- [75] V.C.H. Kroll, H.M. Swaan, S. Lacombe, and C. Mirodatos, Methane Reforming Reaction with Carbon Dioxide over Ni/SiO₂ Catalyst, II. A Mechanistic Study, *Journal of Catalysis* 164 (1997) 387–398
- [76] A.R. McFarlane, I.P. Silverwood, R. Warringham, E.L. Norris, R.M. Ormerod, C.D. Frost, S.F. Parker, S.F. and D. Lennon, The application of inelastic neutron scattering to investigate the dry reforming of methane over an alumina-supported nickel catalyst operating under conditions where filamentous carbon formation is prevalent, *Royal Society of Chemistry Advances* 3 (2013) 16577–16589
- [77] A. Boumaza, L. Favaro, J. Lédion, G. Sattonnay, J.B. Brubach, P. Berthet, A.M. Huntz, P. Royc, R.Tétot, Transition alumina phases induced by heat treatment of boehmite: An X-ray diffraction and infrared spectroscopy study, *Journal of Solid State Chemistry* 182 (2009) 1171–1176
- [78] F. Le Coz, L. Arurault, S. Fontorbes, V. Vilar, L. Datas, P. Winterton, Chemical composition and structural changes of porous templates obtained by anodizing aluminum in phosphoric acid electrolyte, *Surface and Interface Analysis* 42 (2010) 227-233

- [79] T. Niu, L.M. Shen, Y. Liu, Preparation of meso-macroporous α -alumina using carbon nanotube as the template for the mesopore and their application to the preferential oxidation of CO in H₂-rich gases, *Journal of Porous Materials* 20 (2013) 789-798
- [80] J. Zhou, Z. Hua, W. Wu, Z. Liu, Z. Gao, Y. Zhu, Y. Chen and J. Shi, Supplementary Information for: Hollow mesoporous zeolite microspheres: Hierarchical macro-/meso-/microporous structure and exceptionally enhanced adsorption properties (2011)
- [81] S. Y. Foo, C.K. Cheng, T.H. Nguyen, A.A. Adesina, Oxidative CO₂ Reforming of Methane on Alumina-Supported Co-Ni Catalyst, *Ind. Eng. Chem. Res.* 49 (2010) 10450–10458
- [82] B. Coq, D. Tichit, S. Ribet, Co/Ni/Mg/Al layered double hydroxides as precursors of catalysts for the hydrogenation of nitriles: hydrogenation of acetonitrile. *Journal of Catalysis* 189(1) (2000) 117-128
- [83] L. Chen, Q. Zhu, R. Wu, Effect of Co-Ni ratio on the activity and stability of Co-Ni bimetallic aerogel catalyst for methane Oxy-CO₂ reforming, *International Journal of Hydrogen Energy* 36 (2011) 2128-2136
- [84] M. Chareonpanich, N. Teabpinyok, and S. Kaewtaweesub, Effect of Nickel Particle Size on Dry Reforming Temperature, *Proceedings of the World Congress on Engineering and Computer Science 2008, San Francisco, USA*
- [85] C. Li, Y.W. Chen, Temperature programmed reduction studies on Ni oxide Alumina catalysts: effect of the preparation method, *Thermochimica Acta* 256 (1995) 457-465

- [86] D.S. José-Alonso, M.J. Illán-Gómez, M.C. Román-Martínez, Low metal content Co and Ni alumina supported catalysts for the CO₂ reforming of methane, *International Journal of Hydrogen Energy* 38 (2013) 2230-2239
- [87] J.L. Ewbank, L. Kovarik, C.C. Kenvin and C. Sievers, Effect of preparation methods on the performance of Co/Al₂O₃ catalysts for dry reforming of methane, *Green Chemistry* 16 (2014) 885-896
- [88] H.Y. Wang, E. Ruckenstein, Conversions of Methane to Synthesis Gas over Co/ γ -Al₂O₃ by CO₂ and/or O₂, *Catalysis Letters* 75 (2001) 13-18
- [89] S. Andonova, C.N. de Avila, K. Arishtirova, J.M.C. Bueno, S. Damyanova, Structure and redox properties of Co promoted Ni/Al₂O₃ catalysts for oxidative steam reforming of ethanol, *Applied Catalysis B: Environmental* 105 (2011) 346–360
- [90] N.K. Nga, D.K. Chi, Synthesis, Characterizations and Catalytic Activity of CoAl₂O₄ and NiAl₂O₄ Spinel Types oxides for NO_x Selective Reduction, *Advances in Technology of Materials and Materials Processing*, 6(2) (2004) 336-343
- [91] S.J. Gregg, J.D.F. Ramsay, A Study of the Adsorption of Carbon Dioxide by Alumina Using Infrared and Isotherm Measurements, *Journal of Physical Chemistry*, 73(5) (1969) 1243-1247
- [92] M. Cabrejas Manchado, J.M. Guil, A. Pérez Masia, A. Ruiz Paniego, J. M. Trejo Menayo, Adsorption of H₂, O₂, CO, and CO₂ on a γ -Alumina: Volumetric and Calorimetric Studies, *Langmuir* 10(3) (1994) 685-691
- [93] J. Baltrusaitis, J.H. Jensen, V.H. Grassian, FTIR Spectroscopy Combined with Isotope Labeling and Quantum Chemical Calculations to Investigate Adsorbed

Bicarbonate Formation Following Reaction of Carbon Dioxide with Surface Hydroxyl Groups on Fe₂O₃ and Al₂O₃, *Journal of Physical Chemistry B* 110(24) (2006) 12005-12016

[94] P. Galhotra, Carbon dioxide adsorption on nanomaterials, University of Iowa, PhD Thesis (2010)

[95] O.B. Belskaya, I.G. Danilova, M.O. Kazakov, R.M. Mironenko, A.V. Lavrenov and V.A. Likholobov, FTIR Spectroscopy of Adsorbed Probe Molecules for Analyzing the Surface Properties of Supported Pt (Pd) Catalysts, in: T. Theophanides (Ed), *Infrared Spectroscopy-Materials Science, Engineering and Technology* (2012) 149-179

[96] S.U. Rege, R.T. Yang, A novel FTIR method for studying mixed gas adsorption at low concentrations: H₂O and CO₂ on NaX zeolite and γ -alumina, *Chemical Engineering Science* 56 (2001) 3781–3796

[97] M. Casarin, D. Falcomer, A. Glisenti, and A. Vittadini, Experimental and Theoretical Study of the Interaction of CO₂ with α -Al₂O₃, *Inorganic Chemistry*, 42(2) (2003) 436-445

[98] M. García-Díez, I.S. Pieta, M.C. Herrera, M.A. Larrubia, I. Malpartida, L.J. Alemany, Transient study of the dry reforming of methane over Pt supported on different γ -Al₂O₃, *Catalysis Today* 149 (2010) 380–387

[99] S. Takenaka, H. Ogihara, I. Yamanaka, K. Otsuka, Decomposition of methane over supported-Ni catalysts: effects of the supports on the catalytic lifetime, *Applied Catalysis A: General* 217 (2001) 101–110

- [100] M.P. Rosynek, Isotherms and Energetics of Carbon Dioxide on γ -Alumina at 100-300°C, *Journal of Physical Chemistry*, 79(13) (1975) 1280-1284
- [101] C.A. Bernardo, I. Alstrup and J.R. Rostrup-Nielsen, Carbon deposition and steam reforming on silica-supported Ni-Cu catalysts, *Journal of Catalysis* 96 (1985) 517-534
- [102] J.R. Rostrup-Nielsen, Sulfur-passivated nickel catalysts for carbon-free steam reforming of methane, *Journal of Catalysis* 85(1) (1984) 31-43
- [103] M.A. Ermakova, D.Y. Ermakov, A.L. Chuvilin, and G.G. Kuvshinov, Decomposition of Methane over Iron Catalysts at the Range of Moderate Temperatures: The Influence of Structure of the Catalytic Systems and the Reaction Conditions on the Yield of Carbon and Morphology of Carbon Filaments, *Journal of Catalysis* 201 (2001) 183-197
- [104] C. Pham-Huu, R. Vieira, B. Loui, A. Carvalho, J. Amadou, T. Dintzer, M.J. Ledoux, About the octopus-like growth mechanism of carbon nanofibers over graphite supported nickel catalyst, *Journal of Catalysis* 240 (2006) 194-202
- [105] J. Rass-Hansen, C.H. Christensen, J. Sehested, S. Helveg, J.R. Rostrup-Nielsen and S. Dahl, Renewable hydrogen: carbon formation on Ni and Ru catalysts during ethanol steam-reforming, *Green Chemistry* 9 (2007) 1016-1021
- [106] S. Kaya, E. Erünal, R. Shaltaf, Ş. Ellialtıođlu, D. Üner, On the Structure Sensitivity of CO Oxidation on Alumina Supported Pd-Pt Bimetallic Catalysts, *Turkish Journal of Chemistry* 33 (2009) 11-21
- [107] M. Khoshtinat Nikoo and N.A.S. Amin, Thermodynamic analysis of carbon dioxide reforming of methane in view of solid carbon formation, *Fuel Processing Technology* 92 (2011) 678-691

- [108] T.P. Braga, R.C.R. Santos, B.M.C. Sales, B.R. da Silva, A.N. Pinheiro, E.R. Leite, A. Valentini, CO₂ mitigation by carbon nanotube formation during dry reforming of methane analyzed by factorial design combined with response surface methodology, *Chinese Journal of Catalysis* 35 (2014) 514-523
- [109] R.S. Ningthoujam, N.S. Gajbhiye and S. Sharma, Reduction Mechanism of Ni²⁺ into Ni Nanoparticles Prepared from Different Precursors: Magnetic Studies, *Pramana Journal of Physics* 72(3) (2009) 577-586
- [110] N.R. NikRoselina, A. Azizan and Z. Lockman, Synthesis of Nickel Nanoparticles Via Non-Aqueous Polyol Method: Effect of Reaction Time, *Sains Malaysiana* 41(8) (2012) 1037–1042
- [111] C.Y. Lu, H.H. Tseng, M.Y. Wey, L.Y. Liu, K.H. Chuang, Effects of the ratio of Cu/Co and metal precursors on the catalytic activity over Cu-Co/Al₂O₃ prepared using the polyol process, *Materials Science and Engineering B* 157 (2009) 105–112
- [112] K.J. Carroll, J.U. Reveles, M.D. Shultz, S.N. Khanna, and E.E. Carpenter, Preparation of Elemental Cu and Ni Nanoparticles by the Polyol Method: An Experimental and Theoretical Approach, *Journal of Physical Chemistry C* 2011, 115, 2656–2664
- [113] G.G. Couto, J.J. Klein, W.H. Schreiner, D.H. Mosca, A.J.A. de Oliveira, A.J.G. Zarbina, Nickel nanoparticles obtained by a modified polyol process: Synthesis, characterization, and magnetic properties, *Journal of Colloid and Interface Science* 311 (2007) 461–468
- [114] K.S. Chou and K.C. Huang, Studies on the chemical synthesis of nanosized nickel powder and its stability, *Journal of Nanoparticle Research* 3 (2001) 127–132

- [115] L. Bai, J. Fan, Y. Cao, F. Yuan, A. Zuo, Q. Tang, Shape-controlled synthesis of Ni particles via polyol reduction, *Journal of Crystal Growth* 311 (2009) 2474–2479
- [116] G.S. Okram, A. Soni, R. Prasad, The pH-Controlled Particle Size Tuning of Nanocrystalline Ni in Polyol Synthesis Method Without Additional Capping, *Advanced Science Letters*, 4 (1) (2011) 132-135
- [117] E. Bayrakdar, T.Gürkaynak Altınçekiç, M.A.F. Öksüzömer, Effects of PVP on the preparation of nanosized Al₂O₃ supported Ni catalysts by polyol method for catalytic partial oxidation of methane, *Fuel Processing Technology* 110 (2013) 167–177
- [118] D. Ung, Y. Soumare, N. Chakroune, G. Viau, M.-J. Vaulay, V. Richard and F. Fievet, Growth of Magnetic Nanowires and Nanodumbbells in Liquid Polyol, *Chemistry of Materials* 19(8) (2007) 2084-2094
- [119] M. Singh, M. Kumar, F. Štěpánek, P. Ulbrich, P. Svoboda, E. Santava, M.L. Singla, Liquid-Phase Synthesis of Nickel Nanoparticles stabilized by PVP and study of their structural and magnetic properties, *Advanced Materials Letters* 2(6) (2011) 409-414
- [120] G. Viau, P. Toneguzzo, A. Pierrard, O. Acher, F. Fiévet-Vincent and F. Fiévet, Heterogenous nucleation and growth of metal nanoparticles in polyols, *Scripta Materialia* 44(8) (2001) 2263–2267
- [121] K. Nouneh, M. Oyama, R. Diaz, M. Abd-Lefdil, I.V. Kityk, M. Bousmina, Nanoscale synthesis and optical features of metallic nickel nanoparticles by wet chemical approaches, *Journal of Alloys and Compounds* 509(19) (2011) 5882–5886

- [122] B.K. Park, S. Jeong, D. Kim, J. Moon, S. Lim, J.S. Kim, Synthesis and size control of monodisperse copper nanoparticles by polyol method, *Journal of Colloid and Interface Science* 311 (2007) 417–424
- [123] M. Dinç, Ö. Metin, S. Özkaz, Water soluble polymer stabilized iron(0) nanoclusters: A cost-effective and magnetically recoverable catalyst in hydrogen generation from the hydrolysis of sodium borohydride and ammonia borane, *Catalysis Today* 183 (2012) 10–16
- [124] N. Laosiripojana, W. Sutthisripok, S. Assabumrungrat, Synthesis gas production from dry reforming of methane over CeO₂ doped Ni/Al₂O₃: Influence of the doping ceria on the resistance toward carbon formation, *Chemical Engineering Journal* 112 (2005) 13–22
- [125] C.E. Daza, A. Kiennemann, S. Moreno, R. Molina, Dry reforming of methane using Ni–Ce catalysts supported on a modified mineral clay, *Applied Catalysis A: General* 364 (2009) 65–74
- [126] M. Ocsachoque, J. Bengoa, D. Gazzoli, M.G. Gonzalez, Role of CeO₂ in Rh/ α -Al₂O₃ Catalysts for CO₂ Reforming of Methane, *Catalysis Letters* 141 (2011) 1643–1650
- [127] P. Kumar, Y. Sun and R.O. Idem, Nickel-Based Ceria, Zirconia, and Ceria–Zirconia Catalytic Systems for Low-Temperature Carbon Dioxide Reforming of Methane, *Energy & Fuels* 21 (2007) 3113–312
- [128] A. Kambolis, H. Matralis, A. Trovarelli, C. Papadopoulou, Ni/CeO₂-ZrO₂ catalysts for the dry reforming of methane, *Applied Catalysis A: General* 377 (2010) 16–26

- [129] C. de Leitenburg, A. Trovarelli and J. Kaspar, A Temperature-Programmed and Transient Kinetic Study of CO₂ Activation and Methanation over CeO₂ Supported Noble Metals, *Journal of Catalysis*, 166 (1997) 98–107
- [130] P. Kumar, Y. Sun, and R.O. Idem, Comparative Study of Ni-based Mixed Oxide Catalyst for Carbon Dioxide Reforming of Methane, *Energy&Fuels*, 22(6) (2008) 3575-3582
- [131] N. Laosiripojana and S. Assabumrungrat, Catalytic dry reforming of methane over high surface area ceria, *Applied Catalysis B: Environmental* 60 (2005) 107–116
- [132] S. Wang, G.Q.M. Lu, Role of CeO₂ in Ni/CeO₂-Al₂O₃ catalysts for carbon dioxide reforming of methane, *Applied Catalysis B: Environmental* 19 (1998) 267-277
- [133] K. Asami, X. Li, K. Fujimoto, Y. Koyama, A. Sakurama, N. Kometani, Y. Yonezawa, CO₂ reforming of CH₄ over ceria-supported metal catalysts, *Catalysis Today* 84 (2003) 27–31
- [134] V.M. Gonzalez-Delacruz, F. Ternero, R. Pereniguez, A. Caballero, J.P. Holgado, Study of nanostructured Ni/CeO₂ catalysts prepared by combustion synthesis in dry reforming of methane, *Applied Catalysis A: General* 384 (2010) 1–9
- [135] T. Odedairo, J. Chen, Z. Zhu, Metal–support interface of a novel Ni–CeO₂ catalyst for dry reforming of methane, *Catalysis Communications* 31 (2013) 25–31
- [136] Z. Wang, X. Shao, A. Larcher, K. Xie, D. Dong, C.-Z. Li, A study on carbon formation over fibrous NiO/CeO₂ nanocatalysts during dry reforming of methane, *Fuels, Catalysis Today* 216 (2013) 44– 49

- [137] X. Du, D. Zhang, L. Shi, R. Gao, and J. Zhang, Morphology Dependence of Catalytic Properties of Ni/CeO₂, *Journal of Physical Chemistry C*, 116 (2012) 10009–10016
- [138] I. Luisetto, S. Tuti, E.D. Bartolomeo, Co and Ni supported on CeO₂ as selective bimetallic catalyst for dry reforming of methane, *International Journal of Hydrogen Energy* 37 (2012) 15992-15999
- [139] P. Bharali, G. Thrimurthulu, L. Katta, B.M. Reddy, Preparation of highly dispersed and thermally stable nanosized cerium–hafnium solid solutions over silica surface: Structural and catalytic evaluation, *Journal of Industrial and Engineering Chemistry* 18 (2012) 1128–1135
- [140] F. Giordano, A. Trovarelli, C. de Leitenburg, and M. Giona, A Model for the Temperature-Programmed Reduction of Low and High Surface Area Ceria, *Journal of Catalysis* 193 (2000) 273–282
- [141] G.R. Rao, Influence of metal particles on the reduction properties of ceria-based materials studied by TPR, *Bulletin of Materials Science*, 22(2) (1999) 89-94
- [142] A. Laachir, V. Perrichon, A. Badri, J. Lamotte, E. Catherine, J.C. Lavalley, J.E. Fallah, L. Hilaire and F. le Normand, E. Quemere, G.N. Sauvion and O. Touret, Reduction of CeO by Hydrogen Magnetic Susceptibility and Fourier-transform Infrared, Ultraviolet and X-Ray Photoelectron Spectroscopy Measurements, *Journal of Chemical Society, Faraday Transactions*, 87(10) (1991) 1601-1609
- [143] E. Rogemond, R. Frety, V. Perrichon, M. Primet, S. Salasc, M. Chevrier, C. Gauthier and F. Mathis, Preparation of Alumina-Supported Ceria. II. Measurement of Ceria Surface Area after Impregnation with Platinum or Rhodium, *Journal of Catalysis* 169 (1997) 120-131

- [144] G. Kim, Ceria-promoted three-way catalysts for auto exhaust emission control, *Industrial & Engineering Chemistry Product Research and Development* 21(2) (1982) 267–274
- [145] G. R. Rao, B. Mishra, Structural, redox and catalytic chemistry of ceria based materials, *Bulletin of the Catalysis Society of India* 2 (2003) 122-134
- [146] J. Kašpar, P. Fornasiero, and N. Hickey, Automotive catalytic converters: current status and some perspectives, *Catalysis Today* 77 (2003) 419-449
- [147] X. Wang, J.A. Rodriguez, J.C. Hanson, D. Gamarra, A. Martinez-Arias, M. Fernandez-Garcia, Ceria-based Catalysts for the Production of H₂ Through the Water-gas-shift Reaction: Time-resolved XRD and XAFS Studies, *Topics in Catalysis* 49 (2008) 81–88
- [148] P. Djinović, J. Batista, J. Levec, A. Pintar, Influence of morphological, redox and surface acidity properties on WGS activity of CuO-CeO₂ catalysts, *Journal of Chemical Engineering of Japan* 42 (2009) 3-9
- [149] R.J. Gorte, S. Zhao, Studies of the water-gas-shift reaction with ceria-supported precious metals, *Catalysis Today* 104 (2005) 18–24
- [150] L. Tang, M. Salamon, and M. R. D. Guire, Cerium oxide thin films on solid oxide fuel cell anodes, *Science of Advanced Materials*, 2(1) (2010) 79–89
- [151] V.V. Kharton, F.M. Figueiredo, L. Navarro, E.N. Naumovich, A.V. Kovalevsky, A.A. Yaremchenko, A.P. Viskup, A. Carneiro, F.M.B. Marques, J.R. Frade, Ceria-based materials for solid oxide fuel cells, *Journal of Materials Science* 36(5) (2001) 1105-1117

- [152] Y.W. Zhang, R. Si, C.S. Liao, C.H. Yan, C.X. Xiao, and Y. Kou, Facile Alcohothermal Synthesis, Size-dependent Ultraviolet Absorption and Enhanced CO Conversion Activity of Ceria Nanocrystals, *Journal of Physical Chemistry B*, 107 (2003) 10159-10167
- [153] N.M. Zholobak, V.K. Ivanov, A.B. Shcherbakov, A.S. Shaporev, O.S. Polezhaeva, A.Y. Baranchikov, N.Y. Spivak, Y.D. Tretyakov, UV-shielding property, photocatalytic activity and photocytotoxicity of ceria colloid solutions, *Journal of Photochemistry and Photobiology B*. 102(1) (2011) 32-38
- [154] S.K. Meher, G.R. Rao, Tuning, via Counter Anions, the Morphology and Catalytic Activity of CeO₂ Prepared under Mild Conditions, *Journal of colloid and interface science* 373(1) (2012) 46-56
- [155] H. Wu, L. Wang, Shape effect of microstructured CeO₂ with various morphologies on CO catalytic oxidation, *Catalysis Communications*, 12 (2011) 1374-1379
- [156] Tana, M. Zhang, J. Li, H. Li, Y. Li, W. Shen, Morphology-dependent redox and catalytic properties of CeO₂ nanostructures: Nanowires, nanorods and nanoparticles *Catalysis Today*, 148 (2009) 179-183
- [157] F. Sadi, D. Duprez, F. Gérard, A. Miloudi, Hydrogen formation in the reaction of steam with Rh/CeO₂ Catalysts: a tool for characterising reduced centres of ceria, *Journal of Catalysis*, 213(2) (2003) 226-234
- [158] A.B. Kehoe, D.O. Scanlon, G.W. Watson, Role of Lattice Distortions in the Oxygen Storage Capacity of Divalently Doped CeO₂, *Chemistry of Materials*, 23 (2011) 4464-4468

- [159] H.X. Mai, L.D. Sun, Y.W. Zhang, R. Si, W. Feng, H.P. Zhang, H.C. Liu, C.H. Yan, Shape-Selective Synthesis and Oxygen Storage Behavior of Ceria Nanopolyhedra, Nanorods and Nanocubes, *Journal of Physical Chemistry B*, 109 (2005) 24380-24385
- [160] K. Zhou, Z. Yang, S. Yang, Highly Reducible CeO₂ Nanotubes, *Chemistry of Materials* 19 (2007) 1215-1217
- [161] Z. Song, W. Liu, H. Nishiguchi, Quantitative analyses of oxygen release/storage and CO₂ adsorption on ceria and Pt-Rh/ceria, *Catalysis Communications* 8 (2007) 725-730
- [162] E. Rocchini, A. Trovarelli, J. Llorca, G.W. Graham, W.H. Weber, M. Maciejewski and A. Baiker, Relationships between Structural/Morphological Modifications and Oxygen Storage-Redox Behavior of Silica-Doped Ceria, *Journal of Catalysis* 194 (2000) 461-478
- [163] A. Trovarelli, Catalytic Properties of Ceria and CeO₂-Containing Materials, *Catalysis Reviews*, 38(4) (1996) 439-520
- [164] A. Greiner, J.H. Wendorff, Electrospinning: A Fascinating Method for the Preparation of Ultrathin Fibers, *Angewandte Chemie International Edition* 46(30) (2007) 5670-5703
- [165] A. Holmgren, B. Andersson, D. Duprez, Interactions of CO with Pt/ceria catalysts *Applied Catalysis B*, 22 (1999) 215-230

APPENDIX A

EFFLUENT MOLE FRACTIONS DURING REDOX EXPERIMENTS ON COC, ESC AND CPC

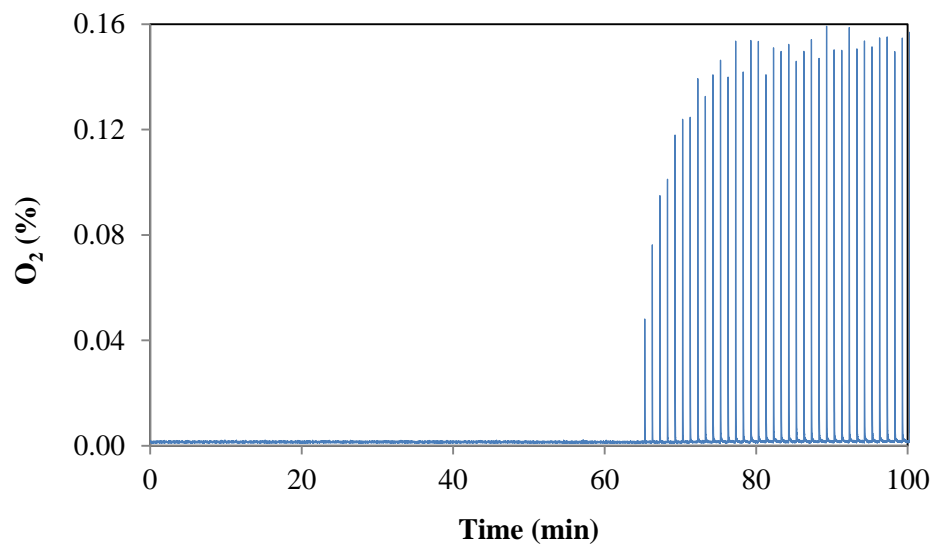


Figure 106. Effluent mole fraction of O₂ during O₂ pulse experiment on COC at 600°C (Step 3)

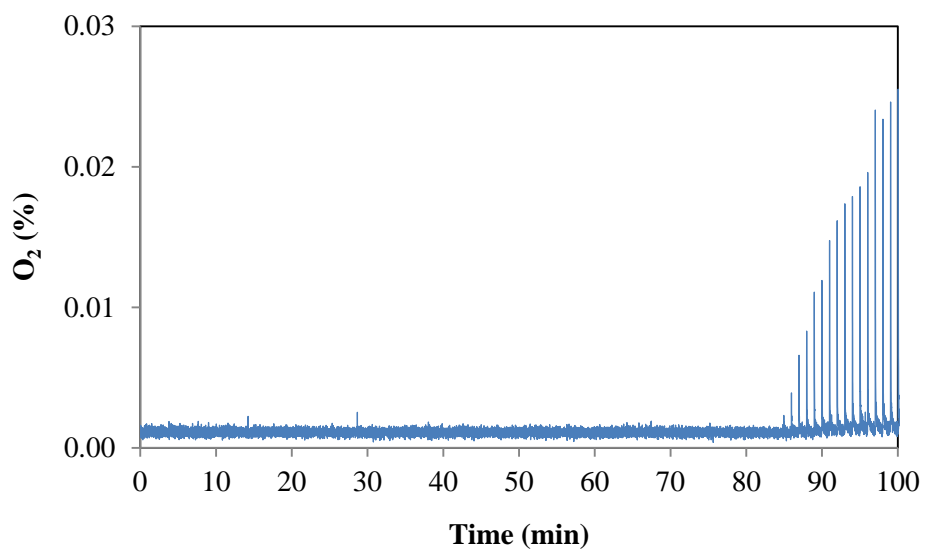


Figure 107. Effluent mole fraction of O₂ during O₂ pulse experiment on ESC at 600°C (Step 3)

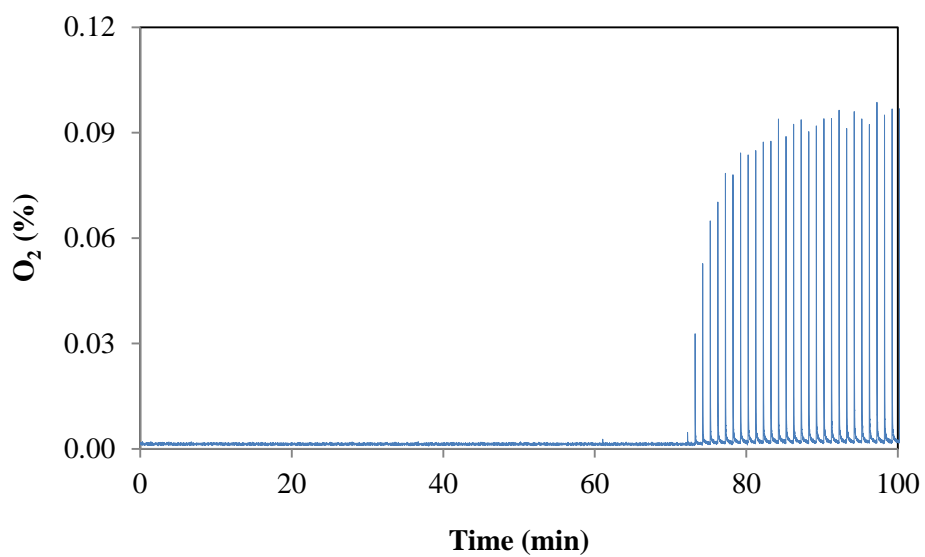


Figure 108. Effluent mole fraction of O₂ during O₂ pulse experiment on CPC at 600°C (Step 3)

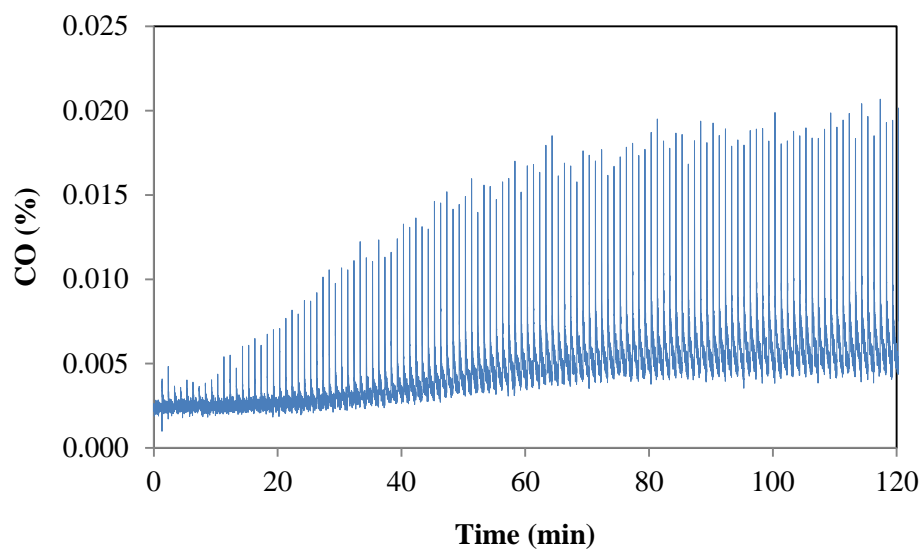


Figure 109. Effluent mole fraction of CO during CO pulse experiment on COC at 600°C (Step 4)

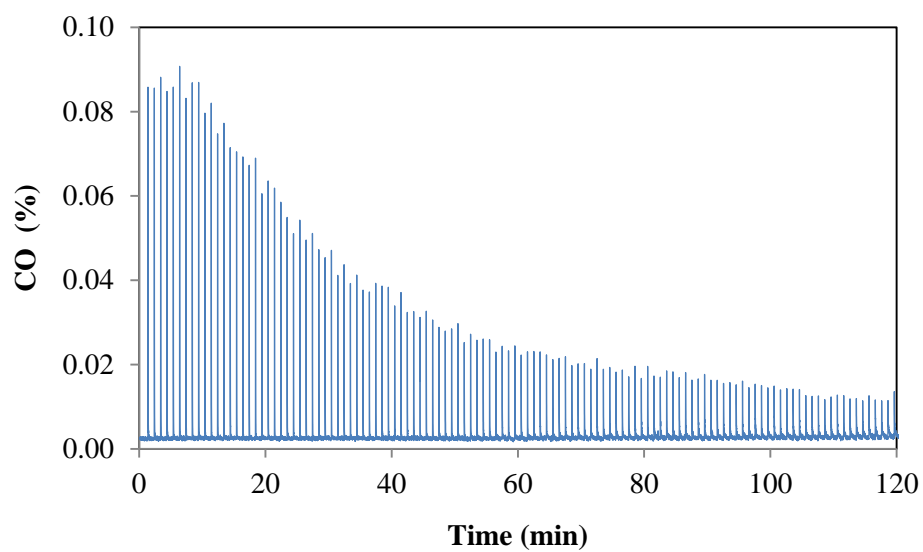


Figure 110. Effluent mole fraction of CO during CO pulse experiment on ESC at 600°C (Step 4)

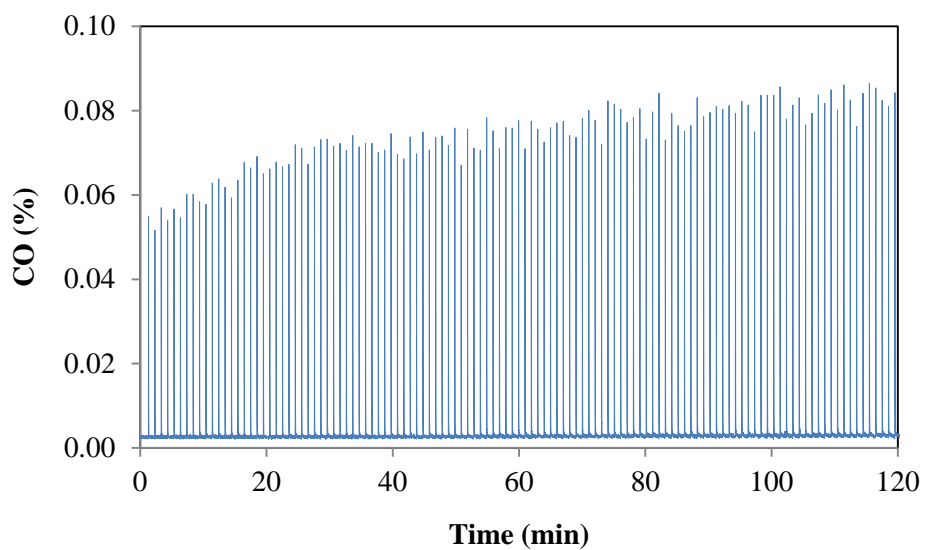


Figure 111. Effluent mole fraction of CO during CO pulse experiment on CPC at 600°C (Step 4)

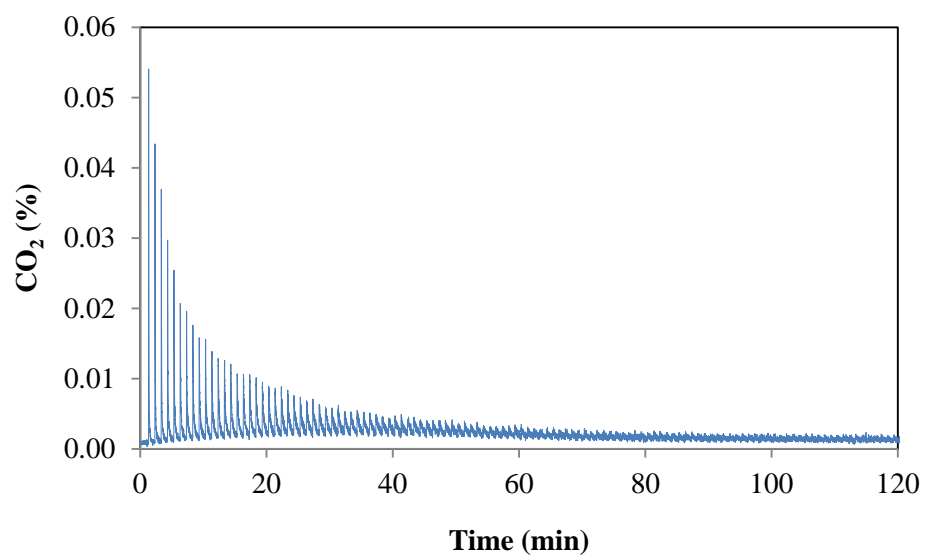


Figure 112. Effluent mole fraction of CO₂ during CO pulse experiment on COC at 600°C (Step 4)

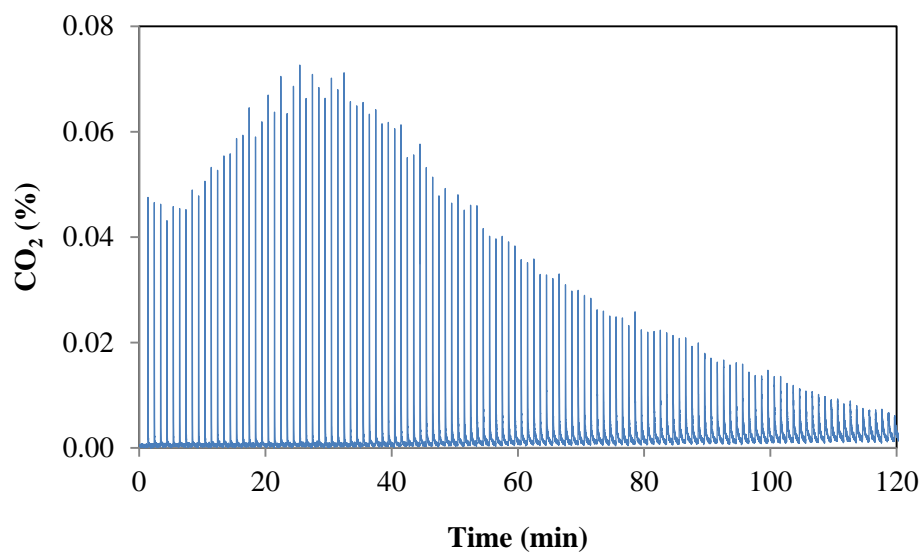


Figure 113. Effluent mole fraction of CO₂ during CO pulse experiment on ESC at 600°C (Step 4)

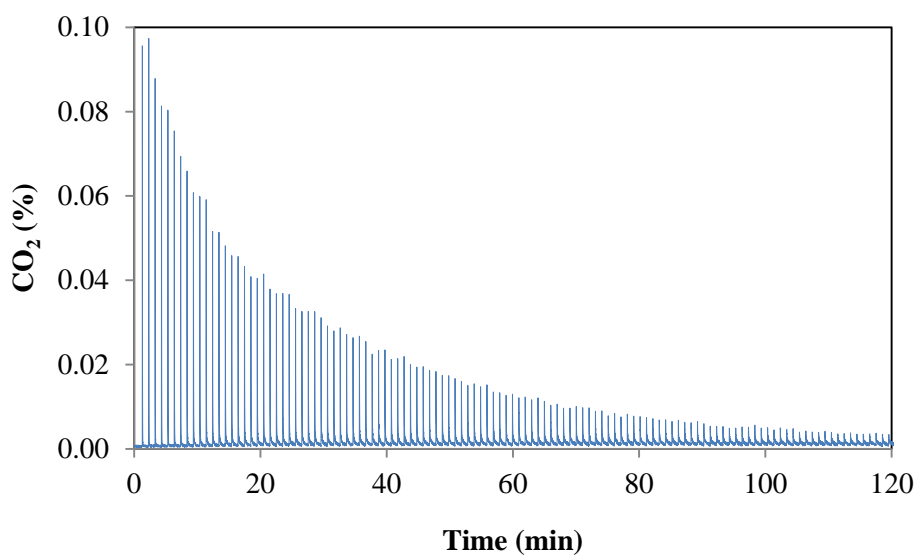


Figure 114. Effluent mole fraction of CO₂ during CO pulse experiment on CPC at 600°C (Step 4)

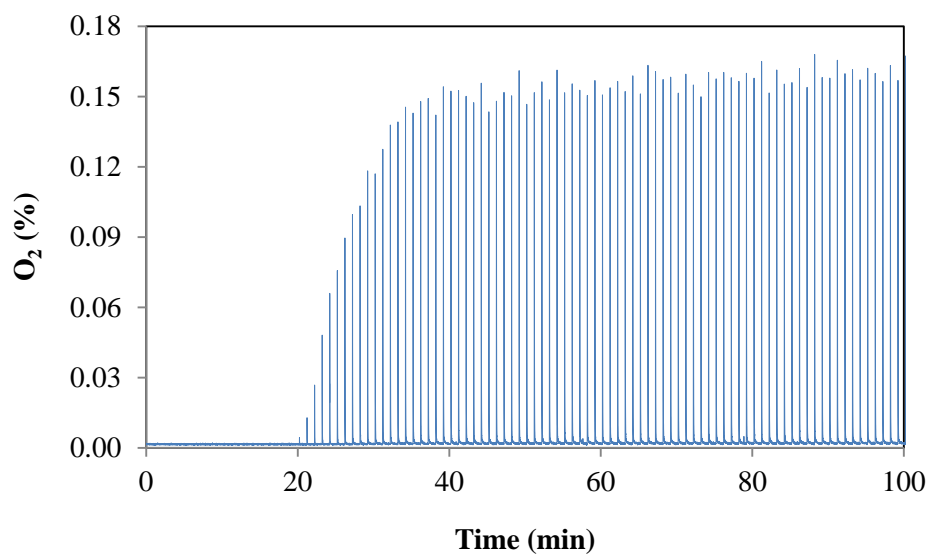


Figure 115. Effluent mole fraction of O₂ during O₂ pulse experiment on COC at 600°C (Step 5)

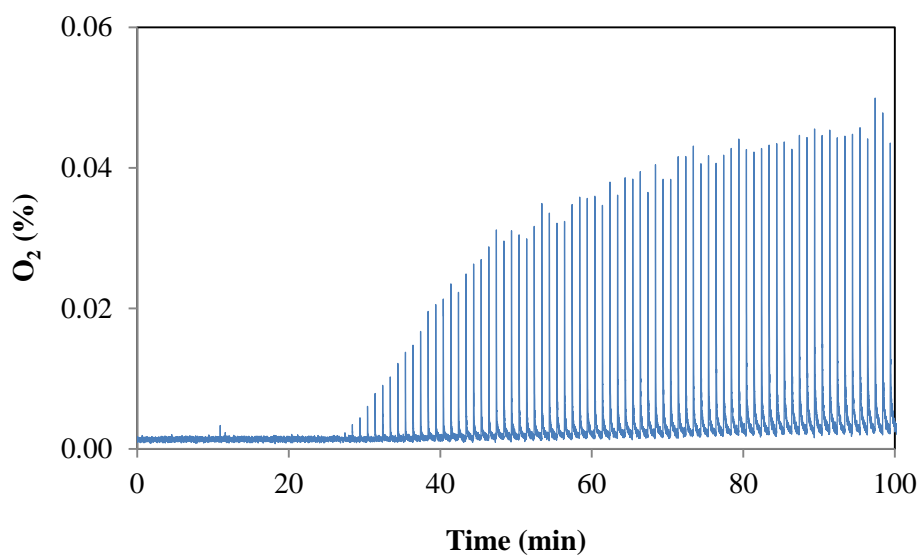


Figure 116. Effluent mole fraction of O₂ during O₂ pulse experiment on ESC at 600°C (Step 5)

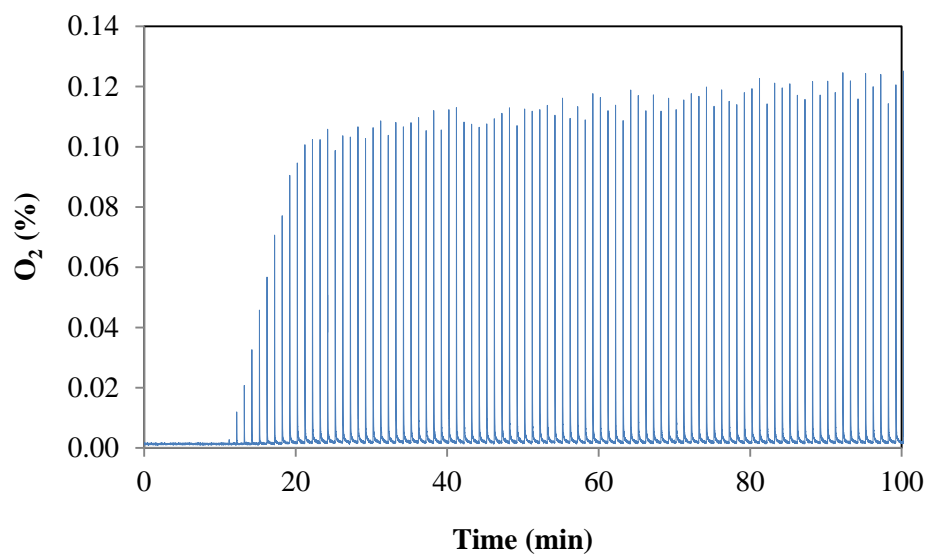


Figure 117. Effluent mole fraction of O₂ during O₂ pulse experiment on CPC at 600°C (Step 5)

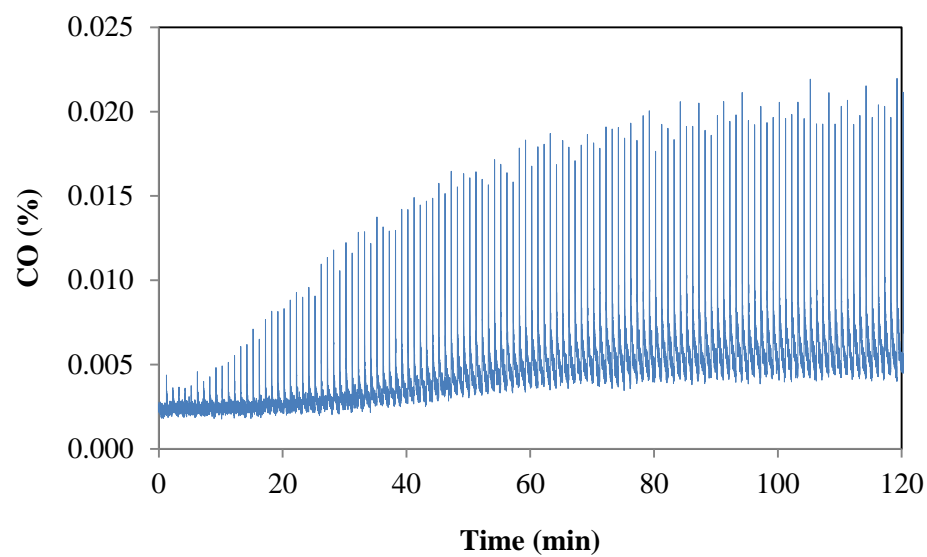


Figure 118. Effluent mole fraction of CO during CO pulse experiment on COC at 600°C (Step 6)

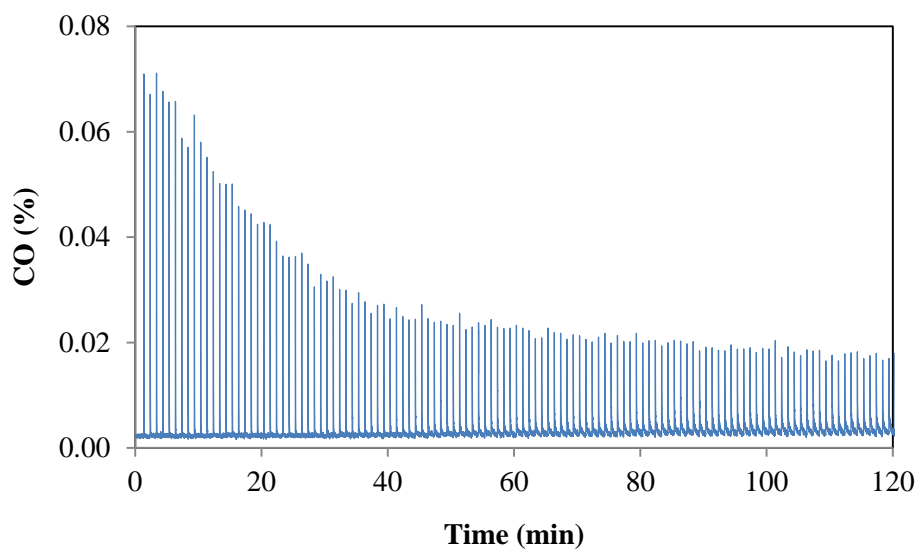


Figure 119. Effluent mole fraction of CO during CO pulse experiment on ESC at 600°C (Step 6)

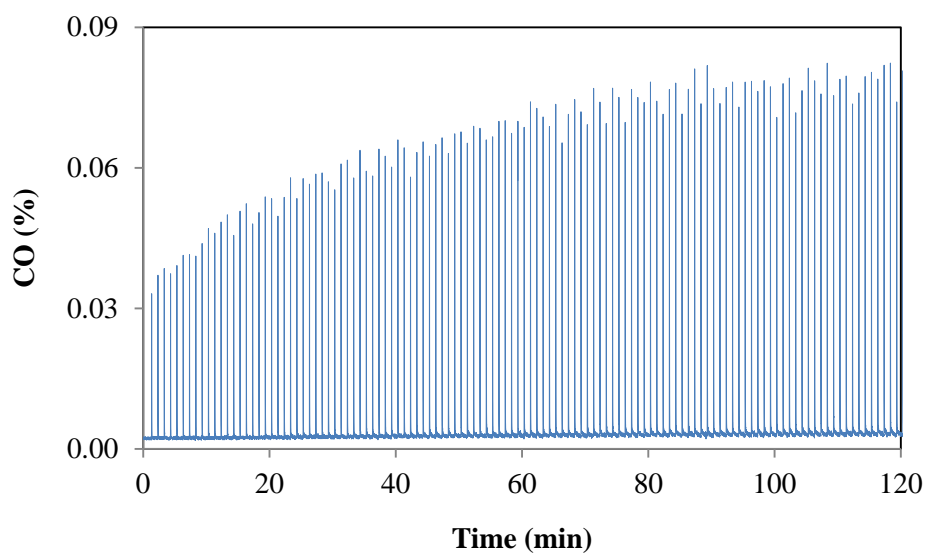


Figure 120. Effluent mole fraction of CO during CO pulse experiment on CPC at 600°C (Step 6)

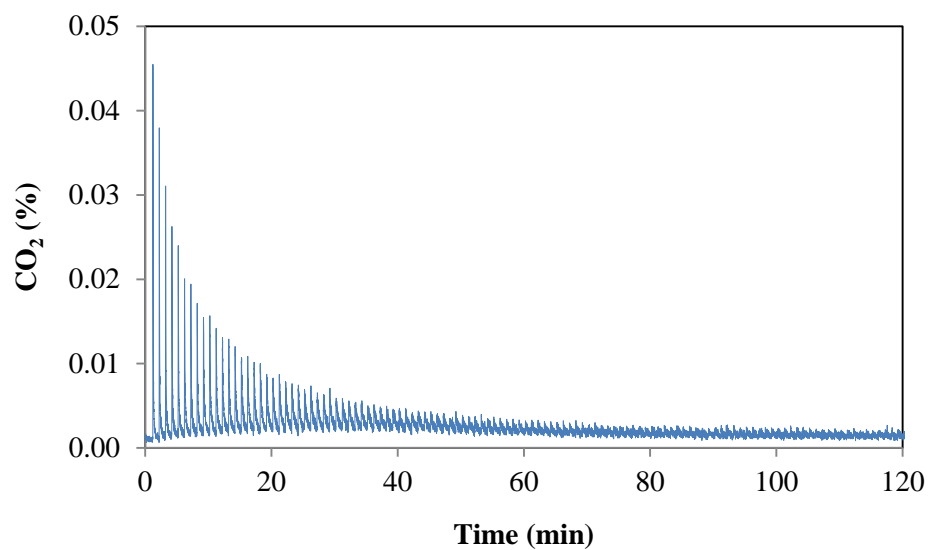


Figure 121. Effluent mole fraction of CO₂ during CO pulse experiment on COC at 600°C (Step 6)

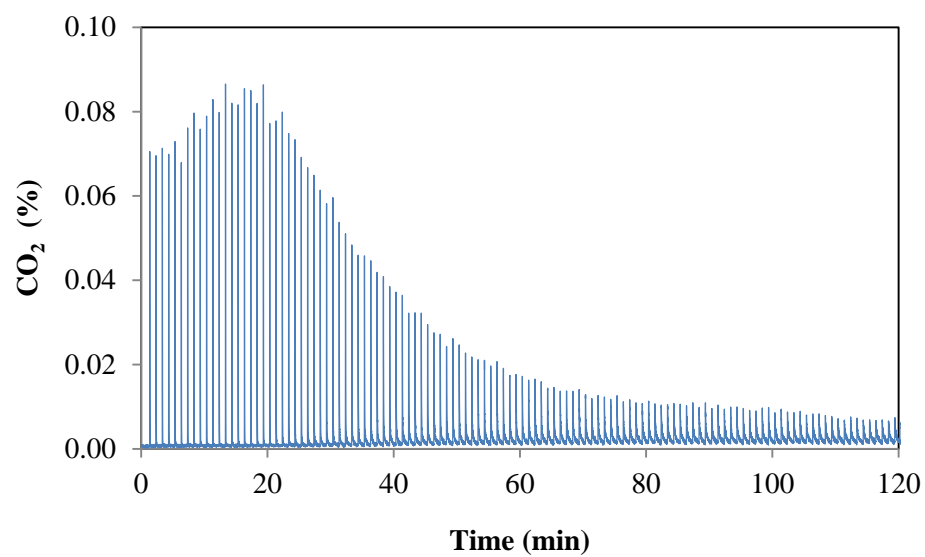


Figure 122. Effluent mole fraction of CO₂ during CO pulse experiment on ESC at 600°C (Step 6)

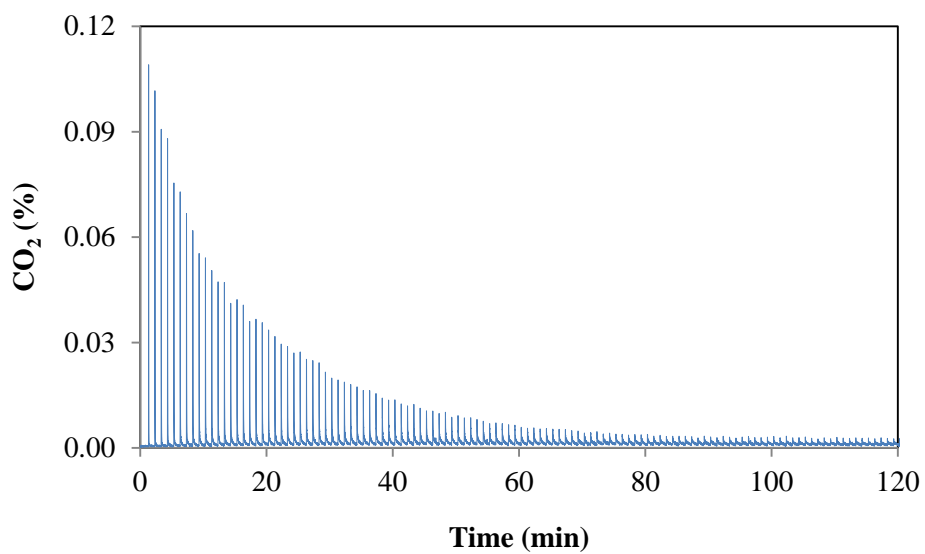


Figure 123. Effluent mole fraction of CO₂ during CO pulse experiment on CPC at 600°C (Step 6)

APPENDIX B

TESTING FOR TRANSPORT LIMITATIONS

Intraparticle mass transfer effects were investigated over Ni/Al₂O₃-700 catalyst by changing the particle size at constant catalyst weight, feed composition and flow rate. It was studied at 700°C and inlet CH₄/CO₂/Ar=1/1/3 stream with a total flow rate of 50 sccm. Since the conversions did not change by decreasing the particle size, it was concluded that pore diffusion resistances were not present.

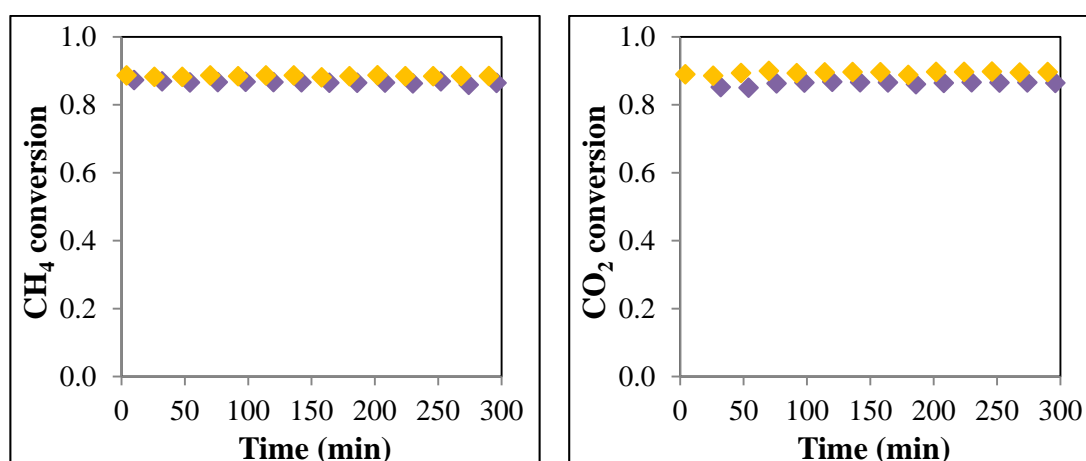


Figure 124. The effect of catalyst particle size on CH₄ and CO₂ conversion,
◆: Ni/Al₂O₃-700-pellet, ◆: Ni/Al₂O₃-700-powder

External mass transfer limitation was investigated over Ni/Al₂O₃-900 catalyst (0.5 mm < particle size < 1 mm) at 700°C and CH₄/CO₂/Ar=1/1/3. The linear velocity was changed by varying inlet flow rate and catalyst weight simultaneously at constant contact time. As seen in Table 17 and Figure 125, CH₄ conversion increased with an increase in total flow rate from 50 sccm to 75 sccm. On the other it was not affected

by further flow rate increase. It was concluded that 50 sccm total flow rate was not sufficient for eliminating the film mass transfer resistance during the harsh reaction conditions of dry reforming of methane reaction.

Table 17. The influence of flow rate on conversion at constant contact time

Catalyst weight (g)	CH ₄ flow (sccm)	CO ₂ flow (sccm)	Argon flow (sccm)	CH ₄ Conversion
0.10	10	10	30	0.86-0.87
0.15	15	15	45	0.97-0.98
0.20	20	20	60	0.98-0.99

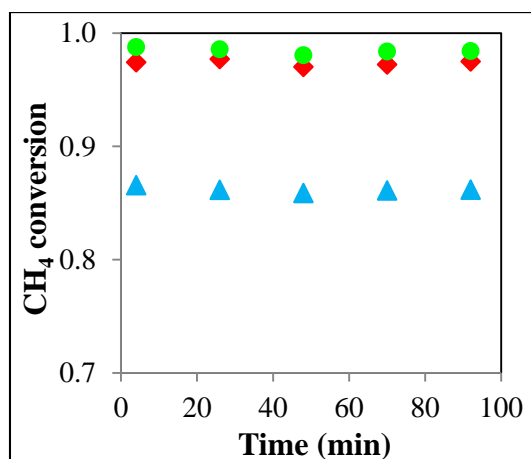


Figure 125. Experimental evaluation of the effect of interphase mass transport

▲ : W=0.1 g and F=50 sccm, ◆ : W=0.15 g and F=75 sccm,
● : W=0.2 g and F=100 sccm

CURRICULUM VITAE

Hale Ay
Middle East Technical University
Department of Chemical Engineering
06800 Ankara/Turkey
haleay.che@gmail.com

Personal Information

Nationality: Turkish (TC)

Date of birth: 07.08.1983

Marital status: Single

Education

Bachelor of Science Degree: Chemical Engineering, METU, 3.40/4.00 (2006)

Master of Science Degree: Chemical Engineering, METU, 3.64/4.00 (2008)

MS Thesis Topic: Single and Multicomponent Ion Exchange of Silver, Zinc and Copper on Zeolite 4A

Doctor of Philosophy: Chemical Engineering, METU, 3.86/4.00 (2014)

PhD Thesis Topic: Carbon Dioxide Reforming of Methane on Ni-based Bimetallic Catalyts

Professional

2006-2013, Teaching and Research Assistant, Department of Chemical Engineering, METU, Turkey

15 November 2012-15 November 2013, Scholar in TUBITAK 1002-112M561 Project- Carbon Dioxide Reforming of Methane on Ni-based Bimetallic Catalyts

1-15 April 2011, Visiting Scientist, Department of Inorganic Chemistry, Technical University of Darmstadt, Germany

18 April-30 June 2011, Visiting Scientist, Department of Industrial Chemistry, Ruhr University Bochum, Germany

National and International Conference Presentations

H. Ay, H. Yücel, 'Single and Multicomponent Ion Exchange of Silver, Zinc and Copper on Zeolite 4A', EMCC-6 (6th Chemical Engineering Conference for Collaborative Research in Eastern Mediterranean Countries), Antalya, Turkey, March 2010, Poster presentation

H. Ay, D. Üner, 'Carbon Dioxide Reforming of Methane to Synthesis Gas Over SBA-15 Supported Co-Ni Catalyst', NCC-3 (3rd National Catalysis Conference), Zonguldak, Turkey, May 2010, Poster presentation

H. Ay, D. Üner, 'Effect of Co on the Performance of Ni/Al₂O₃ Catalysts in Dry Reforming of Methane', EFCATS Summer School (Catalysis & Surface Science for Renewables & Energy), İzmir, Turkey, September 2010, Poster presentation

H. Ay, D. Üner, 'Microcalorimetric and FTIR Studies of Al₂O₃ supported Ni, Co and Ni-Co Catalysts', EuropaCat X, Glasgow, Scotland, September 2011, Poster presentation

H. Ay, D. Üner, 'What is the Precursor for Coke Formation During Dry Reforming of Methane over Ni-based Catalysts?' NCC-4 (4th National Catalysis Conference), Kocaeli, Turkey, March 2012, Poster presentation

H. Ay, M. Naumann, K. Kähler, T. Franzke, J. Schneider, M. Muhler, D. Üner, 'The effect of morphology on using CO₂ as oxidizing agent for CeO_x synthesized via electrospinning', ICC-5 (5th International Catalysis Conference), Munich, Germany, July 2012, Poster presentation

H. Ay, D. Üner, 'How does Cobalt Improve the Performance of Ni-based Catalysts in Dry Reforming of Methane Reaction?' , UKMK 10 (10. National Chemical Engineering Conference), İstanbul, Turkey, September 2012, Oral presentation

H. Ay, D. Üner, 'Creating Metallic Sites for Methane Adsorption by Polyol Process in Dry Reforming of Methane' , EuropaCat XI, Lyon, France, September 2013, Poster presentation

H. Ay, D. Üner, 'Preparation of Ni/Al₂O₃ Catalysts by Polyol Method for Carbon Dioxide Reforming of Methane', NCC-5 (5th National Catalysis Conference), Adana, Turkey, April 2014, Oral presentation

H. Ay, D. Üner, 'Carbon Nanotubes as Side Product of Dry Reforming of Methane', ISCRE 23, 23rd International Symposium on Chemical Reaction Engineering, Bangkok, Thailand, September 2014, Abstract was accepted as Oral presentation.

Publications

H. Ay, D. Üner, ‘Synthesis and Characterization of Al₂O₃ Supported Ni Polyol Catalysts for Dry Reforming of Methane’ manuscript in preparation

H. Ay, D. Üner, ‘Carbon Nanotubes as Side Product of Dry Reforming of Methane’ manuscript in preparation

H. Ay, D. Üner, ‘CeO₂ supported Ni, Co and Ni-Co Catalysts for Dry Reforming of Methane’ manuscript in preparation

Foreign Languages

- Advanced English

Foreign Language Proficiency Examination for State Employees: 90/100 (May 2009)

Interuniversity Board Foreign Language Examination: 97.5/100 (March 2009)

Foreign Language Examination: 86.25 (April 2013)

- Beginner German

Computer skills

Microsoft Office (Word, Excel, PowerPoint, Front Page)

Origin, Fortran, Chemcad, Polymath

Laboratory Equipment Usage Ability

Mass spectrometry

Gas Chromatography

FTIR (Fourier Transform Infrared Radiation)

Microcalorimetry

BET (Surface Area Measurement)

TGA (Thermal Gravimetric Analysis)